Breast Cancer Targeted Therapy Using ZnO Nanostructures

Basmah Othman

Department of materials

Imperial College London

This dissertation is submitted for the fulfilment of the degree of

Doctor of Philosophy (PhD)

2014

Abstract

There are an estimated 14.1 million cancer cases around the world every year, with this number expected to increase to 24 million by 2035. Breast cancer is the most common cancer in the UK, with 50,000 new cases per year. Due to the limitations and side effects of most available anticancer therapy, there is an urgent need to develop new anticancer agents. There has been significant progress in utilizing nanotechnology in several areas of cancer care, including *in vitro* diagnostics, imaging, and therapy. The first generation of novel nanomaterials (NMS) as anticancer agents has successfully entered a widespread use. Recent studies demonstrate that zinc oxide (ZnO) NMS hold a considerable promise as potential anticancer agents. In addition to the novel size and shape properties, ZnO NMS exhibit a pH-sensitive dissolution. These properties of ZnO NMS could potentially allow increased cancer selectivity, changes in pharmacokinetics and amplification of cytotoxic effects. The selectivity of ZnO NMS can be further induced by attaching of cancer target reactive-ligands.

The aim of this study is to test the hypothesis that zinc oxide nanoparticles (ZnO NPs), grafted with RGD peptide, would target tumours that up- regulate integrin alpha v beta 3 (αvβ3) receptors, and that targeting using this peptide would further enhance the antitumor efficacy of ZnO. Therefore, the toxicity and uptake of bare zinc oxide nanostructures and their RGD-targeted counterparts to a panel of malignant breast cancer cell lines was investigated. Two breast cancer cell lines of differing metastatic and invasive capacities were used: MDA-MB-231 cell line that is oestrogen receptor-negative and highly invasive; and, MCF-7 cell line that is oestrogen receptor-positive and non-metastatic. Healthy epithelial MCF-10-2A cell line was used as a control. To test the toxicity of the ZnO NPs (bare and RGD targeted), a combination of cell viability assays including; Alamar Blue, LDH, and ATP assays was used. Flow Cytometry was used to detect necrosis and apoptosis. The intracellular uptake of the ZnO NPs (bare and RGD targeted) was investigated and compared using different correlative microscopy techniques; Transmission electron microscopy (TEM), scanning electron microscopy (SEM), and confocal microscopy. Furthermore, the protein corona formed around the particles was analysed using mass spectroscopy (MS). The bare and RGD targeted ZnO NPs exhibited dose and time dependent

toxicity to the MCF-7 and the MDA-MB-231 cell lines in a concentration range of 10-100 μg/ml. Significant differences in the responses of the MCF-7 and MDA-MB-231 cells after exposure to the bare ZnO NPs were observed in the LDH assay and the Alamar Blue assays. Cell death had features of necrosis and apoptosis with mitochondrial structural changes. RGD-targeting of the ZnO NPs was efficient and successfully increased the toxicity of the ZnO NPs to breast cancer cells at lower doses, while preserving the viability of the healthy cells at the same dose and exposure time indicating that a potential therapeutic dose window exists. In the Alamar Blue viability assay, for example, the IC_{50} values of the bare and targeted ZnO NPs after 24 h exposure to the MDA-MB-231 cells were 30 and 22 μg/ml, respectively. In cell free experiments, the bare ZnO NPs dissolved very rapidly in simulated body fluid of lysosomal pH 5.2, whereas they were more stable at pH 7.4. Confocal and transmission electron microscopy confirmed uptake of both classes of ZnO NPs and a rise in intracellular Zn^{2+} concentration prior to cell death after exposure to ZnO NPs. RGD-grafted ZnO NPs were more associated to MDA-MB-231 cells possibly by binding to integrin αvβ3 compared to the bare ZnO. The kinetics of intracellular dissolution of the RGD-targeted and bare ZnO NPs showed differences. The bare ZnO NPs, showed a clear time dependent increase in intracellular dissolution while the RGD-targeted ZnO NPs showed very low intracellular dissolution with time and then a sudden burst of ionic zinc. Preliminary studies were also performed on one dimensional ZnO nanowires and data are in broad agreement with the NP study, showing dose and time dependent toxicity in the MDA-MB-231 cells. This research establishes a successful NP-based platform for cancer targeting and therapy.

Author's Declaration

I hereby declare that except where specific reference is made to the work of others, the contents of this dissertation are original and have not been submitted in whole or in part for consideration for any other degree or qualification in this, or any other University. This dissertation is the result of my own work and includes nothing which is the outcome of work done in collaboration, except where specifically indicated in the text.

Copyright Declaration

Dedication

I dedicate this thesis with love

To

My mother Ibtisam

And to

The soul of my father Abd Alraheem

For their constant support and unconditional love

Acknowledgments

I would like to express my special appreciation and thanks to my supervisors Dr. Mary Ryan and Dr. Alexandra Porter for their continuous support throughout this work. Their understanding, encouragement and personal guidance have provided good bases for the present study. They were my primary resource for getting my science questions answered, helped me to grow as a researcher and were instrumental in helping me crank out this thesis in a few weeks.

I will forever be thankful to Dr. Jasmeen Merzaban, I was lucky to work under her supervision as part of my PhD project collaboration with King Abdullah University for Science and Technology (KAUST). Her scientific guidance, support, and hospitality have been priceless.

I owe sincere gratitude to Dr. Christeena Greenwood. Her wide knowledge, suggestions, and many insightful discussions have been of great value for me.

I warmly thank the microscopy, analytical, and proteomics core lab members at KAUST, namely Rachid Sougrat, Guangchao Wang, Tahir Yabish, Bashir Warsama, and Aswini Panigrahi. I would also like to thank the electron microscopy group at materials department at Imperial College London namely Ecaterina Ware, Mahmoud Ardakani, Catriona McGilvery, and Angela Goode.

I would like to express sincere thanks to my colleague and friend at Imperial College London, Ioannis Theodorou, for helping in preparing the ZnO nanowires, and for his continuous support. My gratitude is also extended to my colleague at KAUST, Ayman elkhodiery, who introduced me to the tissue culture labs at KAUST and was always there for effective discussions. I also thank my friends (too many to list here but you know who you are!) for their love and constant support when I encountered difficulties. Mustafa Osama is a wonderful and generous friend who I admire his positive outlook and his ability to smile despite the situation. Ahmed Osama, Thamer Nouh, Mohammed Shaqora, and Manal Andejani: I will never forget the many wonderful dinners, trips and fun activities we have done together.

Finally, my deepest gratitude goes to my parents and my brothers and sisters for their unflagging love and support throughout my life; I am indebted to my mother, she always provided unconditional love and care; I do not have suitable words that can fully describe her everlasting love to me. Thank you with all my heart and soul.

List of abbreviations

2D	3- dimensional
3D	3- dimensional
7AAD	7-Aminoactinomycin D
ATCC	American Type Culture Collection
ATP	Adenosine triphosphate
BEGM	Bronchial epithelial growth medium
BSA	Bovine serum albumin
CME	Clathrin mediated endocytosis
Cy5	Indotricarbocyanine dye
DDS	Drug delivery systems
DMEM	Dulbecco's Modified Eagle's Medium
DMEM:F-12	A 1:1 mixture of Dulbecco's Modified Eagle's Medium (DMEM) and Ham's F-12 medium
DNR	Daunorubicin
EDX	Electron dispersive X-ray spectroscopy
FBS	Fetal bovine serum
FDA	Food and Drug Administration
FITC	Fluorescein isothiocyanate
GFP	Green fluorescent protein
HBSS	Hank's Balanced Salt Solution
HEPES	4-(2-hydroxyethyl)-1-piperazineethanesulfonic acid
HSA	Human serum albumin
IC_{50}	Median lethal concentration
IgG	Immunoglobulin
L-15	Leibovitz's L-15 medium
Lyso-SBF	Lysosomal simulated body fluid
MEM	Minimum Essential Medium
MES	2-(N-morpholino) ethane-sulfonic acid
NMS	Nanomaterials
NPs	Nanoparticles
NWs	Nanowires
PE	Phycoerythrin

PIPES	Piperazine-N,N'bis[2-ethanesulfonic acid]
PRMI-1640	Roswell Park Memorial Institute medium
QS	Quantum dots
RT	Room temperature
SEM	Scanning electron microscopy
TEM	Transmission electron microscopy

Table of contents

1 Introduction

Chemotherapy is one of the main systemic treatments for early breast cancer, and its use has led to an improvement in the survival of women diagnosed with breast cancer. However, the non-specific systemic delivery causes damage to normal unaffected tissue resulting in both short- and long- term adverse effects including, myelosupression, heart failure and infertility. Given its non-specific nature and the resultant problems, there is a clear and urgent need to devise new therapies which specifically target and eliminate cancer cells. The homing of the drug, specifically to the cancer cells, reduces the toxicity and increases the antitumor efficacy [1].

Zinc is an essential trace element involved in a number of biological processes [2, 3]; however an increase in the local zinc concentration has been shown to cause cell death [4]. It has been reported that Zn^{2+} has many effects on cancer cells, which includes alteration in gene expression, reduction in cellular metabolism and induction of apoptosis [5]. It has also been reported that Zn^{2+} exhibits anti-apoptotic effects in breast cells. The induction of apoptosis by zinc in cancers appears to be cell type specific [5]. The apoptotic effects of zinc suggests that ZnO nanostructures can be applied as an anticancer agent and provide a potential target for the development of anti-tumor agents [5]. Even more striking are *in vitro* observations indicating that ZnO nanoparticles (NPs) can preferentially kill cancer cells with significantly less toxicity against normal cells [6]. Despite the significant promise of this technology, the clear therapeutic and imaging potential of ZnO NPs *in vivo* has been undermined by their susceptibility to protein fouling and their lack of colloidal stability [7, 8]. These concerns need to be addressed before this technology can be translated to clinic. In particular, it is crucial to characterize the nanomaterials at the point of exposure to cells as changes in the aggregation state or surface chemistry of the nano ZnO could drastically alter their reactivity with cells.

The anti-cancer properties of nanomaterials can be improved by attaching cancer targeting reactive-ligands or antibodies, potentially allowing amplification of cytotoxic effects [9]. ZnO NMS are known to be very sensitive to dissolution in acidic conditions: the phase-solubility diagram of ZnO indicates that it will dissolve below pH 6.7 at physiological temperature and will dissolve rapidly in the acidic pH of the lysosomes (pH~5.7) [10] or in

the acidic (pH~5-6) cancer environment , whereas they will not dissolve in the environment of healthy cells (pH 7.2) [11]. However no prior studies have tested the potential of using fluorescent RGD-ZnO nanomaterials to treat breast cancer. It is hypothesized that, with the right targeting of the ZnO nanostructures to the αvβ3 integrin on the breast cancer cells, the functionalised ZnO NPs can be targeted to cancer cells, specifically kill these cells and a lower therapeutic dose of ZnO NMS could probably be achieved. This approach could probably increase the therapeutic window of ZnO for cancer therapeutics and bioimaging.

Bare ZnO NPs have recently been used to destroy breast cancer cells. Release of Zn^{2+} ions, following incubation of ZnO NPs with MCF-7 breast cancer epithelial cells, leads to generation of reactive oxygen species, resulting in damage to the plasma membrane and mitochondria leading to apoptosis [11]. Another study exploited the intrinsic fluorescent property of ZnO nanowires (NWs) to track the tumour targeting ability of the ZnO NWs *in vivo* [12]. The ZnO NWs were functionalized with an RGD group which selectively binds to the integrin αvβ3 on human glioblastoma cells *in vivo* [12]. However, neither of these studies demonstrated selective toxicity of cell targeting ZnO nanostructures to breast cancer cells, or provided direct evidence that the ZnO NMS are targeted, internalised by the cancerous cells and cause cell death. Furthermore little evidence was provided about the mode by which the ZnO nanostructures cause cell death or the heterogeneity in the resistance between cancer cell types (oestrogen receptor positive and triple negative) to ZnO exposure.

This PhD project aims to further investigate the *in vitro* cancer cell specific targeting and cytotoxicity of bare and cancer cell targeted ZnO nanostructures, and to address the role of physicochemical properties of ZnO NWs such as solubility on their interaction with live cells. The development of our proposed ZnO NP delivery system would reduce the side effects associated with chemotherapy, leading to an improvement in the quality of life of women receiving this treatment, as well as limiting the associated morbidity and mortality.

Thorough characterisation of the physicochemical properties of the ZnO NPs has been performed alone, and in different physiological environments (varying pH, proteins, cell culture medium), to provide an accurate characterisation of the particles at the point of exposure to the cells (Chapter 3). Such characterisation is frequently neglected in the

literature and could provide important information which explains the bioreactivity of the particles *in vitro*. A combination of biochemical assays (Chapter 4), electron and confocal microscopy techniques (Chapter 5) have enabled direct correlation between the uptake and dissolution of the ZnO nanostructures with their effect on the cell health. Protocols were developed to track the dissolution from bare and targeted ZnO NPs inside live breast cancer cells in the confocal optical microscope. This enabled us to correlate ZnO dissolution at the nanoscale, with any changes in cell metabolism inside the live cells in confocal microscope at the cellular level.

The composition of protein corona formed from human plasma protein onto the surface of the bare ZnO NPs at different conditions of temperature, centrifugation force and composition, as well as concentration of human plasma protein were characterised (Chapter 6) to assess how the properties of the particles could become altered *in vivo*.

High aspect ratio ZnO NWs were fabricated by electrochemical deposition into high quality polycarbonate membrane filters and on glass substrates (Chapter 7). The obtained wires were successfully liberated from their polycarbonate templates and glass substrates. The ZnO NWs were characterised using scanning electron microscopy (SEM) and transmission electron microscopy (TEM). Detailed and in-depth analysis of the experimental results shows that the wires have a uniform diameter of 37 nm and are 330 nm long. The ZnO NWs were suspended in ethanol for cell exposure experiments. The ZnO NWs resulted in a dose and time dependent toxicity in the MDA-MB-231 cells.

2 Literature review

The goal of this chapter is to provide a background to the subject. In depth critique of the literature is provided in greater detail in the introduction to each chapter.

2.1 Nanotechnology

The prefix “nano” is derived from the Greek “nanos” meaning “dwarf” [13]. The term ‘nano’ is a unit prefix denoting 10^{-9} for the metric unit of length ‘nanometre’, which denotes one billionth of a meter or 10^{-9} m. Nanotechnology is the manipulation of matter with at least one dimension of 100 nanometres or less. Nanomaterials (NMS) are engineered structures with reduced particle size and increased surface area with high proportion of atoms exposed to the surface. Consequently, NMS have different physical and chemical properties than their bulk forms. Nanotechnology is expected to revolutionize many aspects of human life offering extraordinary opportunities in various technological fields such as electronics, energy management, and information technology, as well as in the pharmaceutical and medical fields. It is projected to become a $1 trillion market by 2015 [14]. However, this increased manufacture and use of NMS has raised serious concerns about their safety for human health and the environment. It has been suggested that certain classes of NMS could become “The asbestos of the 21st Century” [15]. Because of these concerns, a part of nanoscience ‘Nanotoxicology’ has emerged to understand what specific properties of nanomaterials could lead to harmful effects.

2.1.1 Nanotoxicology

At the nano-scale, materials can display unique physical and chemical properties that are neither those of bulk materials, nor those of molecular compounds, therefore they will presumably have unique interactions with biological systems and the environment and could be potentially toxic. Consequently, detailed studies need to be carried out to precisely characterize the physicochemical properties of NMS, their internalization, intracellular distribution, biostability, and to evaluate the possible mechanisms underlying their toxicity. It is very important to ensure safe manufacture and marketing of engineered nanoproducts in particular if they come in contact with the human body. To fully understand the toxic potential of NMS, a multidisciplinary collaboration involving material scientists, physicians

and toxicologists is essential. Indeed, a proper understanding of nanotoxicity could also have a positive impact for achieving their efficient utilization and design in medicine. For example, the unique ability of some NMS to preferentially dissolve locally inside cancerous cells only, as will be shown in this work, and to initiate programmed cell death, could be used as new cancer therapy [14].

The evaluation of the potential hazard of NMS started in 1992 [11]. The toxicity of NMS has been reported using chemical (cell-free) and biological (*in vivo* and *in vitro*) assays, however, the results of the reports were inconclusive. There is an urgent need to develop and validate simple high-throughput *in vitro* assays to determine NMS toxicity because using laboratory animal (*in vivo*) tests could be impossible for both ethical and economic reasons [16-18]. *In vitro* studies using different mammalian cells showed that NMS can produce cytotoxic, genotoxic, inflammatory and oxidative stress responses. Despite collecting voluminous data from *in vitro* and *in vivo* studies, knowledge about the interaction of NMS with biological systems is still in its infancy [19]. Current comparison between *in vitro* and *in vivo* studies found little correlation and the relevancy of the *in vitro* results is questionable [20]. *In vitro* toxicity of NMS has been observed at concentrations much higher than the trace tissue concentrations in animals. The toxicological effects from *in vitro* and *in vivo* studies of some widely used NMS from about 101 publications were summarised by Dhwan and Sharma [19]. The toxic effects ranged from induction of inflammatory responses and oxidative stress to DNA damage and genotoxicity. In response to the recent findings that suggest the use of multiple *in vitro* assays to assess the toxicity of NMS, Kroll *et al*. [20] screened the toxicity of 23 engineered NMS using ten cell lines and three different standardised assays. They concluded that the toxic outcomes from exposure to NMS is not only cell-type-specific, but also depends on the particle type used, as well as on the toxicity endpoint measured. The toxicity of metal oxide NPs, proposed for use in industrial production, has been extensively studied [21-23].

2.1.2 Factors affecting toxicity of nanomaterials

The hazard potential of NMS and their biological activity depends on a combination of material physico-chemical properties rather than a single property as suggested by many *in vitro* toxicity assays [20, 24, 25]. The known indicators of the biological impact of NMS

include the size (surface area and size distribution) [26], chemical composition (purity, crystallinity, *etc.*), surface structure (surface reactivity, surface groups, inorganic or organic coatings, etc.), solubility (in lipid, aqueous, *in vitro* media), shape, and reactive oxygen species generation [14, 22, 27, 28]. The cellular uptake, protein binding, translocation from portal of entry to the target site, and the possibility of causing tissue injury are all determined by these NMS parameters [14]. Therefore, a thorough understanding of NMS specific properties is required for interpretation of toxicological results. The mentioned physicochemical properties of NMS can change with the method of production, preparation process, and storage media and also when the NMS are introduced into the culture media or organism. Consequently, physicochemical characterisation methods should be carefully adapted, and the guidelines for sample preparation, dosimetry, degradation and fate should be newly developed or revised. Recently, many studies emphasized on the importance for conscious characterisation methods beyond the naive application of characterisation methods that claim to cover the relevant parameters of nanotoxicology [22, 29-31].

From toxicological perspective, the particle size and surface area are one of the proposed key material characteristics. The size is a critical key factor that determines translocation across the cell membrane of cells [26, 32, 33]. As the size of a particle decreases, its surface area increases which allows a greater proportion of its atoms or molecules to be displayed on the surface, rather than the interior of the material [14]. Shrinkage in size may create discontinuous crystal planes that increase the number of structural defects, as well as disrupt the well–structured electronic configuration of the material, resulting in altered electronic properties. This could create reactive sites on the surface of the material by exposing specific surface groups. These surface groups can make the NMS hydrophobic or hydrophilic, or catalytically active or passive [14]. Therefore full characterisation of the NMS must be complimented with the actual state of dispersion of the NMS, as well as any changes in their physicochemical properties, in biological media.

2.2 Nanomedicine and nanotechnology in cancer applications

Nanomedicine refers to the application of nanotechnology to medical fields, which aims to set new tools, devices and therapies for the treatment of human diseases. Oncology has benefited and been influenced by this field for several years [34]. The applications of NPs for improved therapeutics are at the forefront of cancer nanotechnology. The advantages of nanoparticle therapeutics are based on enhanced efficacy and reduced side effects, due to more targeted localization in tumours and active cellular uptake.

Various types of nano-sized drug carriers, such as liposomes, polymeric micelles, dendrimers, superparamagnetic iron oxide crystals, and colloidal gold, have been investigated in cancer therapy [35]. Liposomes, which are microscopic phospholipid bubbles with a bilayered membrane structure [36], were the premier drug-delivery NPs in clinical use [37]. Doxorubicin (DNR), a powerful and toxic chemotherapeutic was encapsulated in liposomes and approved for the treatment of metastatic breast cancer and recurrent ovarian cancer since 1995 [38]. Abraxane^{TM}, an albumin-bound form of paclitaxel, is another chemotherapeutic agent approved in January 2005 [39]. Both formulations increased efficacy and reduced toxicity of the anticancer agents. Based on these success stories, the FDA has approved several investigational new drug (IND) applications for the treatment of several types of cancers. Over 20 nanoparticle therapeutics have been approved by the FDA for clinical use [40]. Examples of FDA approved nano-therapeutics for clinical use in breast cancer treatment, as well as nanoscale systems for systemic cancer therapy are listed in Table 1 and Table 2, respectively.

Liposomes and other drug delivery systems (DDS) have often been criticized on the basis of their pharmaceutical and commercial qualities such as complexity, cost, storage stability, and control over the rate and extent of drug bioavailability [41]. Furthermore, there has been growing interest in semiconductor NMS, such as titanium dioxide TiO_2 [42] and ZnO [43], as anticancer drug carriers very recently. For example, the incorporation of daunorubicin (DNR) in cancer cells through the use of ZnO nanorods (20x50 nm) could increase the intracellular concentration of DNR and enhance its potential anti-tumor efficiency in human hepatocarcinoma (SMMC-7721) cells by reactive oxygen species (ROS) [43]. It has also been shown that a pH-triggered controlled doxorubicin release from

mesoporous silica NPs was achieved via intracellular dissolution of ZnO nanolids [44]. These findings revealed that such modality combinations represent a promising approach in cancer therapy because ZnO nanostructures behave as a dual-purpose entity that not only inhibit premature drug release but also has a synergistic antitumor effect on cancer cells due to the release of toxic Zn^{2+} ions.

Table 1: FDA approved nano-therapeutics for clinical use.

Product trade name	composition	Use	Date of approval	Company	reference
Doxil®	Doxorubicin encapsulated into liposomes	Metastatic breast cancer and recurrent ovarian cancer	17/11/1995 FDA19627	Zeneca Pharmaceuticals	[38]
Abraxane®	Albumin nanoparticle comprising paclitaxel	Various cancers	7/01/2005 FDA21660	American Pharmaceutical Partners	[45]
Megace ES®	Nanocrystal/megestrol acetate	Breast cancer	7/5/2005	Elan/Par Pharmaceutical Companies	[45]

Table 2: Nanoscale systems for systemic cancer therapy , adapted from [40].

Platform	Latest stages of development	examples
Liposomes	Approved	DaunoXome, Doxil
Albumin-based particles	Approved	Abraxane
PEGylated proteins	Approved	Oncospar, PEG-Intron, PEGASYS, Neulasta
Biodegradable polymer–drug composites	Clinical trials	Doxorubicin Transdrug
Polymeric micelles	Clinical trials	Genexol-PM*, SP1049C, NK911, NK012, NK105, NC-6004
Polymer–drug conjugate-based particles	Clinical trials	XYOTAX (CT-2103), CT-2106, IT-101, AP5280, AP5346, FCE28068 (PK1), FCE28069 (PK2), PNU166148, PNU166945, MAG-CPT, DE-310,
Dendrimers	Preclinical	Polyamidoamine (PAMAM)

2.3 Uptake of nanomaterials

The mechanisms of cellular uptake of NMS are extensively studied recently [46-49]. NPs enter the cell through a process called endocytosis, which is generally classified into two broad categories- phagocytosis and pinocytosis. Phagocytosis is involved in the uptake of large particles (as large as 20 μm) and is characteristic of specialised professional phagocytosis, such as, macrophages, monocytes, and dendritic cells [50]. Pinocytosis, on the other hand, is present in all types of cells, and has multiple forms depending on the cell origin and function. The most recent classification of pinocytosis is based on the proteins involved in different endocytic pathways (Figure 1). According to this approach, pinocytosis is classified as clathrin-dependent endocytosis (also known as clathrin-mediated endocytosis (CME)) and clathrin-independent endocytosis [51]. The clathrin-independent pathways are further classified as macropinocytosis, caveolae-mediated endocytosis, and clathrin- and caveolae-independent endocytosis [52] (Figure 1). Another classification of endocytosis, based on NMS interaction with the cellular membrane (receptor-mediated, adsorptive, fluid phase), has also been used to describe cellular uptake of NMS [48]. However, nanomedicine community has been recently advised to utilize the classification based on endocytosis proteins, as the latter classification is less precise and often mistakenly used interchangeably with the previously described classification (e.g., receptor-mediated endocytosis is sometimes confused with CME) [48].

It has been reported that most NMS exploit more than one pathway to gain cellular entry [48]. The most current tools utilised in trafficking cellular uptake of NMS involve either colocalisation of NMS with specific endocytosis markers and structures or exclusion of specific endocytosis mechanisms by inhibitors of endocytosis or cell mutants [48]. A summary of most methods utilised in trafficking the uptake of NMS summarised by Sahay *et al.* in 2010 [48].

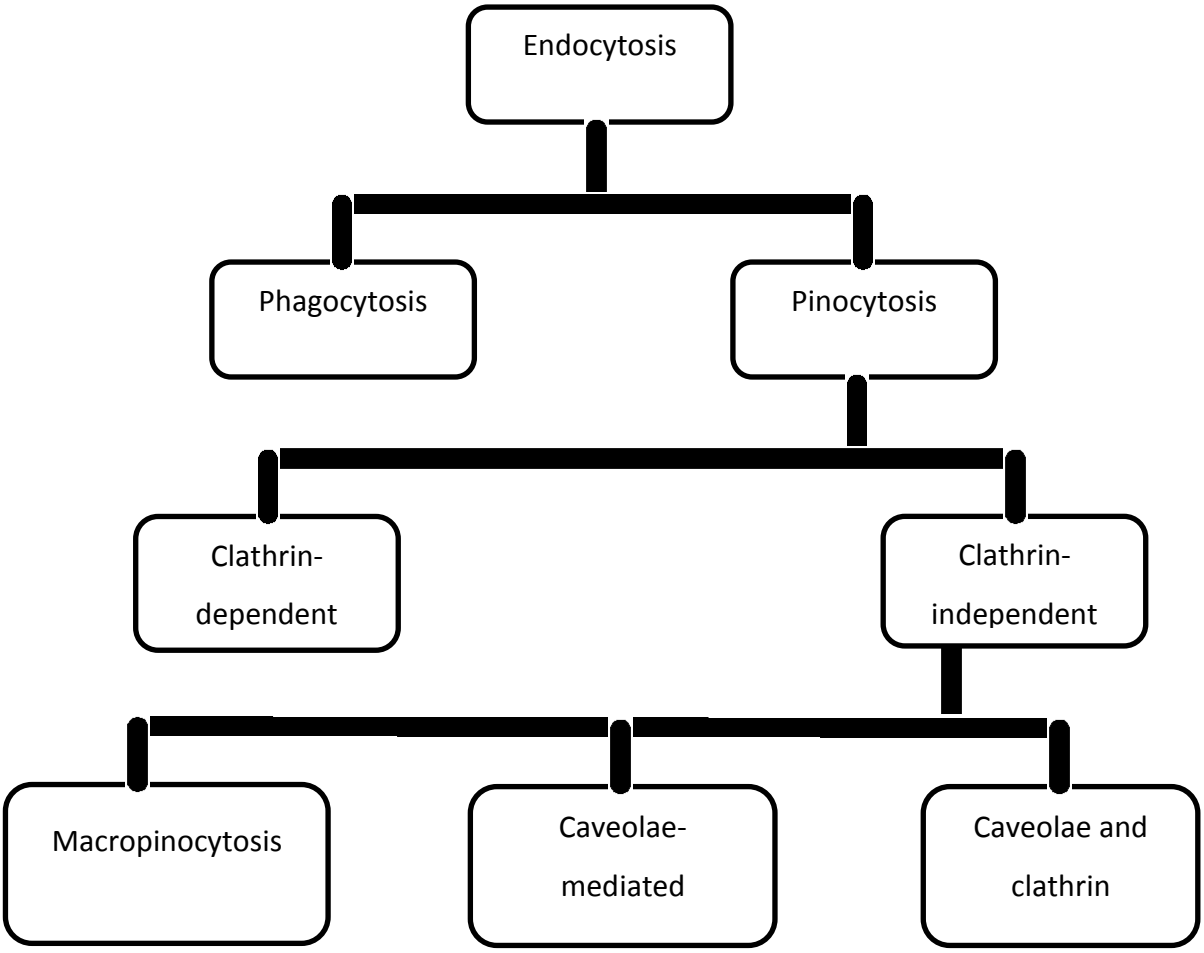

Figure 1: Classification of endocytosis based on endocytosis proteins that are involved in the initial entry of particles and solutes.

2.4 Zinc oxide nanomaterials

ZnO nanostructures have recently attracted a big interest because of their useful electronic and optoelectronic properties. ZnO is an important II-VI direct band gap (3.40 eV at room temperature) semiconducting oxide for smart devices and optoelectronics. ZnO is characterised by photocatalytic and photo-oxidising ability against chemical and biological species [53]. This makes it an ideal material for nano-scale optoelectronics and biotechnology applications. Among the various morphologies of ZnO, nanowires (NWs) have recently attracted particular attention due to their unique one dimensional structure with highly controlled length and diameters.

2.4.1 Toxicity of zinc oxide nanostructures

The toxicity of ZnO nanostructures against a wide range of mammalian cells has been extensively studied in recent years [54-56]. The number of publications in ISI Web of Science (WoS) on May 5th and 6th, 2013 concerning uptake, oxidative stress and other mechanistic nanotoxicological information (damage to membranes, mitochondria, DNA and lipid peroxidation) on ZnO against mammalian cells was 286 [55]. Some of these studies are summarised in Table 3. ZnO NMS has been reported to be more toxic than other metal oxides [55, 56]. A review on the toxicity of ZnO NPs to mammalian cells has been reported by Vandebriel *et al*. in 2012 [57]. Vandebriel *et al*. [57], concluded that the induction of oxidative stress is the most important and the most likely mechanism underlying ZnO NP toxicity. However, only few reports on the cellular uptake of ZnO NMs are available [10, 49, 58-60], and that was mainly attributed to either rapid intracellular dissolution of ZnO NPs or the effect of protein corona on the uptake [8]. All these studies will be critically discussed in Chapter 5.

Table 3: Summary of toxicity studies of ZnO nanostructures on mammalian cells. Blank cells represent information that is not given in the specific publication.

Year	ZnO nanostructures/size/shape	Tested cells	Results	Assays and techniques used to assess the toxicity	Suggested mechanism of toxicity
2006 [54]	NPs[a], MPs[b]	Normal human Osteoblast cells	-NPs were less toxic than MPs[b]		
2007 [61]	NPs (rod shaped) 20-70 X 100-200 nm	Human aortic endothelial cells (HAECs)	IC_{50}[c]= 50 µg/mL (0.6 mM) after 4 h.	-TEM - PCR (Real-time polymerase chain reaction) - ELISA[d] - ICP-MS[e]	
2007 [62]	NPs≈ 13 nm	Human-T lymphocytes	Not toxic at conc. < 400 µg/mL (5mM) IC_{50}≈ 800 µg/mL (10 mM) after 24 h	-Flow cytometry -viability assays	
2008 [49]	NPs ≈ 13 nm	Human bronchial epithelial cells (HBES-2B)	12.5 µg/ml Toxic	PI[f] MTS viability assay	ROS[g]
		Mouse leukaemic macrophage cell line (RAW 264.7 cells)	25 µg/ml toxic		
2008 [63]	NPs ≈ 20 nm	Primary mouse embryo fibroblast (PMEF) cells	IC_{50}[c]= 15 µg/ml (0.25 mM) after 24 h exposure	MTT viability assay WST viability assay	Oxidative stress
2008 [64]	NWs[h] 100 nm x 1.5 µm	Hela epithelial cells	Nontoxic at conc. up to 100 µg/ml	MTT viability assay	
		Subcutaneous connective tissues (L-929)	IC_{50}= 100 µg/ml.		

Year	ZnO nanostructures/size/shape	Tested cells	Results	Assays and techniques used to assess the toxicity	Suggested mechanism of toxicity
2009 [65]	NPs 10, 30, 60 and 200 nm	Mouse neural stem cells (MNCs)	IC_{50}[c] (10 nm)=9.3-11.3 µg/ml IC_{50} (200 nm) =10.2-13.5 µg/ml after 24 h. Dose dependent, size independent toxicity.	Confocal microscopy TEM FACS (Fluorescence-activated cell sorting)	
2010 [10]	NWs[h] 327 nmX10.5 µm	Human monocyte macrophages (HMMs)	IC_{50}[c]= 14.5 µg/ml	Confocal microscopy Neutral red	Zn^{2+} ions dissolution of ZnO NWs inside the cells
2010 [66]	NPs 20 nm	Human bronchial epithelial cells (HBES-2B)	Dose and time dependent toxicity IC_{50}[c]= 8 µg/ml after 24 h exposure	LDH viability assay	ROS[g] and oxidative stress
2010 [67]	NPs 20, 30 and 40 nm	Human embryonic lung fibroblasts (HELF) cells	- Toxic at concentrations tested (2.5-150 µg/ml) -Toxicity was independent on the particle size	MTT viability assay SEM (Scanning electron microscopy)	Zn^{2+} ions and (penetration of NP inside the cells)
2010 [68]	NPs - 10-30 nm, spherical - 30 nm, 100 nm, and fine rod shaped	Mouse macrophage Ana-1 cells	IC_{50}[c]≈ 40 µg/ml - Dose dependent but size independent toxicity - Spherical NPs were slightly more toxic than Nanorods	LDH viability assay CCK-8 viability assay	ROS[d]
2010 [69]	NPs ≈ 10 nm	Human bronchial epithelial cells (HBES-2B)	IC_{50}[c]≈ 20 µg/ml (0.25 mM) after 24 h exposure	WST-8 viability assay	ROS[g] and oxidative stress

Year	ZnO nanostructures/size/shape	Tested cells	Results	Assays and techniques used to assess the toxicity	Suggested mechanism of toxicity
2011 [70]	NPs ≈75.6 ± 19 nm	Glomerular mesangial cell (IP15)	Dose-dependent toxicity IC_{50}[c]≈3.04 µg/ml After 24 h	Neutral Red MTT viability assay WST-1 viability assay	ROS[g] and Oxidative stress
		Proximal epithelial tubular cell line HK-2	IC_{50}[c]≈ 2.42 µg/ml After 24 h		

[a]Nanoparticles (NPs), [b]Microparticles (MPs), [c]Median lethal concentration (IC_{50}): is a measure of the effectiveness of a substance in inhibiting a specific biological or biochemical function, [d]Enzyme-linked immunosorbent assay (ELISA), [e] Inductively coupled plasma-mass spectroscopy (ICP-MS), [f] Propedium Iodide (PI), [g]reactive oxygen species (ROS), [h]Nanowires (NWs)

2.4.2 The role of zinc ions in the toxicity of ZnO nanostructures and factors affecting dissolution of ZnO NPs

When the thermodynamic properties of ZnO nanostructures (including surface free energy) favour dissolution in a suspending media or biological environment, toxic Zn^{2+} ions may be generated [71]. Zinc oxide NPs can dissolve in an aqueous media to form hydrated Zn^{2+}; this dissolution is enhanced in acidic pH as well as the presence of biological components such as amino acids and peptides [49]. Several studies attributed the toxicity of nano-ZnO to the free zinc ions and labile zinc complexes released upon dissolution of ZnO [67].

The involvement of zinc ions in the toxicity ZnO NMS necessitates a proper understanding of the role of zinc in the body. Zinc is an essential trace element involved in a number of biological processes. The daily recommended dose of Zn^{2+} for adult men and women is 9.5 and 7.0 mg, respectively. It acts prominently as a structural part of proteins and the heart of the catalytic site of enzymes [72]. There is also a fraction of zinc that is not in strong association with organic molecules, called “vesicular” or “chelatable” [73]. Zinc can protect from oxidative stress, and it plays a regulatory role in apoptosis, ageing and the immune system [2, 74]. Within mitochondria of yeast cells, zinc is equally abundant to iron and appears to be a component of many proteins involved in mitochondrial protein

transport and folding of newly imported mitochondrial proteins within the matrix. Studies suggest that pools of bioavailable iron, copper and zinc exist in the mitochondrial matrix and that the regulation of this pool size is important for correct metallation reactions [75]. However, excessive zinc concentrations have been shown to be toxic to a number of organisms and to alter cellular morphology. For instance, exposure of different species of ciliates to excess zinc leads to various ultrastructural alterations, such as cytoplasmic vacuolation; nuclear changes such as chromatin condensation and nucleolus fusion; mitochondrial degeneration; autophagosome formation and formation of immature cyst walls [76]. Evidence is also mounting that zinc is toxic to neurons by inhibition of cellular ATP production and has been classified as an endogenous neurotoxin [4]. Zinc is very abundant in the brain with levels of ~ 200 ng/mg protein. This zinc pool exists either tightly bound to intracellular proteins, sequestered into vesicles together with glutamate or as a labile, free pool in the cytoplasm. One study suggests an LC_{50} for free Zn^{2+} of 300 nM in cultured neurons [77]. Zinc has to enter the cell to exert its toxicity, as treatments that decrease Zn^{2+} influx, increase Zn^{2+} efflux or increase intracellular Zn^{2+} buffering, all ameliorate its toxicity. Therefore any treatment that traffics local dose of Zn^{2+} into the cells is more likely to be effective therapeutically.

2.4.3 Where do ZnO NPs and released Zn^{2+} ions end up in the body

The liver could act as the main organ for disposal of ZnO NPs [78, 79] . Wang *et al.* [80] observed increase in zinc concentration in the liver and kidney in ZnO NPs-treated rats after 12 h exposure.

2.4.4 The use of ZnO nanomaterials in cancer therapy

Tumour tissues are characterised by increased capillary permeability or what is called ‘enhanced permeability and retention’ effect (EPR) proposed by Matsumura and Maeda [81]. According to their report, solid tumors have abnormal blood vessels with loose junction and insufficient lymphatic drainage, so that the NPs easily escape from the blood vessel and accumulate in tumor tissues but they hardly return to the blood stream again. EPR effect-based drug delivery is considered as the “gold standard” in anticancer drug design and anticancer strategies using macromolecular drugs. The EPR effect allows an increased rate of tumoural uptake of NPs [82]. In contrast, the EPR effect-driven drug

delivery does not occur in normal tissues. ZnO NMS have been reported recently to show a high degree of cancer cell selectivity with potential use in cancer imaging and therapy [14, 83, 84].

ZnO nanostructures are known to be very sensitive to dissolution in acidic conditions: the phase-solubility diagram of ZnO indicates that it will dissolve below pH 6.7 at physiological temperature and will dissolve rapidly in the acidic pH of the lysosomes (pH 5.7) [10] or in the acidic (pH 5-6) cancer environment [11] whereas they will not dissolve in the environment of healthy cells (pH 7.2).

It has been recently reported the use of ZnO NWs in cell-localized photodynamic therapy for breast cancer [85]. The ZnO NWs were conjugated to a photosensitizer which was then successfully delivered by ZnO NWs to breast cancer cells. The green emission from ZnO NWs after UV exposure activates the photosensitizer and initiates necrosis within few minutes [85]. Zhang *et al.* [86] reported the use of ZnO nanorods as drug carriers for the chemotherapeutic drug DNR. The antitumor activity of DNR against hepatocarcinoma cells was improved significantly by its combination with ZnO NWs. The increase in the intracellular concentration of DNR and in its anti-tumour activity by the wires indicates the potential application of ZnO NWs in drug delivery into target cancer cells. A recent study reported the potential use of ZnO NPs as a pH-sensitive drug delivery system that minimizes drugs toxicity [87]. ZnO NPs has also reported to preferentially kill cancer cells and activated human T-cells [6]. Punnoose *et al.* [88] has recently registered a patent for the use of ZnO against cancerous T-cells. They showed that ZnO NPs exhibit a strong preferential ability to kill cancerous T-cells (~ 28-35 x) compared to normal T-cells.

Targeting tumor cells has gained credence as an alternative approach for treating cancer and offers both an increased therapeutic index and decreased drug resistance. The use of ZnO NMS as a targeted fluoroprobe due to its intrinsic fluorescent properties has been investigated. ZnO quantum dots (QDs) was targeted to the breast cancer MDA-MB-231 cells by transferrin ligand. The NPs were biocompatible with selective binding to the cell surface receptor and they were internalised through receptor mediated endocytosis [89]. RGD- targeted ZnO NWs to αvβ3 integrin receptors expressed on the glioblastoma cells were found biocompatible for imaging purposes [12]. Both studies indicated the potential

use of ZnO NMS for cancer targeted imaging and drug delivery. Porous ZnO nanorods conjugated with folic acid were used to target and deliver the anticancer drug doxorubicin to MDA-MB-231 cells [90]. The αvβ3 integrin receptors are better targets than transferrin and folic acid [91]; transferrin is expressed at elevated levels on cancer cells but also on brain capillaries, endocrine pancreas, or Kupffer cells of the liver [92]. In addition, folate, which is supplied by food, show naturally high concentrations in the human body and thus might compete with the NP-conjugated ligand for binding to the receptor, and consequently reducing the intracellular concentration of delivered drug [93].

2.5 Protein corona formation around nanoparticles

2.5.1 Effect of protein corona on the pharmacokinetics and toxicity of nanomaterials

Blood plasma is the liquid component of whole blood, and makes up approximately 55% of the total blood volume. It is composed primarily of water with small amounts of minerals, salts, ions, nutrients, and proteins in solution. Plasma contains a large variety of proteins including human serum albumin (HAS), immunoglobulins (IgG), and clotting proteins such as fibrinogen. Albumin constitutes about 60% of the total protein in plasma and is present at concentrations between 35 and 55 mg/mL [94]. When NPs come in contact with biological fluids, they interact with proteins and other biomolecules. This interaction of NPs with protein molecules results in the formation of a dynamic layer of proteins on the surface of the NPs (Figure 2). This conjugated system is known as “NP-protein corona” [95]. Professor Dawson's group of collaborators introduced the concept of a “hard protein corona” seven years ago [96]. At equilibrium, the corona would have a unique composition of proteins. The adsorption of proteins onto metal oxides have been found to reach equilibrium within the first few minutes of incubation [8]. The NP-protein corona is composed of a dynamic layer of proteins, low affinity proteins being gradually replaced by lower abundance, higher affinity proteins [33]. The low affinity proteins form the “soft corona”, while the higher affinity proteins form the “hard corona” [97]. The hard corona proteins interact directly with the nanomaterial surface, while the soft corona proteins interact with the hard corona via weak protein–protein interactions [98]. A schematic of soft and hard protein corona formed on the surface of NPs is presented in Figure 3.

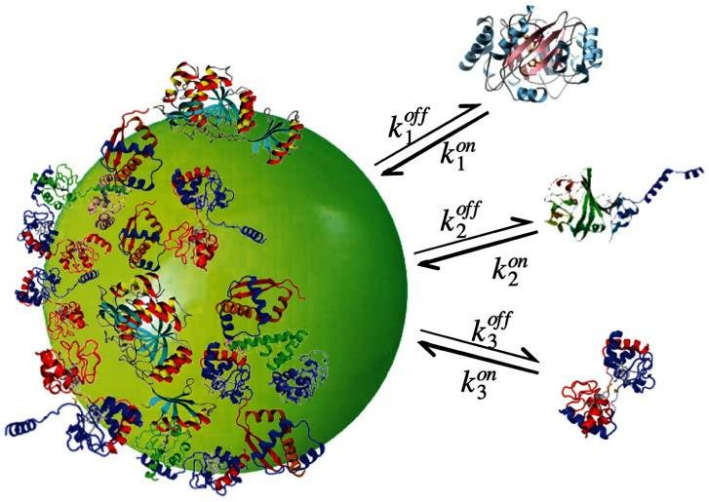

Figure 2: Simplified schematic of nanoparticle-protein corona formation process. Single type (*i*) protein attached to the nanoparticle surface at a rate K_i^{on}, leaving the nanoparticle at rate K_i^{off}. On average, a total number of n_i proteins can fully cover the nanoparticle surface [99]. Analytical Results from Population Balance Equations by Sahneh, F.D., C. Scoglio, and J. Riviere is licenced under creative Commons Attribution (CC BY) 4.0 international.

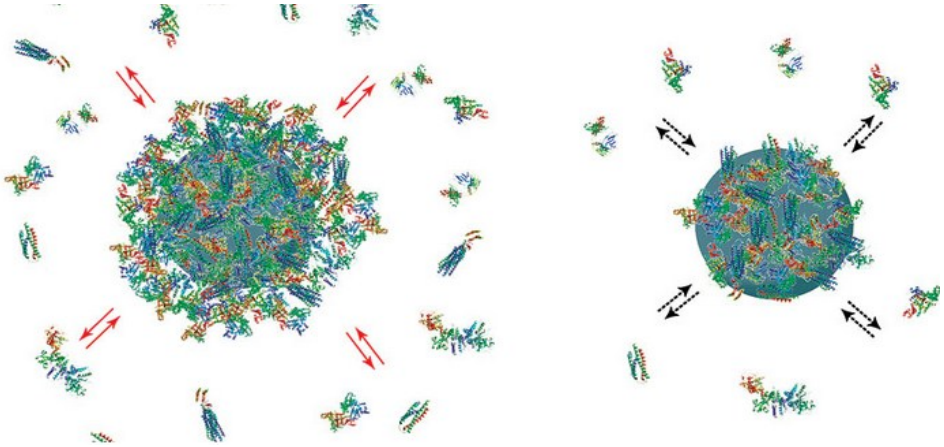

Figure 3: Schematic of soft and hard protein corona formed on the surface of NPs. In plasma, NPs are surrounded by a corona of proteins. Left, a weakly bound dynamic protein outer layer on the surface on a NP in exchange with proteins in the plasma (soft corona). Right, with time a more strongly bound "hard" corona on the surface of NPs are formed [100] "Courtesy of F. Bombelli".

The extent of adsorption of protein on the surface of NPs as well as the effect on the protein structure and stability are dependent on the chemical nature, shape [8], surface charge [101-105], size [106-108], colloidal stability of NPs [109], types of proteins [110], and ambient temperature [111]. For example, despite comparable surface charges, ZnO NPs showed different plasma protein binding profiles compared to TiO_2 and SiO_2 [8]. Electrostatic interactions may also determine the nature and extent of protein binding. NPs with an acidic surface will preferentially bind to proteins with isoelectric point (pI) greater than 5.5,

while NPs with basic surfaces predominantly bind to proteins with pI less than 5.5. It has been shown that the composition of the protein corona of silicon NPs was different for the nanospheres, nanorods, and nanotubes [8].

This adsorption of proteins at the NPs surface may lead to a substantial change of the physicochemical properties of the NPs and could result in NPs of different identity. The protein-NPs interaction could also result in the change of proteins' structure and activity. Since protein corona could change NPs properties such as polarity, charge, shape and size, they could in turn critically affect the interaction of these NPs with the lipid bilayer of cell membrane and eventually their biodistribution [60]. The protein corona could also affect uptake mechanisms, and intracellular localisation of the NPs *in vivo*. Therefore, evaluation of the protein corona is crucial for understanding the biological responses to the NPs. The contradictory reports of nanomaterial toxicity could also be resolved by understanding the effect of serum proteins within toxicology assays.

Chemical fabrication of the surface of the NPs to avoid adsorption of proteins can be carried out using polyethylene glycol (PEG) [112], also referred to as "PEGylation" and through siliconate treatment of the surface of the NPs [8] .

2.5.2 Effect of protein corona on opsonisation

Protein corona formed on the surface of NPs could act as 'opsonins'. Opsonins can be recognised by scavenger receptors on the macrophage cell surface and internalised. This internalisation by macrophages leads to significant loss of NPs from the circulation. The macrophages responsible for the loss of injected dose of NPs are also known as the reticuloendothelial system (RES). Consequently, understanding how and why plasma proteins are adsorbed to these NPs may be important for understanding their biological responses and will be the key point for developing a long circulation time NP formulation.

Size, charge and surface chemistry of NPs greatly influence their opsonisation and consequently their PK and fate *in vivo* [32, 65]. Prolonged blood circulation and an increased level of tumour delivery are achieved by NPs that have a mean diameter of approximately 100 nm, ζ potential within 10 mV, and PEGylation [32]. The most commonly used strategy to minimise opsonisation is conjugation of PEG polymer onto the surface of the NPs. PEG is a

relatively inert hydrophilic polymer that provides good steric hindrance for preventing protein binding. Several studies reported that PEGylation reduces the rate of RES uptake and increases circulation half-life for various types of NPs [32]. However, PEGylation also weakens the interaction of NPs and the target cells causing an inefficient intracellular delivery.

2.5.3 Effect of protein corona on active targeting yield of nanoparticles

It has been found that protein corona reduces the targeting capability of NPs by screening the active sites of the targeting ligands [113]. A schematic of the process is shown in Figure 4.

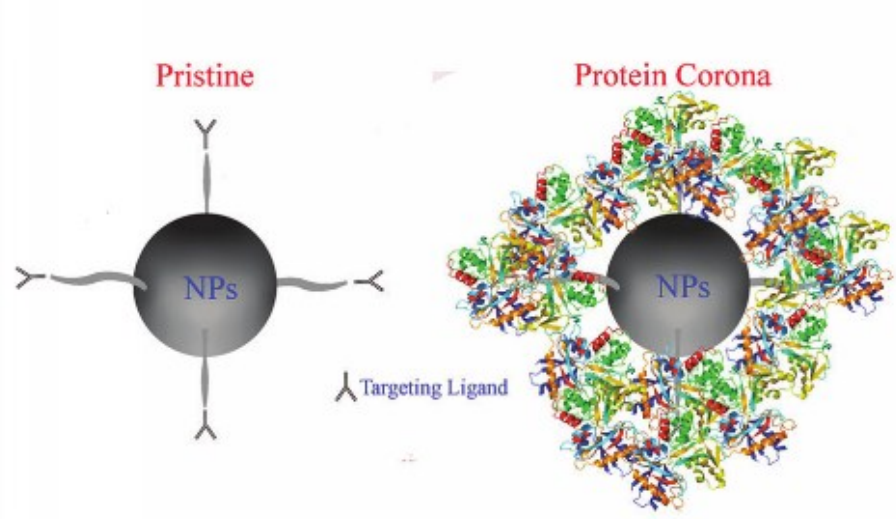

Figure 4: Simplified schematic of reduction of targeted NP delivery by protein corona. Left, NP with surface targeting ligand. Right, protein corona bound to the surface of NP screened NP targeting ligands, preventing the ligands from binding to their targets on a cell surface, "Mirshafiee, V., et al., Protein corona significantly reduces active targeting yield. Chemical communications (Cambridge, England), 2013. 49(25): p. 2557-2559- Reproduced by permission of The Royal Society of Chemistry" [113].

2.6 Aims of the study

The aim of this work is to investigate the *in vitro* cancer cell specific targeting and cytotoxicity of ZnO NPs and nanowires to different breast cancer cell lines.

Specific aims:

1. To demonstrate selective targeting and toxicity of RGD surface-modified ZnO NMS by comparing targeting, uptake and cytotoxicity in a panel of malignant breast cancer cells compared with healthy breast epithelial cells.

2. To correlate targeting, intracellular destination and local dissolution of the surface-modified ZnO NPs with their toxicity mechanism.

3. To investigate the mechanism of cell death induced by the ZnO NPs in the malignant breast cancer cells.

4. To assess ZnO NWs toxicity to malignant breast cancer cells.

3 Characterization and functionalisation of bare zinc oxide nanoparticles

In this chapter, the physicochemical properties of ZnO NPs have been investigated. These include, shape, size, zeta potential and hydrodynamic size distribution. The dissolution of these NPs in the different cell culture media used in this study is also discussed. Characterisation of the ZnO NPs was conducted using transmission electron microscopy (TEM), Zetasizer and inductively coupled plasma optical emission spectroscopy (ICP-OES).

3.1 Materials and methods

3.1.1 Bare ZnO NPs

Bare ZnO NPs were purchased from SkySpring Nanomaterials, Inc., (product number 8410DL, Westhollow Drive, Houston, USA) at 99.8% purity and nominal size of 10-30 nm. The powder was white to light yellow in colour, and was stored at room temperature (RT) and vacuum sealed.

3.1.2 Cell culture media and chemicals

Dulbecco's Modified Eagle's Medium (DMEM), Minimum Essential Media (MEM), a 1:1 mixture of Dulbecco's Modified Eagle's Medium (DMEM) and Ham's F-12 media (DMEM:F-12) and horse serum were obtained from Gibco (Life Technologies Ltd, UK), fetal bovine serum (FBS) was purchased from Cellgro, Mediatech, Inc. Leibovitz's L-15 (L-15) medium was obtained from American Type Culture Collection (ATCC, Manassas, USA). Epidermal growth factor was purchased from Invitrogen. Penicillin-Streptomycin, Cholera toxin, insulin, hydrocortisone and $CaCl_2$ (≥99%) were purchased from Sigma Aldrich, Ltd, UK. HEPES (4-(2-hydroxyethyl)-1-piperazineethanesulfonic acid, ≥99%), NaCl (≥99.5 %), $MgCl_2$, KCl, and $MgSO_4$ (≥99%), were purchased from Fisher Scientific Ltd, UK. 2-Deoxy-D-glucose (99%) and MES (2-(N-morpholino) ethane-sulfonic acid) were purchased from Acros Organics, US.

3.1.3 Preparation of cell culture media and buffers

MEM, DMEM, and L-15 media were supplemented with 10% FBS, and Penicillin-Streptomycin solution (100 units/ml penicillin, 100 µg/ml streptomycin). DMEM:F-12

medium was supplemented with 20 ng/ml epidermal growth factor, 100 ng/ml cholera toxin, 0.01 mg/ml insulin, 100 ng/ml hydrocortisone, Penicillin-Streptomycin solution (100 units/ml penicillin, 100 μg/ml streptomycin), and 5% horse serum. Herein, these will be referred to as complete media (CMEM, CDMEM, CL-15, and CDMEM: F-12, respectively). HEPES confocal imaging buffer was prepared as 10 mM HEPES at pH 7.4, containing 145 mM NaCl, 5 mM KCl, 1 mM $MgSO_4$, 1.5 mM $CaCl_2$, and 0.16% glucose. Lysosomal simulated body fluid (Lyso-SBF) was also prepared as 25 mM MES-NaOH at pH 5.2, containing 0.5 mM $CaCl_2$, 1 mM $MgCl_2$, and 200 mM KCl.

3.1.4 Functionalisation of ZnO nanoparticles

The targeting peptide conjugated to the ZnO NPs was prepared by our collaborators in the department of chemistry, Montana State University, and was labelled with a green fluorescent protein (GFP). The method used to prepare the targeting peptide by our collaborators is novel. Cell targeting of the ZnO NPs was achieved using an immobilization of dual domain peptides which is composed of cell targeting domain and ZnO binding domain. Cell targeting domain comprises peptides with established cell-specific tumor targeting sequences (CDCRGDCFC). ZnO binding motif (HCV) is a tripeptide composed of histidine (His), cysteine (Cys), and valine (Val) which binds to αvβ3 integrin upregulated in breast tumor. The targeting motif (RGD) is a tripeptide composed of L-arginine, glycine, and L-aspartic acid. These peptide sequences have been discovered using *in vivo* phage display selection and combinatorial library methods and have been shown to maintain targeting capability when presented on other nanoscale platforms. These two peptide domains were connected via a glycine linker to ensure flexibility. These short peptides were produced heterologously in an E.coli. The dual domain peptides were genetically conjugated with green fluorescence protein (GFP) so that fluorescence microscopy is available to evaluate cellular uptake and targeting of modified ZnO NMS.

The exact binding mechanism of the HCV peptide motif to ZnO NPs is not fully investigated. I their study, Okochi, M., et al. [114] showed that 99.6% of the 6-mer peptide HCVAHR were adsorbed onto ZnO NPs and the kinetic binding constant (Ka) of the peptide against ZnO NPs was 9.8x106 M-1, and its maximum amount of adsorption was 2 mmol peptides/g ZnO (105 peptides/ZnO particle). In [114], they suggested that the His is the key

amino acid for binding to ZnO and by ZnO-binding assay, they confirmed that the His residues, which possess the imidazolium cation, were involved in the ZnO interaction. Also, the Cys-substitution found to increase the binding especially with next to His. These results seem to be related to the amino acids associated with Zn2+ in zinc fingers and metalloproteins [3]. The thiol–Zn interaction might modulate the His-binding to ZnO nanoparticles [114]. Therefore, His–Cys motif would increase the binding capacity and specificity. Based on the strong binding of the HCV motif to the surface of ZnO, it is expected that the targeting peptide is expected to stay attached to the NP during culture and internalisation. However, the stability of the targeting ligand as the NP dissolves during culture and internalisation are to be investigated.

After preparing the targeting peptide, it was suspended in HEPES buffer (HEPES 50mM, NaCl 100mM) at pH 7.5. The peptide was then diluted with the same buffer to an absorbance of 1.6 at 490 nm. The bare ZnO NPs were suspended in HEPES buffer (50 mM HEPES, 100 mM NaCl) at pH 7.5 and a concentration of 10 mg/ml. The particles were then incubated with the diluted protein solution to a concentration of 1 mg/ml over night at RT in the dark with gentle shaking. Finally, the NPs dispersions were centrifuged at 13,000 rpm for five min on a table-top centrifuge. To test the efficiency of binding of the targeting peptide to ZnO NPs, the absorbance of the protein solution, before and after incubation with the particles, was measured at 490 nm. A schematic of the functionalisation peptide is presented in Figure 5. A negative control peptide (HCV-GGG-GFP) which has the ZnO binding motif (HCV) and a GGG peptide instead of receptor binding motif (RGD) was also prepared. The ZnO-HCV-GGG-GFP NPs were also prepared using the same procedure described above.

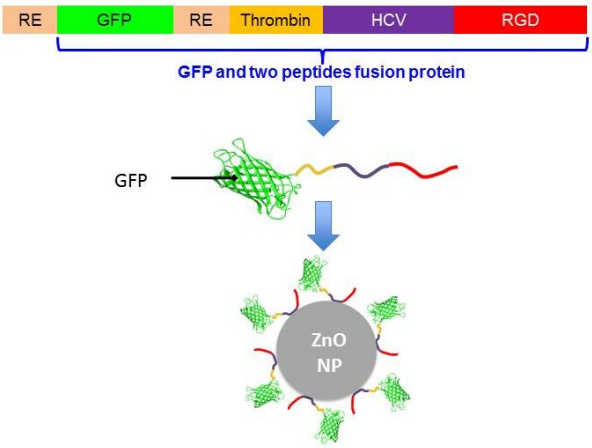

Figure 5: Simplified schematic of ZnO functionalization peptide. The peptide is composed of a ZnO binding peptide (HCV, purple), and a targeting peptide (RGD, red). To track binding of the targeting peptide to the surface of the bare ZnO NPS, the NPs were tagged with a GFP protein (green). RE: restriction enzyme. This schematic was prepared by Masaki Uchida with modification.

3.1.5 Size and morphology of the bare zinc oxide nanoparticles

The particle size distribution and morphology of the bare ZnO NPs were evaluated on FEI Tecnai T-12 transmission electron microscope (TEM) operated at 120 V. The particles were suspended in ethanol and sonicated for 20 min, then 2 µL of the suspension was dropped on a carbon grid and allowed to air-dry before examination in the TEM. To measure the particle size distribution from the TEM images, 200 particles were randomly selected and the long and short diameters were measured (since not all of the particles were spherical) with the help of ImageJ (http://rsbweb.nih.gov/ij). The size of each NP was calculated as an average of the two lengths, and a frequency plot was prepared using a class interval of 10 nm.

3.1.6 Hydrodynamic radii and zeta potential of bare and functionalised ZnO nanoparticles

The hydrodynamic radii of bare ZnO NPs in different vehicles (deionised distilled water, CMEM, CDMEM, CDMEM: F-12, 10 mM HEPES+50 mM NaCl at pH 7.4 (used for protein binding experiment in Chapter 6) and HEPES confocal imaging buffer at pH=7.4), as well as their zeta potential in deionised-distilled water at pH 6.3 were analysed using a Zetasizer Nano ZS (Malvern Instruments INC, UK). Bare ZnO NPs, dispersed in ethanol were sonicated for 20 min, and then diluted at 100 µg/ml before hydrodynamic size measurement. This concentration was chosen as a previous study [115] which showed that the hydrodynamic size was the same for concentrations between 10-100 µg/ml. To check the effect of

adsorbed proteins from the FBS on the size distribution of the bare ZnO NPs in the cell culture media, the same experiment was repeated with DMEM and MEM using 1% instead of 10% FBS, and with DMEM:F-12 using 1% instead of 5% horse serum. To assess the effect of the targeting protein (HCV-RGD-GFP) on the agglomeration status of the ZnO NPs, the hydrodynamic radii of the ZnO-HCV-RGD-GFP NPs were measured in the HEPES imaging buffer. The targeted ZnO NPs stock dispersion in 10 mM HEPES+50 mM NaCl was sonicated for 30 s and 100 µg/ml dispersion in HEPES confocal imaging buffer was prepared for hydrodynamic size measurements. The targeted ZnO NPs were sonicated for 30 s only to prevent any possible break down of the targeting peptide that might consequently reduce the targeting efficiency of ZnO NPs to the cancer cells.

The zeta potential of the bare ZnO NPs was measured in deionised distilled water at pH 6.3 and 10 mM HEPES buffer at pH 7.4. The bare ZnO NPs ethanolic dispersions were sonicated for 20 min, and then diluted at 100 µg/ml before zeta potential measurements. The effect of the adsorbed FBS proteins on the surface charge of ZnO NPs was also analysed. The bare ZnO NPs were incubated in CDMEM at 100 µg/ml for 1 h at 37°C while shaking. At the end of incubation time, the NP-protein complex was centrifuged at 12,000 xg and the supernatant was removed. The pellet was then washed three times with 10 mM HEPES buffer at pH=7.4. Finally, the NP-protein complexes were resuspended in 10 mM HEPES buffer at 100 µg/ml and the zeta potential was measured, as described previously.

For the measurement of zeta potential and hydrodynamic radii, DTS 1061-folded capillary cells (Malvern), and D51588 (SARSTEDT AG and Co.) disposable sizing cuvettes were utilized, respectively. All the measurements were repeated at least 3 times and the average result was calculated.

3.1.7 Dissolution of zinc oxide NPs in cell culture media and simulated body fluids (ICP OES)

The dissolution of bare ZnO NPs in CMEM, CDMEM, CL-15, and CDMEM: F-12, HEPES confocal imaging buffer at pH 7.4 and Lys- SBF at pH 5.2 were analysed using a Varian 720-ES Axial ICP-OES. The ZnO NPs dispersed in ethanol were sonicated for 20 min, and 100 µg/ml dispersions in CDMEM, CMEM, and confocal imaging buffer at pH 7.4 were prepared. The dispersions were then incubated immediately at 37°C for 0, 1, 2, 4, 8, 24 and 48 h. For

the lys-SBF at pH 5.2, 600 μg/ml of bare ZnO NPs dispersion was prepared and additional time points at 5, 15 and 30 min were prepared as described previously. Undissolved ZnO NPs were removed at each time point by centrifugation for 30 min at 12,000 xg at RT in a table-top centrifuge using Vivacon 500 filter inserts (2 KDal molecular weight cut off; Sartorius Stedium Biotech, Germany). An aliquot of the filtrate was then diluted using 2% aqueous HNO_3 for measurement of total Zn^{2+} concentration. Each experiment was repeated three times.

To study the effect of FBS on the dissolution of bare ZnO NPs in culture media, 100 μg/ml dispersion of bare ZnO NPs in MEM supplemented with 1% FBS was prepared, and the dispersions were processed, as above.

For the ZnO-HCV-RGD-GFP, the dissolution was studied in the HEPES confocal imaging buffer. The targeted ZnO NPs were sonicated for 30 s and 100 μg/ml dispersions in the HEPES confocal imaging buffer at pH 7.4 were prepared. The dispersions were then incubated immediately after preparation at 37°C for 0, 1, 2, 4, 8, 24 and 48 h. Samples for ICP-OES analysis were prepared, as described above with the bare ZnO NPs.

Quantification of the amount of ionic zinc was undertaken *via* external calibration with a series of matrix-matched zinc standard solutions in the approximate range of 0.1-1000 μg/ml Zn^{2+}.

3.2 Results and Discussion

3.2.1 Size and morphology of the bare zinc oxide nanoparticles

The morphology and the relative frequency size distribution of the bare ZnO NPs are shown in Figure 6. While most of the NPs were spherical, a small proportion were irregular in shape, and aggregates of different sizes of the NPs, which could be due to room temperature drying artefacts, could be observed (Figure 6 (a-c)). (Figure 6, a-c). Characteristic peaks of zinc (K and L at 8.63 and 1.012 keV, respectively) could be observed in the EDX profile (Figure 6, d). The size of the bare ZnO NPs provided by the manufacturer was 10-30 nm; however the average size measured by TEM was 56.7 ± 21.7 nm. The bare ZnO NPs had a wide size distribution, ranging from 20 to 150 nm (Figure 6, e).

3.2.2 Functionalisation and binding of targeting peptide to ZnO NPs

To test the efficiency of binding of the targeting peptide (HCV-RGD-GFP) to ZnO NPs, the absorbance of the targeting protein solution before and after incubation with the particles was measured at 490 nm.

Both the targeting peptide (HCV-RGD-GFP) and the negative control (HCV-GGG-GFP) proteins were found to bind to ZnO NPs after incubation, as shown by a reduction in the UV-Visible absorbance measured at 490 nm (Figure 7, a and b). This binding was effective after only 1h of incubation of the particles with the proteins. The GFP protein without the HCV binding motif did not show any binding to the ZnO NPs (data not shown).

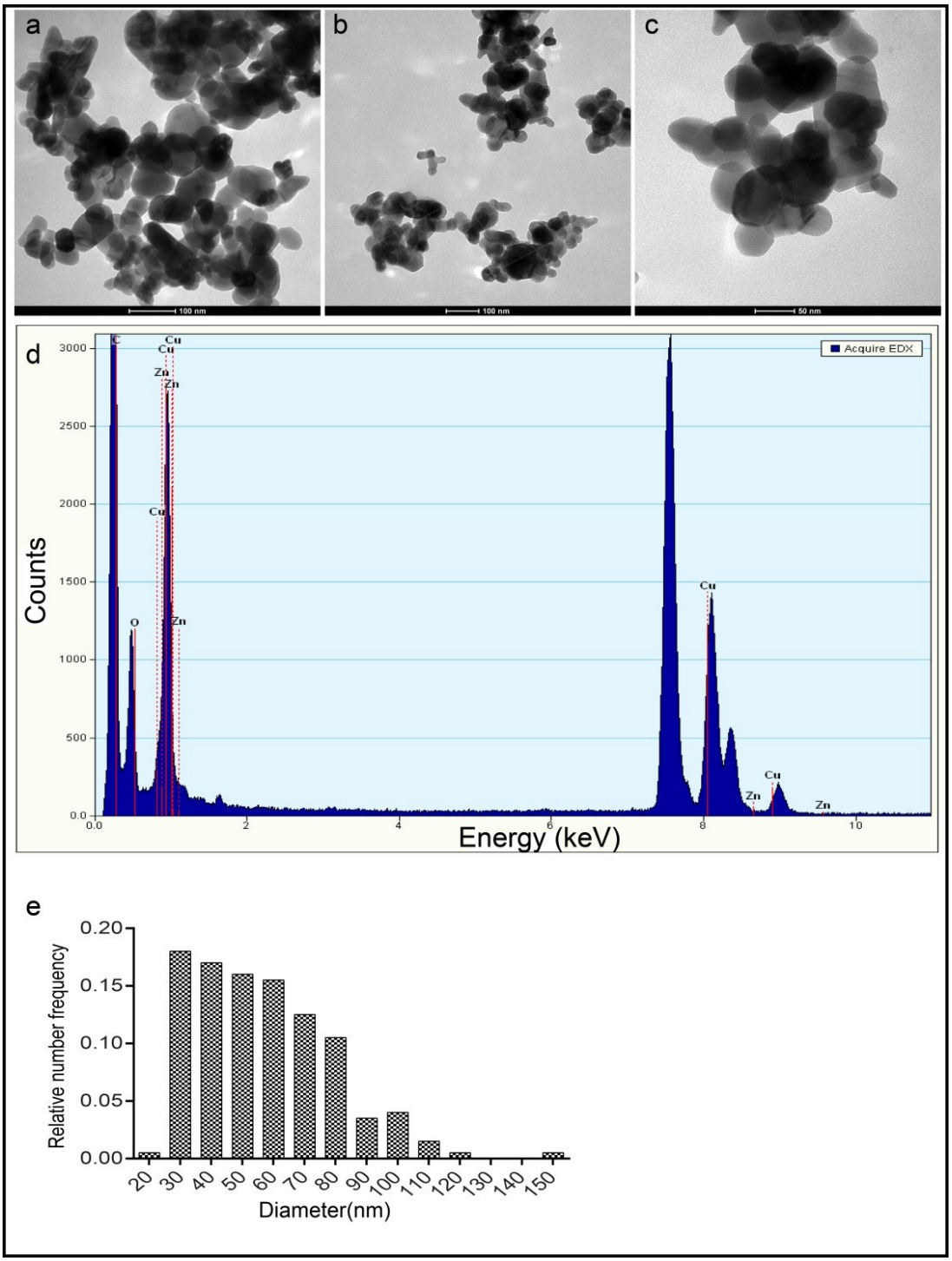

Figure 6: Bright field TEM images (a-c), EDX spectrum (d), and the relative diameter frequency distribution (e) of the bare ZnO NPs.

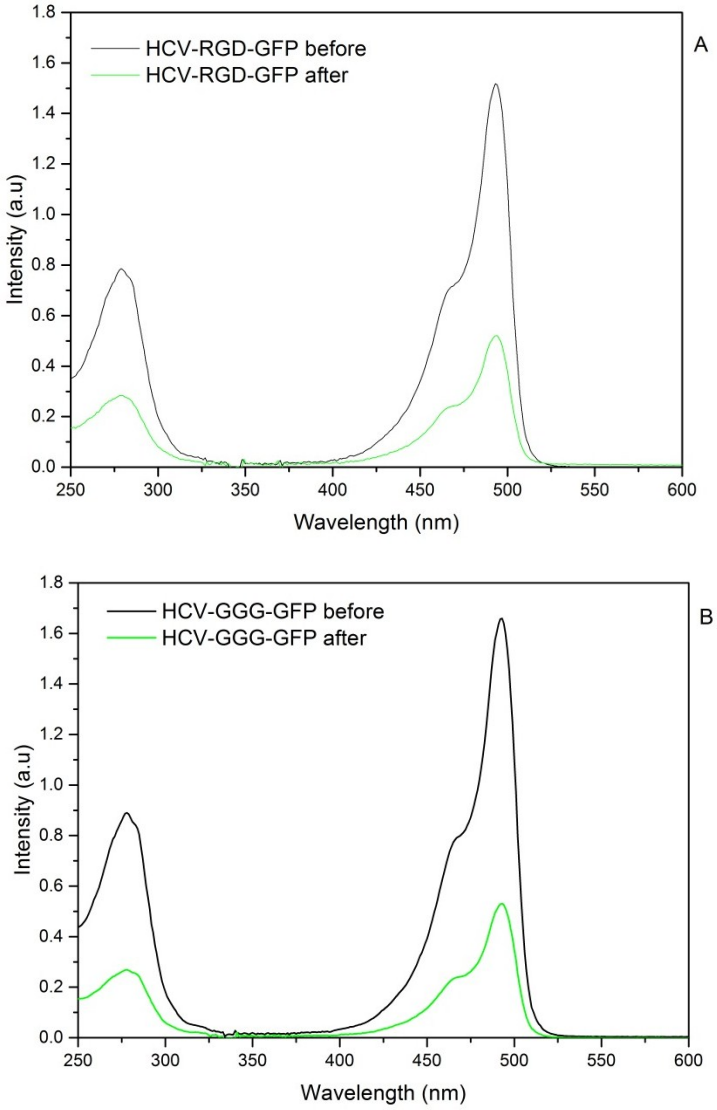

Figure 7: Binding of GFP proteins to ZnO NPs. (A) HCV-RGD-GFP protein and (B) HCV-GGG-GFP protein. Bare ZnO NPs were prepared in 50 mM HEPES buffer containing 100 mM NaCl at pH 7.5 and then incubated with the proteins in the same buffer at a concentration of 1 mg/ml for 12 h at RT in the dark and absorbance was measured at 490 nm.

3.2.3 Hydrodynamic radii and zeta potentials measurement of the ZnO nanoparticles

To assess the effect of culture media on the dispersion state of the particles and their subsequent cellular uptake and bioreactivity, dispersions of the bare ZnO NPs in the different vehicles (deionised water, CMEM, CDMEM, CDMEM:F-12, and HEPES confocal imaging buffer) used throughout the study were analysed using a Malvern Nanosizer. The hydrodynamic size of the ZnO-HCV-RGD-GFP NPs was measured in HEPES confocal imaging buffer. The frequency size distribution curves of the bare ZnO NPs in the different vehicles are presented in Figure 8-Figure 12. The frequency size distribution curve of the ZnO-HCV-

RGD-GFP NPs in the HEPES confocal imaging buffer is presented in Figure 13. The mean hydrodynamic diameter of the bare and targeted ZnO NPs in the different vehicles, as determined by DLS, is summarized in Table 4.

The results suggested that both the bare and the targeted ZnO NPs aggregated. The PdI of the bare ZnO NPs was < 0.25 in all tested vehicles, while the PdI of the targeted ZnO-HCV-RGD-GFP NPs was high (0.76), which means a very heterogeneous size distribution of the targeted ZnO NPs in the HEPES confocal buffer. However, the Malvern Zetasizer analyses the laser light scattered from the particles and does not directly measure the aggregate size; moreover, the average size of the aggregates measured can be skewed by the presence of extremely large or small aggregates [116, 117]. This agglomeration of ZnO nanostructures in cell culture media has been reported previously; Moos *et al.*, [118] showed that 8-10 nm ZnO NPs formed micrometre-sized ZnO NPs in DMEM supplemented with 2% FBS. The aggregation of the NPs in different media used is most probably due to high ionic strength of the media. It has been reported that the stability of metal oxide NPs in aqueous solutions depends to a large extent on the ionic strength [119-122]. Suspensions of 4 nm ZnO NPs were found to be more stable at low ionic strength while they were prone to aggregation as the ionic strength was increased [122]. It has also been shown that the zeta potential of ZnO NPs decreases with increasing ionic strength, and thus ZnO NP-NP interaction is quite repulsive at low ionic strength (below 0.04 M NaCl) [122]. In this study, the bare and targeted ZnO NPs were prepared in HEPES confocal imaging buffer. The HEPES confocal imaging buffer was prepared as 10 mM HEPES at pH 7.4, containing 145 mM NaCl, 5 mM KCl, 1 mM $MgSO_4$ 1.5 mM $CaCl_2$, and 0.16% Glucose to simulate body fluids. This high ionic strength buffer could cause aggregation of the ZnO NPs. This aggregation could affect the uptake of the ZnO NPs and consequently their toxicity. It would have been too ambitious in this study to develop methods to increase the colloidal stability of ZnO NPs and also target them to cancer cells. This should be the subject of future investigations. Instead my work is a platform for future studies to understand how and by which mechanism ZnO NPs interacts with cancer cells and whether is safe to use. These fundamental studies need to be performed to understand whether ZnO NPs have the potential to be used in cancer therapy before designing much more sophisticated nanoparticles for testing.

The effect of FBS in MEM, DMEM and DMEM: F-12 media on the hydrodynamic size distribution of ZnO NP-protein complexes was also investigated. The ZnO NP-protein complex size distribution in MEM and DMEM supplemented with 1 and 10% FBS, (or 1 and 5% horse serum in DMEM: F-12) is presented in Figure 9- Figure 11. The results suggest a smaller ZnO NP aggregate size was formed in the media supplemented with a higher percentage of serum (10% FBS in MEM and DMEM, and 5% horse serum in DMEM: F-12). This finding could indicate that the size distribution of ZnO NP dispersions is more stable in the presence of FBS. This effect of proteins on the size stabilisation of ZnO NPs has been reported previously [60], and could be due to the reduction of surface free energy of the ZnO NPs, preventing significant aggregation.

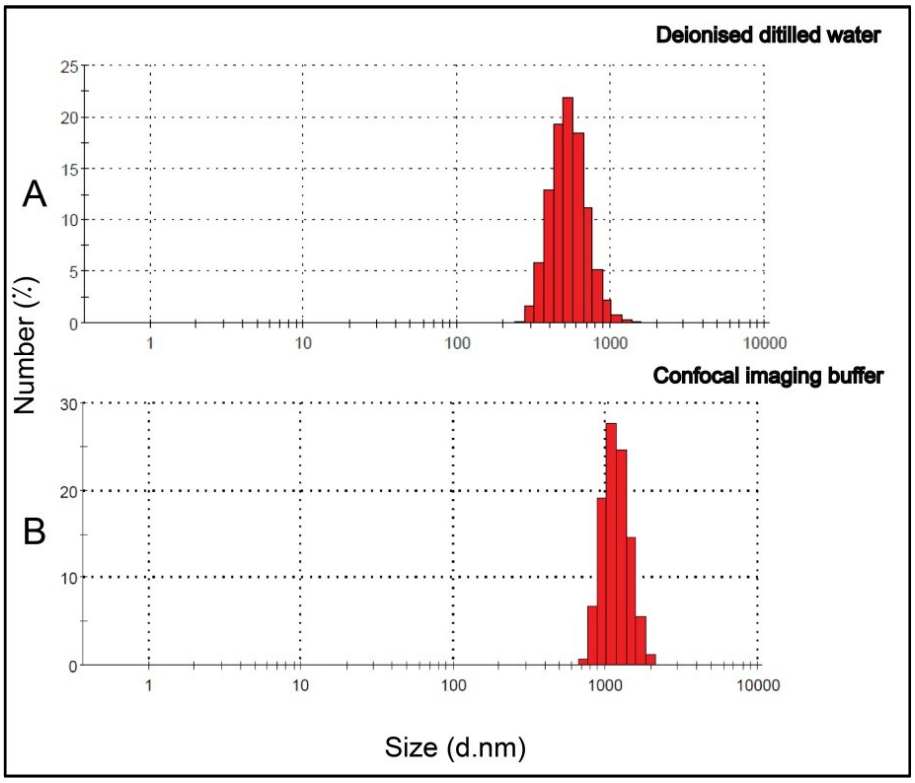

Figure 8: Hydrodynamic size distribution of the bare ZnO NPs after dispersion in (A) deionised distilled water (pH 6.3) and (B) Confocal imaging buffer (pH 7.4). The average diameter ZnO NPs was 703.8 and 1231 nm, respectively.

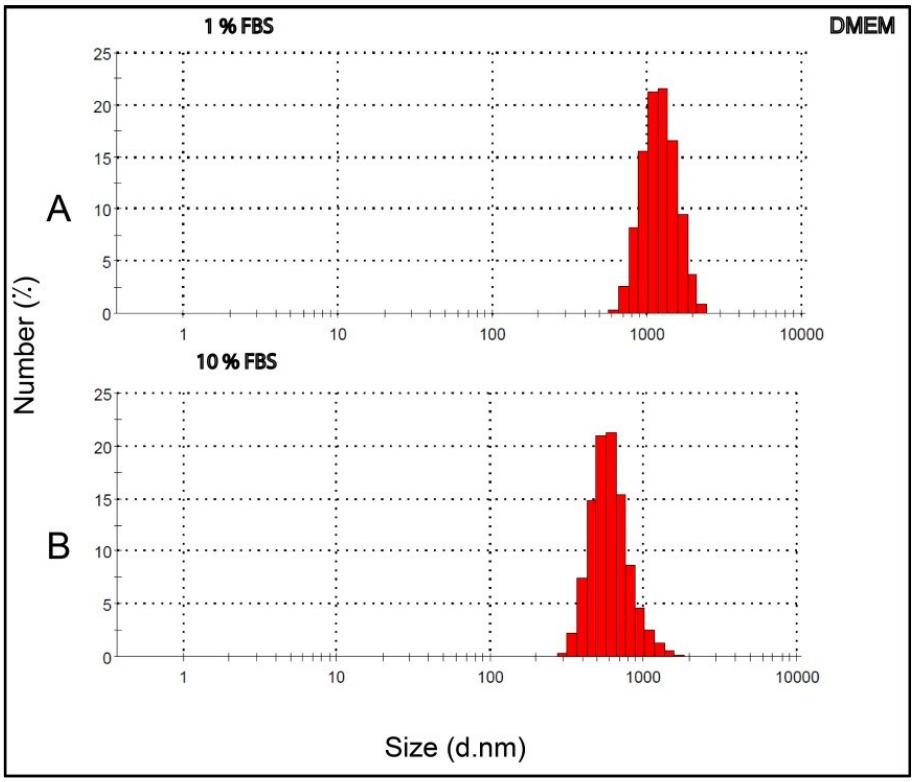

Figure 9: Hydrodynamic size distribution of the bare ZnO NPs after dispersion in DMEM supplemented with (A) 1% FBS and (B) 10% FBS. The average diameter ZnO NPs was 1375 and 797 nm, respectively.

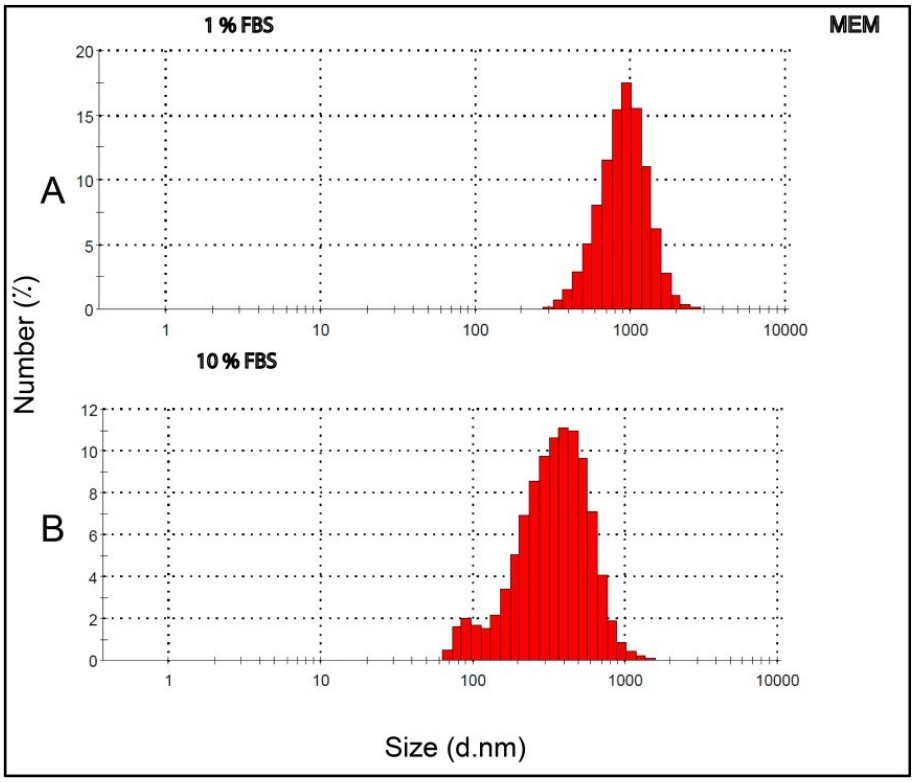

Figure 10: Hydrodynamic size distribution of the bare ZnO NPs after dispersion in MEM culture media supplemented with (A) 1% FBS and (B) 10% FBS. The average diameter ZnO NPs was 1335 and 480.6 nm, respectively.

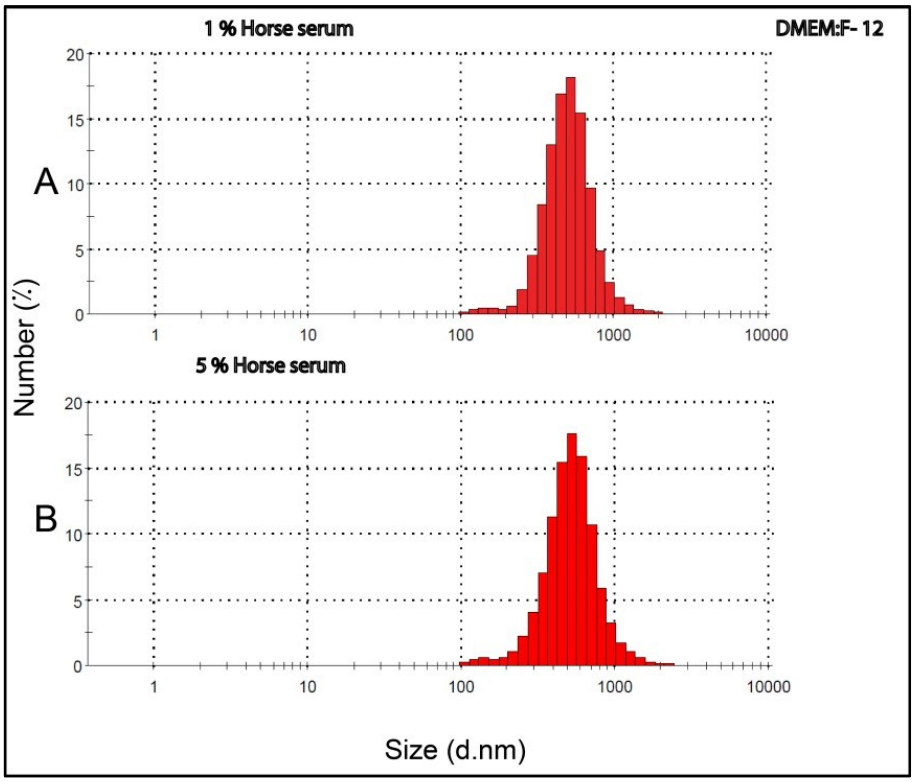

Figure 11: Hydrodynamic size distribution of the bare ZnO NPs after dispersion in DMEM: F-12 culture media supplemented with (A) 1% horse serum and (B) 5% horse serum. The average diameter ZnO NPs was 784.3 and 746.9 nm, respectively.

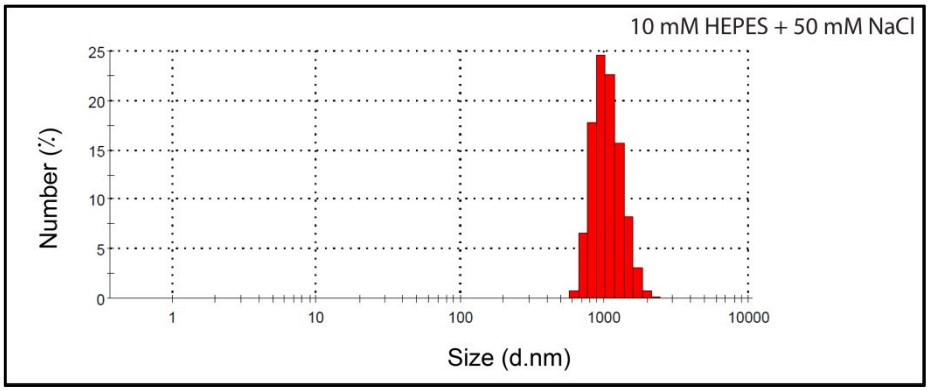

Figure 12: Hydrodynamic size distribution of the bare ZnO NPs after dispersion in HEPES buffer at pH 7.4 (10 mM HEPES+50 mM KCl) used for protein binding experiments. The average diameter ZnO NPs was 1121 nm, and the PdI was 0.102.

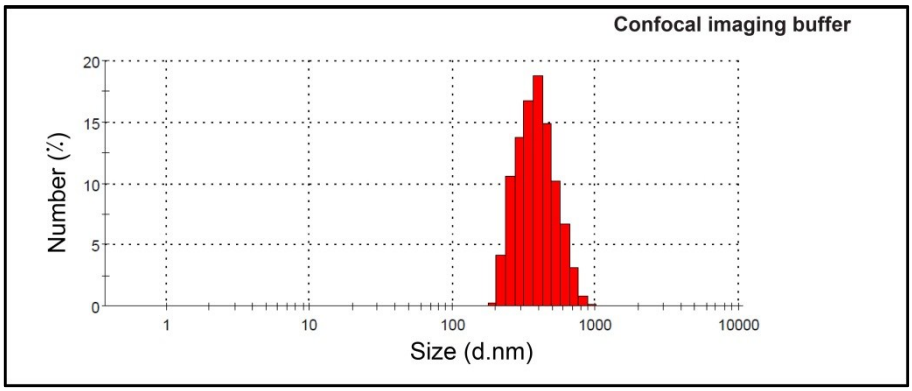

Figure 13: Hydrodynamic size distribution of ZnO-HCV-RGD-GFP NPs after dispersion in 10 mM HEPES confocal imaging buffer. The average diameter ZnO NPs was 1370 nm, PdI=0.760.

The zeta potential measurements of the bare ZnO NPs in deionised water at pH 6.3 showed that the particles had a positive zeta potential of +39.6 mV (Figure 14). The zeta potential of the bare ZnO NPs was not possible to measure in the different culture media used in this study, even in the absence of FBS. This is because the proteins in the FBS and amino acids in the cell culture media interfered with the measuring electrodes of the cell used for the zeta potential measurements. Therefore, to study the effect of adsorbed proteins on the surface charge of the bare ZnO NPs, the NPs were washed three times after incubation in CDMEM before resuspended in 10 mM HEPES buffer (pH=7.4). The zeta potential of the bare ZnO NPs was +28.6 mV (Figure 15) compared to -28.6 mV with the protein corona in 10 mM HEPES buffer (pH 7.4) (Figure 16) showing that the adsorbed proteins on the surface of ZnO NPs dramatically change the zeta potential of the ZnO NPs. The observed charge reversal of the bare ZnO NPs provided evidence for the adsorption of negatively charged serum proteins onto the ZnO NPs. This change in the surface charge of the bare ZnO NPs, upon adsorption of serum proteins, may affect the mobility and interaction of these particles with cellular membranes [123].

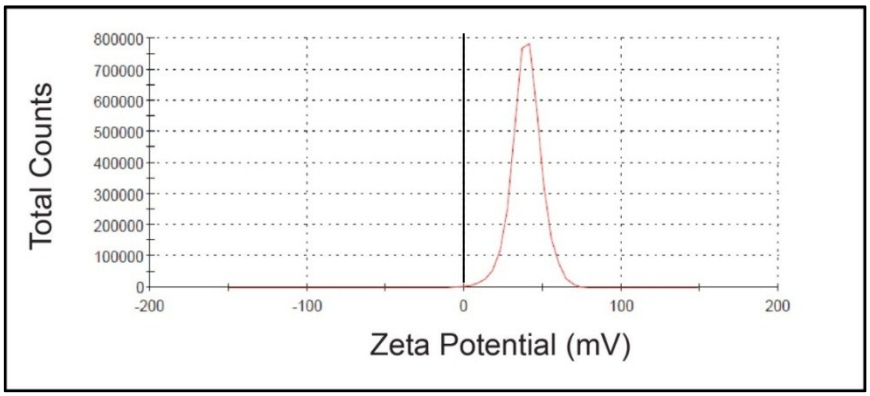

Figure 14: Zeta potential of 0.1 mg/ml bare ZnO NPs in deionised distilled water at pH 6.3 (+39.6 mV).

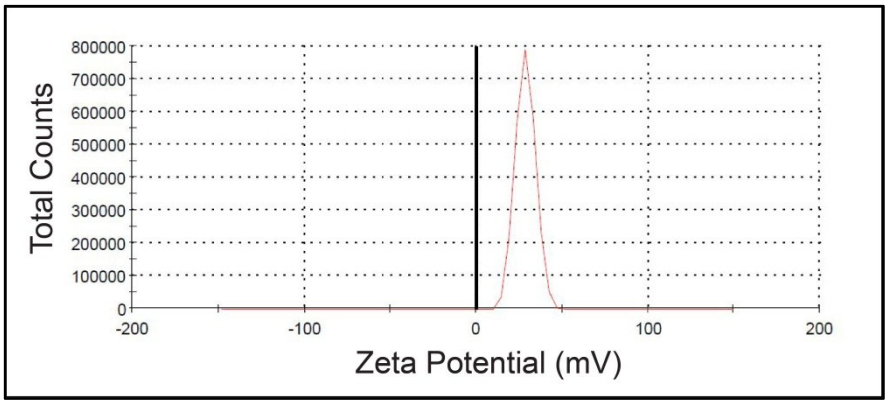

Figure 15: Zeta potential of 0.1 mg/ml bare ZnO NP-protein complex in 10 mM HEPES buffer at pH 7.4 (+28.6 mV).

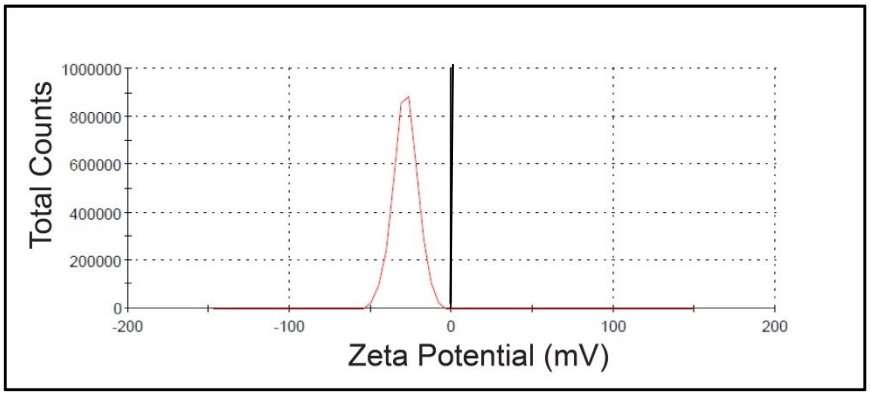

Figure 16: Zeta potential of 0.1 mg/ml bare ZnO NP-protein complex in 10 mM HEPES buffer at pH 7.4 (-28.6 mV).

Table 4: Average size distribution and PdI of ZnO NPs in different media.

NPs	Media	Average diameter (nm)	PdI	Zeta potential (mV)
Bare ZnO	DMEM+1% FBS	1375	0.203	
	DMEM+10% FBS	797	0.219	
	MEM+1%FBS	1335	0.274	
	MEM+10%FBS	480.6	0.318	
	DMEM:F-12+1% horse serum	784.3	0.299	
	DMEM:F-12+5% horse serum	746.9	0.255	
	Deionised distilled water (pH=6.3) water	703.8	0.233	+39.6
	Confocal imaging buffer	1231	0.141	
	10 mM HEPES buffer (pH 7.4)			+28.6
	10 mM HEPES+ 50 mM NaCl (pH 7.4)	1121	0.102	
Bare ZnO with protein corona from FBS	10 mM HEPES buffer (pH 7.4)			-28.6
ZnO-HCV-RGD-GFP	Confocal imaging buffer	1370	0.760	

3.2.4 Dissolution of zinc oxide nanoparticles in cell culture media and simulated body fluids

When the thermodynamic properties of ZnO nanostructures (including surface free energy) favour dissolution in a suspending media or biological environment, toxic Zn^{2+} ions may be generated [71]. Zinc oxide NPs can dissolve in an aqueous media to form hydrated Zn^{2+}. This dissolution is enhanced in acidic pH, as well as in the presence of biological components such as amino acids and peptides [49]. As illustrated in section 2.4.2, several studies had shown that the toxicity of ZnO NPs is attributed to the release of ionic zinc [124]. Since different cell culture media have a different composition, it is necessary to measure the dissolution of ZnO NPs in each medium before its use in any viability studies. However, few studies quantified the amount of released Zn^{2+} from ZnO NMS into the media used for their studies. Some of the reported dissolution studies on ZnO NPs in different culture media are illustrated in Table 5. However, saturated concentrations of ionic zinc as well as zinc ion complexes were not apparent in these studies. In Reed *et al.* study [125], for instance,

saturated conditions with respect to ionic zinc were not apparent in studied matrices, even after more than 1,000 h of dissolution. These studies reported a higher solubility of ZnO NPs in culture media compared to ultrapure water [125]. The high solubility of ZnO NPs in the culture media was attributed to the formation of aqueous complexes of Zn^{2+} with organic or inorganic constituents of the complex media. After dissolution, zinc ions generate a range of poorly soluble Zn-containing NPs (e.g. zinc phosphate, -carbonate, and/or -sulphides) when added to commonly used mammalian cell culture media [125-129]. Therefore the Zn^{2+} released by dissolving ZnO NPs in a given matrix may simply precipitate in another form and not be present as either ZnO NPs or dissolved Zn^{2+}.

In this study, the dissolution of the bare ZnO NPs in different complete culture media used throughout this study, as well as in the HEPES confocal imaging buffer (pH=7.4) and lyso-SBF (pH=5.2), was measured (Figure 17, a and b). The bare ZnO NPs showed ≤ 10% dissolution in all cell culture media (pH 7.3) and in the confocal imaging buffer at pH 7.4 (Figure 17, a). The maximum dissolved zinc ions concentration was achieved rapidly within the first hour of incubation of the bare ZnO NPs in the different media, and therefore the dissolution profile before equilibrium conditions was not obvious (Figure 17, a). The dissolved zinc ions interact with the inorganic salts present in the different culture media (e.g. phosphate, carbonate and/or sulphate), which results in reprecipitation of ionic zinc as zinc phosphates and phosphate (Figure 17, a). However, the dissolved zinc ions reached equilibrium within the first 8 h of incubation in all cell culture media buffered at pH=7.3 (Figure 17, a). The dissolution of ZnO NPs in DMEM in Xia *et al*. [49] and Reed *et al.* [125], was 14.63 µg/ml and >34 µg/ml, respectively (Table 5), which is much higher than the values obtained in this study (Figure 17, a). As expected from the phase-solubility diagram of zinc oxide [130], the bare ZnO NPs completely dissolved in lyso-SBF (pH=5.2) (Figure 17, b). The presence of proteins from 10% FBS in MEM media slightly increased the amount of dissolved Zn^{2+} from the bare ZnO NPs compared to 1% FBS in the same medium. The effect of the media on the dissolution of the ZnO NPs was clear in L-15 medium. Almost 52% of the total amount of the bare ZnO NPs dissolved in CL-15 after 3 h of incubation at 37°C (Figure 18). Therefore, if L-15 or other media with similar Zn solubility profile was used in ZnO toxicity studies, it could be incorrectly concluded that the ZnO NPs are responsible for any observed toxic effect, even though no actual exposure of the cells to ZnO NPs would have

occurred, as they would have completely dissolved. The composition of all culture media used in this study is illustrated in the eppendix at the end of this thesis.

To assess any effects of the RGD-targeting peptide on the dissolution of the NPs, the dissolution of the ZnO-HCV-RGD-GFP NPs was studied in HEPES confocal imaging buffer at pH 7.4 (Figure 19). The targeted ZnO-HCV-RGD-GFP NPs experienced a low amount of dissolution (< 1%) in the HEPES confocal imaging buffer (Figure 19).

Table 5: Reported dissolution of zinc oxide particles in DMEM, BEGM, RPMI cell culture media and water.

Study	Primary particle size of ZnO (nm)	Total amount of ZnO used	Conditions		Maximum dissolved zinc concentration			
			Time	Temperature (°C)	DMEM[a]	BEGM[b]	RPMI[c]	water
Xia *et al.*, [49]	13	Excess amount	4 days	22	225 µM (14.63 µg/ml)	190 µM (12.35 µg/ml)		
Song *et al.*, [68]	10-30 nm, 30 nm, 100 nm, fine particles	40 µg/ml	24 h	37			153.79 µM (10.0 µg/ml)	nanopure water 7.18–7.40 µg/ml
Reed *et al.*, [125]	159±4	100 mg/ml	24 h	20	>34 µg/ml		5 µg/ml	

[a]DMEM: Complete Dulbecco's modified eagle media which contains 10% fetal bovine serum (FBS)
[b]BEGM: Bronchial epithelial growth medium, which includes growth factors, cytokines, and supplements (no serum)
[c]PRMI-1640: Roswell Park Memorial Institute medium with 10% fetal bovine serum (FBS)

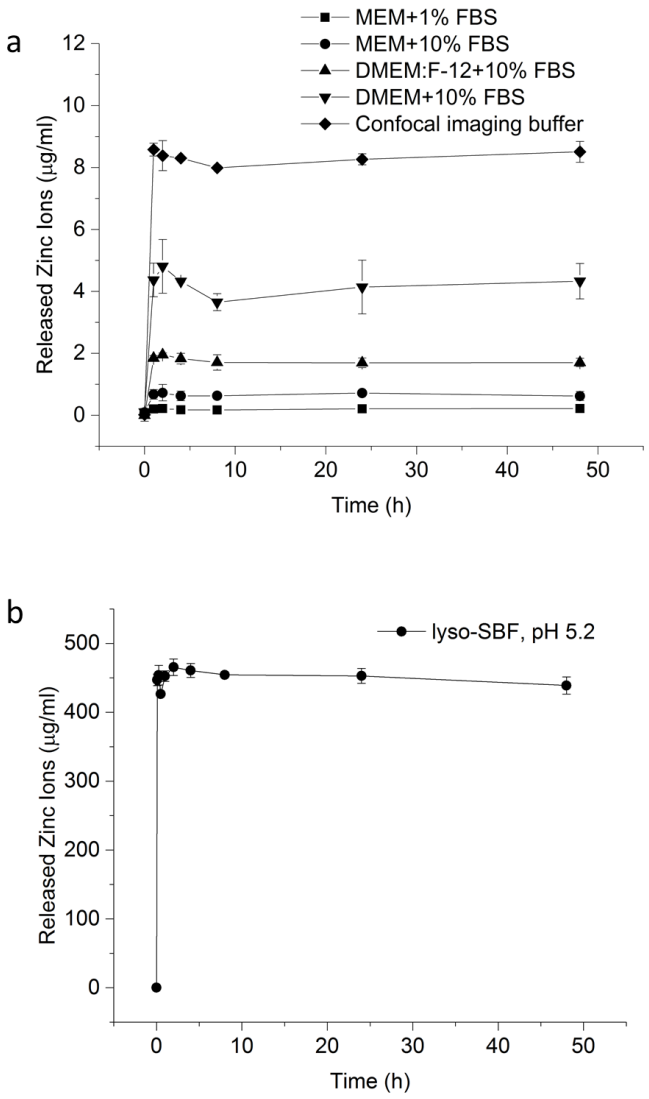

Figure 17: Dissolution of bare ZnO NPs in (a) MEM with 1% and 10% FBS, CDMEM: F-12, CDMEM, and HEPES confocal imaging buffer (pH=7.4), (b) lyso-SBF at pH 5.2. A 100 and 600 µg/ml ZnO NPs µg/ml were prepared at zero time for curve (a) and (b) respectively. Experiments were repeated in triplicate in three independent experiments. Concentrations are presented as mean ± SD (n=3).

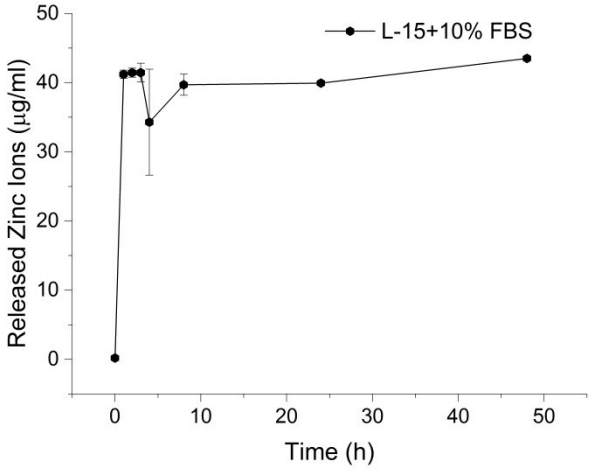

Figure 18: Dissolution of bare ZnO NPs in L-15+10 % FBS. 100 µg/ml ZnO-HCV-RGD-GFP NPs dispersions were prepared at zero time. Experiments were repeated in triplicate in three independent experiments. Concentrations are presented as mean ± SD (n=3).

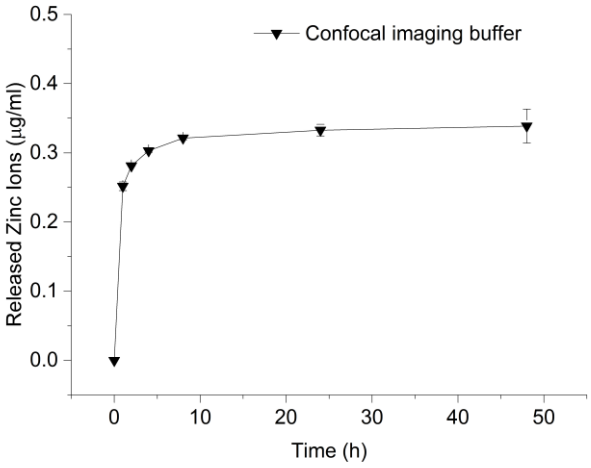

Figure 19: Dissolution of ZnO-HCV-RGD-GFP in 10 mM confocal imaging buffer pH 7.4. 100 µg/ml ZnO-HCV-RGD-GFP NPs dispersions were prepared at zero time. Experiments were done in triplicate in three independent experiments. Bars are presented as mean ± SD (n=3).

3.3 Summary and conclusions

ZnO NPs were prone to rapid agglomeration and they tend to have a wide size distribution once they are dispersed in different media. The use of surfactants is reported to stabilize NPs dispersions [131], but this will change the surface chemistry of the NPs and subsequently their bioreactivity. The adsorbed protein corona formed onto the surface of the NPs was found to stabilize the dispersions of the ZnO NPs. Aggregation of the NPs could decrease the available surface area of the NPs, which would decrease the dissolution rate.

ZnO dissolution was affected by the pH and the type of vehicle. The bare ZnO NPs showed a low solubility in MEM, DMEM and DMEM: F-12 cell culture media, and HEPES confocal imaging buffer. Therefore, these media could be used for the viability and uptake studies with the ZnO NPs. The L-15 medium, which is recommended by the ATCC for culture of MDA-MB-231 cells, on the other hand dissolved more than 52% of the particles within 1 h. Consequently L-15 could not be used in this study and DMEM was used instead. The bare ZnO NPs were completely dissolved in the lys-SBF at pH 5.2.

One of the major features of solid tumour tissues is the acidic pH of their extracellular matrix. The acidic extracellular pH of tumour tissues is due to the anaerobic metabolism which releases lactic acid and due to poor perfusion of the tumour tissues [132, 133]. This extracellular acidity of solid tumours is suggested to have varying effects on the response of cells to conventional anticancer drugs and it might allow the development of new and relatively specific types of therapy [134]. The pH-specific dissolution of ZnO NPs can be utilised to target these NPs to tumor tissue. At acidic pH, the ZnO NPs will dissolve and exert their toxic effects, with minimal effects on healthy cells. In *in vitro* assays, however, the cells are grown in media with buffers that maintain the pH at 7.4, so the cells are not likely to have such extracellular acidic pH. Therefore, upon exposure of the breast cancer cells to ZnO NPs in *in vitro* assays, the NPs will dissolve intracellularly inside the lysosomes after their uptake. Herein, the ZnO NPs dissolved quickly in the lyso-SBF at pH 5.2; consequently, they are expected to dissolve in the tumor tissue acidic extracellular pH, as well as within the acidic pH of the lysosomes upon their cellular uptake.

The protein corona on the surface of the bare ZnO NPs changed the surface charge of the bare ZnO NPs from +28.6 to -28.6. This change in the surface charge of the NPs can change their bioreactivity [135, 136].

In conclusion, before *in vitro* testing, the toxicity of NPs on cells, a thorough characterisation of the NPs which include their hydrodynamic size, their solubility, and interaction with proteins or with other component of cell culture media, is crucial. Upon interaction of the NPs with proteins and cell culture media, their physicochemical properties (e.g. surface charge) may be altered and this could affect their bioreactivity and consequently their toxicity.

4 Toxicity of bare and RGD-targeted zinc oxide NPs to breast cancer cells

The aim of this chapter was to study the toxicity of ZnO NPs to breast cancer cells. Breast cancer is a complex and heterogeneous disease that can be classified according to the presence of predictive markers like oestrogen receptor (ER), progesterone receptor (PR) and human epidermal growth factor receptor 2 (HER-2) [137, 138]. Approximately 60–70% of breast cancers express estrogen receptors (ER) and/or progesterone receptors (PR) and approximately 20–30% of breast cancers have amplified HER-2 and express high levels of the HER-2 protein [138]. Molecular targeted therapies that inhibit the oestrogen pathway or that target amplified HER-2 are effective in the treatment of breast cancer cells in patients whose tumours express these targets [138]. In approximately 15–20% of patients with breast cancer, the tumours do not express ER or PR and do not have amplification of HER-2 and these are called triple-negative breast cancer and they do not respond to hormonal therapy [138, 139]. In the laboratory, breast cancer is often modelled using established cell lines. In this study, two breast cancer cell lines have been used; MCF-7 and MDA-MB-231 cells. We have chosen these cell lines for the following reasons; first, these breast cancer cells have been widely used *in vitro* as a model to study toxicity against breast cancer cells [140]. Second, MCF-7 and MDA-MB-231 cells were used as ER+, PR+/–, HER2– and ER–, PR–, HER-2– cell models, respectively. MCF-7 cells, which are the most commonly used breast cancer cell line in the world, express estrogen receptors but not HER2 and they respond to hormonal therapy [137]. MDA-MB-231 cells, on the other hand, are triple negative breast cancers, so they do not respond to hormonal therapy. Third, treatment options of triple negative breast cancers are limited because of lack of targeted treatments [138, 139]. Thus, identification of novel, targeted therapies for triple-negative breast cancer would be of great benefit.

One of the serious drawbacks of the current cancer chemotherapy is the non-specific systemic delivery to cancer cells. This results in damage to normal unaffected tissue as well as to cancer cells and can result in both short-term and long-term negative damaging effects. Therefore, in this study the effect of ZnO NPs on healthy MCF-10-2A breast

epithelial cell line was also investigated. MCF-10-2A cells have been used as a model of healthy breast cells in several breast cancer studies [141-143].

The effect of RGD-targeting of the ZnO NPs to integrin αvβ3 receptors on the toxicity of breast cancer cell lines was also investigated. We have chosen to attach an RGD peptide (discussed in section 3.1.4) to the bare ZnO NPs that specifically binds the integrin αvβ3 receptors expressed on breast cancer cells, but not on the healthy epithelial cells. We will refer to the targeted NPs as ZnO-HCV-RGD-GFP NPs. Integrin αvβ3 is present on the surface of several cancer cells [91, 144, 145]. Analysis of metastatic breast tumours showed 10-15- fold higher expression levels of integrin αvβ3 receptors vs. healthy epithelial cells [146, 147]. Consequently, is considered an ideal cancer biomarker [148] and a potential delivery systems for cancer therapeutics [149]. The tripeptide sequence, Arg-Gly-Asp has been found to be highly selective for the integrin αvβ3 [91, 150, 151]. Recently, one study has successfully used the RGD as a ligand for ZnO NPs targeting to the integrin αvβ3 of human glioblastoma cells to detect these cells optically [12].

A number of different assays have been used to evaluate the toxicity of ZnO NMS in different cells in the literature. Different viability assays measure different cytotoxic end points such as oxidative stress, metabolic activity, and cell death [20]. Consequently, comparisons between the outcomes of these assays can be difficult. For example, the Alamar Blue assay measures cell metabolic activity, while the lactate dehydrogenase (LDH) assay measures cell membrane integrity. After certain time exposure to the NPs, the cell could be metabolically inactive, but its cell membrane may not be compromised, and therefore it will be recorded as dead (or not viable) in the Alamar Blue assay but not dead in the LDH assay. Furthermore, some viability assays (e.g. MTT, Alamar Blue, etc.), which are based on the detection of the metabolic activity of the cells after exposure to the NPs, require a long incubation time with the cells and this could lead to a false-positive results. These false positive results could be due to the fact that the NPs are not fully removed before adding the assay solution or inefficient washing of the NPs before adding the assay solution. Consequently, a number of viability assays should be used in combination to assess the toxicity of the NPs. Therefore, in this study, three viability assays have been used; the Alamar Blue, lactate dehydrogenase (LDH), and adenosine triphosphate (ATP) assays. The

toxicity of the bare and targeted ZnO NPs at different concentrations and exposure times has been studied in order to find a concentration window at which the ZnO NPs will exert toxic effects to the breast cancer cell lines, but not to the healthy epithelial breast cells.

Finally, to detect whether the cell death induced by the bare ZnO NPs occurred through apoptotic or necrotic pathways, an Annexin V/7-Aminoactinomycin D (7AAD) assay was conducted. Cell death is typically discussed as either apoptosis or necrosis. Apoptosis is described as an active, programmed process that results in cellular fragmentation into apoptotic bodies which are engulfed by macrophages or adjacent cells without eliciting inflammation [152]. Necrosis, on the other hand, has been characterized as passive, accidental cell death process that elicit uncontrolled inflammatory cellular responses [153]. As apoptosis is considered to be a regulated and controlled process, its occurrence during cancer treatment has received great attention [154, 155].

Through in depth understanding of the cellular responses resulting from ZnO NPs interactions with breast cancer cells, the inherent toxicity and selectivity of ZnO NPs against cancer may be further improved to make them attractive new anti-cancer agents.

4.1 Materials and methods

PE-Annexin V Apoptosis Detection Kit was from BD Pharmingen, UK. Hank's Balanced Salt Solution (HBSS) was purchased from Invitrogen Ltd, UK. $ZnCl_2$ (98%), Trypsin (0.25%) and Triton X-100 were purchased from Sigma Aldrich Ltd, UK. Mouse anti-human integrin αvβ3 antibody (cat.no CBL544, clone 23C6) was purchased from Millipore (Temecula, CA, USA).

4.1.1 Cell culture

The MDA-MB-231, MCF-7 and MCF-10-2A cell lines were purchased from ATCC (Manassas, VA, USA). The MDA-MB-231 and MCF-7 were maintained in DMEM, MEM, respectively. MEM and DMEM media were supplemented with 10% fetal bovine serum (FBS), and Penicillin/Streptomycin solution (100 units/ml penicillin, 100 µg/ml streptomycin). Cells were maintained in a humidified incubator at 37°C and 5% CO_2. MCF-10-2A cells were grown in DMEM:F-12 media supplemented with 20 ng/ml epidermal growth factor (Invitrogen, Life Technologies Ltd, UK), 100 ng/ml cholera toxin (Sigma-Aldrich Ltd, UK), 0.01 mg/ml insulin, 100 ng/ml hydrocortisone, Penicillin/Streptomycin solution (100 units/ml penicillin, 100

μg/ml streptomycin) and 5% horse serum was used. MCF-10-2A cells were maintained in a humidified incubator at 37°C and 5% CO_2.

4.1.2 Cell viability assays

For the cytotoxicity testing, three assays; Alamar Blue, LDH and ATP assays were employed. In all assays, cells were used from passages 5-25 and plated in flat-bottomed 96-well plates (Fisher Scientific Ltd, UK). The MCF-7 and MCF-10-2A were plated at a density of 3×10^5 cells mL^{-1} (9×10^4 cells/cm^2), while MDA-MB-231 was plated at a density of 2×10^5 cells mL^{-1} (6×10^4 cells/cm^2). These cell densities were chosen to ensure almost 80-90% confluency for each cell line. The plates were incubated at 37°C and 5% CO_2 in a humidified incubator for 24 hours. Then, supernatants from the culture plates were removed and fresh aliquots of growth medium containing different concentrations of ZnO NPs (bare and targeted) were added to the cells and then incubated with the cells for another 3, 24 h and/or 48 h for toxicity and IC_{50} analysis. The cytotoxicity was determined in at least three independent experiments performed in triplicate.

Stock suspensions of the bare ZnO NPs were prepared in ethanol, to ensure the NPs sterility for the assays. In each viability study, the particles were freshly prepared in media by sonication of the stock dispersions for 20 min on a bench sonicator and the particles were diluted to the desired concentration in the media and directly applied to breast cancer cell lines. The targeted ZnO NPs stock suspensions were prepared in 50 mM HEPES+100 mM NaCl buffer at pH 7.5. In each viability study, the targeted ZnO-HCV-RGD-GFP NPs were freshly prepared in media by sonication of the stock dispersions for 30 s on a bench sonicator and the particles were diluted to the desired concentration in the media and directly applied to breast cancer cell lines.

As the NPs have been shown to interact with dyes in the colorimetric assays [117], control experiments using the Alamar Blue, LDH and ATP assays were performed using the same protocol as the experiments in this study, but without the cells-in order to confirm that the ZnO NPs did not interfere with the viability assays. No effects were observed for all assays (data not shown).

4.1.2.1 Alamar Blue assay

To assess the metabolic activity of the cells after exposure to ZnO NPs, the Alamar Blue assay was carried out using the water soluble reagent, Alamar Blue (Invitrogen). Alamar Blue detects the reducing environment of living cells. Reduction of Alamar Blue can indicate the impairment of cellular metabolism and not only mitochondrial dysfunction [156]. In this assay, the cells were registered as viable, as long as they maintained their ability to reduce Alamar Blue.

The Alamar blue assay was used according to the manufacturer's protocol. Briefly, at the end of the incubation time (3 and 24 h) with the bare (10, 20, 25, 30, 35, 40, 50, and 60 µg/ml) and targeted (10, 20, 25, 30, 35, 40, 50, 60 and 100 µg/ml) ZnO NPs, the medium was removed and the cells were washed twice with fresh media. Alamar Blue was diluted with the medium to 10% (v/v) in the dark, and the plates were then treated with 100 µL of Alamar Blue 10% solution and incubated in a humidified atmosphere at 37°C and 5% CO_2. After an appropriate incubation time, *i.e*. 4, 9, and 11 h for MCF-10-2A, MCF-7, and MDA-MB-231, respectively, the spectrophotometric absorbance was measured at two wavelengths 570 nm (reduced form of Alamar Blue) and 600 nm (oxidised form of Alamar Blue) using a Bio-Rad plate-reader. The mean absorbance reading from the wells without the particles was used as the control (100% viability) and those treated with 1% Triton X-100 was used as a positive control (0% viability). The toxicity of the targeting peptide (GFP-HCV-RGD) to the cells was tested at the highest concentration used in the assays (50 µg/ml). IC_{50} values were determined by interpolation of the resulting curves.

Expression of integrin αvβ3 by breast cancer and normal epithelial cells

Expression of integrin αvβ3 receptors on cells has been shown to be cell line specific [157]. Therefore and since the ZnO-HCV-RGD-GFP NPs were used in our study to target the integrin αvβ3 receptors on the breast cancer cells, it was important to assess the expression of these receptors on all cell lines used in this study before exposure to the RGD-targeted ZnO NPs.

The expression of integrin αvβ3 was determined in the two breast cancer cell lines MDA-MB-231, MCF-7 and in the healthy breast MCF-10-2A cells. The cells were harvested

from T-175 flasks using 3 ml Accutase, counted, and washed with HBSS. A total of 500,000 cells were incubated with, or without, 10 µg/ml of purified mouse anti-human integrin αvβ3 antibody (cat.no CBL544, clone 23C6, Millipore, Temecula, CA, USA) in 50 µL HBSS for 30 min at 4°C. The cells were then washed three times with ice-cold HBSS, suspended in 200 µL of HBSS, and then incubated with 10 µg/ml secondary antibody (Alexa Fluor 488 Goat Anti-Mouse IgG (H+L), Invitrogen, UK) for 15 min on ice. The cells were washed twice and resuspended in 500 µL HBSS and subjected to flow cytometric analysis on a FACSCanto II flow cytometer (BD bioscience, Franklin lakes, NJ). Mouse IgG1 (Biolegend, UK) was used as an isotype control.

4.1.2.2 Lactate dehydrogenase (LDH) assay

LDH is a cytoplasmic enzyme that is released into the supernatant upon cell lysis. The LDH assay, therefore, is a measure of membrane integrity. The kit includes a catalyst (diaphorase/ NAD+) and a dye solution (iodotetrazolium chloride (INT) and sodium lactate). The LDH enzyme oxidizes lactate to pyruvate which reacts with the tetrazolium salt to form formazan. The water-soluble formazan dye is then detected spectrophotometrically [158]. In this assay, a dying cell could register as viable as long the cell membrane was intact for LDH release.

The LDH released upon exposure to ZnO NPs from damaged cells into the culture media was determined by Takara LDH Kit (Takara, CA, USA) and using the manufacturer's protocol. Briefly, after 24 and 48 h incubation with the bare particles (10, 20, 25, 30, 35, 40, 50, 60, and 100 µg/ml), 50 µL of the culture media above the cells was collected both cell and nanoparticle- free and incubated for 30 min with the reaction mixture (mentioned above) from the kit, and the reaction was stopped using 1 M HCL to a final concentration of 0.2 M. The rate of reduction of tetrazolium is directly proportional to LDH activity in the cell medium. Absorbance was measured using a Bio-Rad plate reader at 490 nm. The LDH assay requires low-serum medium because FBS contains LDH and thus can increases background absorbance [159], and therefore all culture media used were supplemented with 1% FBS for the MCF-7 and the MDA-MB-231 cells, and 1% horse serum for the MCF-10-2A cells. The mean absorbance reading from the wells without the particles was used as the negative

control (100% viability), and those treated with 1% Triton X-100 was used as a positive control (0% viability) [11].

4.1.2.3 ATP assay

The ATP assay determines the number of viable cells in culture based on quantification of the ATP present, which signals the presence of metabolically active cells, which produce ATP as energy for respiration and other vital processes. ATP content was determined using CellTiter-Glo Luminescent Cell Viability kit (Promega, Madison, USA). The kit includes the enzyme luciferase and the substrate luciferin. In the presence of ATP, luciferin is reduced to oxyluciferin with the production of light. The Light signal is proportional to the amount of ATP present which correlates with the number of viable cells present. Because ATP assay was used to assess the viability results obtained from the Alamar Blue assay, only MDA-MB-231 cells were tested using this assay.

After 24 and 48 h incubation of MDA-MB-231 cells with the bare (10, 20, 30, 40, 50, and 100 μg/ml) and targeted (20, 30, and 50 μg/ml) ZnO NPs particles, the plate and its contents were equilibrated at RT for approximately 30 min. Then 100 μL of the CellTiter-Glo® Reagent was added to each well and the contents were mixed for 2 min on an orbital shaker to induce cell lysis. The plates were then incubated at RT for 10 min to stabilize luminescent signal. Finally, chemical luminescence was measured with a GloMax Luminometer (Promega, UK). The toxicity of ZnO-HCV-GGG NPs used as a negative control for RGD targeting was also tested at the same concentrations. The experiment was repeated twice (n=2) for each NP type and the percentage cell cytotoxicity and cellular level of ATP were expressed as a percentage of the nontreated control (100% viability). Triton X-100 was used as a positive control (0% viability).

4.1.3 Mode of Cell death by Annexin V- 7AAD (necrosis and apoptosis)

The mode of cell death induced by the bare ZnO NPs was evaluated using a PE Annexin V-7AAD Apoptosis Detection Kit (BD Bioscience, CA, USA). Briefly, the cells were plated in flat-bottomed 96- well plates as described in section 4.1.2, and they were then exposed to bare ZnO NPs (20, 30, 50 μg/ml) for 3, 8, and 12 h, and to the whole range of concentrations of the bare ZnO NPs (10, 20, 25, 30, 35, 40, 50, 60, and 100 μg/ml) for 24 h. Following each

incubation time, the untreated and treated cells were harvested from triplicate wells, and washed with ice-cold HBSS. Subsequently, the cells were mixed with 100 µL of pre-diluted Annexin V-binding buffer (1×). Annexin V-PE (5 µL) and 7AAD (5 µL) were added sequentially to the cell suspension and further incubated at RT in the dark. After 15 min of incubation, 400 µL of binding buffer (1×) was added into each tube. The percentage of cells undergoing apoptosis and necrosis was quantified on a FACSCanto II flow cytometer (BD bioscience, Franklin lakes, NJ) equipped with FlowJo 7.6 software within 1 h. Cells without treatment with ZnO NPs were used as negative control. Cells staining with Annexin V-/7AAD+ were recognized as necrotic, those staining with Annexin V+/7AAD+ were taken as late apoptotic or secondary necrotic, whilst Annexin V+/7AAD- cells were recognized as apoptotic cells [79].

The apoptotic and/or necrotic effects of ionic Zn^{2+} on breast cancer cell lines was also measured and compared to those of the bare ZnO NPs to assess the role of ionic zinc in the mechanism of cellular death. After 24 h plating the cells in flat-bottomed 96 well plates, the MDA-MB-231 and the MCF-7 cells were exposed to $ZnCl_2$ solutions with concentrations of 16, 24, and 40 µg/ml of ionic zinc (Zn^{2+}). These concentrations of ionic zinc (Zn^{2+}) are equivalent to the ionic zinc contents of 20, 30 and 50 µg/ml bare ZnO NPs, respectively. The cells were then incubated with the $ZnCl_2$ solutions for 3, 8, 12 and 24 h of exposure as mentioned with the bare ZnO NPs, and the apoptotic and/or necrotic cells were analysed after each exposure time.

4.1.4 Statistical Analysis

Statistical analysis was carried out using a paired Student's *t*-test in all the viability assays. One way analysis of variance (ANOVA) was used to determine the statistical significance in the Annexin V/7AAD assay. The level of significance was accepted at $p \leq 0.05$. The levels of significance was indicated by the Asterisks: *p < = 0.05, **p < = 0.01, ***p < = 0.001, and ****p < = 0.0001 [160].

4.2 Results and Discussion

4.2.1 Cell viability assays

4.2.1.1 Alamar Blue

4.2.1.1.1 Alamar blue assay of bare ZnO NPs

The effect of the bare ZnO NPs on the metabolic activity of the ER+, PR+/–, HER2– MCF-7 and the triple negative MDA-MB-231 breast cells, as well as the healthy breast MCF-10-2A cells was tested using the Alamar Blue assay. The bare ZnO NPs were used in a concentration range of 10-60 μg/ml. This range of concentration was chosen after several preliminary experiments with different range of concentrations of the bare ZnO NPs, and showed a trend in reduction in the viability of both breast cancer cell lines.

The effect of the bare ZnO NPs on the viability of the cells was evaluated after 24 h exposure. Figure 20 shows that the bare ZnO NPs did not reduce the viability of the MDA-MB-231 and the MCF-7 cells at 10 μg/ml. The MDA-MB-231 and the MCF-7 cells showed a dose dependent reduction in viability at concentrations 20-60 and 30-60 μg/ml of the bare ZnO NPs, respectively (Figure 20). Compared to nontreated controls (100% viability), the reduction in the viability of the cells was significant at concentrations 30-60 and 35-60 μg/ml in the MDA-MB-231 and the MCF-7 cells, respectively ($p<0.05$) (Figure 20). The estimated median lethal concentration (IC_{50}) of the bare ZnO NPs on the MDA-MB-231 and the MCF-7 after 24 h exposure was 30 (Figure 21) and 36 μg/ml (Figure 22), respectively. Although the MDA-MB-231 cells were more sensitive to the toxic effects of the bare ZnO NPs than the MCF-7 cells, this was only significant ($p<0.01$) at 40 μg/ml (Figure 20). The MDA-MB-231 cells showed a linear response ($r^2=0.9983$) to the bare ZnO NPs concentrations 20-40 μg/ml (Figure 21). The exposed MCF-7 cells, on the other hand, did not show this linear response to the bare ZnO NPs and they exhibited, instead, a sudden reduction of 30% in their viability between 25-30 μg/ml and between 40-50 μg/ml of the bare ZnO NPs (Figure 22). A similar sudden drop in the cell viability after exposure to bare ZnO NPs has been previously reported in human monocyte derived macrophages (HMM) and lung epithelial cells [10, 49, 117, 161, 162]. This metabolic collapse in the MCF-7 is considered as one of the hallmarks of necrosis [163]. It has been reported that zinc induces apoptosis in cancer cells, and this

effects of zinc, in the regulation of apoptosis, appear to be cell type specific [5]. The effect of the bare ZnO NPs on the metabolic activity of the healthy MCF-10-2A cells after 24 h exposure was conducted only twice, and no reproducibility in the results was obtained (data not shown), however, this will be completed in the future work.

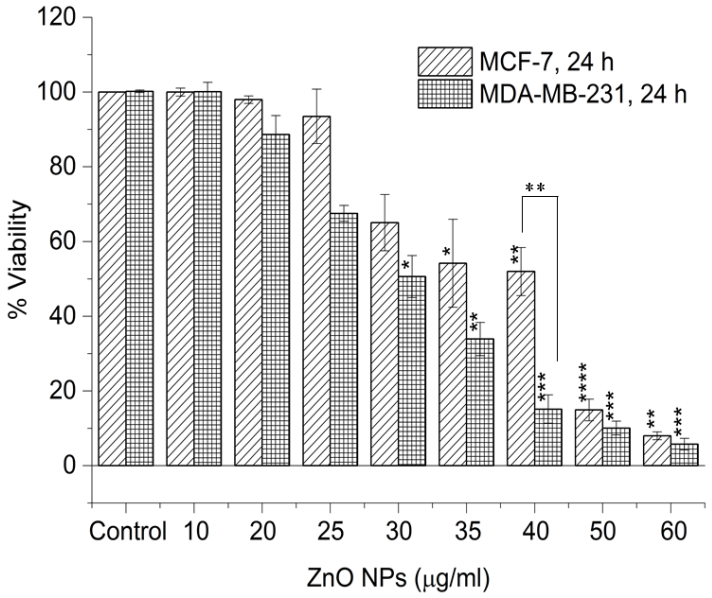

Figure 20: Alamar Blue viability assay of MCF-7 and MDA-MB-231 cells exposed to bare ZnO NPs for 24 h. Cells treated under similar conditions but without ZnO NPs were used as controls. The values represent the mean ± STD of three experiments each performed in triplicate. *p ≤ 0.05; **p ≤ 0.01; ***p ≤ 0.001, ****p ≤ 0.0001.

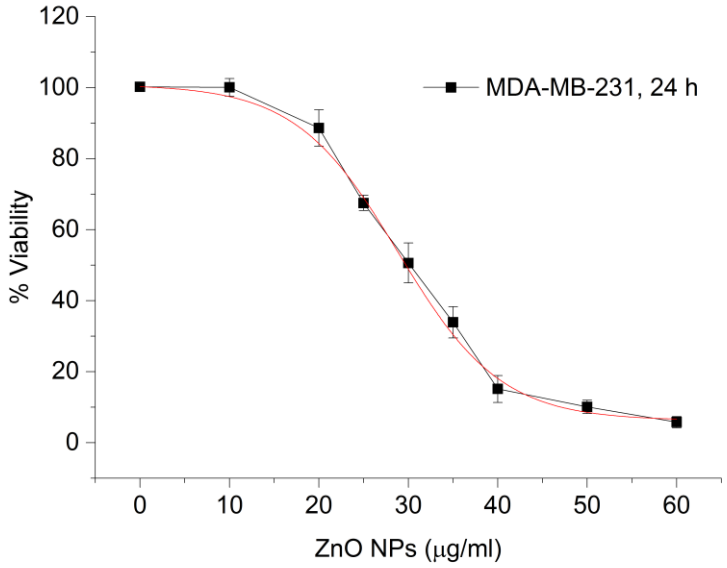

Figure 21: Dose response sigmoidal fit of viability of MDA-MB-231 cells exposed to bare ZnO NPs for 24 h. IC_{50}= 30 µg/ml. The values represent the mean ± STD of three experiments each performed in triplicate.

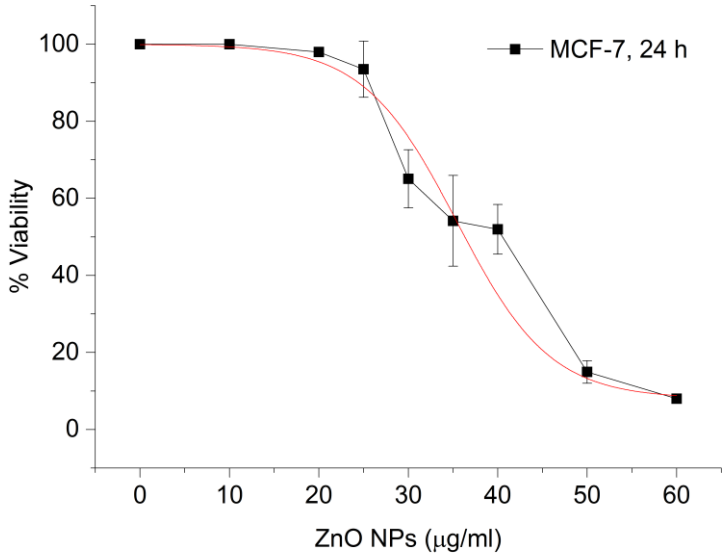

Figure 22: Dose response sigmoidal fit of viability of MCF-7 cells exposed to bare ZnO NPs for 24 h. IC_{50}= 36 µg/ml. The values represent the mean ± STD of three experiments each performed in triplicate.

To assess if the reduction in the viability in the breast cancer cells by the bare ZnO NPs starts at earlier exposure time, the Alamar Blue assay was conducted after 3 h of exposure to the bare ZnO NPs. The effect of the bare ZnO NPs on the viability of the healthy epithelia MCF-10-2A cells was also studied after 3 h exposure to the bare ZnO NPs. Figure 23

shows the viability results of the MDA-MB-231, MCF-7 and MCF-10-2A cells after 3 h exposure to the bare ZnO NPs at concentrations 10-60 μg/ml. The three cell lines experienced differential responses to the bare ZnO NPs after 3 h exposure (Figure 23). The viability of the three cell lines was not reduced at 10 μg/ml of the bare ZnO NPs (Figure 23). At 20 μg/ml, the bare ZnO NPs did not reduce the viability of both the triple negative MDA-MB-231 breast cancer cells and the healthy epithelial MCF-10-2A cells, while the MCF-7 showed a metabolic collapse, indicative of cell necrosis, at that concentration (Figure 23). The same figure shows that all cells experienced a concentration dependent trend in the reduction of their viability after 3 h exposure to the bare ZnO NPs. In the MDA-MB-231 cells, the reduction in the viability was significant ($p < 0.05$) at 25, 35-60 μg/ml, while it was significant ($p<0.05$) in the MCF-7 cells at concentrations 25-50 μg/ml. In the healthy epithelial MCF-10-2A cells, which experienced a higher viability at all concentrations tested, the reduction in viability was only significant ($p<0.05$) at concentrations 40-60 μg/ml. The MCF-7 cells were significantly ($p<0.05$) more sensitive to the bare ZnO NPs compared to the MCF-10-2A cells at concentrations between 35-50 μg/ml. This difference in the viability of the breast cancer cells and the healthy MCF-10-2A cells could be probably due to the differences in the effect of the bare ZnO NPs on the metabolic activity of the cells and the mechanism by which they induce the toxicity in each cell line.

Figure 24 to Figure 26 show the IC_{50} values of the bare ZnO NPs in the three cell lines after 3 h exposure. The IC_{50} values of the bare ZnO NPs calculated after 3 h exposure was 21, 34, and 45 μg/ml for MCF-7, MDA-MB-231, and MCF-10-2A cells, respectively. Therefore, for clinical applications, 35 μg/ml of the bare ZnO NPs could be used as a toxic dose to the breast cancer MCF-7 and MDA-MB-231 cells with minimal toxic effects on the healthy breast MCF-10-2A cells, which showed >65% viability at this concentration.

This finding of the ability of the bare ZnO NPs to selectively kill the breast cancer cells but not the healthy epithelial cells, as well as, its ability to effectively kill the triple negative MDA-MB-231 breast cancer cells, which account for a high proportion of breast cancer mortality due to the lack of effective therapies [64], will open new options for this material in cancer therapy.

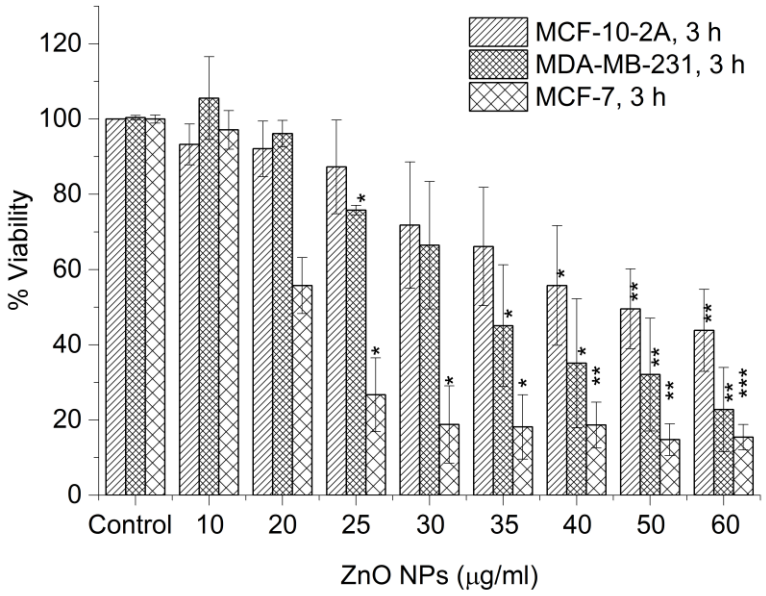

Figure 23: Alamar Blue viability assay of MCF-10-2A, MDa-MB-231 and MCF-7 cells exposed to bare ZnO NPs for 3 h. The NPs were significantly more toxic to MCF-7 compared to MCF-10-2A at 35 and 50 μg/ml. Cells treated under similar conditions but without ZnO NPs were used as controls. The values represent the mean ± STD of three experiments each performed in triplicate. *p ≤ 0.05; **p ≤ 0.01.

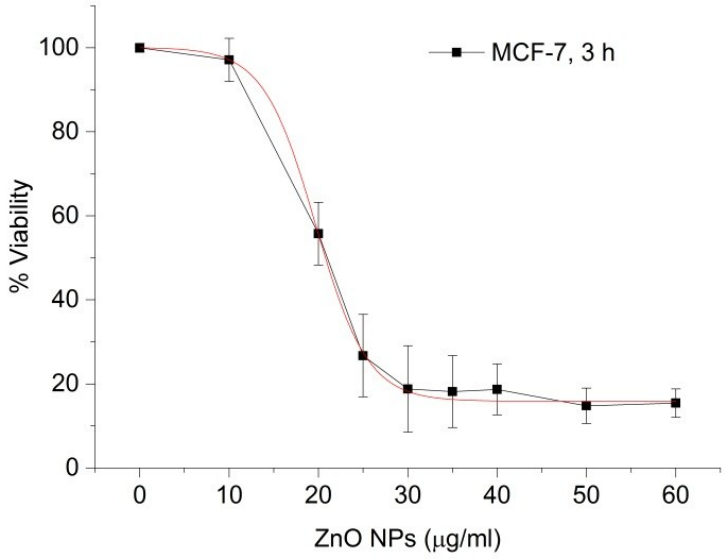

Figure 24: Dose response sigmoidal fit of viability of MCF-7 cells exposed to bare ZnO NPs for 3 h. IC_{50}= 21 μg/ml. The values represent the mean ± STD of three experiments each performed in triplicate.

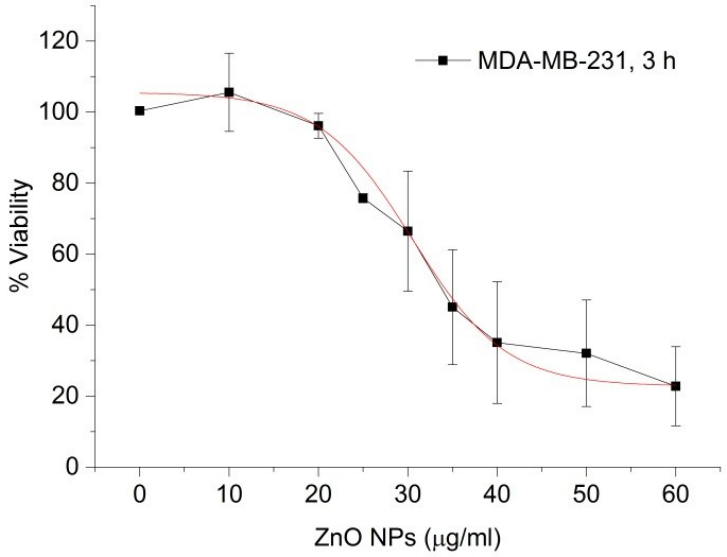

Figure 25: Dose response sigmoidal fit of viability of MDA-MB-231 cells exposed to bare ZnO NPs for 3 h. IC_{50}= 34 μg/ml. The values represent the mean ± STD of three experiments each performed in triplicate.

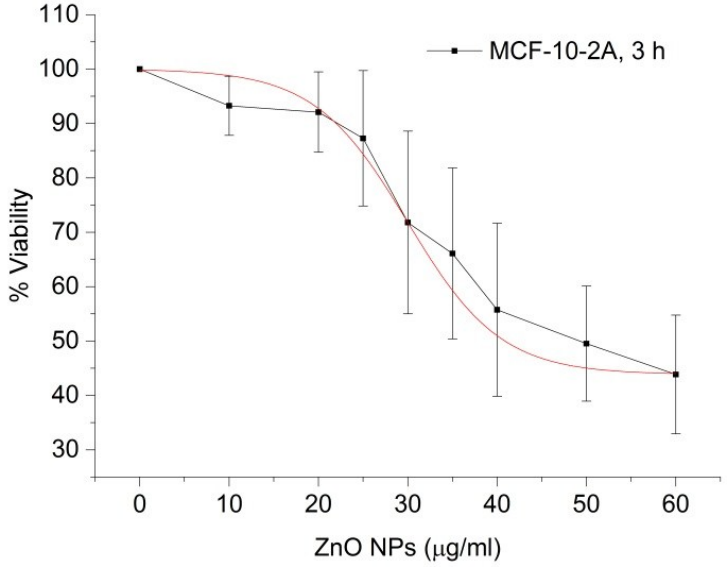

Figure 26: Dose response sigmoidal fit of viability of MCF-10-2A cells exposed to bare ZnO NPs for 3 h. IC_{50}= 45 μg/ml. The values represent the mean ± STD of three experiments each performed in triplicate.

The bare ZnO NPs showed a dose dependent reduction in the viability of breast cancer cells after 3 and 24 h of exposure at concentrations 10-60 μg/ml. In order to assess the effect of exposure time on the viability after exposure to the bare ZnO NPs, the viability of each breast cancer cell line after 3 and 24 h of exposure was compared using the Alamar

Blue assay (Figure 27 and Figure 28). Figure 27 shows that the bare ZnO NPs resulted in a time dependent reduction in the viability of the MDA-MB-231 cells at all tested concentrations; however, this time dependent toxicity of the bare ZnO NPs in the MDA-MB-231 cells was not significant ($p > 0.05$) at any tested concentration (Figure 27). On the other hand, the less aggressive ER+ MCF-7 cells did not show reduction in their viability with time after exposure to the bare ZnO NPs (Figure 28). The MCF-7 cells showed a higher viability after 24 h exposure compared to 3 h exposure, at all tested concentrations (10-60 μg/ml) (Figure 28). The difference in the viability of the MCF-7 after 3 and 24 h exposure to the bare ZnO NPs was highly significant ($p<0.05$) at 25 and 40 μg/ml (Figure 28). There is no such response of the MCF-7 cells to toxins reported in the literature. However, this higher viability of the cells after 24 h exposure compared to 3 h exposure could indicate recovery of the cells upon long exposure times with the NPs, and could be due to the complex effects of zinc on the metabolic activity of cancer cells [5]. This requires further investigation to fully understand the underlying factors.

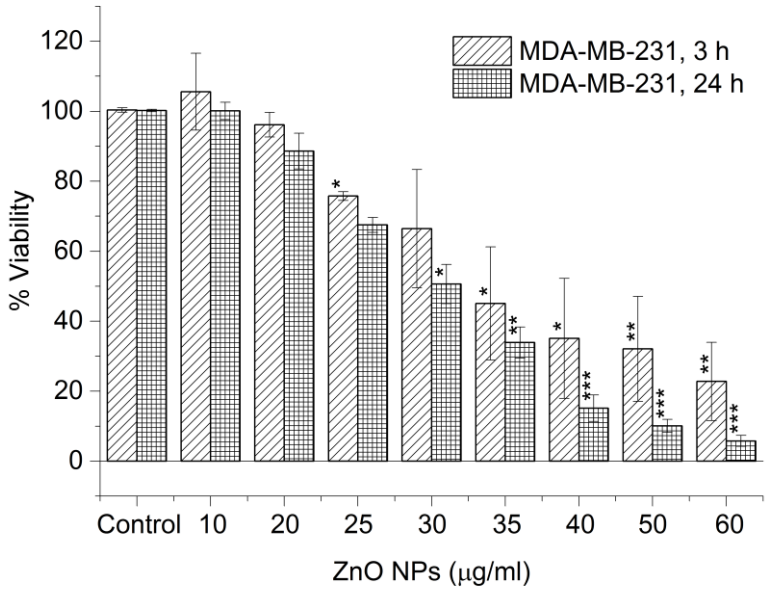

Figure 27: Alamar Blue viability assay of MDA-MB-231 cells exposed to bare ZnO NPs for 3 and 24 h. Cells treated under similar conditions but without ZnO NPs were used as controls. The values represent the mean ± STD of three experiments each performed in triplicate. *p ≤ 0.05; **p ≤ 0.01; ***p ≤ 0.001.

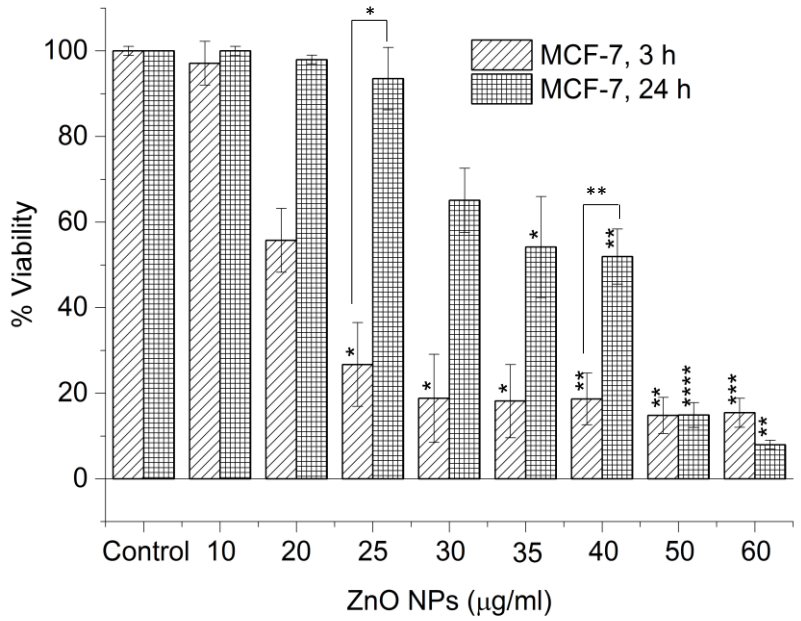

Figure 28: Alamar Blue viability assay of MCF-7 cells exposed to bare ZnO NPs for 3 and 24 h. The values represent the mean ± STD of three experiments each performed in triplicate. *p ≤ 0.05; **p ≤ 0.01; ***p ≤ 0.001, ****p ≤ 0.0001.

4.2.1.1.2 Alamar blue assay of targeted ZnO-HCV-RGD-GFP NPs

Expression of integrin αvβ3 by breast cancer and normal epithelial cells

To increase the selectivity of the ZnO NPs to cancer cells, we have chosen to target the ZnO NPs to the integrin αvβ3 receptors of the breast cancer cells which are shown to express a higher percentage of these receptors compared to the healthy breast cells [146, 147]. Before testing the effect of RGD-targeting on toxic effects of the ZnO NPs to the breast cells, the expression of integrin αvβ3 receptors by the breast cancer cells as well as the healthy epithelial cells was measured by flow cytometric analysis.

Figure 29 shows that both breast cancer cell lines expressed the integrin αvβ3 receptor, while the healthy epithelial MCF-10-2A breast cells did not show expression of these receptors. The MDA-MB-231 cells showed almost two times increased expression of the integrin αvβ3 receptors compared to the MCF-7 cells (Figure 29). Therefore, the RGD-targeted ZnO NPs were hypothesised to selectively target and destroy MCF-7 (ER+) and more significantly the triple negative MDA-MB-231 (ER-, PR-, HER2-) breast cancer cells, with minimal toxicity towards the healthy breast MCF-10-2A cells.

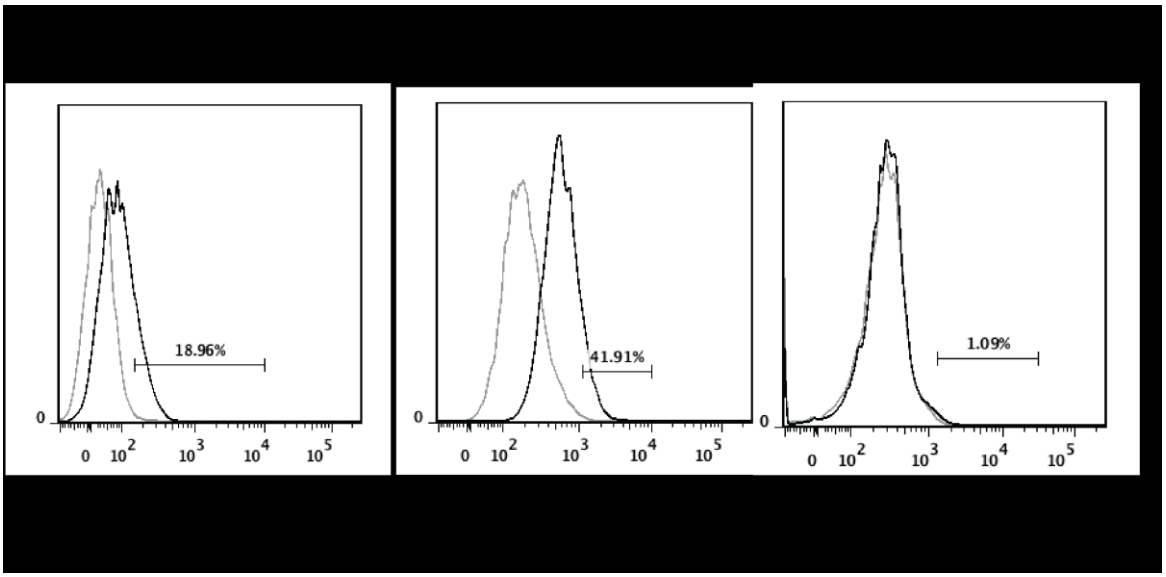

Figure 29: Flow cytometric analysis of integrin αvβ3 in MCF-7, MDA-MB-231, and MCF-10-2A cells. Cells were harvested and incubated with the mouse antihuman αvβ3 antibody, followed by incubation with a fluorescent-labelled secondary antibody and then analysed by flow cytometry (black lines). IgG1 antibody was used as an isotype control (grey lines).

Figure 30 shows the effect of RGD-targeting of the ZnO NPs on the viability of the MDA-MB-231 and MCF-7 cells. The breast cancer cells were exposed to concentrations of 10-100 µg/ml ZnO-HCV-RGD-GFP NPs for 24 h. At 10 µg/ml, the ZnO-HCV-RGD-GFP did not reduce the viability of both MCF-7 and MDA-MB-231 cells (Figure 30). At 20 µg/ml, and compared to nontreated control, a rapid and significant ($p<0.05$) drop in the viability of both cell lines was observed. This reduction in the cell viability at 20 µg/ml was different between the two breast cancer lines, and this difference was statistically significant ($p>0.05$); while the MCF-7 cells experienced a metabolic collapse and lost >90% of their viability, the more aggressive MDA-MB-231 cells maintained > 60% of their viability. The MDA-MB-231 and the MCF-7 cells lost their viability at concentrations of 25 and 30 µg/ml, respectively (Figure 30). The IC_{50} of the ZnO-HCV-RGD-GFP NPs to the MCF-7 and MDA-MB-231 cells after 3 h exposure was 16 and 22 µg/ml, respectively (Figure 31 and Figure 32). This higher sensitivity of the MCF-7 cells to the targeted ZnO NPs could be again due to their higher sensitivity to zinc ions released from the RGD-targeted ZnO NPs upon their intracellular dissolution. It has been reported that zinc induce apoptosis in cancers and this appear to be cell type specific [5].

Compared to the bare ZnO NPs, the RGD- targeted ZnO NPs resulted in a massive reduction in the viability of both breast cancer cell lines. The measured IC_{50} of the ZnO NPs

after 24 h exposure to the MCF-7 and the MDA-MB-231 cells was reduced by 56 and 27 %, respectively, by RGD-targeting of the ZnO NPs (Figure 31 and Figure 32, Table 6). This implies that the targeted ZnO-HCV-RGD-GFP NPs were more toxic to breast cancer cells than the bare NPs, and therefore, a lower dose of the ZnO-HCV-RGD-GFP NPs is required to kill the breast cancer cells. This higher toxicity of the RGD-targeted ZnO NPs compared to the bare ZnO NPs could be related to several factors. First, both cell lines expressed the integrin αvβ3 receptors, as previously shown in Figure 29, and therefore the RGD-targeting of the ZnO NPs may increase the concentration of the targeted ZnO NPs at the surface of the cells, as suggested by Pastorino *et al.*, in 2013 [164]. Second, after binding to the cell membrane, the RGD-targeted ZnO NPs could be taken up by the integrin αvβ3 receptor (clathrin-mediated endocytosis) as well as by clathrin-independent endocytosis, which leads to higher intracellular concentrations of ZnO and consequently a higher toxicity. On the other hand, the uptake of the bare ZnO NPs could be restricted to clathrin-independent endocytosis. Cellular fate and processing of the ZnO NPs after these two different uptake mechanisms could be different. It has been shown very recently that the transport of the NPs across the cell membrane dictates the NPs fate and toxicity [165]. Third, the surface chemistries of both the targeted and the bare ZnO NPs could be different, which again could cause different interactions with the cells. It has been shown that the surface chemistry of NPs largely affect their toxic outcomes [166, 167]. The higher sensitivity and the rapid drop in the viability of the cells after exposure to the targeted ZnO-HCV-RGD-GFP NPs, compared to the bare ZnO NPs, could also be due to the heterogeneity within the same breast cancer cell line. While the targeted ZnO-HCV-RGD-GFP could be equally toxic to both the sensitive and the highly resistant breast cells within the same breast cancer cell line, the bare ZnO NPs could be highly toxic to the sensitive cells, and higher doses are needed to eradicate the more aggressive cancer cells. Further investigations are required address these points.

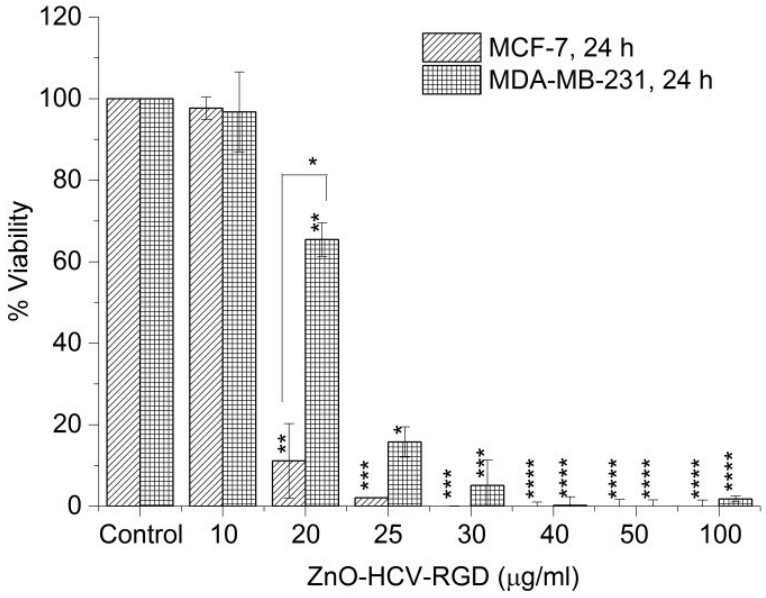

Figure 30: Alamar Blue viability assay of MCF-7 and MDA-MB-231 cells exposed to ZnO-HCV-RGD-GFP NPs for 24 h. The values represent the mean ± STD of three experiments each performed in triplicate. *p ≤ 0.05; **p ≤ 0.01; ***p ≤ 0.001, ****p ≤ 0.0001.

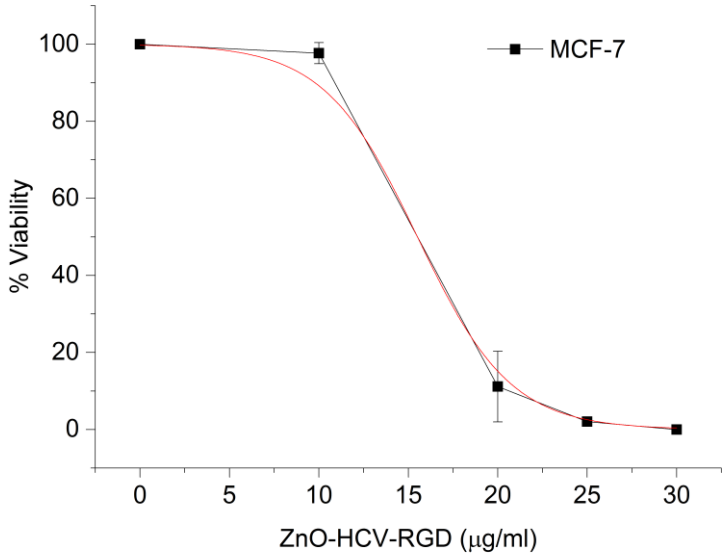

Figure 31: Dose response curve of MCF-7 cells exposed to ZnO-HCV-RGD-GFP NPs for 24 h, IC_{50}= 16 μg/ml. The values represent the mean ± STD of three experiments each performed in triplicate.

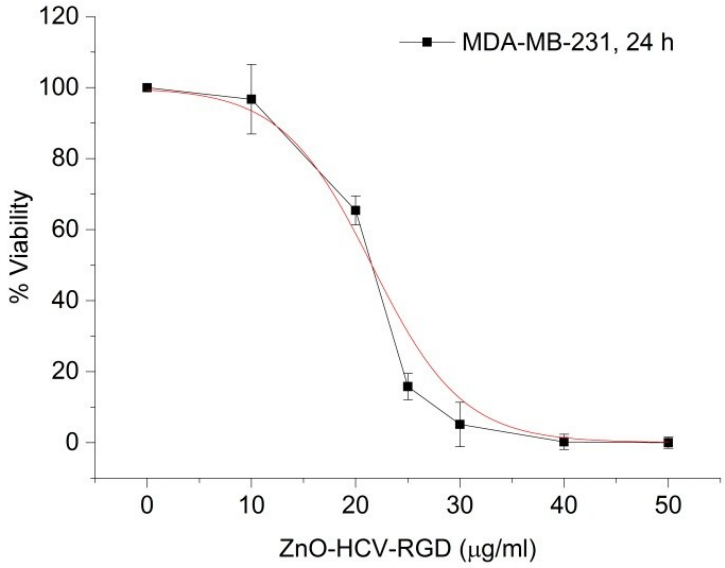

Figure 32: Dose response curve of MDA-MB-231 cells exposed to ZnO-HCV-RGD-GFP NPs for 24 h, IC_{50}= 22 μg/ml. The values represent the mean ± STD of three experiments each performed in triplicate.

Since the targeted ZnO NPs manifested high toxic outcomes to both breast cancer cell lines at concentrations 10-100 μg/ml, and a rapid drop in the viability was observed between 10-20 μg/ml of the targeted ZnO NPs after 24 h exposure (Figure 30), a reduced exposure time to the targeted ZnO NPs was tested. Both the MCF-7 and the MDA-MB-231 cells were exposed to the targeted ZnO NPs for 3 h at concentrations 10-100 μg/ml. The measured viability of the MCF-7 and MDA-MB-231 cells after 3 h exposure is presented in Figure 33 and Figure 34, respectively, and compared to that after 24 h exposure. The targeted ZnO-HCV-RGD-GFP NPs showed a dose dependent reduction in the viability of the MCF-7 and MDA-MB-231 cells at concentrations 20-40 μg/ml, and 20-100 μg/ml after 3 h exposure, respectively. Both cell lines showed a time dependent reduction in the viability after 3 and 24 h exposure at each concentration of the targeted ZnO-HCV-RGD-GFP NPs tested. The MCF-7 did not show a significant time dependent reduction in the viability ($p>0.05$) at all tested concentrations <30 μg/ml of the targeted ZnO NPs (Figure 33), therefore the IC_{50} of the ZnO-HCV-RGD-GFP to the MCF-7 after 3 h exposure was still 16 μg/ml (Figure 35) which is the same as that obtained after 24 h of exposure (Figure 31). In the MDA-MB-231 cells, however, the toxicity was time dependent and was significant ($p< 0.05$) at all concentrations between 20-100 μg/ml of the targeted ZnO-HCV-RGD-GFP NPs. The ZnO-HCV-RGD-GFP NPs showed an IC_{50} of 33 μg/ml after 3 h exposure to the MDA-MB-

231 cells (Figure 36), which is higher than that measured after 24 h, which was 22 µg/ml (Figure 32).

A summary of all values of IC_{50} of both bare and targeted ZnO NPs against MCF-7 and MDA-MB-231 breast cancer cell lines, as well as the healthy epithelial breast cells MCF-10-2A measured by Alamar Blue assay after 3 and 24 h, is summarized in Table 6 in the section of summary and conclusions of this chapter.

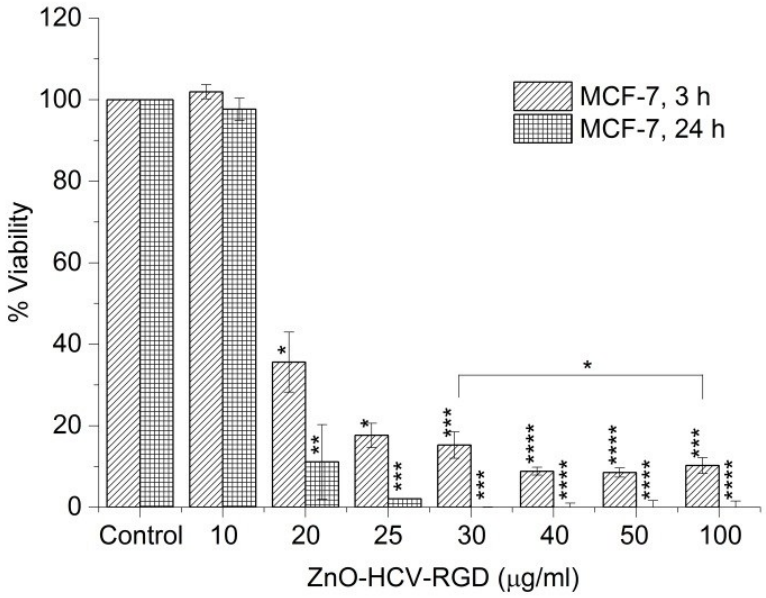

Figure 33: Alamar Blue viability assay of MCF-7 cells exposed to ZnO-HCV-RGD-GFP NPs for 3and 24 h. The values represent the mean ± STD of three experiments each performed in triplicate. *p ≤ 0.05; **p ≤ 0.01; ***p ≤ 0.001, ****p ≤ 0.0001.

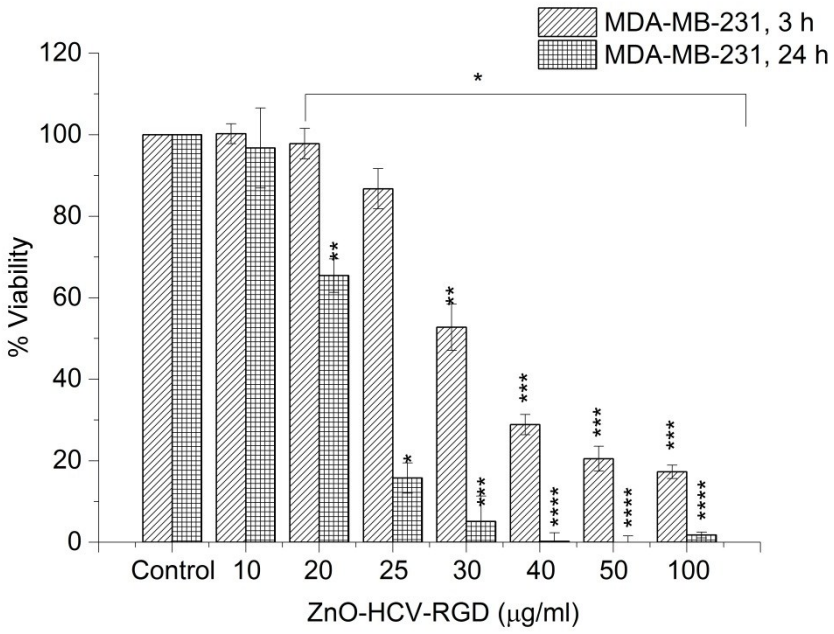

Figure 34: Alamar Blue viability assay of MDA-MB-231 cells exposed to ZnO-HCV-RGD-GFP NPs for 3 and 24 h. The values represent the mean ± STD of three experiments each performed in triplicate. *p ≤ 0.05; **p ≤ 0.01; ***p ≤ 0.001, ****p ≤ 0.0001.

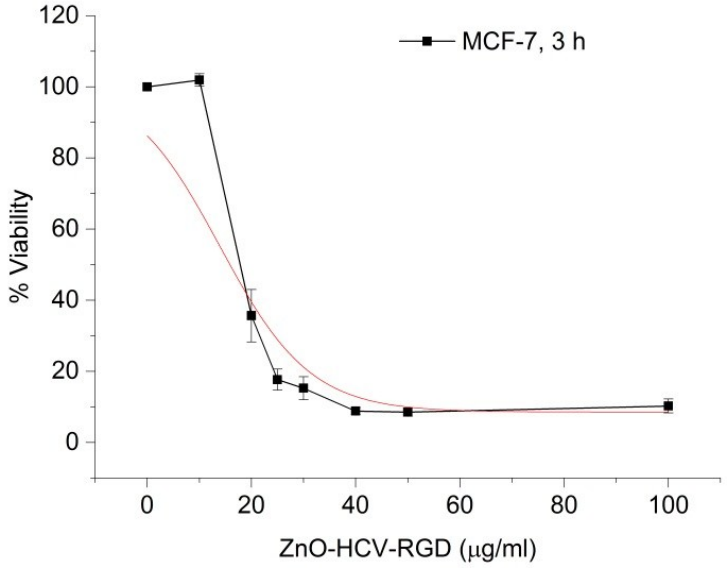

Figure 35: Dose response curve of MCF-7 cells exposed to ZnO-HCV-RGD-GFP NPs for 3 h, IC_{50}= 16 μg/ml. The values represent the mean ± STD of three experiments each performed in triplicate.

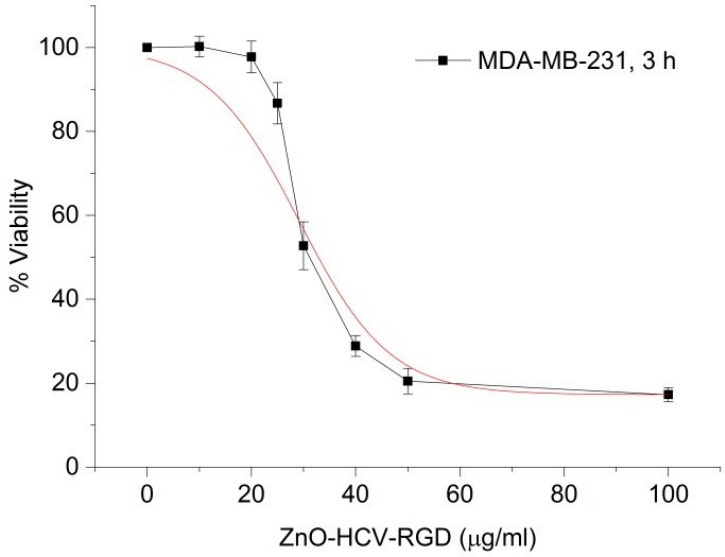

Figure 36: Dose response curve of MDA-MB-231 cells exposed to ZnO-HCV-RGD-GFP NPs for 3 h, IC_{50}= 33 μg/ml. The values represent the mean ± STD of three experiments each performed in triplicate.

4.2.1.2 LDH assay of bare ZnO nanoparticles

Theoretically, necrosis always results in disruption of the cytoplasmic membrane and necrotic cells release cytoplasmic LDH into the medium [168]. The effect of the bare ZnO NPs on plasma membrane permeability of the MCF-7 and the MDA-MB-231 cells was evaluated using the LDH assay. The cells were treated with the bare ZnO NPs at a concentration range from 10-100 μg/ml for 24 h. Figure 37 shows that, compared to the positive control (1% Triton X-100), the bare ZnO NPs exhibited a significant ($p<0.05$) dose dependent toxicity in the MCF-7 cells at all tested concentrations after 24 h exposure. The bare ZnO NPs were toxic to 57% of the MCF-7 cells at 100 μg/ml concentration. In the MDA-MB-231 cells, the bare ZnO NPs did not show a clear dose dependent toxicity at concentrations 10-100 μg/ml after 24 h exposure. In the MDA-MB-231 cells, the toxicity was only significant at 60 μg/ml of the bare ZnO NPs, and the bare ZnO NPs were toxic to <25% of the cells at 100 μg/ml (Figure 37).

Figure 37 also shows that there was a significant difference ($p<0.05$) in the LDH release between the MCF-7 and the MDA-MB-231 cells after 24 h exposure to the bare ZnO NPs at concentrations between 20-60 μg/ml. The bare ZnO NPs were more toxic to the MCF-7 cells than to MDA-MB-231 cells. The IC_{50} of the bare ZnO NPs in the MCF-7 cells after 24 h

exposure was 48 µg/ml (Figure 38). In the MDA-MB-231 cells, the IC_{50} could not be determined since the bare ZnO NPs were only toxic to < 25% of the MDA-MB-231 cells after 24 h exposure even at the highest concentration tested (100 µg/ml) (Figure 37). The increased LDH release in the MCF-7 cells, but not in the MDA-MB-231 cells, after 24 h exposure to the bare ZnO NPs could indicate that the bare ZnO NPs cause necrosis in the MCF-7 cells. It has been reported that MCF-7 cells are less prone to apoptosis due to the lack of caspase-3 activation [169, 170].

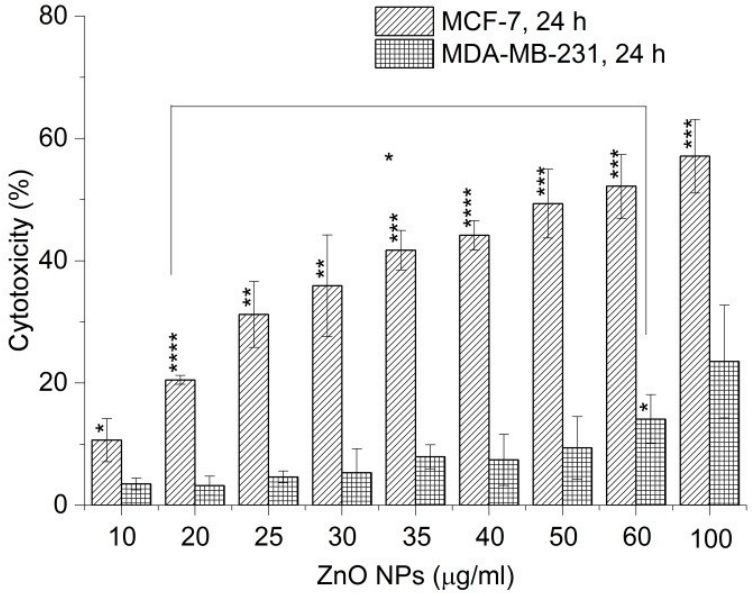

Figure 37: LDH viability assay of MCF-7 and MDA-MB-231 breast cancer cells exposed to bare ZnO NPs for 24 h at increasing concentrations (10-100 µg/ml). The values represent the mean ± SD of three experiments each performed in triplicate. *p ≤ 0.05; **p ≤ 0.01; ***p ≤ 0.001; ****p ≤ 0.0001.

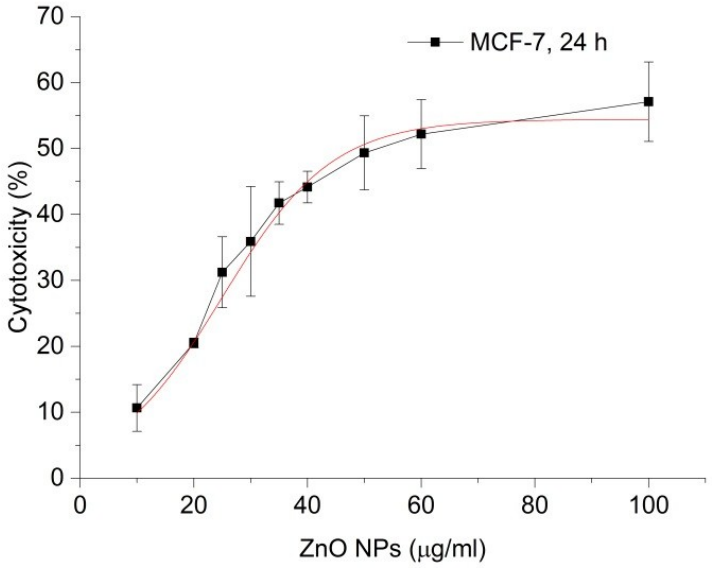

Figure 38: LDH dose response curve of MCF-7 cells exposed to the bare ZnO NPs for 24 h, IC_{50}= 48 μg/ml. The values represent the mean ± STD of three experiments each performed in triplicate.

Since the maximum release of LDH was <25% in the MDA-MB-231 cells after 24 h exposure to the bare ZnO NPs even at the highest concentration tested (100 μg/ml), a longer incubation time (48 h) was tested for both cell lines. The breast cancer cells were exposed to the same range of concentrations of the NPs (10-100 μg/ml) for 48 h. The bare ZnO NPs induced a time dependent toxicity to the MCF-7 and the MDA-MB-231 cells after 24 and 48 h exposure (Figure 39 and Figure 41, respectively). The increase in the toxicity of the bare ZnO NPs after 48 h compared to 24 h was statistically significant ($p<0.05$) at concentrations 20-100 μg/ml in the MCF-7 cells and at 20-60 μg/ml in the MDA-MB-231 cells (Figure 39 and Figure 41, respectively). The toxicity of the bare ZnO NPs in the MCF-7 after 48 h exposure was still dose dependent, with an IC_{50} <20 μg/ml (Figure 40) with more than 70% of the cells were dead at 25 μg/ml. On the other hand, cellular death in the MDA-MB-231 cells treated for 48 h was dose independent at concentrations between 10-60 μg/ml of the bare ZnO NPs (Figure 41). All concentrations between 10-60 μg/ml of the bare ZnO NPs showed almost 50% toxicity to the MDA-MB-231 cells after 48 h exposure, and therefore the IC_{50} of the bare ZnO NPs in the MDA-MB-231 cells could not be measured after 48 h exposure. At the concentration of 100 μg/ml, the bare ZnO NPs showed 80% toxicity to the MDA-MB-231 cells after 48 h exposure.

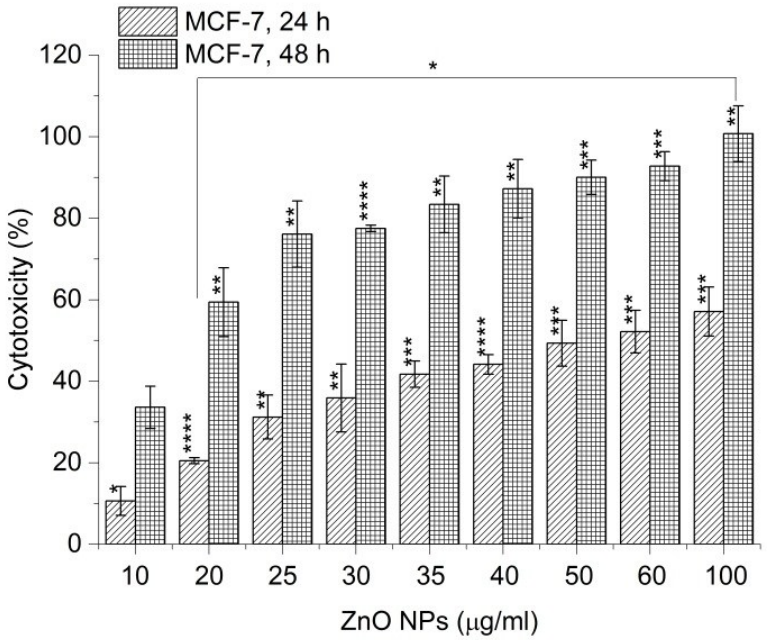

Figure 39: LDH viability assay of MCF-7 breast cancer cells exposed to bare ZnO NPs for 24 and 48 h at increasing concentrations (10-100 μg/ml). The values represent the mean ± SD of three experiments each performed in triplicate. *p ≤ 0.05; **p ≤ 0.01; ***p ≤ 0.001; ****p ≤ 0.0001.

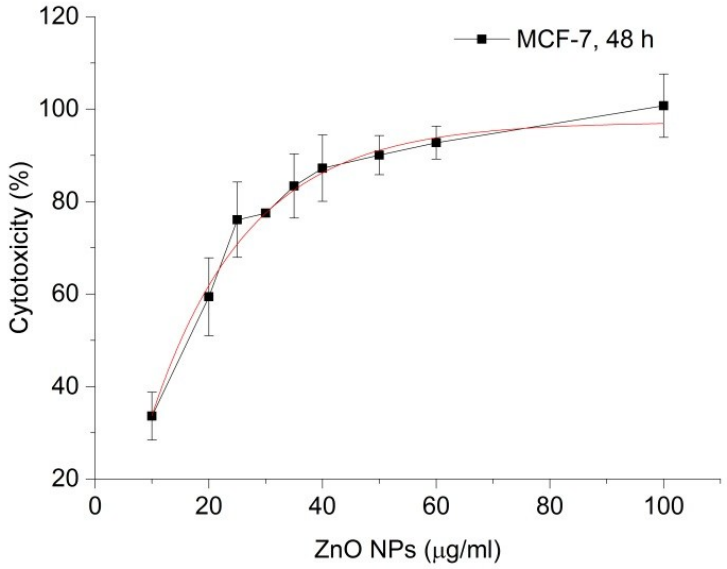

Figure 40: LDH dose response curve of MCF-7 cells exposed to the bare ZnO NPs for 48 h, IC_{50}< 20 μg/ml. The values represent the mean ± STD of three experiments each performed in triplicate.

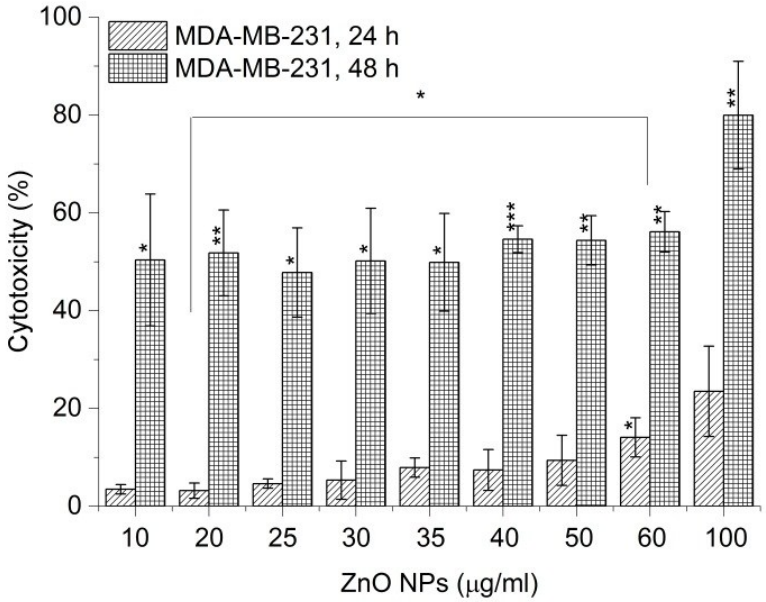

Figure 41: LDH viability assay of MDA-MB-231 breast cancer cells exposed to bare ZnO NPs at increasing concentrations (10-100 μg/ml). The values represent the mean ± SD of three experiments each performed in triplicate. *p ≤ 0.05; **p ≤ 0.01; ***p ≤ 0.001.

The LDH assay was also used to test the sensitivity of the MCF-10-2A cells to the bare ZnO NPs. The MCF-10-2A cells were exposed to the bare ZnO NPs at concentrations 10-100 μg/ml for 24 and 48 h and the percentage toxicity due to the release of LDH from the cells was calculated. The bare ZnO NPs showed time, but not dose dependent toxicity to the MCF-10-2A cells (Figure 42). After 24 h, the percentage necrosis observed at the highest concentration of the bare ZnO NPs tested (100 μg/ml) was <20%. The IC_{50} of the bare ZnO NPs to the MCF-10-2A cells after 24 h exposure could not be measured because the bare ZnO NPs were still not toxic to > 80% of the cells at 100μ/ml (Figure 42), therefore the IC_{50} is > 100 μg/ml. After 48 h exposure, however, the cells were completely dead at the lowest concentration tested (10 μg/ml). The higher IC_{50} of the bare ZnO NPs to the MCF-10-24 cells after 24 h exposure compared to the breast cancer cells again has important implications for the use of this material in cancer therapy.

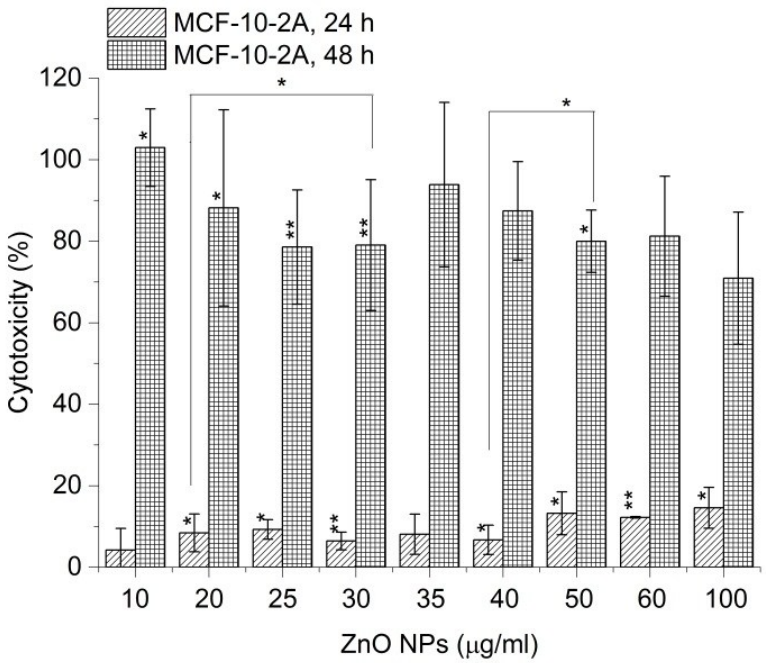

Figure 42: LDH viability assay of MCF-10-2A breast cancer cells exposed to bare ZnO NPs for 24 and 48 h at increasing concentrations (10-100 μg/ml). The values represent the mean ± SD of three experiments each performed in triplicate. *p ≤ 0.05; **p ≤ 0.01; ***p ≤ 0.001.

4.2.1.3 ATP assay

The Alamar Blue and LDH assays evaluate the viability of cells based on their metabolic activity and cell membrane integrity, respectively. Since after exposure to ZnO NPs, the cells could be metabolically inactive, but still maintain their membrane integrity, they could be recorded as dead in Alamar Blue, but viable in LDH assay. Furthermore, the Alamar blue assay requires a long incubation time with cells, which varies between the cells (*i.e.* 4, 9, and 11 h for the MCF-10-2A, MCF-7, and MDA-MB-231, respectively). Although the ZnO NPs were washed twice out of the cells at the end of the incubation time, and before the addition of the Alamar Blue, some aggregates of the ZnO NPs were observed to still adhere to the cells (data not shown). These adhered NPs could continue to exert their toxic effects during prolonged incubation of the cells with Alamar Blue reagent, giving false positive toxicity. In addition, in the LDH assay, the ZnO NPs were prepared in culture media with 1% FBS, as recommended by the manufacturer, to avoid the high background signal from LDH present in FBS, while they were prepared in media with 10% FBS in the Alamar Blue assay. All these factors made comparison between the results of two assays difficult. For this

reason, the ATP assay was used as another viability assay to evaluate the metabolic activity of the cells upon exposure to ZnO NPs.

The ATP assay determines the number of viable cells in culture based on quantification of the ATP present, which signals the presence of metabolically active cells which produce ATP as energy for respiration and other vital processes. The assay is based on lysing the cells at the end of exposure to the NPs and consequently, false positive toxicity due to long incubation time with the kit is avoided. The MDA-MB-231 cells were used in the ATP assay since they showed a dose dependent and linear reduction in the viability after exposure to the bare ZnO NPs in the Alamar Blue assay. Six concentrations of the bare ZnO NPs (10, 20, 30, 40, 50, and 100 μg/ml), and three concentrations (20, 30, and 50 μg/ml) of the targeted ZnO-HCV-RGD-GFP NPs were tested. Lower range of concentrations of the targeted ZnO NPs was tested due to the limited volumes available at the time of the assay.

4.2.1.3.1 ATP assay of the bare ZnO nanoparticles

The metabolic activity of the MDA-MB-231 cells after exposure to the bare ZnO NPs at concentrations 10-100 μg/ml was evaluated using the ATP assay. To have a better comparison to LDH assay, the ZnO NPs (10-100 μg/ml) were prepared in media supplemented with 1% FBS before exposure to the cells. The toxicity of the bare ZnO NPs against the MDA-MB-231 cells was measured after 24 and 48 h exposure.

Figure 42 shows the viability of the MDA-MB-231 cells after 24 and 48 h exposure to the bare ZnO NPs. The bare ZnO NPs resulted in a dose and time dependent reduction in the viability of the MDA-MB-231 cells at concentrations 10-100 μg/ml (Figure 42). After 24 h, the reduction in the viability of the cells was significant ($p<0.05$) at concentrations 50-100 μg/ml of the bare ZnO NPs, and the viability was reduced to 30% at 100 μg/ml of the bare ZnO NPs (Figure 43). The IC_{50} of the bare ZnO NPs after 24 h of exposure was 36 μg/ml and the reduction in viability was almost linear between 10-100 μg/ml ($r^2=0.99$) (Figure 43). This linear reduction in the viability of the MDA-MB-231 cells after exposure to the bare ZnO NPs was also observed in the Alamar Blue assay, and the IC_{50} measured from the ATP assay (36 μg/ml) was the same as that measured from the Alamar Blue assay (Figure 20). The reduction in the viability of the MDA-MB-231 cells after 48 h to the bare ZnO was significant

(p<0.05) at all tested concentrations 10-100 µg/ml compared to nontreated control (Figure 43). The cells lost >60% of their viability at all concentrations tested; therefore, the IC_{50} is < 10 µg/ml. The viability was completely lost at 100 µg/ml after 48 h exposure to the bare ZnO NPs (Figure 43).

Figure 44 shows a comparison of the viability of the MDA-MB-231 cells measured from the ATP and the Alamar Blue after 24 h exposure to the bare ZnO NPs. The viability measured from the ATP assay are comparable to these measured from Alamar Blue, and no significant differences were obtained except at 40 and 50 µg/ml (Figure 43). For example, the viability measured at 50 µg/ml of the bare ZnO NPs using the Alamar Blue and the ATP assays, was 10 and 47 %, respectively (Figure 45). The lower viability of the MDA-MB-231 cells measured by the Alamar blue at concentrations higher than the IC_{50} (36 µg/ml) could be false positive result due to longer incubation time of the Alamar Blue with the cells compared to the ATP, as discussed earlier in the introduction of this chapter.

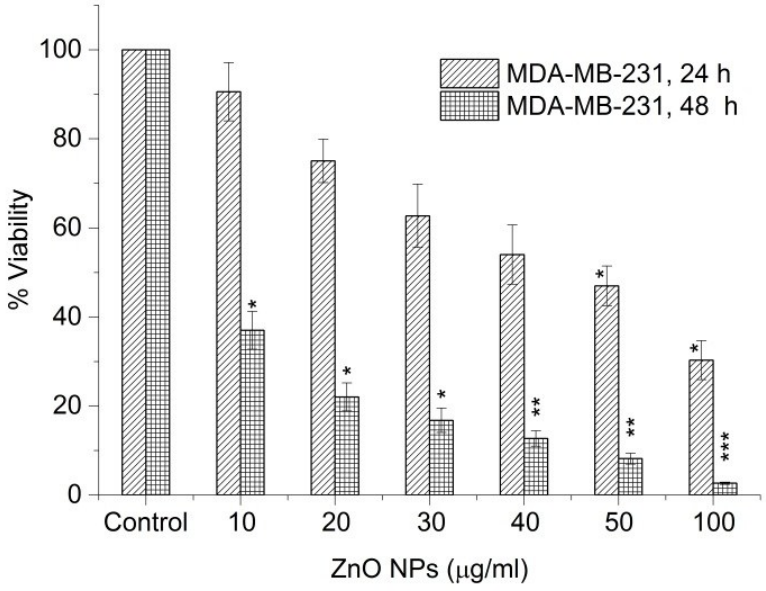

Figure 43: ATP viability assay of MDA-MB-231 cells exposed to bare ZnO NPs. Experiments were repeated twice (n=2) and represented as the mean ± SD. *P ≤ 0.05, **P ≤ 0.01, ***P ≤ 0.001.

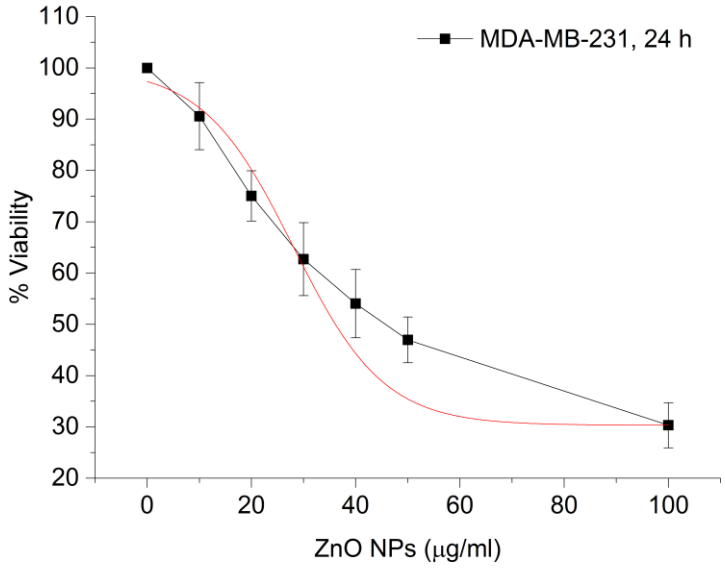

Figure 44: Dose response sigmoidal fit of viability of MDA-MB-231 cells exposed to bare ZnO NPs for 24 h. IC_{50}= 36 μg/ml. The values represent the mean ± STD of two experiments each performed in triplicate.

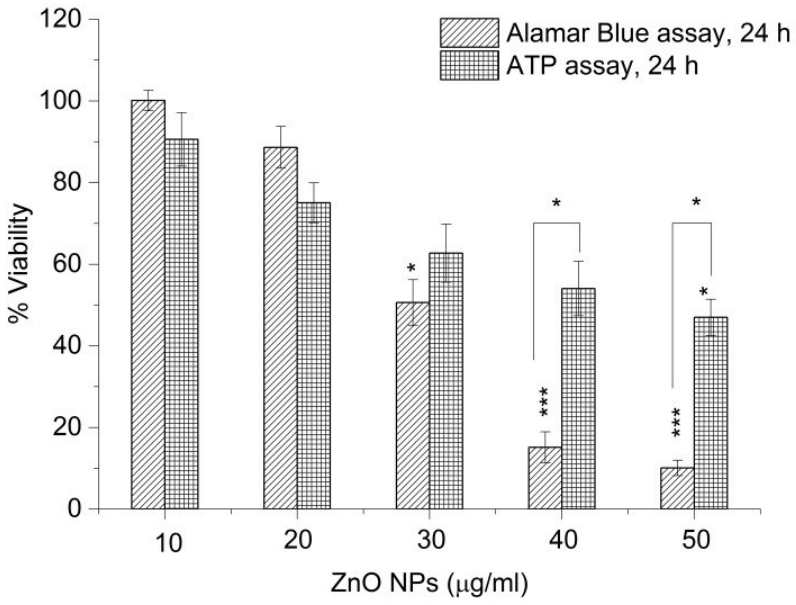

Figure 45: Viability of MDA-MB-231 cells exposed to bare ZnO NPs for 24 h measured by Alamar Blue and ATP assays. Experiments were repeated twice (n=2) and represented as the mean ± SD. *P ≤ 0.05, **P ≤ 0.01, ***P ≤ 0.001.

4.2.1.3.2 ATP assay of the targeted ZnO-HCV-RGD-GFP nanoparticles

The viability of the MDA-MB-231 cells after 24 and 48 h exposure to 20, 30 and 50 μg/ml ZnO-HCV-RGD-GFP NPs was measured by the ATP assay. Figure 46 shows that the MDA-MB-

231 cells experienced a dose and time dependent reduction in the viability after exposure to the targeted ZnO-HCV-RGD-GFP NPs. Compared to untreated controls, the reduction in the viability was statistically significant ($p<0.05$) at 50 µg/ml ZnO-HCV-RGD-GFP NPs after both 24 and 48 h exposure to the targeted ZnO NPs (Figure 46). The time dependent reduction in the viability of the cells was statistically significant ($p<0.05$) at 30 and 50 µg/ml of the ZnO-HCV-RGD-GFP NPs (Figure 46). The IC_{50} of the ZnO-HCV-RGD-GFP NPs against the MDA-MB-231 cells measured by the ATP assay was 33.5 and 24.6 µg/ml after 24 and 48 h exposure, respectively (Figure 47 and Figure 48).

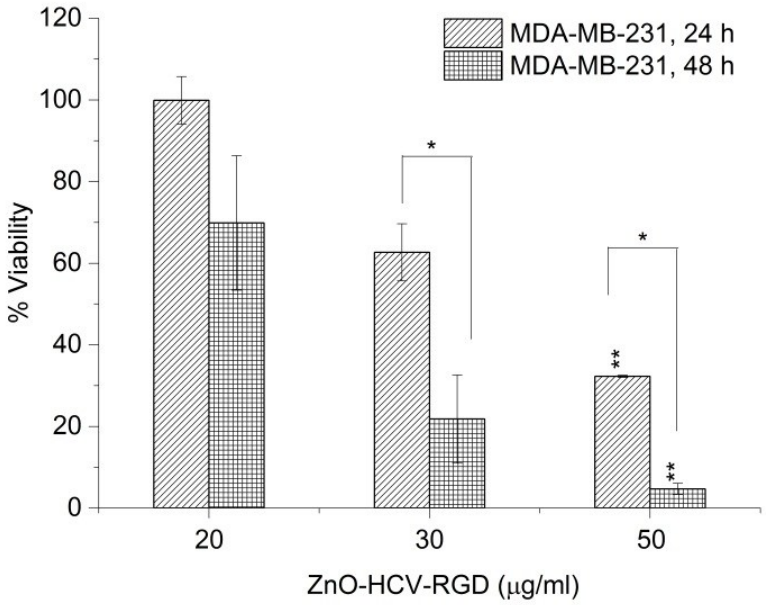

Figure 46: ATP viability assay of MDA-MB-231 cells exposed to ZnO-HCV-RGD-GFP NPs. Experiments were repeated in duplicate (n=2) and represented as the mean ± SD. *P ≤ 0.05, **P ≤ 0.01.

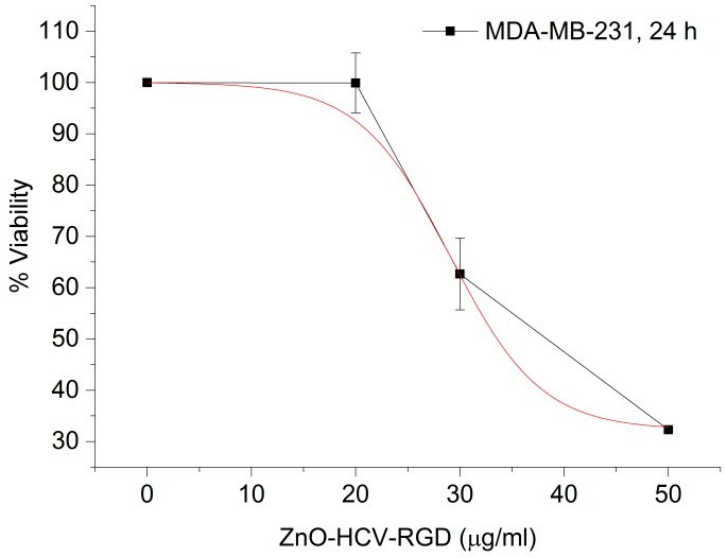

Figure 47: Dose response sigmoidal fit of viability of MDA-MB-231 cells exposed to ZnO-HCV-RGD-GFP NPs for 24 h measured by ATP assay. IC_{50}= 33.5 μg/ml. The values represent the mean ± STD of two experiments each performed in triplicate.

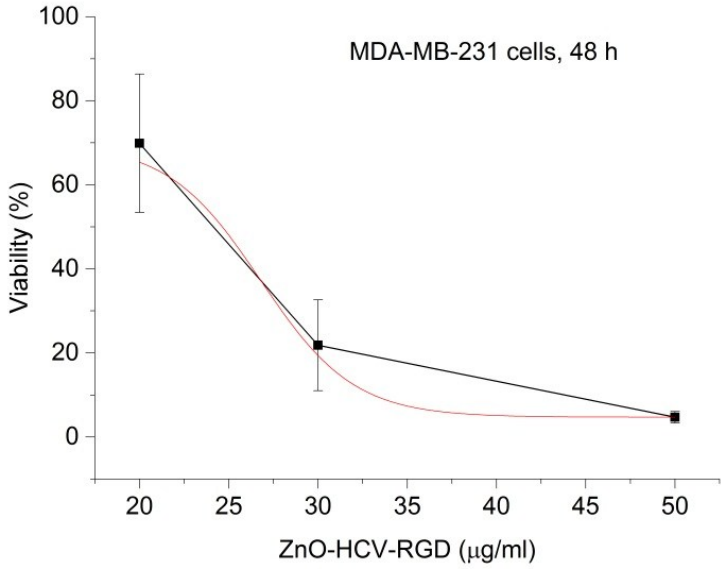

Figure 48: Dose response sigmoidal fit of viability of MDA-MB-231 cells exposed to ZnO-HCV-RGD-GFP NPs for 24 h measured by ATP assay. IC_{50}= 24.6 μg/ml. The values represent the mean ± STD of two experiments each performed in triplicate.

Figure 49 shows the viability of the MDA-MB-231 cells measured by the ATP and the Alamar Blue assays after 24 h exposure to 20, 30 and 50 μg/ml ZnO-HCV-RGD NPs. As observed with the bare ZnO NPs (Figure 45), the ATP assay recorded a higher viability of the

cells compared to the Alamar Blue assay; however, no significant difference was recorded between the two assays at any tested concentration (Figure 49). The lower viability measured using the Alamar Blue compared to the ATP assay, could be again due to the long incubation time with the Alamar Blue reagent as explained earlier. The IC_{50} measured for the ZnO-HCV-RGD-GFP NPs from the Alamar Blue and the ATP assay after 24 h exposure was 22 and 33.5 µg/ml (Figure 32 and Figure 47), respectively. It should be noted here that only three concentrations were tested with the ATP assay and they were not enough to obtain a complete dose response curve. An IC_{50} of 30.6 µg/ml would be obtained from the Alamar Blue assay when the dose response curve was constructed from the three concentrations (20, 30, and 50 µg/ml). Although the IC_{50} values measured after 24 h exposure to the Bare and targeted ZnO NPs from the Alamar Blue assay were lower than those measured from the ATP assay, the rate of change of the value was almost the same for the bare and the targeted ZnO NPs in the two assays (36 and 30 µg/ml for the bare ZnO NPs and 33.5 and 22 µg/ml for the targeted ZnO NPs from ATP and Alamar blue assays, respectively).

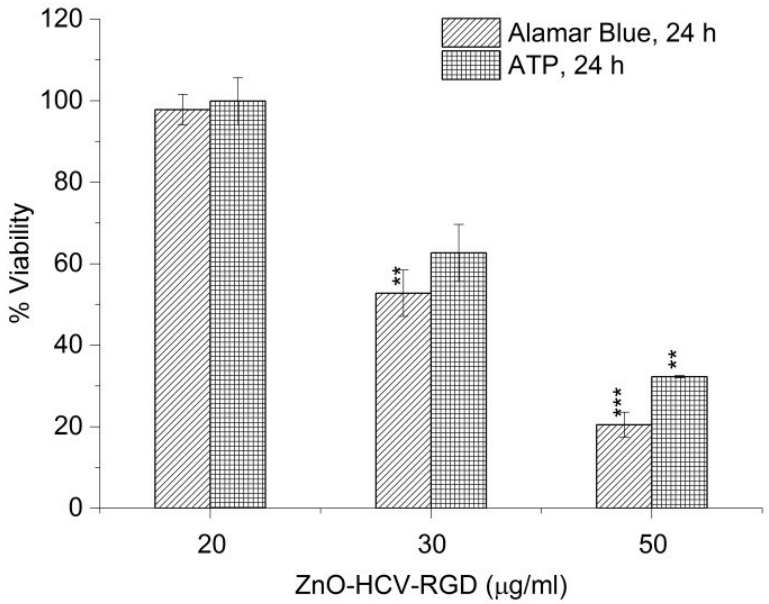

Figure 49: Comparison of the viability of MDA-MB-231 cells exposed to ZnO-HCV-RGD-GFP NPs measured by Alamar Blue and ATP assay. Experiments were repeated twice (n=2) and represented as the mean ± SD. *P ≤ 0.05, **P ≤ 0.01, ***P ≤ 0.001. No significant difference at any concentration

The reduction in the viability of the MDA-MB-231 cells after 24 and 48 h exposure to the ZnO-HCV-RGD-GFP NPs was compared to the negative control ZnO-HCV-GGG NPs.

Figure 50 shows that the ZnO-HCV-RGD-GFP NPs caused a higher reduction in the viability of the cells compared to the ZnO-HCV-GGG NPs after 24 and 48 h and at all tested concentrations (20, 30 and 50 μg/ml) (Figure 50). This difference was statistically significant ($p<0.05$) after 24 h exposure to 50 μg/ml of both NPs (Figure 50, a); while more than 70% of the MDA-MB-231 cells were dead after exposure to 50 μg/ml of the ZnO-HCV-RGD-GFP NPs, only 45% were dead at the same concentration of the ZnO-HCV-GGG NPs. This indicates that the RGD-targeting of the NPs was efficient and it could increase the toxicity of the ZnO NPs. After 48 h, the ZnO-HCV-RGD-GFP NPs were still more toxic than the negative control (ZnO-HCV-GGG NPs); however, this was not statistically significant ($p>0.05$) at all tested concentrations.

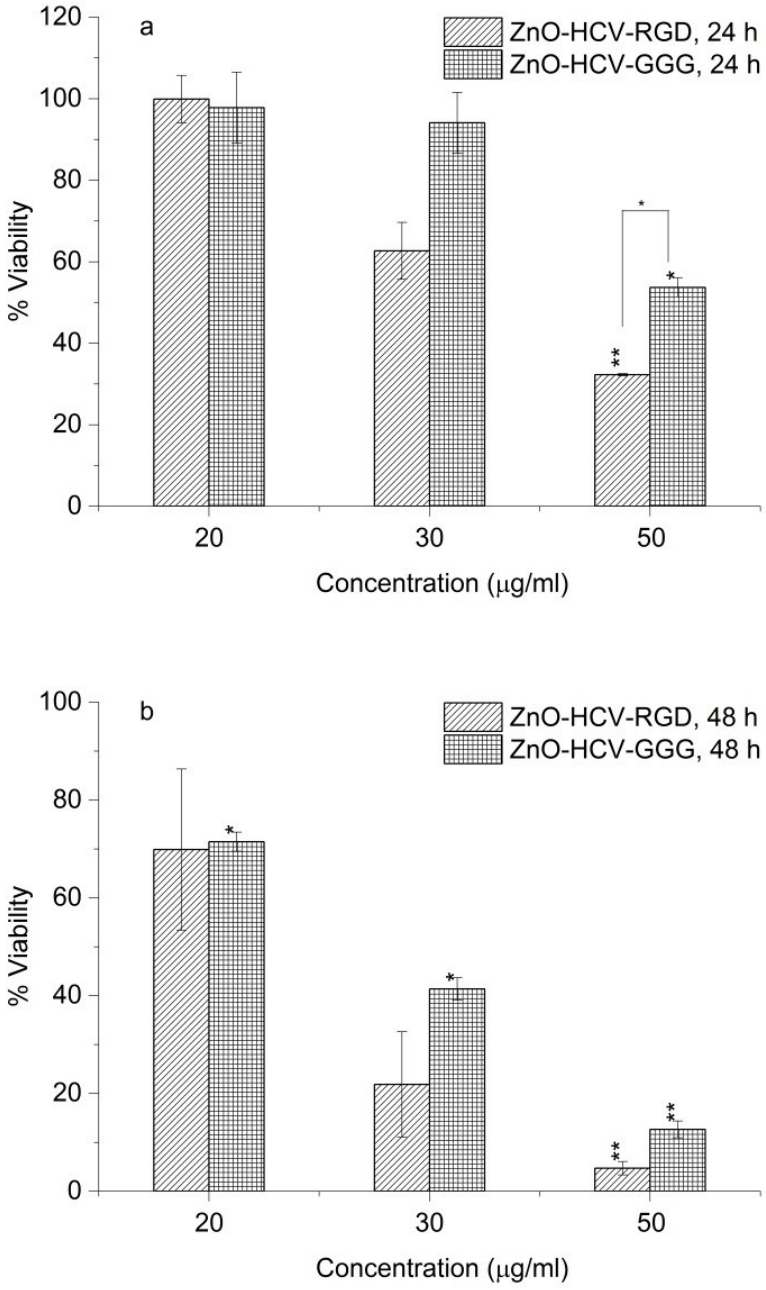

Figure 50: ATP viability assay of MDA-MB-231 cells exposed to ZnO-HCV-RGD-GFP and ZnO-HCV-GGG-GFP for (a) 24 h and (b) 48 h. Experiments were repeated in duplicate (n=2) and represented as the mean ± SD. *P ≤ 0.05, **P ≤ 0.01.

To assess the effect of targeting of the ZnO NPs, the viability of the MDA-MB-231 cells measured by the ATP assay after 24 and 48 h exposure to both the bare and the targeted ZnO NPs for 24 and 48 h was compared (Figure 51). At doses smaller than the IC_{50} (20 μg/ml), the bare ZnO NPs caused a higher reduction in the viability of the cells compared to the targeted ZnO NPs after both 24 and 48 h exposure; however, this difference was not

statistically significant ($p<0.05$). This higher effect of the bare ZnO NPs on the viability of the MDA-MB-231 cells could be due to smaller aggregate sizes in the medium used for the ATP assay (DMEM+1% FBS) compared to that of the ZnO-HCV-RGD-GFP NPs. The average aggregate size of the bare ZnO NPs measured in DMEM+1% FBS medium was 1375 nm (Figure 9). The aggregate size of the ZnO-HCV-RGD-GFP NPs in the same medium was not measured, due to their limited amount available, but the targeted ZnO-HCV-RGD-GFP NPs formed aggregates of higher size than those of the bare ZnO with a high PdI in the confocal imaging buffer (Table 4). The smaller size of the bare ZnO NPs could lead to their higher uptake by the MDA-MB-231 cells and subsequent higher toxicity. It has been shown that the size of the NPs is a critical factor that affects their uptake [171, 172]. The IC_{50} of the targeted ZnO NPs after 24 h exposure to the MDA-MB-231, however, was lower than that measured for the bare ZnO NPs (33.5 and 36 μg/ml, respectively). This indicates that RGD targeting increased the toxicity of the ZnO NPs, due to enhanced uptake by the cells through binding of the ZnO-HCV-RGD-GFP NPs to the integrin αvβ3 receptors.

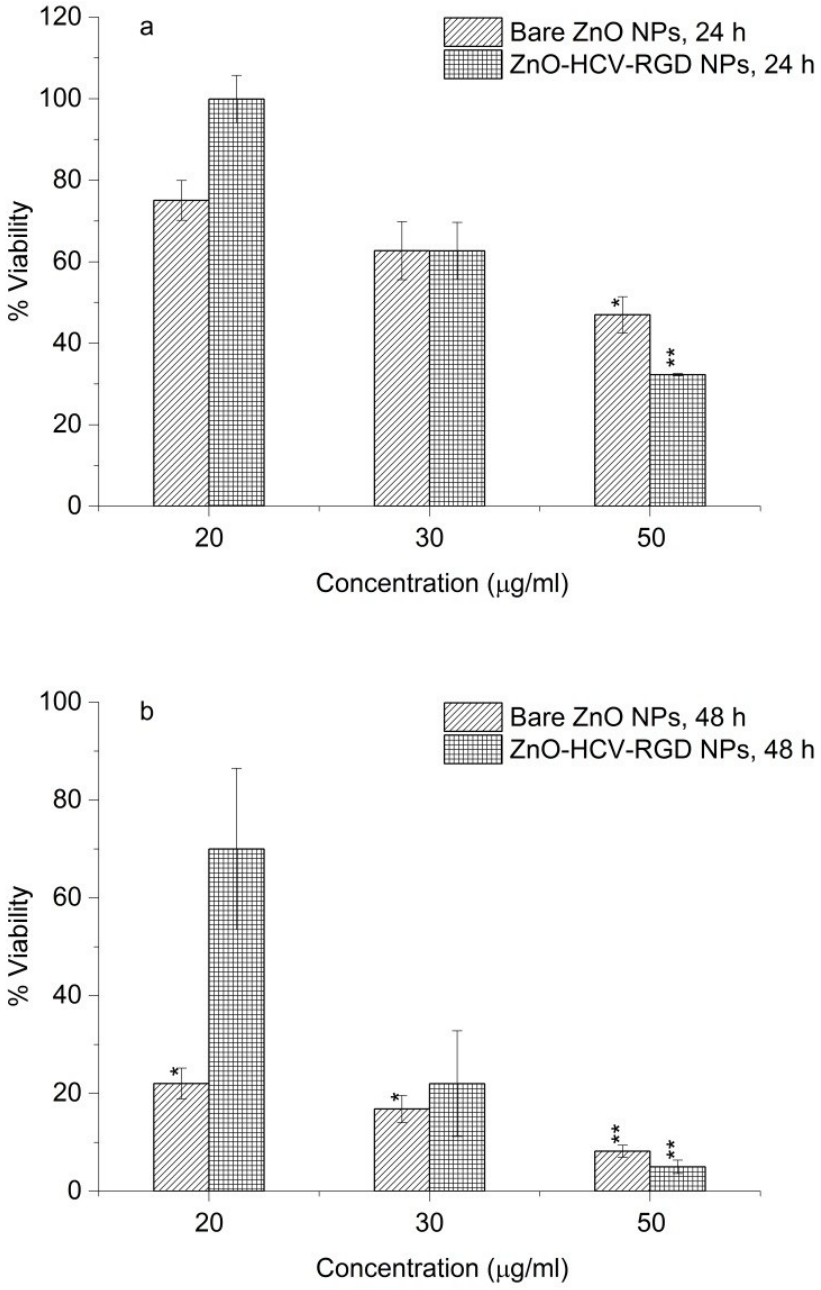

Figure 51: Comparison of ATP viability assay of MDA-MB-231 cells exposed to bare and ZnO-HCV-RGD-GFP NPs for (a) 24 h and (b) 48 h. Experiments were repeated in duplicate (n=2) and represented as the mean ± SD. *P ≤ 0.05, **P ≤ 0.01.

4.2.2 Mode of Cell death by Annexin V-7AAD (necrosis and apoptosis)

Necrosis and apoptosis are two distinct modes of cell death which differ in morphology, mechanism and incidence [163]. Apoptosis is mainly initiated by detachment and shrinkage of the cells, separation of blebs (protrusions of the plasma membranes) and finally the formation of apoptotic bodies that are packed densely with cellular organelles and nuclear

fragments [173]. *In vivo*, the apoptotic bodies will subsequently be engulfed by macrophages or adjacent cells and thus do not go through lysis. In contrast, *in vitro*, apoptotic bodies that are formed will ultimately swell and the apoptotic process proceeds to an autolytic necrotic outcome due to the absence of phagocytes [152, 174, 175]. Here, the term late apoptosis or secondary necrosis, which is the natural outcome of the complete apoptotic program, is used to describe dead cells that have reached this state via apoptotic program as named by Wyllie *et al.* [175, 176]. In apoptosis the cytoplasmic and the lysosomal membrane remains intact [175]. Necrosis, on the other hand, has been characterized as passive, accidental cell death process that elicit uncontrolled inflammatory cellular responses [153]. The most characteristic features of necrosis are cell swelling, lysosomal membrane permeabilization and cell membrane permeabilization [175]. As apoptosis is considered to be a regulated and controlled process, its occurrence during cancer treatment has received great attention [154, 155].

The biological effects of the ZnO NPs on the breast cancer cell lines were investigated in the previous sections of this chapter using the Alamar Blue, the LDH and the ATP assays. The Alamar blue assay monitors the metabolic activity of the living cells [177, 178]. The LDH assay, on the other hand, is used to quantitate LDH release from lysed cells [168]. Therefore in the Alamar Blue both apoptotic and necrotic cells will lose their metabolic activity and will be recorded as not viable (dead), while in the LDH assay only necrotic cells will release LDH and will be recorded as not viable (or dead) bot not the cells in an early apoptosis. The bare ZnO NPs could be inducing different mechanisms of cellular death in the MCF-7 and the MDA-MB-231 cells. The bare ZnO NPs may be inducing apoptosis in the MDA-MB-231 cells but necrosis in the MCF-7 cells. We based our assumption here on the following facts; the bare ZnO NPs are hypothesized to be taken up by the cells by clathrin-independent endocytosis, and then end up in the acidic lysosomes of the cells where they dissolve to release the zinc ions and labile zinc complexes [10, 49, 124, 179]. Zinc is reported to cause toxicity in breast cancer cells [180] and this toxicity could be related to different modes of cellular death in different cancers [180, 181] . In our study, the metabolic collapse, probably due to lysosomal membrane damage, and the high release of LDH enzyme measured in the MCF-7 cells are indicative of necrosis [163]. On the other hand, the MDA-MB-231 cells showed a linear reduction in the viability after exposure to the

ZnO NPs, because their lysosomal membranes were probably still intact and the ZnO NPs were still dissolving after their uptake, and they also showed a low LDH release after 24 h of exposure, both observations indicate apoptosis. To confirm these assumptions, Annexin V/7AAD assay, which measure apoptosis, was conducted.

The possible mechanism of death of the MCF-7 and the MDA-MB-231 cells after exposure to the ZnO NPs was further explored by Annexin V/ 7AAD assay which measure apoptosis. As mentioned at the beginning of this section, the apoptotic program in the cells is characterized by certain morphologic features. During early events of apoptosis, the externalization of the phospholipid phosphatidylserine (PS) occurs at the cell membrane while the membrane integrity remains unchallenged [182]. This translocation of PS to the outer leaflet of the lipid bilayer occurs very early in the apoptotic process [174]. The exposed PS could be detected by Annexin V, an endogenous human protein that has high affinity to bind, in a calcium dependent manner, to PS. This binding of Annexin V to PS can be detected using fluorescently labelled Annexin V and a flow cytometer. The 7AAD is a standard flow cytometric viability probe and is used to distinguish viable from nonviable cells. Viable cells with intact membranes exclude 7AAD, whereas the membranes of dead and damaged cells are permeable to 7AAD staining [183]. Therefore, staining with Phycoerythrin conjugated Annexin V (PE Annexin V) is typically used in conjunction with 7AAD.

Herein, to distinguish between cells that have undergone apoptotic death versus those that have died as a result of a necrotic pathway, apoptosis was first measured over time after exposure to the bare ZnO NPs. The breast cancer cells were exposed to the bare ZnO NPs for 3, 8, and 12 h concentrations 20, 30 and 50 µg/ml. At 24 h time point, more concentrations of the ZnO NPs were tested; 10, 20, 25, 30, 35, 40, 50, 60, and 100 µg/ml to have a good comparison with the viability assays in section 4.2.1. After exposure to the bare ZnO NPs, the cells were stained with PE Annexin V/7AAD for FACS analysis. Four different populations can be gated using PE Annexin V/7AAD; Live, necrotic, apoptotic, and late apoptotic cells. A representative plot of gating of the populations of cells after exposure to the ZnO NPs is illustrated in Figure 52. In Annexin V/7AAD assay, the cells can be gated into four populations; PE Annexin V negative and 7AAD positive cells (necrosis, membrane

integrity is lost, Q1), PE Annexin V and 7AAD positive cells (late apoptosis or secondary necrosis, Q2), PE Annexin V positive and 7AAD negative cells (apoptosis, membrane integrity is present, Q3), and PE Annexin V and 7AAD negative (live, or no measurable apoptosis, Q4).

It is not simple to distinguish whether the cells that reached Q2 had experienced primary necrosis or they are secondary necrotic/Late apoptotic cells. This is because primary necrotic cells cannot stain 7AAD positive and Annexin V negative; upon lysis, the cell becomes permeable to both 7AAD and Annexin V inside the cell, Annexin V could bind PS and consequently the cell will stain Annexin V positive/7AAD positive and will appear in Q2. Furthermore, apoptotic cells have short half-life [163]; in *in vitro* cultured cells, when massive apoptosis occurs and phagocytosis is limited, the apoptotic cells will lyse (become necrotic) and they will be stained double positive for Annexin V/7AAD and will appear in Q2. However, if the PS is lost in one of the previous cases, the cell will stain 7AAD positive and Annexin V negative and will appear in Q1.

Because we assumed that the different effects of the ZnO NPs on the viability of the MCF-7 and the MDA-MB-231 cells could be related to the release of zinc ions, the effect of ionic zinc from $ZnCl_2$ on the mode of cell death was also investigated using Annexin V/7AAD assay. The MCF-7 and the MDA-MB-231 cells were exposed to 16, 24, and 40 µg/ml of ionic zinc (Zn^{2+}) from $ZnCl_2$ for 3, 8, 12 and 24 h, and the cells were processed in the same way as with the ZnO NPs. These concentrations of ionic zinc are equivalent to the ionic zinc contents of 20, 30, and 50 µg/ml ZnO NPs, respectively.

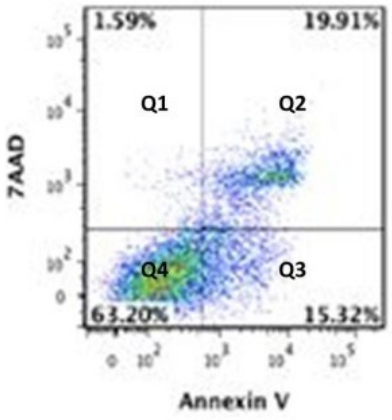

Figure 52: A representative flow cytometric density dot showing gating of necrotic (Q1), late apoptotic (Q2), apoptotic (Q3), and live (Q4) MCF-7 cells exposed to 50 µg/ml bare ZnO NPs for 3 h. Cells were exposed to the bare ZnO Ps and then stained with Annexin V-PE and 7AAD.

The percentage of the different populations of the cells; live, apoptotic, late apoptotic, and necrotic, after exposure to either the bare ZnO NPs or ionic zinc, was calculated after each exposure time. A representative FACS analysis after 24 h exposure of the MCF-7 and the MDA-MB-231 cells to both the bare ZnO NPs and $ZnCl_2$ from one experiment is illustrated in Figure 53 (a-d). It can be clearly observed from the flow cytograms in Figure 53 that the cells experienced a dose and time dependent reduction in the live cell population compared to untreated controls. Whether this reduction in the cell viability is due to apoptotic cell death or not will be discussed here.

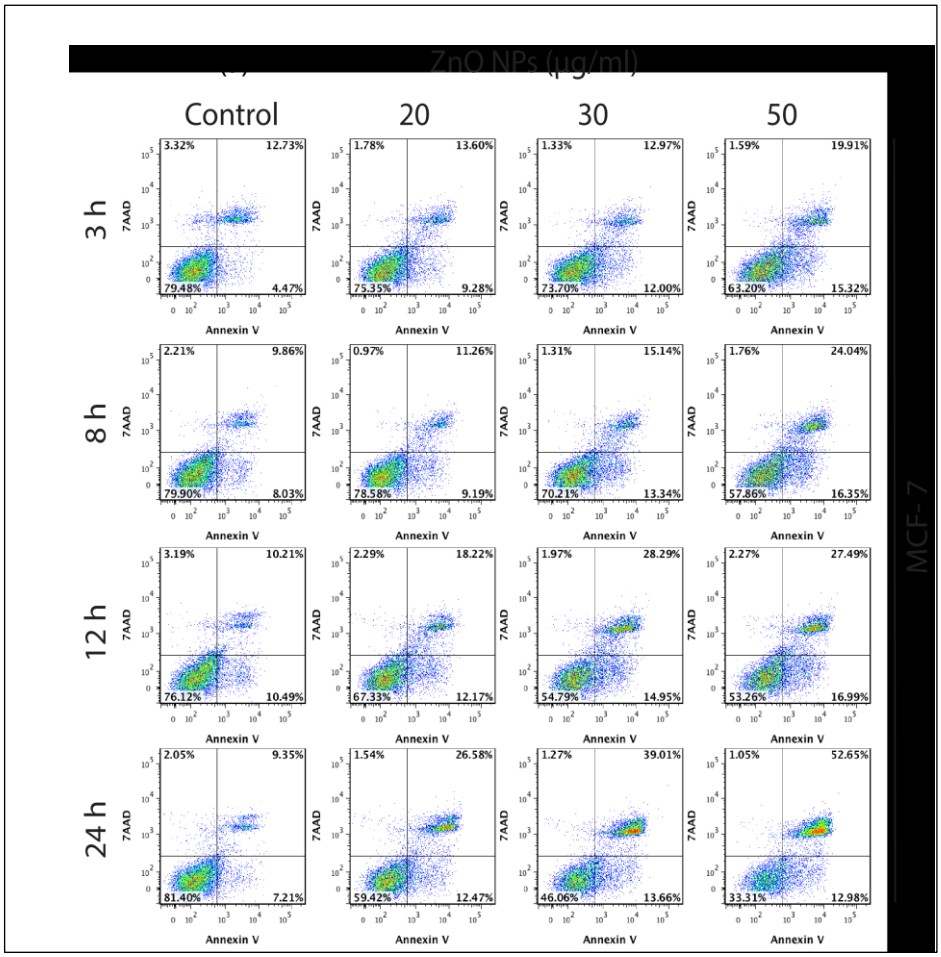

Figure 53 (a): Flow cytogram images of MCF-7 cells treated with 20, 30 and 50 µg/ml bare ZnO NPs for 3, 8, 12 and 24 h NPs. Representative figures show population of viable (Annexin V-/7AAD-), apoptotic (Annexin V+/7AAD-), late apoptotic (Annexin V+/7AAD+) and necrotic (Annexin V-/7AAD+).

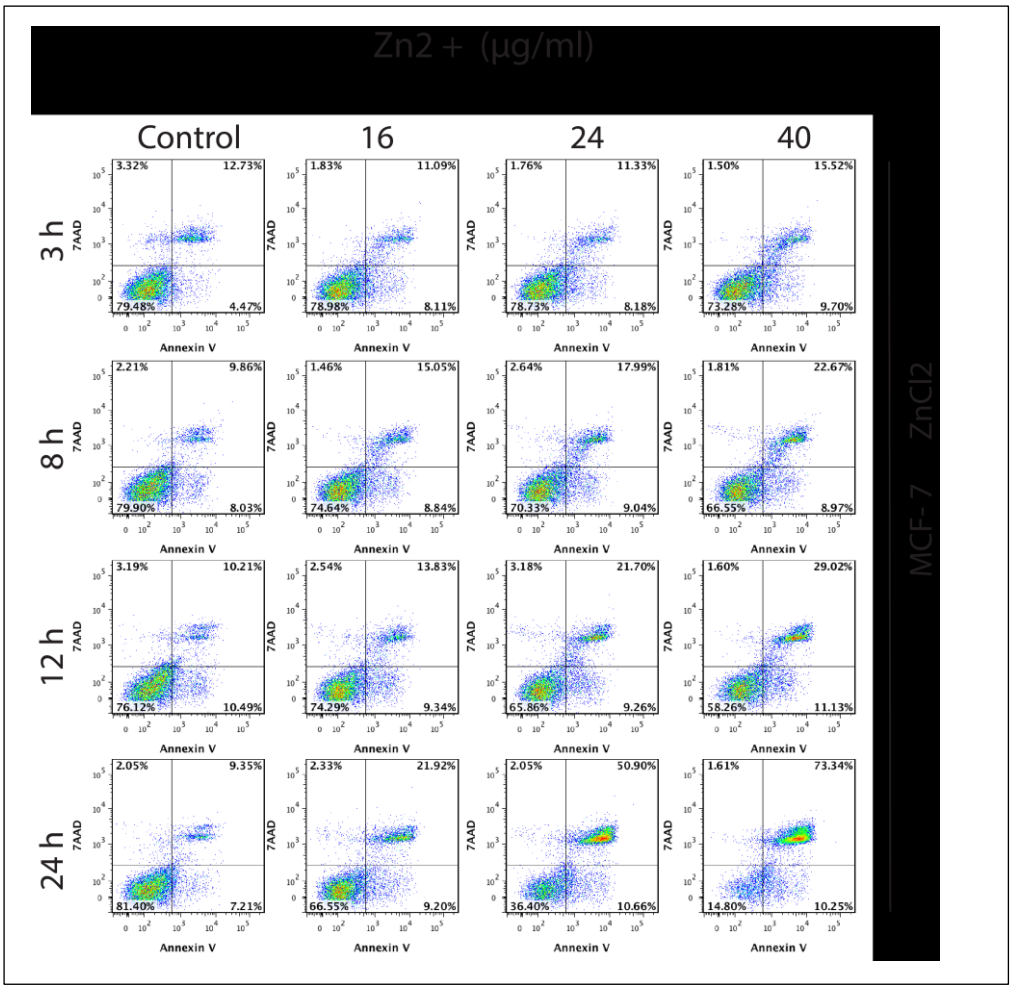

Figure 52 (b): Flow cytogram images of MCF-7 cells treated with 16, 24, and 40 µg/ml $ZnCl_2$ for 3, 8, 12 and 24 h. Representative figures show population of viable (Annexin V-/7AAD-), apoptotic (Annexin V+/7AAD-), late apoptotic (Annexin V+/7AAD+) and necrotic (Annexin V-/7AAD+).

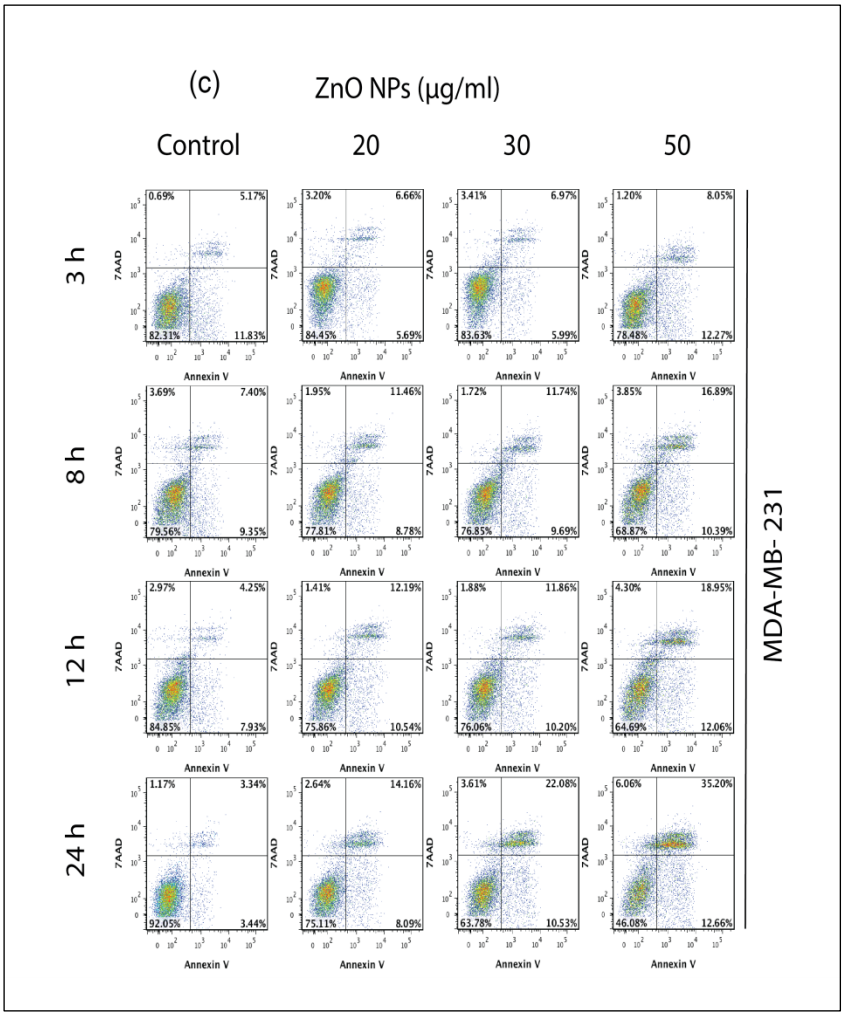

Figure 52 (c): Flow cytogram images of MDA-MB-231 cells treated with 20, 30 and 50 µg/ml bare ZnO NPs for 3, 8, 12 and 24 h. Representative figures show population of viable (Annexin V-/7AAD-), apoptotic (Annexin V+/7AAD-), late apoptotic (Annexin V+/7AAD+) and necrotic (Annexin V-/7AAD+).

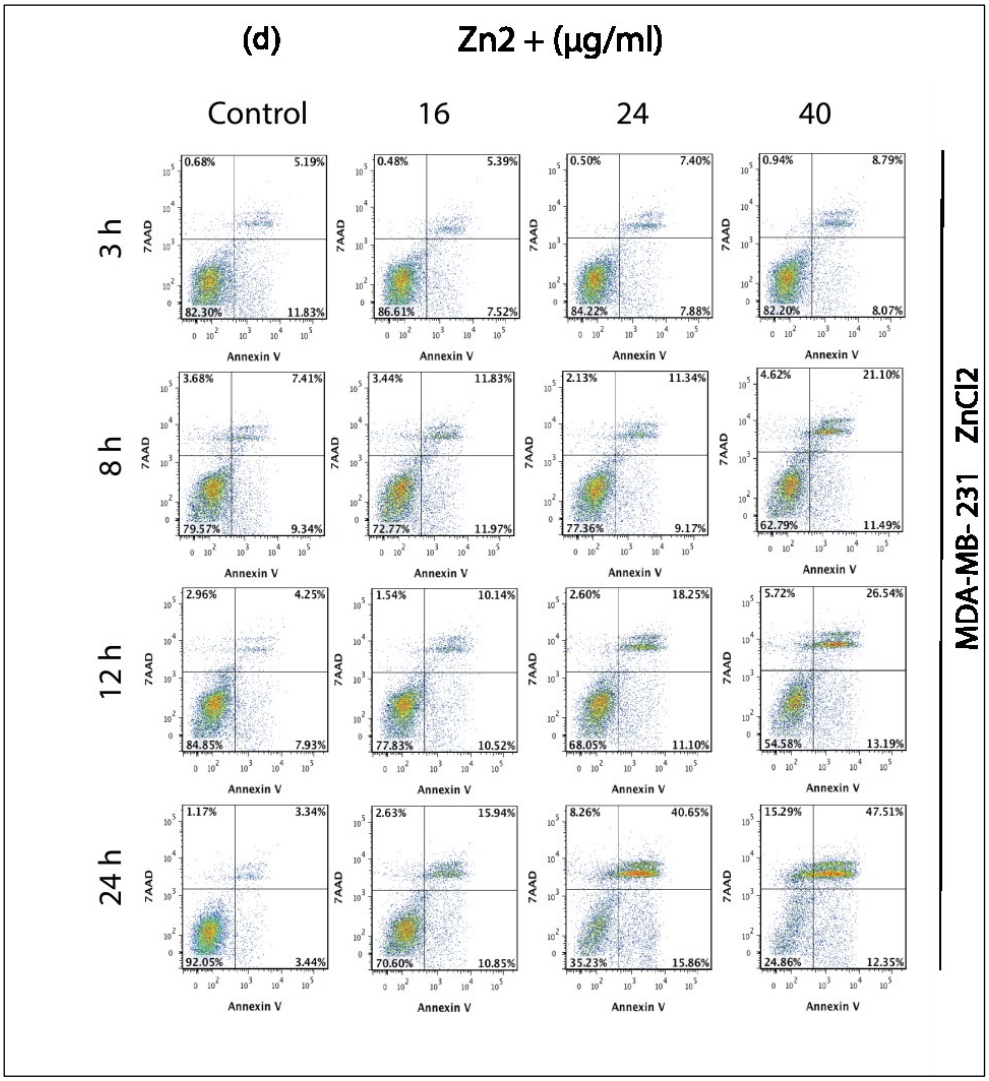

Figure 52 (d): Flow cytogram images of MDA-MB-231 cells treated with 16, 24, and 40 µg/ml $ZnCl_2$ for 3, 8, 12 and 24 h. Representative figures show population of viable (Annexin V-/7AAD-), apoptotic (Annexin V+/7AAD-), late apoptotic (Annexin V+/7AAD+) and necrotic (Annexin V-/7AAD+).

Figure 54 shows the change in the percentage of apoptotic cells within the MCF-7 and the MDA-MB-231 cells over time of 3, 8, 12 and 24 h, to three concentrations of the bare ZnO NPs (20, 30 and 50 µg/ml). The MDA-MB-231 cells showed a very significant increase ($p<0.05$) in the apoptotic population over time (3, 8, 12, and 24 h) at all tested concentrations (Figure 54, a). The MCF-7 cells, on the other hand, did not show any significant increase in the apoptotic population over time at all tested concentrations (Figure 54, b). The highest percentage of the apoptotic population in the MCF-7 cells exposed to 50 µg/ml ZnO NPs was observed at the lowest exposure time *i.e.* 3 h (Figure 54, b). Interestingly, the MDA-MB-231 cells treated for 3 h with small doses of 20 and 30 µg/ml of the bare ZnO NPs showed a reduction in the apoptosis compared to nontreated control; however, that was not the case in the MCF-7 cells (Figure 54). This effect of the bare ZnO NPs on apoptosis could be related to the release of ionic zinc from the NPs inside the cells. Ionic zinc has been reported to either reduce or induce apoptosis in the same cell line depending on the dose of exposure [184].

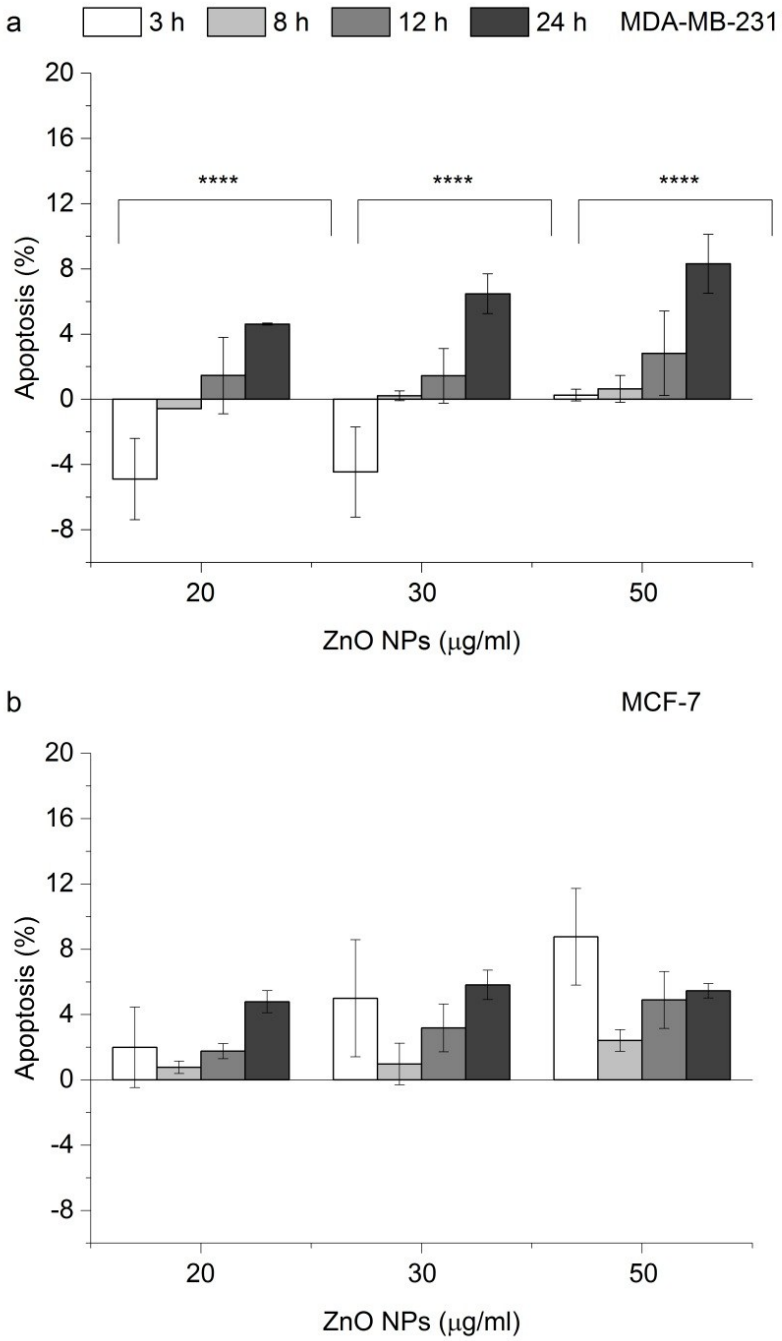

Figure 54: FACS analysis of cells undergoing apoptosis (Annexin V +/7AAD - (Q3)) from (a) MDA-MB-231 and (b) MCF-7 cells treated for 3, 8, 12, and 24 h with 20, 30, and 50 µg/ml ZnO NPs. At each time point, the apoptotic population from the untreated control was subtracted from that in the treated cells at each concentration. Experiments were performed in triplicate in three independent experiments. Bars are presented as mean ± SD (n=3). ****p ≤ 0.0001.

Figure 55 shows the effect of different concentrations of zinc ions from $ZnCl_2$ on the apoptotic population of the MCF-7 and the MDA-MB-231 cells over time. The ionic zinc had the same effects on the apoptotic population of both breast cancer cell lines as those of the bare ZnO NPs. In the MDA-MB-231 cells, zinc ions induced a significant increase ($p<0.05$) in apoptosis with time at all tested concentrations of zinc ions. In MCF-7, however, there

was no significant increase in apoptosis ($p>0.05$) except at 24 µg/ml Zn^{2+}. The same observation of the reduction in the apoptosis of the MDA-MB-231 cells after 3 h exposure to the bare ZnO NPs was recorded here at 16, 24, and 50 µg/ml $ZnCl_2$ compared to untreated control (Figure 55, a). Such reduction in apoptosis was not observed in the MCF-7 cells (Figure 55, b). This could be due to different effects of zinc on apoptosis at such short exposure time, as discussed earlier.

Comparing the bare ZnO NPs and $ZnCl_2$ results obtained by Annexin V/7AAD indicated no statistical difference ($p>0.05$) between the effect of the ZnO NPs and the ionic zinc on the apoptotic cell population in the MCF-7 cells at all tested concentrations. In the MDA-MB-231 cells, however, there was a significant difference ($p<0.05$) between the ZnO NPs and the zinc ions from $ZnCl_2$ at all tested concentrations after 3 h , and at all time-points at 30 µg/ml ZnO NPs (24 µg/ml $ZnCl_2$).

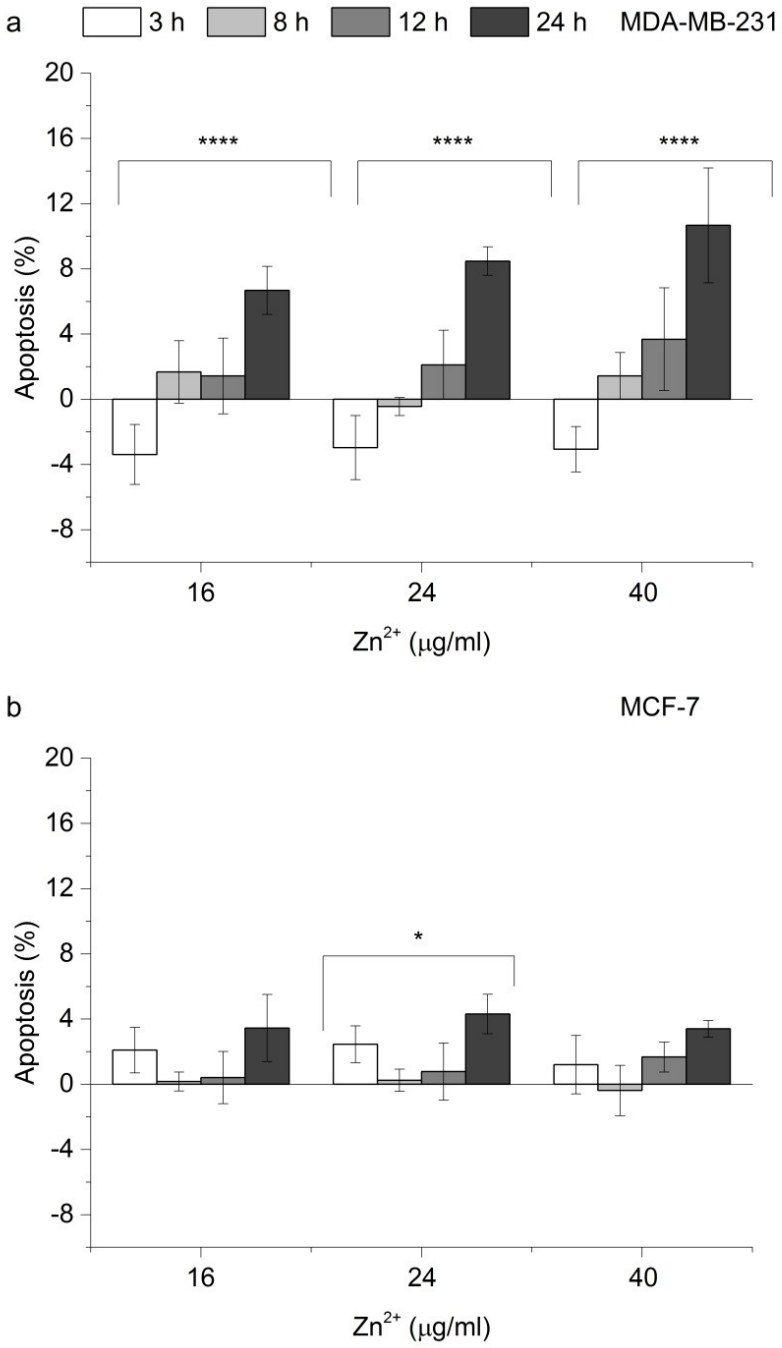

Figure 55: FACS analysis of cells undergoing apoptosis (Annexin V +/7AAD -, (Q3)) from (a) MDA-MB-231 and (b) MCF-7 cells treated for 3, 8, 12, and 24 h with 16, 24, and 40 μg/ml Zn^{2+} from $ZnCl_2$ (equivalent Zn^{2+} concentrations from 20, 30, and 50 μg/ml ZnO NPs). At each time point, the apoptotic population from the untreated control was subtracted from that in the treated cells at each concentration. Experiments were performed in triplicate in three independent experiments. Bars are presented as mean ± SD (n=3). *p ≤ 0.05; **p ≤ 0.01; ***p ≤ 0.001, ****p ≤ 0.0001.

The apoptotic and late apoptotic populations of the MCF-7 and the MDA-MB-231 cells after 24 h exposure to the ZnO NPs measured from Annexin V/7AAD assay were compared (Figure 56). In the MDA-MB-231 cells, compared to untreated control, there was a significant increase ($p<0.05$) in the apoptotic and late apoptotic populations at

concentrations 10-100 μg/ml and 20-100 μg/ml ZnO NPs, respectively (Figure 56, a). The MCF-7 cells, on the other hand, showed a significant increase ($p<0.05$) in the apoptotic and late apoptotic population only at 35-100 μg/ml and 20-35 μg/ml ZnO NPs, respectively (Figure 56, b). There was no statistical difference ($p>0.05$) between apoptotic cell population in the MCF-7 and the MDA-MB-231 cells after 24 h exposure to 10-100 μg/ml ZnO NPs.

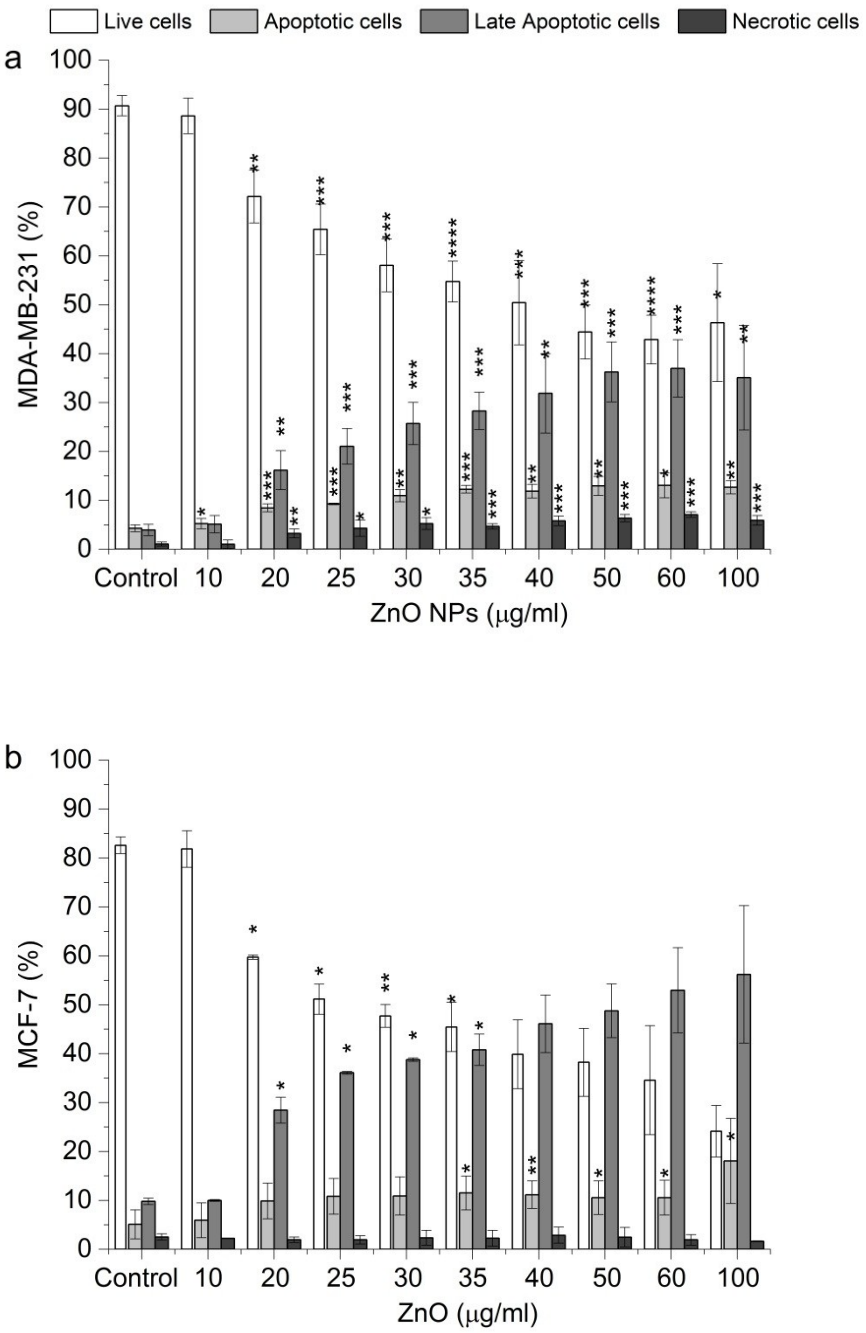

Figure 56: FACS analysis of percentage necrosis, apoptosis and late apoptosis results of (a) MDA-MB-231 and (b) MCF-7 cells treated for 24 h with 10, 20, 25, 30, 35, 40, 50, 60 and 100 µg/ml ZnO NPs. Experiments were repeated in triplicate in three independent experiments. Bars are presented as mean ± SD (n=3). *p ≤ 0.05; **p ≤ 0.01; ***p ≤ 0.001, ****p ≤ 0.0001.

4.3 Summary and conclusions

The results of the viability assays showed that the bare and the targeted ZnO NPs were toxic to the breast cancer MDA-MB-231 and MCF-7 cells. The ZnO NPs (both bare and targeted) caused a reduction in the metabolic activity, as well as cellular membrane damage in the MCF-7 and the MDA-MB-231 cells. The IC_{50} values obtained for the bare and the targeted ZnO NPs to the MDA-MB-231 and the MCF-7 breast cancer cells, as well as the healthy epithelial MCF-10-2A cells, at different exposure times are summarized in Table 6. Significant differences in the responses of the MCF-7 and MDA-MB-231 cells after exposure to the bare ZnO NPs were observed in the Alamar Blue and the LDH assays. This could indicate that ZnO NPs induce a variety of cellular damage responses in both cell lines that influence the final outcome.

Taking all the results of this chapter into account, we proposed that the ZnO NPs (both bare and targeted) could probably induce necrosis in the MCF-7, but apoptosis in the MDA-MB-231 cells at concentrations 10-60 μg/ml. The MCF-7 showed signs of necrosis, which includes the sudden drop in the metabolic activity at concentrations around the 24 h IC_{50}, and cell lysis with high release of LDH. The MDA-MB-231 cells, on the hand, showed signs of apoptosis after 24 h exposure to the bare and targeted ZnO NPs, which includes the linear reduction in the metabolic activity and the low release of LDH. These findings were further confirmed by Annexin V/7AAD assay; the MDA-MB-231 cells showed significant time and dose dependent increase in the apoptotic population, while the MCF-7 cells, on the hand, did not show any increase in the apoptotic population compared to untreated control at any tested concentration (20, 30, and 50 μg/ml). It has been reported that MCF-7 cells lack caspase-3, which is required for DNA fragmentation and morphological changes associated with apoptosis [170]. However, Sasidharan *et al.* [11] showed that incubation of ZnO nanocrystals (NCs) (5 nm) with MCF-7 breast cancer epithelial cells lead to significant impairment of metabolic function of the cancer cells that took place within 12 h of incubation with ZnO NCs. The same study showed no significant LDH leakage within 12 h and only after 24 h did the cancer cells treated with ZnO NCs showed LDH leakage. The IC_{50} of ZnO NCs in MCF-7 cells after 24 h determined in [11] was ~150 μM (12.21 μg/ml) and they suggested that the delayed occurrence of plasma membrane permeabilization is a

signature of late stage apoptosis. The same study investigated the toxicity of ZnO NCs in normal breast epithelial cells and highly invasive breast cancer cells, MDA-MB-231, and they concluded that ZnO NCs were toxic to cancer cells but not normal epithelia cells. However, only metabolic activity assay, MTT, was used to determine the effect of ZnO NCs on viability of MDA-MB-231 and normal breast epithelial cells and no apoptotic assay was performed to confirm the mechanism of toxicity induced by ZnO NCs. It has been reported that cellular responses like apoptosis in the presence of ZnO NPs require the potent tumor suppressor p53 as the molecular master switch towards apoptosis [185]. It has been reported that he p53 pathway was activated in BJ cells (skin fibroblasts) upon ZnO NPs treatment with a concomitant decrease in cell numbers [185]. Furthermore, in the wild type form, p53 aides in inhibiting growth of cancerous cells, but this is not the effect seen in mutant p53 [186]. Therefore, the differences observed in the responses of the MCF-7 and the MDA-MB-231 cells to the ZnO NPs could be due to the fact that MCF7 expresses wild type p53 and MDA-MB-231 expresses hyperactive, mutant p53 [186].

The bare and the RGD-targeted ZnO NPs showed different cytotoxicity to each breast cancer cell line. The RGD-targeted ZnO NPs were more toxic to the breast cancer cells than the bare NPs; however, this difference was not highly manifested after 3 h exposure in the MDA-MB-231 cells. Herein, the effect of the bare and the targeted ZnO NPs on the breast cancer cells was compared based on the IC_{50} values obtained for each NPs from the Alamar Blue (Table 6). In the MDA-MB-231 cells, the targeted ZnO NPs showed 3% increase in the toxicity compared to the bare NPs after 3 h exposure. After 24 h exposure, however, the RGD-targeted ZnO NPs were 27% more toxic to the MDA-MB-231 cells than the bare NPs. This higher toxicity of the targeted ZnO NPs compared to the bare ZnO NPs after 24 h exposure could be probably due to the higher binding of the targeted ZnO NPs to the integrin αvβ3 receptors of the MDA-MB-231 cells, which showed 42% expression of these receptors, and therefore higher internalisation and toxicity. The lower difference in the toxicity of the bare and targeted ZnO NPs in the MDA-MB-231 cells after 3 h exposure could indicate that the RGD-binding to the integrin αvβ3 receptor and then internalisation require time that could be >3 h, or that the intracellular processing and dissolution of the RGD-targeted ZnO NPs, after their internalisation, requires time that is >3 h. These assumptions could be further supported by the observation that the toxicity of the targeted ZnO NPs to

the MDA-MB-231 cells was increased by 33% after 24 h compared to 3 h exposure. In the MCF-7 cells, neglecting the unexplained higher cytotoxic effects of the bare ZnO NPs after 3 h compared to 24 h exposure, the targeted ZnO NPs were 24 and 56 % more toxic to the cells than the bare ZnO NPs after 3 and 24 h exposure, respectively. The targeted ZnO NPs, however, did not show any time dependent increase in the toxicity after 3 and 24 h exposure to the MCF-7 cells (*i.e.* the IC_{50} was the same at the two time points). The higher toxicity of the targeted ZnO NPs in the MCF-7 cells compared to the bare ZnO NPs could be still related to the higher binding of the targeted ZnO NPs to the integrin αvβ3 receptors, which were expressed by 19% of the MCF-7 cells. The unchanged toxicity of the targeted ZnO NPs to the MCF-7 cells after 24 h compared to 3 h exposure could indicate that the targeted NPs are internalised and dissolve inside the MCF-7 cells shortly after their binding to the cell surface.

The reduction in the metabolic activity after exposure to the ZnO NPs (bare and RGD-targeted) could be related to the toxic Zn^{2+} released from the bare and targeted ZnO NPs after their intracellular dissolution. It has been reported that Zn^{2+} has many effects on cancer cells, which includes alteration in gene expression, reduction in cellular metabolism and induction of apoptosis [5]. The release of Zn^{2+} ions, following incubation of ZnO nanocrystals (NCs) (5 nm) with MCF-7 breast cancer epithelial cells lead to significant impairment of metabolic function of the cancer cells and caused damage to the plasma membrane [11]. In this study, the apoptotic population in the MCF-7 cells showed no statistical difference ($p>0.05$) after exposure to the bare ZnO NPs and equivalent concentrations of Zn^{2+} from $ZnCl_2$. In the MDA-MB-231 cells, however, there was significant difference in the apoptotic populations resulted from $ZnCl_2$ and the bare ZnO NPs exposures at the 24 h IC_{50} of the bare ZnO NPs (*i.e.* 30 μg/ml). Based on these results, the different mechanisms of death induced by the ZnO NPs in the MCF-7 cells could be related to the effects of zinc ions. In the MDA-MB-231 cells, however, in addition to the effects of the released zinc ions, the ZnO NPs could be initiating other types of cell injury that contribute to its cytotoxicity.

The toxicity of the bare ZnO NPs to the cells used in this study, based on the 3 h exposure IC_{50} obtained from the Alamar Blue assay, could be suggested in the following

order; MCF-7> MDA-MB-231> MCF-10-2A cells. The bare ZnO NPs showed a selective toxicity to the breast cancer cell lines compared to the healthy breast epithelial cells at concentrations 25-40 μg/ml of the bare ZnO NPs after 3 h exposure. A dose of 35 μg/ml of the bare ZnO NPs could be used as a toxic dose to the breast MCF-7 and MDA-MB-231 cancer cells with minimal toxic effects on the healthy breast MCF-10-2A cells, which showed >65% viability at this concentration. The ability of the targeted ZnO NPs to selectively kill the breast cancer cells but not the healthy epithelial cells, as well as its ability to effectively kill the triple negative MDA-MB-231 breast cells, which account for a high proportion of breast cancer mortality due to the lack of effective therapies [64], will open new options for this material in cancer therapy.

Both breast cancer cell lines expressed the integrin αvβ3 receptor, while the healthy epithelial breast cells MCF-10-2A showed almost negligible expression of these targeted receptors. Therefore, with the combination of the right dose and exposure time, and effective targeting, ZnO NMS would have potential for clinical applications in breast cancer therapy.

The RGD targeting of the ZnO NPs to the integrin αvβ3 receptors, which are selectively expressed on breast cancer cells, but not on healthy breast epithelial cells, together with the EPR effect of the tumor tissues, will increase the local concentrations of these NPs at the tumor site *in vivo*. In addition, the fact that the targeted ZnO NPs do not dissolve at neutral pH of 7.4 but completely dissolve in the acidic pH (in tumor microenvironment or inside the lysosomes of tumor cells) will increase the relevancy of our *in vitro* findings that the targeted ZnO NPs are more toxic to breast cancer cells than normal breast epithelial cells.

Finally, careful decisions should be made regarding the choice of the suitable viability assays to be used to assess the toxic effects of NMS to cells. These viability assays are originally designed to test the toxicity of chemicals, and not NMS, and therefore they could have different interactions with NMS that might affect their outcomes. In this study, we can conclude that ATP and LDH but not Alamar Blue assays could be used effectively to test the toxicity of ZnO NMS.

Table 6: A summary of IC_{50} values obtained for MCF-7, MDA-MB-231 breast cancer cell lines, and the healthy epithelial MCF-10-2A breast cells after exposure to bare and targeted ZnO NPs as determined from the viability assays.

Assay	Cells	IC_{50} (µg/ml)					
		Bare ZnO-NPs			ZnO-HCV-RGD-GFP NPs		
		3 h	24 h	48	3 h	24 h	48 h
Alamar blue							
	MCF-7	21	36	NA	16	16	NA
	MDA-MB-231	34	30	NA	33	22	NA
	MCF-10-2A	45	NA	NA	NA	NA	NA
LDH							
	MCF-7	NA	48	<20	NA	NA	NA
	MDA-MB-231	NA	Dose independent >100	Dose independent ≤ 10	NA	NA	NA
	MCF-10-2A	NA	>100	Dose independent (could not be measured)	NA	NA	NA
ATP							
	MCF-7	NA	NA	NA	NA	NA	NA
	MDA-MB-231	NA	36	<10	NA	33.5	24.6
	MCF-10-2A	NA	NA	NA	NA	NA	NA
NA: not measured							

5 Uptake and intracellular dissolution of bare and RGD-targeted zinc oxide nanoparticles in breast cancer cells

The design of smart multifunctional platforms for intracellular imaging and targeted therapeutic applications requires a thorough understanding of the uptake and bioreactivity of the NMS. Several studies have been conducted recently on the toxicity of ZnO NMS to different mammalian cells lines [49, 53, 65, 187], and its potential applications for imaging and targeted therapeutics [12]. ZnO NMS have been found to be toxic to different mammalian cells [53, 65, 67, 69, 187]. In many reports, the cytotoxicity of ZnO NMS to cancer cells has been attributed to free zinc ions and zinc complexes released upon dissolution of ZnO [10, 11]. However, only few reports on the cellular uptake of ZnO NMs are available [10, 49, 58]. It has been reported, by confocal microscopy, that ZnO NPs remnants are internalised by caveolae mediated uptake in BEAS-2B cells and toxic Zn^{2+} has been shown to accumulate in the lysosomal compartment in mouse macrophages (RAW 264.7) [49]. It has also been shown that a pH-triggered controlled doxorubicin release from mesoporous silica NPs was achieved via intracellular dissolution of ZnO nanolids [44]. Only one study provided transmission electron microscopy (TEM) imaging data of binding of ZnO NPs to Human Bronchial Epithelial (BEAS-2B) Cells [124]. Lin W., *et al.* also showed agglomerates of ZnO NPs in endosomes in bronchoalveolar carcinoma- derived cells (A549) after 24 h exposure to 12 μg/ml ZnO NPs [161], however, their study lacks EDX data to confirm the presence of ZnO NPs. Therefore, there is still much debate around whether the ZnO NMS are taken up by cells and then dissolve only intracellularly or whether they dissolve in the extracellular matrix releasing ionic zinc which diffuses into the cells. One study has successfully targeted fluorescent ZnO NWs to tumours *in vivo* by targeting the integrin αvβ3 [12]. Again this study did not demonstrate whether the NWs are internalised by cells and where the zinc dissolves and exert its toxic effects. A summary of the size and zeta potential of ZnO NMS used in these studies is shown in Table 7.

Table 7: Primary and hydrodynamic size of ZnO NMs used in literature. Blank cells represent information that is not given in the specific publication.

Reference	Cells tested	ZnO NMS						
		Shape	Primary size	Hydrodynamic size (nm)			Zeta potential (mV)	
				DMEM	BEGM	Ham's F-12	DMEM	BEGM
Xia *et al.* [49]	RAW 264.7 BEAS-2B	NPs	11 nm	36[a]	184[b]		-5[a]	-16[b]
Gilbert *et al*. [124]	BEAS-2B	NPs	20 nm (no Fe) 10 nm (Fe doped)		aggregated[c] 100, 1000, >1000			negative
Lin *et al.* [161]	A549	NPs	70 nm, 420 nm			≈300 nm[d]		
Hong *et al.* [12]	U87MG	NWs	20-50 nm in diameter and 0.5-1 μm in length					

RAW 264.7: Mouse leukaemic monocyte macrophage cell line, BEAS-2B: Normal human bronchial epithelial cells, A549: Human bronchoalveolar carcinoma-derived cells, U87MG: Human glioblastoma cells.

DMEM: Complete Dulbecco's modified eagle media. BEGM: Bronchial epithelial growth medium, [a]: contains 10% fetal FBS.

[b]The medium contains growth factors, cytokines, and supplements (no serum). [c] The medium contains 2 mg/mL bovine serum albumin (BSA).

[d] The medium contains 5% FBS.

Internalisation of NPs into living cells is a two-step process, which involves binding of the NPs to the surface of the cells and then their uptake by cells [10]. ZnO nanostructures are known to dissolve under acidic conditions. The phase-solubility diagram of ZnO [188] indicates that ZnO NPs will dissolve at pH below 6.7 at physiological temperature, and it will rapidly dissolve in the acidic pH of the lysosomes (pH 5.7) after their uptake. It is hypothesized that ZnO NPs can be targeted to cancer cells and specifically kills, by releasing Zn^{2+} ions inside these cells independently of their metabolic rate. It has been previously shown that the release of Zn^{2+} ions, following incubation of bare 5 nm ZnO NPs with MCF-7 breast cancer epithelial cells, lead to generation of reactive oxygen species, resulted in damage to the plasma membrane and mitochondria leading to apoptosis [11]. However, in

ref. [11], they did not directly image whether the particles are internalised by the cells or where dissolution of ZnO NPs occurs. It is also likely that the ZnO NPs used in ref. [11] dissolved in the cell culture media due to their small size. The tendency of ZnO NPs to dissolve in aqueous solutions, especially biological fluids, has been well documented [10, 117], but direct identification of the chemical form of zinc taken up (i.e. whether the ZnO NPs dissolve in the extra and intracellular environments), has not yet been shown.

It is extremely challenging to assess the relative contributions of nanoparticulate and dissolved zinc to the uptake, subcellular localization, and mechanism(s) of toxicity. Sasidharan *et al.* suggested that rapid dissolution of ZnO NCs in acidic cancer microenvironment is the main cause of apoptosis in cancer cells [11]. However, a study by Muller *et al.* used zinc sensitive dyes to show that zinc oxide NWs dissolution only occurs inside macrophage cells and that raised Zn^{2+} ion concentrations can be correlated directly to cell death [10]. Gilbert *et al*. combined high resolution X-ray spectromicroscopy and high elemental sensitivity X-ray microprobe analyses to determine the fate of ZnO and less soluble iron-doped ZnO NPs following exposure to cultures of human bronchial epithelial cells (BEAS-2B) [124]. The data suggested cellular uptake of ZnO NPs and a mechanism of zinc accumulation; following uptake, ZnO NPs dissolved completely generating intracellular Zn^{2+} complexed by molecular ligands [124]. A combination of atomic force microscopy and scanning transmission x-ray microscopy (STXM) were used to prove this question, however these techniques do not probe depth information [124] and the STXM data did not demonstrate significant changes in the zinc absorption edge in the cells exposed to ZnO NPs. Therefore conclusions cannot be drawn from this work. In cancer cells, direct identification of the chemical format of zinc taken up by cells exposed to ZnO NPs, and its intracellular fate, has not yet been achieved.

To track binding, cellular uptake and intracellular dissolution of the ZnO NPs and death of the breast cancer cells, confocal microscopy of live cells was utilized to generate real time information about these processes. The confocal microscope does not have the spatial resolution to detect individual ZnO NMs, therefore correlative confocal and electron microscopy imaging and analysis of exactly the same cells imaged in the confocal and transmission electron microscopes, was used to confirm that the particles are internalised

by the cells and to assess their morphology inside the cells. Electron microscopy was also used to study how the ultrastructure of the cells was altered by the ZnO NPs to provide clues about the mode of cell death.

It was shown in Chapter 4 of this study that a higher amount of integrin αvβ3 is expressed on breast cancer cells, compared to healthy breast epithelial cells. Therefore, it was hypothesized that RGD-ZnO NPs, will selectively target and destroy breast cancer cells, compared to healthy cells, and that these effects will follow the order MDA-MB-231 > MCF-7> MCF-10-2A cells.

The aim of this chapter is to correlate and compare targeting, intracellular destination and local dissolution of the bare and RGD-ZnO NPs directly with their toxicity mechanisms.

5.1 Materials and methods

5.1.1 Chemicals

Propidium iodide (PI) was purchased from Sigma, UK. CellMask™ Deep Red Plasma membrane Stain, Hoechst 33342, and FluoZin3-AM from were purchased from Invitrogen. Zinquin-AM was purchased from Interchim, France. $CaCl_2$ was from Sigma Aldrich Ltd, UK. PIPES (piperazine-N, N'bis [2-ethanesulfonic acid]) and $MgCl_2$ were purchased from Fisher scientific Ltd, UK. MES was purchased from ACROS Organics, US. Accutase and Versene were purchased from Gibco (Life Technologies Ltd, UK). CD24-FITC was purchased from MACS (Miltenyi Biotech, UK, Cat. No., 120-008-097) and CD44-PE was from Biolegend, UK (Cat. No. 338802; mouse monoclonal (BJ18). CD90-PE-Cy 5 (Cat. No. 555597), EpCAM-PE-CY5 (Cat. No. 347199) and the isotype control IgG1 were purchased from BD Bioscience, UK. Sodium cacodylate trihydrate (≥98%) was purchased from Sigma Aldrich Ltd, UK. PIPES (piperazine-N, N'bis [2-ethanesulfonic acid]).

5.1.2 Cell Culture

The cells were cultured as described in section 4.1.1.

5.1.3 Confocal microscopy of breast cells exposed to targeted and bare ZnO nanoparticles

5.1.3.1 Correlation of uptake and dissolution of the targeted ZnO NPs by MDA-MB-231 cells

5.1.3.1.1 Uptake of ZnO-HCV-RGD-GFP NPs by live MDA-MB-231 cells

1. <u>Live cells nuclei staining using Hoechst 33342</u>

The MDA-MB-231 cells were cultured for 48 h on 35 mm glass-based culture dishes (Nest Biotech Co, LTD, 35X12 mm style, 20 mm glass bottom) at $6x10^4$ cells/cm^2. The cells were rinsed once with the HEPES confocal imaging buffer at pH 7.4, 37°C. The cells were loaded with 5 µg/ml Hoechst 33342 in 1 ml of the HEPES confocal imaging buffer for 30 min at 37°C. At the end of incubation time, the cells were washed twice with imaging buffer (at 37°C). PI (20 µg/ml) was prepared in 1 ml of the HEPES confocal imaging buffer and added to the cells (the final concentration incubated with the cells was 10 µg/ml). PI is a cell impermeable dye and excluded from viable cells. Upon destruction of the plasma cell membrane, PI penetrates the cell, and upon binding DNA and RNA, its fluorescence intensity is enhanced 20-30 fold. The targeted ZnO-HCV-RGD-GFP NPs stock dispersion, prepared in 50 mM HEPES+100 mM NaCl buffer at pH 7.5, was sonicated for 30 s on a bench sonicator. Then 1 ml of 300 µg/ml ZnO-HCV-RGD-GFP NPs prepared in the HEPES confocal imaging buffer was added to the cells, just before imaging (the final concentration was 150 µg/ml). Confocal live imaging was started immediately after addition of the ZnO-HCV-RGD-GFP NPs dispersion to the cells using a Zeiss LSM 710 confocal microscope, with the environmental chamber set to 37°C. Bright field confocal imaging was used to view changes in the cell morphology and to track the uptake of the targeted NPs across the cell membrane. Images were processed using ZEN 2009 Confocal Software.

The 405 nm laser line was used to excite Hoechst 33342 (λexc\λem= 355/461 nm), the 561 nm laser was used to excite PI (λexc\λem= 538/617 nm) and the 488 nm laser was used to track the GFP labelled ZnO-HCV-RGD (λexc\λem=488/509 nm). Images were acquired over a time period of 3-4 h to track the uptake of the particles (1 frame/2 min)

using a 20x objective/0.8 numerical aperture (NA), and the pinhole was set at 1 AU. Images were processed using ZEN 2009 Confocal Software.

To obtain 3D images of the targeted NPs inside the cells after their uptake, and to assess the viability of the cells, the experiment described above was repeated and images were acquired at different Z-stacks over a time period of 8-9 h (1 frame/1.5 min) using a 20x objective/0.8 NA. The cells were incubated at 37°C with the targeted NPs up to 18 h exposure and the cells were then imaged to assess the viability of the cells.

2. <u>Plasma membrane staining of live MDA-MB-231 cells using CellMask Deep Red</u>

CellMask Deep Red is a convenient marker of the plasma membrane and can be utilized to track the translocation of ZnO-HCV-RGD-GFP NPs across the plasma membrane. CellMask™ Deep Red is an amphipathic molecule providing a lipophilic moiety for excellent membrane loading and a negatively charged hydrophilic dye for "anchoring" of the probe in the plasma membrane.

To track the internalisation of ZnO-HCV-RGD-GFP NPs by the cells, the MDA-MB-231 cells were cultured for 48 h on 35 mm glass-based culture dishes (Nest Biotech Co, LTD, 35X12 mm style, 20 mm glass bottom) at $6x10^4$ cells/cm^2. At the end of incubation time, the cells were rinsed once with the HEPES confocal imaging buffer at 37°C. The cells were then loaded with 5 μg/ml CellMask Deep Red plasma membrane stain for 5 min at 37°C. The cells were washed twice with the imaging buffer and incubated in 1 ml imaging buffer at 37°C. The targeted ZnO-HCV-RGD-GFP stock dispersion, prepared in 50 mM HEPES+100 mM NaCl buffer at pH 7.5, was sonicated for 30 s on a bench sonicator. Then 1 ml of 300 μg/ml ZnO-HCV-RGD-GFP NPs prepared in the HEPES confocal imaging buffer was added to the cells, just before imaging (the final concentration was 150 μg/ml). Confocal live imaging was started immediately after addition of the ZnO-HCV-RGD-GFP NPs dispersion to the cells using a Zeiss LSM 710 confocal microscope, with the environmental chamber set to 37°C. Images were processed using ZEN 2009 Confocal Software.

The 561 nm laser line was used to excite CellMask Deep Red plasma membrane stain and the 488 nm laser was used to track the ZnO-HCV-RGD-GFP NPs. Confocal live imaging was

carried out for 10 h (1 frame/2min) using 20x objective/0.8 NA, and the pinhole was set at 1 AU. Images were processed using ZEN 2009 Confocal Software.

5.1.3.1.2 Dissolution kinetics of ZnO-HCV-RGD-GFP nanoparticles inside live MDA-MB-231 cells

The MDA-MB-231 cells were cultured for 48 h on 35 mm glass-based culture dishes (Nest Biotech Co, LTD, 35X12 mm style, 20 mm glass bottom) at $6x10^4$ cells/cm^2. The cells were then rinsed once with the HEPES confocal imaging buffer at pH 7.4 and 37°C. The cells were then loaded with 10 µM of the cell-permeant Zn^{2+} indicator Zinquin-AM in 1 ml of the HEPES confocal imaging buffer for 30 min at 37°C. After rinsing the cells twice with imaging buffer at 37°C to remove any dye that is non-specifically associated with the cell surface, the cells were incubated for a further 30 min to allow complete de-esterification of intracellular AM esters of Zinquin. PI (20 µg/ml) was prepared in 1 ml HEPES confocal imaging buffer and added to the cells (the final concentration incubated with the cells was 10 µg/ml). Then 300 µg/ml ZnO-HCV-RGD-GFP NPs were prepared in 1 ml HEPES imaging buffer and was added to the cells just before imaging (final concentration exposed to the cells is 150 µg/ml). Confocal live imaging was started immediately after addition of the ZnO-HCV-RGD-GFP NPs dispersion to the cells using a Zeiss LSM 710 confocal microscope with the environmental chamber set to 37°C. A control MDA-MB-231 cells were incubated with 1 ml of the HEPES confocal imaging buffer alone.

The 405 nm laser line was used to excite Zinquin (λexc\λem = 344/385 nm), 561 nm laser was used to excite PI (λexc\λem= 538/617 nm) and the 488 nm laser was used to excite GFP labelled ZnO-HCV-RGD (λexc\λem=488/509 nm). Images were acquired over a time period of 24 h (1 frame/4 min) using a 20x objective/0.8 NA and the pinhole was set at 1 AU. To monitor the dissolution of ZnO-HCV-RGD-GFP NPs inside the cells and subsequent cell death, the intensity of Zinquin and PI was tracked for 20 cells in the imaging frame over 24h. Images were processed using ZEN 2009 Confocal Software.

5.1.3.2 Uptake of ZnO-HCV-RGD-GFP nanoparticles by live MCF-7

The MCF-7 cells were cultured for 48 h on 35 mm glass-based culture dishes (Nest Biotech Co, LTD, 35X12 mm style, 20 mm glass bottom) at $9x10^4$ cells/cm^2. The cells were then

rinsed once with the HEPES confocal imaging buffer at pH 7.4 and 37°C. The cells were then loaded with 5 µg/ml Hoechst 33342 in 1 ml of the HEPES confocal imaging buffer for 30 min at 37°C. At the end of incubation time, the cells were washed twice with HEPES confocal imaging buffer at 37°C. PI (20 µg/ml) was prepared in 1 ml HEPES confocal imaging buffer and added to the cells (the final concentration was 10 µg/ml). Then 150 µg/ml of the ZnO-HCV-RGD-GFP NPs were prepared in 1 ml HEPES confocal imaging buffer and was added to the cells just before imaging (the final concentration was 75 µg/ml). Confocal imaging of live cells was started immediately after addition of the ZnO-HCV-RGD-GFP NPs dispersion to the cells using a Zeiss LSM 710 confocal microscope with the environmental chamber set to 37°C. A control experiment was performed, in which the MCF-7 cells were incubated with 1 ml of the HEPES confocal imaging buffer alone.

The 405 nm laser line was used to excite Hoechst 33342 (λexc\λem = 355/461 nm), the 561 nm laser was used to excite PI (λexc\λem= 538/617 nm) and the 488 nm laser was used to excite GFP labelled ZnO-HCV-RGD (λexc\λem=488/509 nm). Images were acquired over a time period of 13 h to track the uptake of the particles and viability of the cells (1 frame/2 min) using a 20x objective/0.8 NA, and the pinhole was set at 1 AU. Images were processed using ZEN 2009 Confocal Software.

5.1.3.3 Uptake of ZnO-HCV-RGD-GFP nanoparticles by Live MCF-10-2A cells

The MCF-10-2A cells were cultured for 48 h on 35 mm glass-based culture dishes (Nest Biotech Co, LTD, 35X12 mm style, 20 mm glass bottom) at $9x10^4$ cells/cm^2. The cells were then treated using the same method described in section 5.1.3.2. Confocal imaging of live cells was started immediately after addition of the ZnO-HCV-RGD-GFP NPs dispersion to the cells using a Zeiss LSM 710 confocal microscope with the environmental chamber set to 37°C.

The 405 nm laser line was used to excite Hoechst 33342 (λexc\λem = 355/461 nm), the 561 nm laser was used to excite PI (λexc\λem= 538/617 nm) and the 488 nm laser was used to excite GFP labelled ZnO-HCV-RGD (λexc\λem=488/509 nm)Images were acquired over 24 h to track the uptake of the particles and viability of the cells (1 frame/4 min) using a 20x objective/0.8 NA, and the pinhole was set at 1 AU. A control experiment was performed, in

which the MCF-10-2A cells were incubated with 1 ml of the HEPES confocal imaging buffer alone. Images were processed using ZEN 2009 Confocal Software.

5.1.3.4 Correlation of uptake and dissolution of bare ZnO nanoparticles by MDA-MB-231 cells

The MDA-MB-231 cells were cultured for 48 h on 35 mm glass-based culture dishes (Nest Biotech Co, LTD, 35X12 mm style, 20 mm glass bottom) at $6x10^4$ cells/cm^2. The cells were then rinsed once with the HEPES confocal imaging buffer at pH 7.4, 37°C. The cells were then loaded with 5 μM of the cell-permeant Zn^{2+} indicator FluoZin3-AM (Invitrogen, UK) in 1 ml HEPES confocal imaging buffer for 20 min at 37°C. After rinsing the cells twice with imaging buffer (37°C), to remove any dye that was nonspecifically associated with the cell surface, the cells were incubated for a further 30 min to allow complete de-esterification of intracellular AM esters of FluoZin. Then, 150 μg/ml of the bare ZnO NPs were prepared in 2 ml HEPES confocal imaging buffer and PI was added to the ZnO dispersion just before imaging at a final concentration of 10 μg/ml. Finally, the ZnO/PI dispersion was added to the cells and live imaging was started immediately after addition of the bare ZnO NPs using a Zeiss LSM 710 confocal microscope with the environmental chamber set to 37°C. A control experiment was performed, in which the MDA-MB-231 cells were incubated with 1 ml of the HEPES confocal imaging buffer alone.

The 488 nm laser line was used to excite FluoZin3 (λexc\λem= 494/516 nm) and the 561 nm laser was used to excite PI (λexc\λem= 538/617 nm). Images were acquired over a time period of 16 h (1 frame/2 min) using a 20x objective/0.8 NA and the pinhole was set at 1 AU. Images were processed using ZEN 2009 Confocal Software.

5.1.4 Cellular uptake of ZnO nanoparticles and their effects on cell structure by electron microscopy

5.1.4.1 SEM imaging and analysis of bare ZnO nanoparticles binding in MDA-MB-231 cells

To examine binding of the bare ZnO NPs to the MDA-MB-231 cells and their distribution around the cells, the MDA-MB-231 cells were grown on 10 mm ϕ Melinex coverslips (Agar

Scientific) coated with 20 μg/ml Poly-L-ornithine (PLO) at a density of $6x10^4$ cells/cm^2 for 24 h at 37°C in 5% CO_2 humidified environment. The cell culture medium was then removed and the cells were washed once in the medium. The cells were then incubated with 30 μg/ml of the bare ZnO NPs for 4 h at 37°C in 5% CO_2 humidified environment. The cells were then fixed with 2% formaldehyde and 2% glutaraldehyde prepared in 0.1 M PIPES buffer at pH 7.4 for 1 h at 4°C. This cocktail has been shown to preserve cell structure and chemistry for elemental analysis [189]. The cell culture medium and the fixative was aspirated off the cells and the cells were then washed three times with deionised water and allowed to dry at RT before SEM imaging and analysis. The cells were carbon coated and SEM was carried out with a Magellan 400 FEG SEM. Images were acquired with an accelerating voltage of 2 kV and EDX was performed at 20 kV.

5.1.4.2 TEM imaging and analysis of bare and targeted ZnO NPs uptake

The uptake of the bare ZnO NPs by the MCF-7 and MDA-MB-231 cells was investigated using TEM. The MDA-MB-231 cells were tested with the ZnO-HCV-RGD NPs for binding because our experimental results showed that the MDA-MB-231 cells express a higher percentage of the RGD-targeting receptor (integrin αvβ3).

5.1.4.2.1 Bare ZnO nanoparticles

The MDA-MB-231 and MCF-7 were seeded on 60 mm tissue culture dishes (CELLTREAT, China) for 24 h, at a density of $6x10^4$ and $9x10^4$ cells/cm^2, respectively. The cell culture medium was then removed and the cells were washed once in the medium. The bare ZnO NPs ethanolic stock dispersion was sonicated for 20 min on a bench sonicator. The cells were then incubated with 20 μg/ml of the bare ZnO NPs, prepared in CDMEM medium, for 6 and 24 h at 37°C in 5% CO_2 humidified environment. After exposure, the cells were rinsed with 0.1M cacodylate buffer (pH=7.4), and were then fixed with 2.5% glutaraldehyde/0.1 M cacodylate buffer pH 7.4 for 1 h at 4°C. The samples were bulk stained using a cocktail of 1% OsO_4, 0.15% potassium ferricyanide, and 2 mM $CaCl_2$ in 0.1 M cacodylate buffer for 1 h at RT. The samples were washed several times with 0.1 M cacodylate buffer at pH 7.4. Dehydration of the samples in graded solutions of ethanol (30, 50, 70, 90, 95, and 100%), and infiltration in graded solutions (30, 50, 70, and 100%) of Spurr's resin in acetone was

carried out using a Leica EM TP tissue processor (Leica Biosystems, UK). The samples were then embedded in Spurr's Epoxy resin (Ted Pella, USA). Ultrathin sections (80-120 nm) of the cell pellets were prepared by ultramicrotomy using a 35° diamond knife and collected onto 300 mesh copper grids (TED PELLA, USA) in a water bath. The sections were post-stained for 2 min in lead citrate. Images were acquired using a FEI Tecnai T12 TEM (Tecnai bio Twin, FEI Company, Hillsboro, OR) operated at 120 kV, unless otherwise specified. Images were recorded on a 2k x 4K CCD camera (Gatan Inc., Pleasanton, CA).

5.1.4.2.2 ZnO-HCV-RGD-GFP nanoparticles

To determine the best incubation time for binding and uptake of the targeted ZnO NPs by the MDA-MB-231 cells, confocal microscopy of live cells incubated with the particles was conducted prior to TEM. The MDA-MB-231 cells were cultured for 48 h on 35 mm glass-based culture dishes (Nest Biotech Co, LTD, 35X12 mm style, 20 mm glass bottom) at a density of $6x10^4$ cells/cm^2. The cells were then rinsed once with the HEPES confocal imaging buffer at 37°C. The cells were then loaded with 1 μg/ml of the cell permeable nucleus stain Hoechst 33342 in 1 ml HEPES confocal imaging buffer for 30 min at 37°C. After rinsing the cells twice with imaging buffer (at 37°C), PI was added to the cells in 1 ml of the same buffer (final concentration 10 μg/ml). The targeted ZnO-HCV-RGD-GFP stock dispersion, prepared in 50 mM HEPES + 100 mM NaCl buffer at pH 7.5, was sonicated for 30 s on a bench sonicator. Finally, ZnO-HCV-RGD-GFP NPs were prepared in 1 ml HEPES confocal imaging buffer (to a final concentration 150 μg/ml) and 3D imaging of live cells was started immediately after addition of the sample solution, using a Zeiss LSM 710 confocal microscope with an environmental chamber set to 37°C. The 405 nm laser line was used to excite Hoechst 33342 (λexc\λem=355/461 nm), 561 nm laser was used to excite PI (λexc\λem=535/617 nm) and the 488 nm laser was used to track GFP labelled ZnO-HCV-RGD NPs. The pinhole was set at 1 AU and imaging was started (1 frame/2 min) using a 20x objective/0.8 NA. Images were processed using ZEN 2009 Confocal Software.

Once the ZnO-RGD-HCV-GFP NPs were bound to the surface of the cells (after 22 min exposure), confocal live imaging was stopped and the cells were immediately fixed with 4% glutaraldehyde in 0.1 M cacodylate buffer at pH 7.4. Cells were then rinsed, pre-embedded in gelatin 10% and infiltrated in 2.3 M sucrose, prepared in 0.1 M HEPES buffer at

pH 7.4, overnight at 4°C. Sucrose infiltrated samples were then frozen by immersion into liquid nitrogen for 3 s. 90 nm ultrathin sections were cut using an ultramicrotome at -110°C using diamond knife and collected using a drop of MS (1% methyl cellulose and 1.15 M sucrose) held on a wire loop, and transferred to 300 mesh copper grids (TED PELLA, USA). Cells were then imaged and analysed in Titan ST operated at 300 kV. Because the Cu grid interfered with the EDX energy peaks of Zn, new sections were prepared the same way but collected onto a gold grid. Pre-embedding in gelatin, infiltration, and sectioning of the cells was carried out with the help of Dr. Rachid Sougrat and Guangchao Wang at KAUST.

5.1.5 Cancer stem cell markers

For analysis of the cancer stem cell surface markers, the MCF-7 and the MDA-MB-231 cells were plated for 24 hours in 12-well plates to 80 % confluency. The cells were then detached using ice cold EDTA (0.48 mM Versene) solution. The cells were counted and then washed with Hank's Balanced Salt Solution (HBSS). A total of $2X10^6$ cells were incubated with specific antibodies for 30 min at 4°C in the dark. Unbound antibody was washed out through two cycles of washing with HBSS and the cells were analysed on a BD FACSCanto II flow cytometer (BD bioscience, Franklin lakes, NJ). The data were analysed using FlowJo 7.6.1 and at least 50,000 events per sample was collected. The antibodies used were anti-CD44 [phycoerythrin (PE)], anti CD24 [FITC], anti CD90 [PE-Cy5], anti EpCAM [PerCP-Cy™5.5], and IgG1 was used an isotype control.

5.2 Results and Discussion

5.2.1 Confocal microscopy of live MDA-MB-231, MCF-7 and MCF-10-2A cells exposed to bare and RGD-targeted ZnO nanoparticles

Binding, uptake, dissolution and cytotoxicity of the targeted ZnO NPs in the breast cancer MDA-MB-231 and MCF-7 cell lines were investigated. The MDA-MB-231 cells were chosen as a model of estrogen receptor-negative and highly invasive cells that shown to express the integrin αvβ3 [157]. The MCF-7 cells are used here as a model of an ER+ and non-metastatic breast cells that shows lower expression of these receptors [190].

In MDA-MB-231 cells, Imaging was carried out using confocal microscopy of live cells exposed to the targeted ZnO-HCV-RGD-GFP NPs. The first objective was to track binding,

uptake and intracellular distribution of these NPs and subsequent death of the breast cancer cells. To achieve these goals, the targeted ZnO-HCV-RGD NPs were labelled with the GFP, and the nucleus or the plasma membrane of the cells was labelled with fluorescent probes. The second objective was directed to study the dissolution of the targeted ZnO-HCV-RGD-GFP NPs inside the cells and correlate ZnO-HCV-RGD-GFP NPs uptake directly to rise of intracellular Zn^{2+} and cell death. Zinc-sensitive and cell permeable fluorescent probes were used to track the dissolution of the ZnO-HCV-RGD-GFP NPs inside the cells. PI, which is excluded by the intact cell membrane of live cells, was used as a viability indicator.

Since the MDA-MB-231 cells and the MCF-7 cells showed different responses to the ZnO-HCV-RGD-GFP NPs in the Alamar Blue and the ATP assays (Table 6), and they also expressed different percentage of the integrin αvβ3 targeted receptor (Figure 29), the cellular responses to the targeted ZnO-HCV-RGD-GFP NPs in the MDA-MB-231 cells were compared to those in the MCF-7 cells. The cellular responses of the healthy breast MCF-10-2A cells after exposure to the ZnO-HCV-RGD-GFP NPs were also studied.

The efficiency of targeting and mechanisms of uptake of the targeted ZnO-HCV-RGD-GFP NPs, as well as intracellular rise of Zn^{2+} in the MDA-MB-231 cells were compared to those of the bare ZnO NPs. Finally, the intracellular rise of Zn^{2+} after exposure of the MDA-MB-231 cells to $ZnCl_2$ was also investigated.

A number of fluorescent dyes were used for confocal microscopy imaging of the cells; a list of these is shown in

Table 8. Hoechst 33342 is a cell permeable dye that fluoresce blue upon binding the DNA of live nuclei. FluoZin3-AM and Zinquin-AM were used as Zn^{2+}- sensitive probes. FluoZin fluoresces green while Zinquin fluoresces blue when complexed with Zn^{2+}; therefore the latter was used with the green fluorescent RGD-targeted NPs. Both FluoZin3-AM and Zinquin-AM probes are cell-permeable fluorescent esters which are cleaved by cytosolic esterases to a cell-impermeant FluoZin and Zinquin that carry a negative charge, preventing their efflux across the plasma membrane. They also exhibit high Zn^{2+}-binding affinity that is unperturbed by Ca^{2+} concentrations up to at least 1 μM [40]. A schematic representation of the confocal microscopy experiments performed in this study is shown in Figure 57.

Table 8: Fluorescent dyes used for confocal imaging.

Dye used	Excitation wave length (λexc)* (nm)	Emission wave length (λem)** (nm)	Excitation wave length used (nm)	Function	Fluorescent colour
Hoechst 33342	355	461	405	Live cells nuclei stain	blue
PI	538	617	561	Viability indicator	red
FluoZin3-AM	494	516	488	Zinc ions sensitive dye	green
Zinquin-AM	344	385	405	Zinc ions sensitive dye	blue
GFP	488	509	488	Label for ZnO-HCV-RGD NPs	green
CellMask Deep Red	649	666	561	Plasma membrane stain	red
*λexc: excitation wave length, **λem: emission wave length					

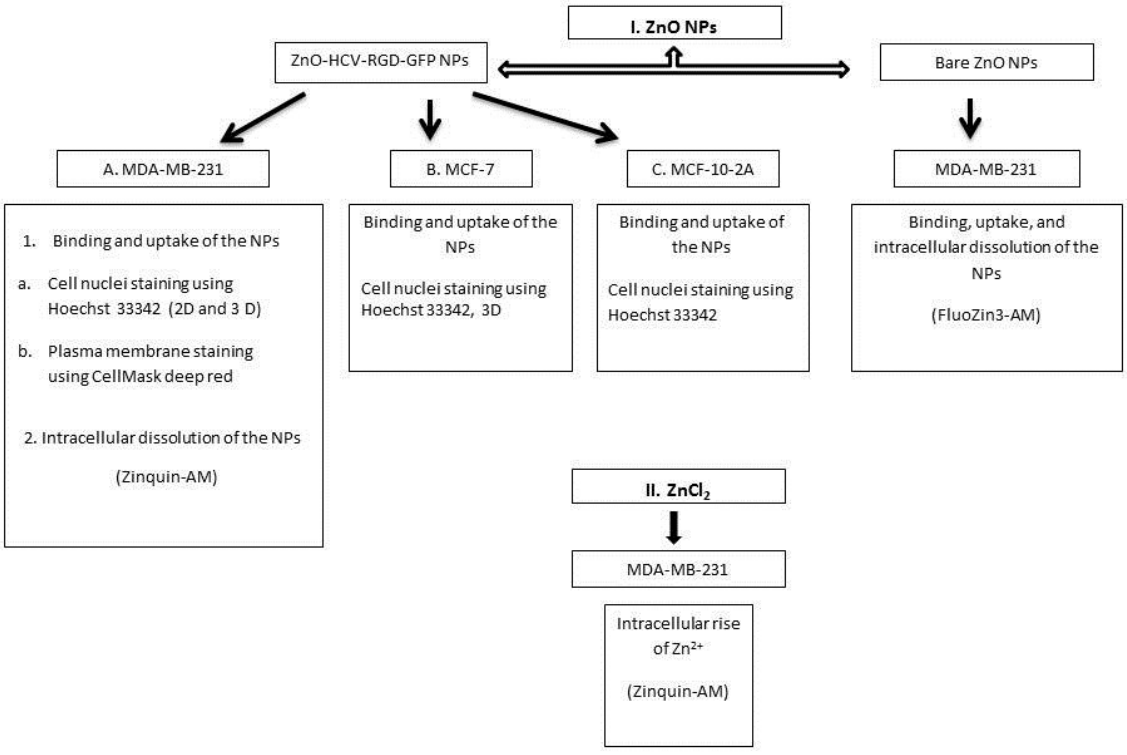

Figure 57: A schematic representation of the confocal microscopy experiments performed in this study.

5.2.1.1 Correlation of uptake and dissolution of ZnO-HCV-RGD-GFP nanoparticles by live MDA-MB-231 cells

5.2.1.1.1 Uptake of ZnO-HCV-RGD-GFP NPs into live MDA-MB-231 cells

1. Live cells nuclei staining using Hoechst 33342

2D cell imaging of uptake of ZnO-HCV-RGD-GFP NPs into live MDA-MB-231 cells

The MDA-MB-231 cells were loaded with the live nuclei stain Hoechst 33342, and were then incubated with the ZnO-HCV-RGD-GFP NPs. Images were acquired over a time period of 3-4 h every 2 min. PI was used to stain the nuclei of dead cells. Bright field imaging was used to view the changes in cell morphology and to track the uptake of the NPs. The results are summarised in the following sections.

I. Changes in cell morphology upon exposure to ZnO-HCV-RGD-GFP NPs

Figure 58 shows the changes in the MDA-MB-231 cells' morphology upon exposure to the ZnO-HCV-RGD-GFP NPs. Before exposure to the ZnO-HCV-RGD-GFP NPs, the MDA-MB-231 cells had a healthy morphology, and were elongated with large intercellular spaces and they were adhered to the culture plate (Figure 58, a). Some circular cells had grown on the top of the elongated cells (Figure 58, a). All cells were viable as indicated by Hoechst stain of their nuclei and the absence of PI staining (Figure 58, a). After exposure to the ZnO-HCV-RGD-GFP NPs, the cells changed their morphology and became round as soon as they were incubated with the particles (Figure 58, b-d). It has been recently reported that Zn^{2+} (0.654-3.27 μg/ml) induced a dose-dependent inhibition of cell adhesion of MDA-MB-231 cells to fibronectin used as an extracellular matrix [191]. In this study, the targeted ZnO-HCV-RGD-GFP NPs dispersions released about 0.35 μg/ml of ionic zinc (Zn^{2+}) in the confocal imaging buffer as indicated by the ICP dissolution experiment of the NPs (Figure 19). Therefore, it is possible that this alteration in morphology arose due to the release of a small amount of soluble Zn^{2+} in the imaging buffer. Large green aggregates of the ZnO-HCV-RGD-GFP NPs could also be observed around the cells (Figure 58, b-d).

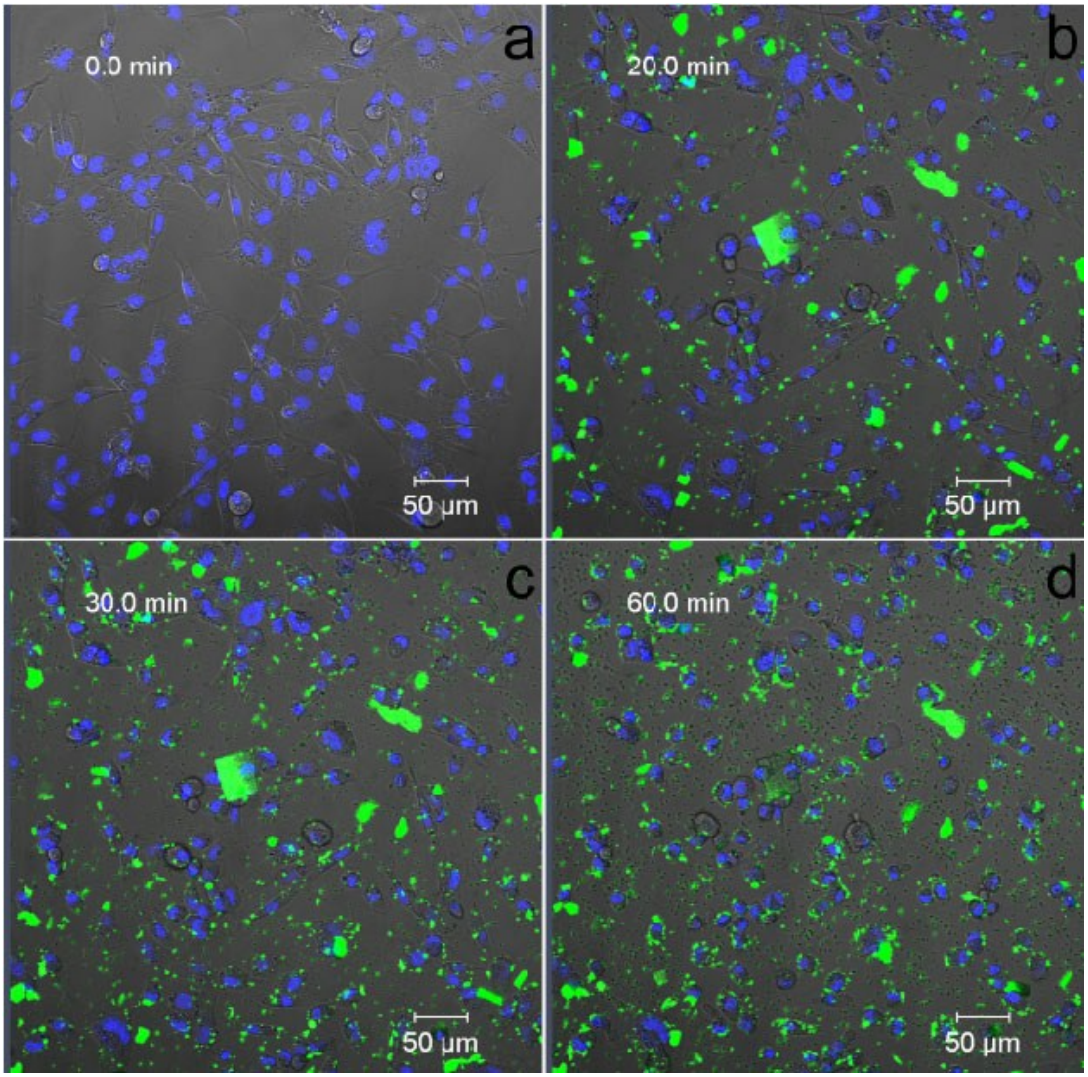

Figure 58: Confocal and bright field images of MDA-MB-231 cells incubated with ZnO-HCV-RGD-GFP NPs (green). (a) MDA-MB-231 cells before exposure to the NPs. (b, c, d) MDA-MB-231 cells after 20, 30 and 60 min exposure to the targeted ZnO NPs, respectively. The cells nuclei were stained with Hoechst 33342 (blue).

II. Binding and uptake of ZnO-HCV-RGD-GFP nanoparticles by MDA-MB-231 cells

Binding and uptake of the ZnO-HCV-RGD-GFP NPs by the MDA-MB-231 cells were followed over time (Figure 59). Upon exposure to the targeted ZnO NPs, the MDA-MB-231 cells lost their shape rapidly (Figure 59, a-h). Large projections from the plasma membrane of the cells that extend into the matrix have developed (Figure 59, a-n). These projections surrounded the ZnO-HCV-RGD-GFP NPs (white arrows) and fused together so that the ZnO-HCV-RGD-GFP NPs has become completely engulfed (Figure 59, a-n). Other ZnO-HCV-RGD-GFP NPs bound to the cell membrane possibly through a receptor-mediated process (Figure 59, f, arrow heads). Blebbing (Figure 59, o, black arrows) of the MDA-MB-231 cells, which is a marker of apoptosis, was observed at 78 min exposure to the ZnO-HCV-RGD-GFP NPs.

Figure 60 shows binding of the ZnO-HCV-RGD-GFP NPs (white arrows in a-c) to the cell membrane possibly through a receptor-mediated process. After 2 h exposure, the MDA-MB-231 cells were coated by almost a complete layer of ZnO-HCV-RGD-GFP and diffuse green fluorescence from the GFP could be observed inside the cells (Figure 60, d, white arrow). This diffuse green fluorescence could be present due to dissolution of the ZnO-HCV-RGD-GFP NPs inside the highly acidic compartments of the lysosomes. Figure 61 shows a more clear presentation of the diffuse layer of GFP (white arrows) inside the MDA-MB-231 cells. A video that shows the binding and uptake of the ZnO-HCV-RGD-GFP into live MDA-MB-231 cells is attached (Video 1, MDA-MB-231 cells, ZnO-HCV-RGD-GFP NPs, uptake).

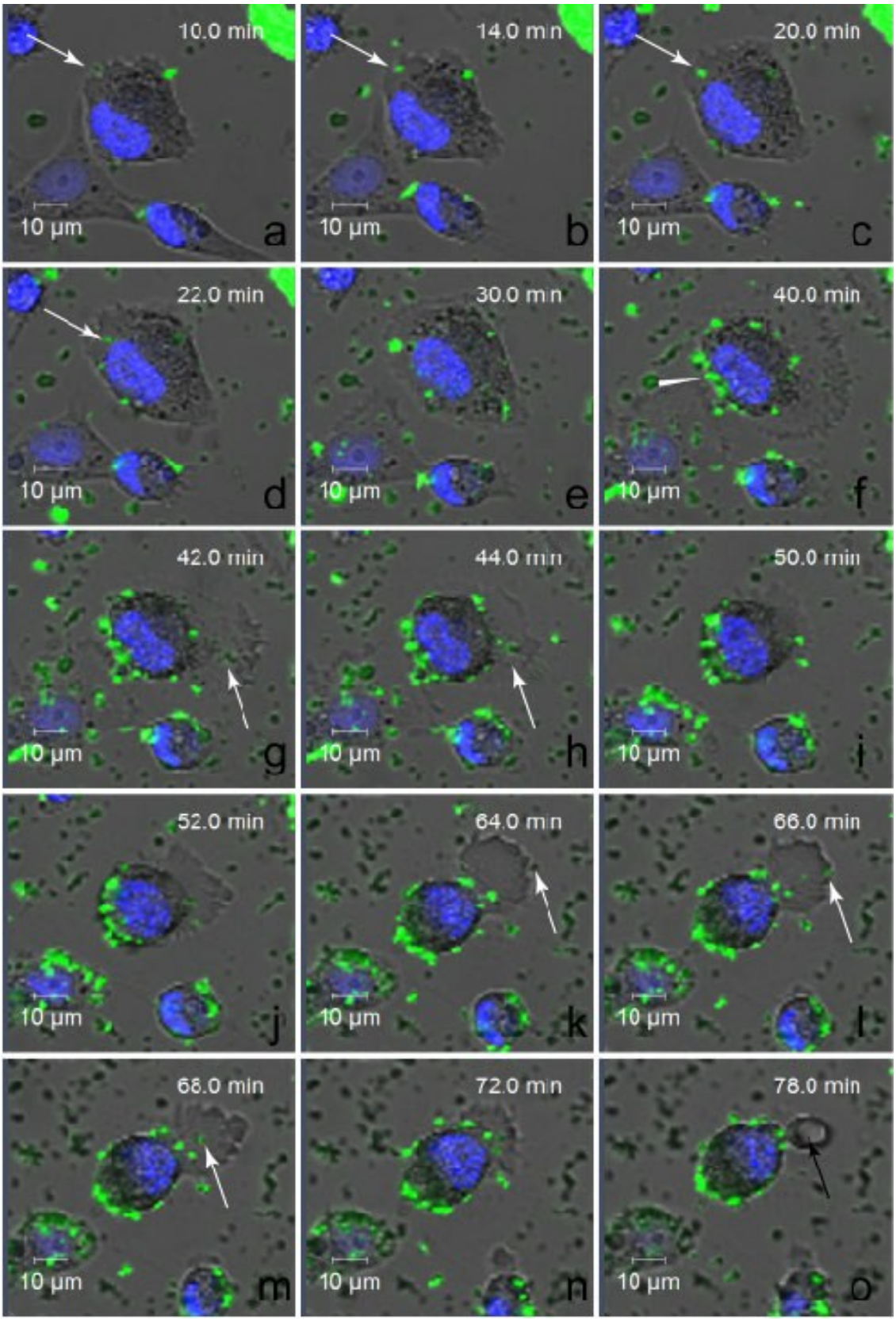

Figure 59: Confocal images showing binding and uptake of ZnO-HCV-RGD-GFP NPs to live MDA-MB-231 cells. The MDA-MB-231 cells were exposed to 150 µg/ml ZnO-HCV-RGD-GFP NPs (green) and confocal imaging was carried out for 3-4 h. ZnO-HCV-RGD-GFP NPs (white arrows) binds to the cells soon after incubation. Blebbing (black arrows in O) of the MDA-MB-231 cells was observed after 78 min exposure to the NPs. Hoechst (blue) was used to stain live cells nuclei blue.

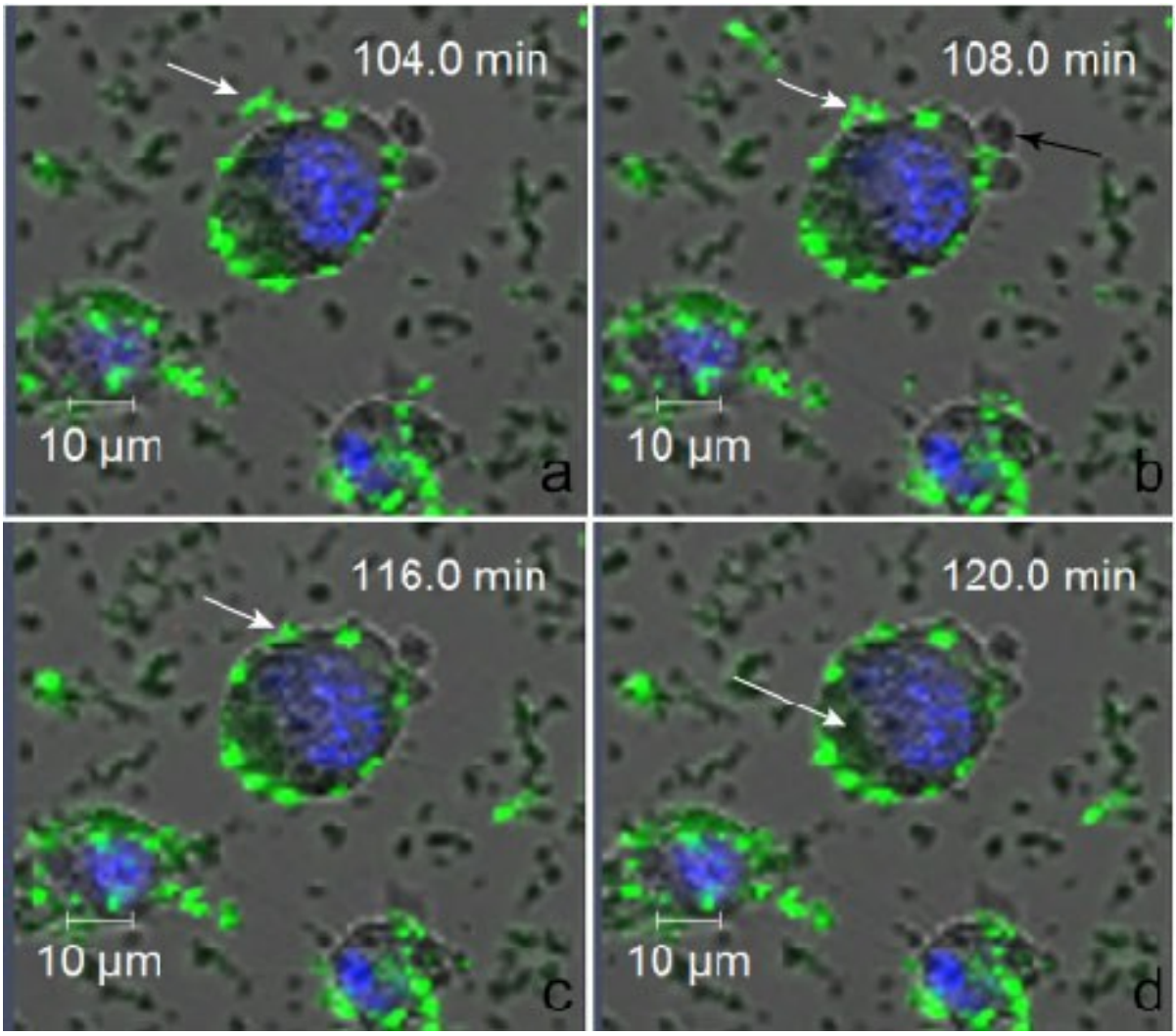

Figure 60: Confocal images showing binding and uptake of ZnO-HCV-RGD-GFP NPs by live MDA-MB-231 cells. The MDA-MB-231 cells were exposed to 150 µg/ml ZnO-HCV-RGD-GFP NPs (green) and confocal imaging was carried out for 3-4 h. ZnO-HCV-RGD-GFP NPs (white arrows in a-c) bound to the surface of the cells. A diffuse green layer of GFP (white arrow in d) could be observed inside the cells. Hoechst (blue) was used to stain live cells nuclei blue.

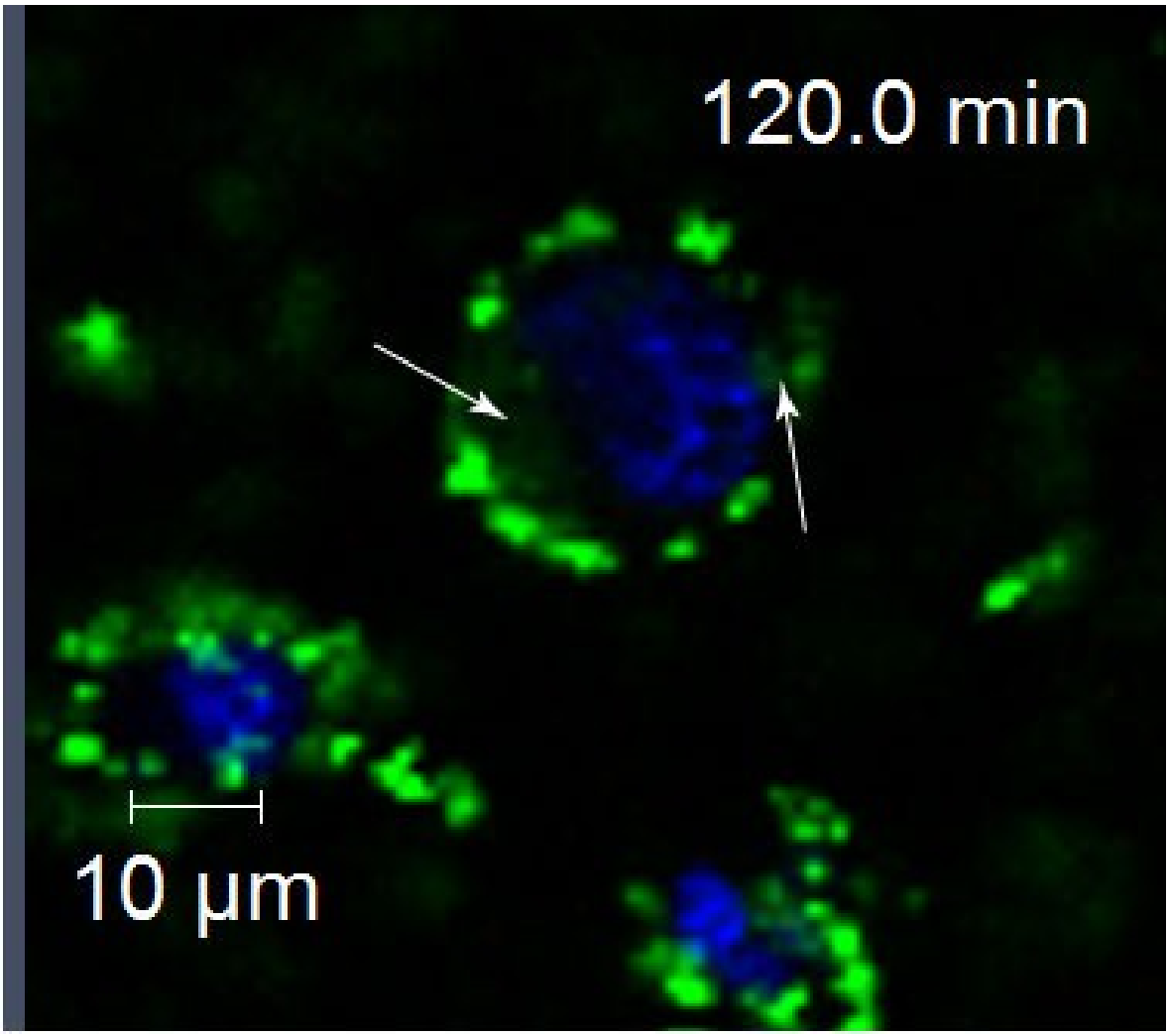

Figure 61: Confocal image showing a diffuse layer of GFP (white arrows) inside the cells MDA-MB-231 cells after 2 h exposure to ZnO-HCV-RGD-GFP NPs. The MDA-MB-231 cells were exposed to 150 µg/ml ZnO-HCV-RGD-GFP NPs (green) and confocal imaging was carried out for 3-4 h. Hoechst (blue) was used to stain live cells nuclei blue.

The binding of the ZnO-HCV-RGD-GFP NPs to the cell membrane of the MDA-MB-231 cells seemed to be heterogeneous (Figure 62). A single channel of the GFP, after 1.5 h exposure to the ZnO-HCV-RGD-GFP NPs, shows difference in the GFP colour between individual cells (Figure 62, right image). This indicates systematic variations between NPs association levels due to phenotypic variations in ZnO-HCV-RGD-GFP NPs uptake and/or processing by the MDA-MB-231 cells (as will be discussed in section 5.2.3). This observation could also be due to different levels of expression of the integrin αvβ3 by the MDA-MB-231 cells.

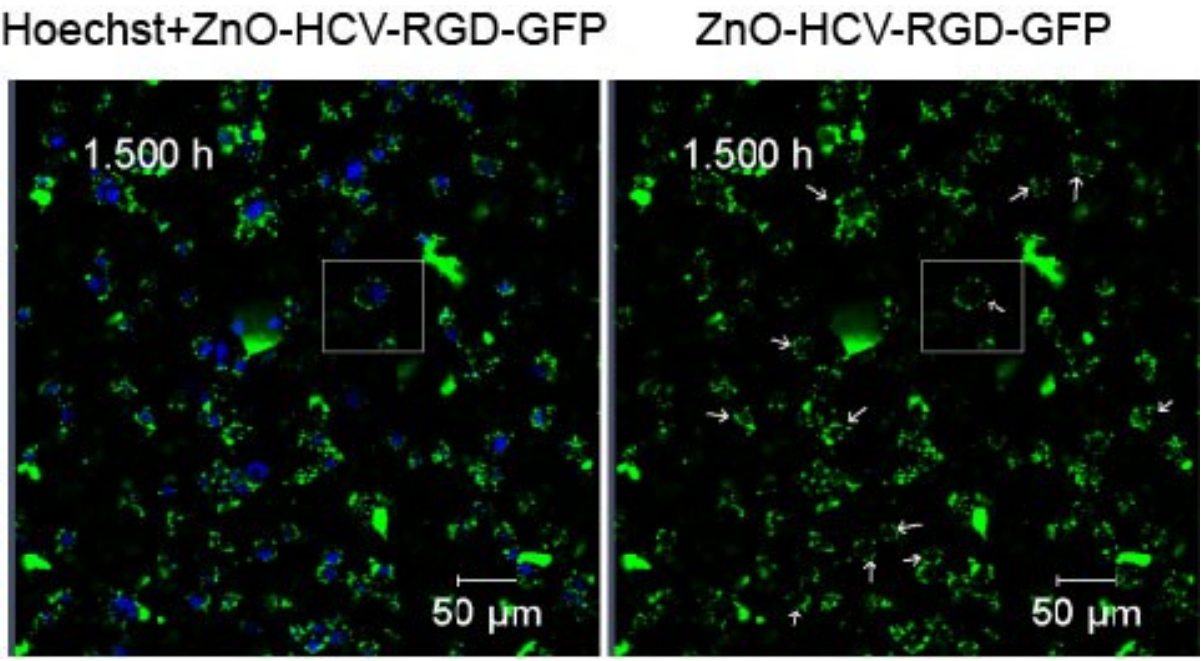

Figure 62: Confocal images showing binding of ZnO-HCV-RGD-GFP NPs to live MDA-MB-231 cells. The MDA-MB-231 cells were exposed to 150 µg/ml ZnO-HCV-RGD-GFP NPs (green) and confocal imaging was carried out for 3-4 h. ZnO-HCV-RGD-GFP (white arrows) bound to the cells very rapidly after incubation. The difference in the GFP colour between individual cells indicates systematic variations between NP association levels due to phenotypic variations in NP uptake and/or processing by the cells. Hoechst 33342 was used as live nuclei stain. PI was used as a viability indicator

3D live cell imaging of uptake of ZnO-HCV-RGD-GFP nanoparticles by MDA-MB-231 cells

To check for uptake into 3D volume of the cells, the previous experiment was repeated under the same conditions except images were acquired at different Z-height through the cell at each time point, and images were acquired every 1.5 min for 8-9 h. To check for cell viability, the cells were then stored at 37°C and reimaged after 18 h exposure.

The MDA-MB-231 cells showed the same behaviour upon exposure to the ZnO-HCV-RGD-GFP NPs in 3D imaging. This includes; the development of large projections from the plasma membrane of the cells that extend into the matrix (Figure 63, b, white arrows), changes in the cell morphology (Figure 63, a-f), binding and uptake of the ZnO-HCV-RGD-GFP (Figure 63, b-d, arrow heads). Some agglomerates of the ZnO-HCV-RGD-GFP NPs, however are bound to the surface of the cells without being taken up by the cells. It has been reported that after binding of NPs to their receptors, the receptors associated with their ligands are engulfed to a coated pit, and the assembled vesicle is then pinched off from the plasma membrane [48]. Therefore, it is most probably that these agglomerates of the ZnO NPs are too big for integrin αvβ3 receptor mediated uptake. Because the cells were imaged for longer time, cellular death could be tracked. After 270 min of incubation with the ZnO-HCV-RGD-GFP NPs, the MDA-MB-231 cells started to undergo apoptosis as indicated by blebbing (Figure 63, g and h, black arrows). After blebbing, the MDA-MB-231 cells lost their cell membrane integrity as indicated by the intracellular penetration of PI and the double staining of their nuclei (Figure 63, i). A single channel of Hoechst 33342 and PI staining of the nucleus is shown in Figure 64.

An orthogonal view through a stack of images of the MDA-MB-231 cells shows the ZnO-HCV-RGD-GFP NPs inside the cells at the same focal plane of the nucleus (Figure 65). Furthermore, 3D confocal images of the MDA-MB-231 cells after 13.5, 16.5, and 19.5 min exposure to ZnO-HCV-RGD-GFP NPs show the NPs inside the cells at a Z height within the cell that is at the same focal plane of the nucleus (Z2) but not at the other Z planes just below and above Z2 separated by 1.28 µm (Figure 66). However, after 22.5 min exposure to the ZnO-HCV-RGD-GFP NPs, the intensity of the GFP at Z2 was reduced and a more diffused green colour could be observed, which could probably indicate the dissolution of the NPs inside the cells (Figure 66). This indicates that the targeted ZnO-HCV-RGD-GFP ZnO NPs are

internalised, then dissolve inside the cells and cause cytotoxic responses in the MDA-MB-231 cells. A video that shows the uptake of the ZnO-HCV-RGD-GFP NPs by live MDA-MB-231 cells is attached (Video 2, MDA-MB-231 cells, ZnO-HCV-RGD-GFP NPs, uptake).

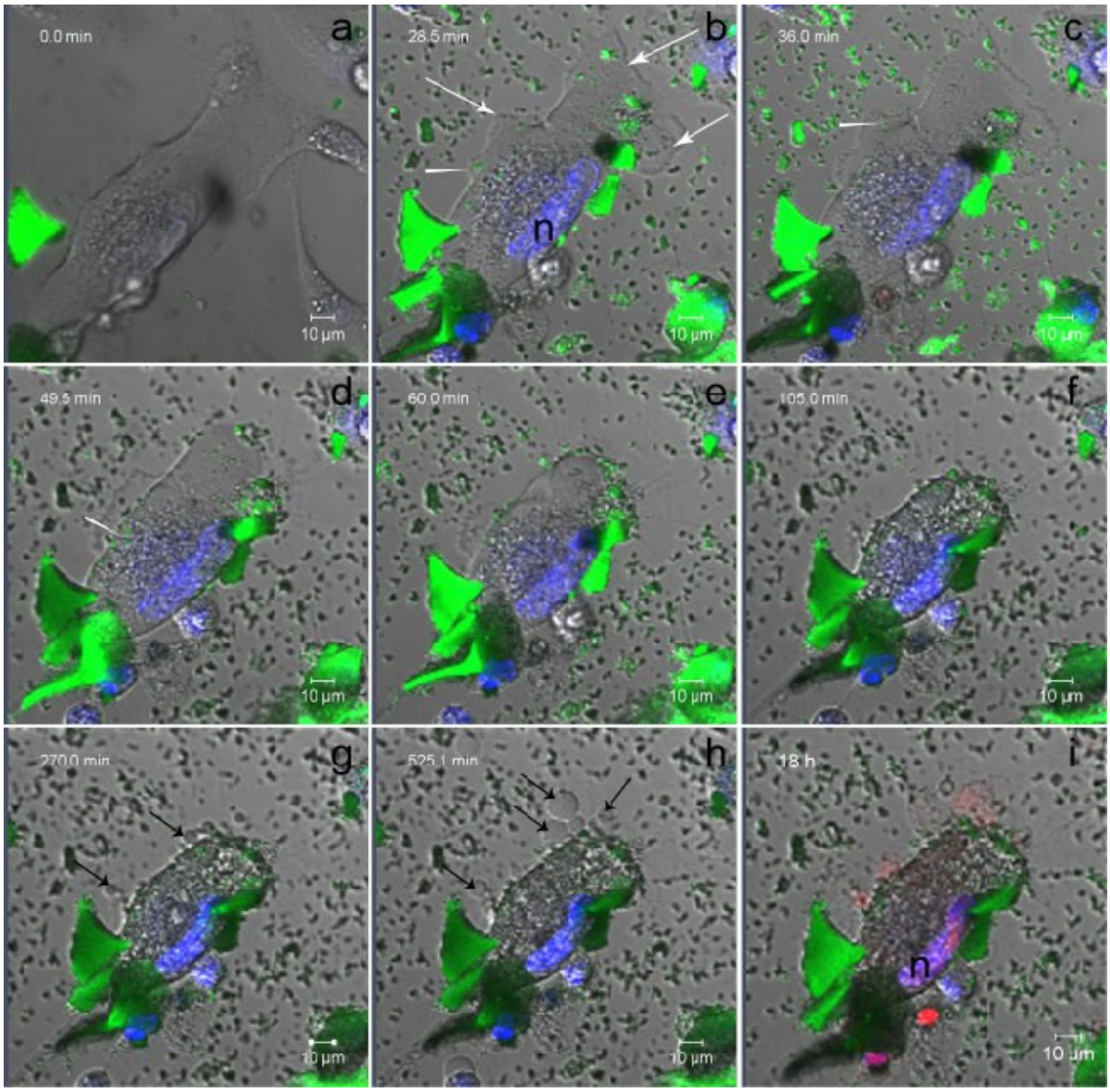

Figure 63: Confocal images showing binding and uptake of ZnO-HCV-RGD-GFP NPs by live MDA-MB-231 cells. The MDA-MB-231 cells were exposed to 150 µg/ml ZnO-HCV-RGD-GFP NPs (green) and confocal imaging was carried out for 8-9 h, the cells were then incubated at 37°C and imaged after 18 h exposure. (a-d) Extensions of large projections from the plasma membrane (white arrows) were developed to engulf ZnO-HCV-RGD-GFP (white arrow heads). (e,f) Shrinkage in cell size after exposure to the ZnO-HCV-RGD-GFP NPs. (g, h) Blebbing (black arrows) of the cells in process of apoptosis. (i) Cell death as indicated by red staining of the nucleus (n). Hoechst (blue) was used to stain live cells nuclei blue. PI (red) was used as a viability indicator.

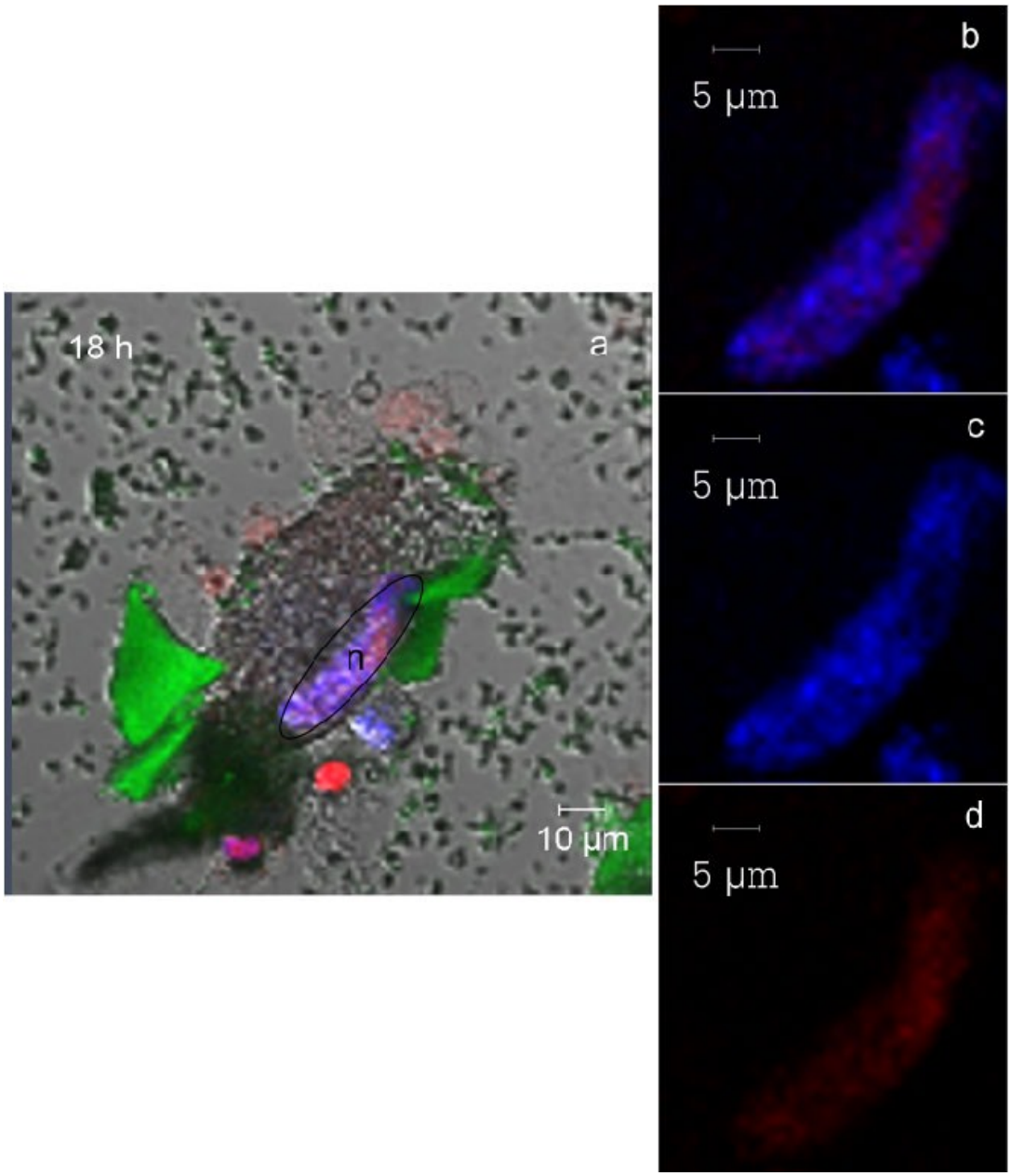

Figure 64: Confocal image of MDA-MB-231 cells after 18 h exposure to ZnO-HCV-RGD-GFP NPs. MDA-MB-231 cells were exposed to 150 µg/ml ZnO-HCV-RGD-GFP NPs (green) for 18 h at 37°C. (a) A dead MDA-MB-231 cell imaged after 18 h of incubation with the NPs, showing the nucleus stained with both Hoechst 33342 and PI. (b) Nucleus of the cell in image a, stained with Hoechst 33342 (blue) and PI (red). (c) and (d) are Hoechst 33342 and PI staining of the nucleus, respectively.

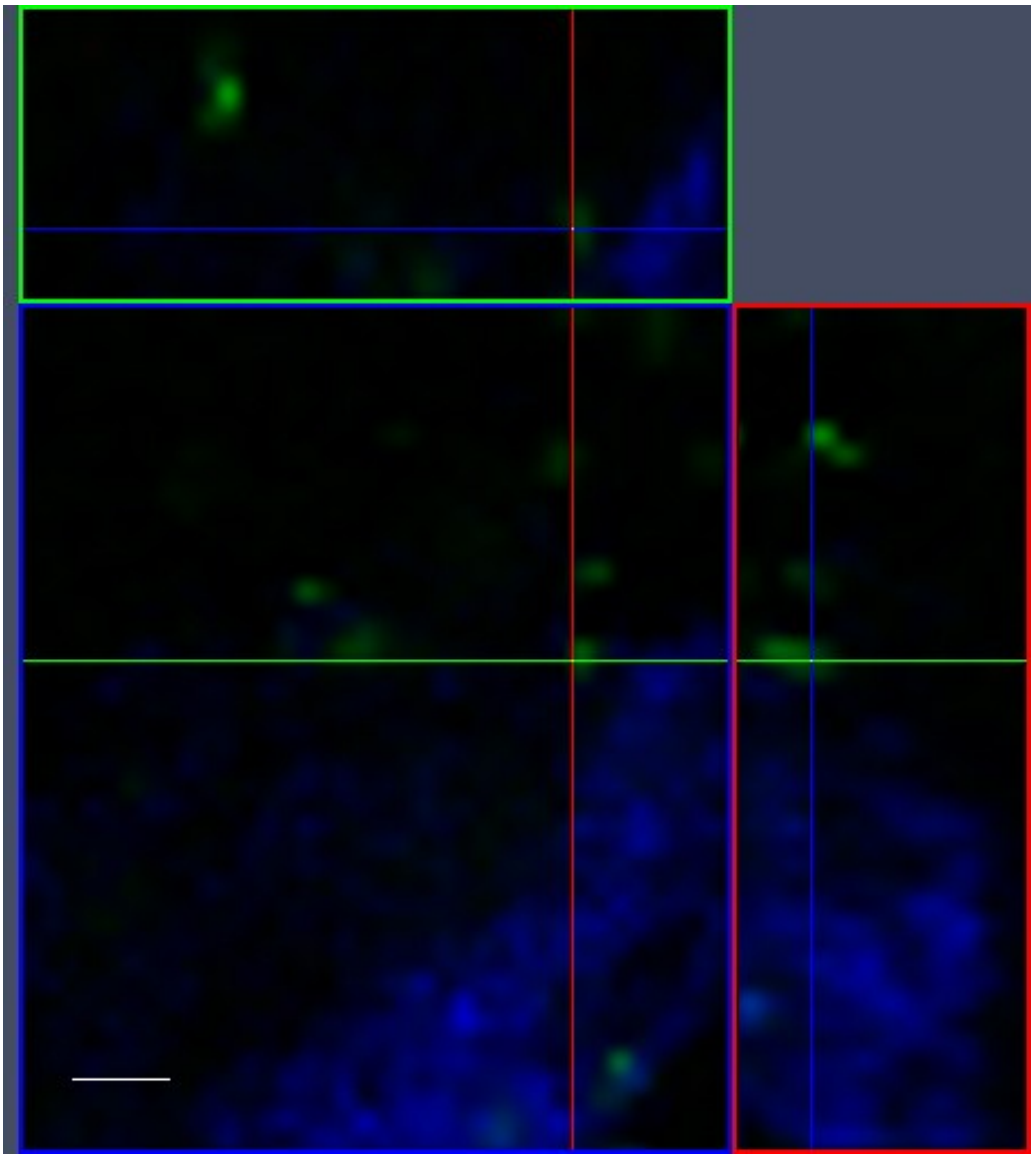

Figure 65: A Z-Stack image in an orthogonal view of ZnO-HCV-RGD-GFP NPs penetrating the cytoplasm of MDA-MB-231 cells (green=ZnO-HCV-RGD-GFP, blue=nuclei, green line= XZ plane, red line =YZ plane, blue line=XY). MDA-MB-231 cells were incubated with 150 µg/ml ZnO-HCV-RGD-GFP NPs. Hoechst 33342 was used as viable nuclei stain. Scale bar is 5 µm.

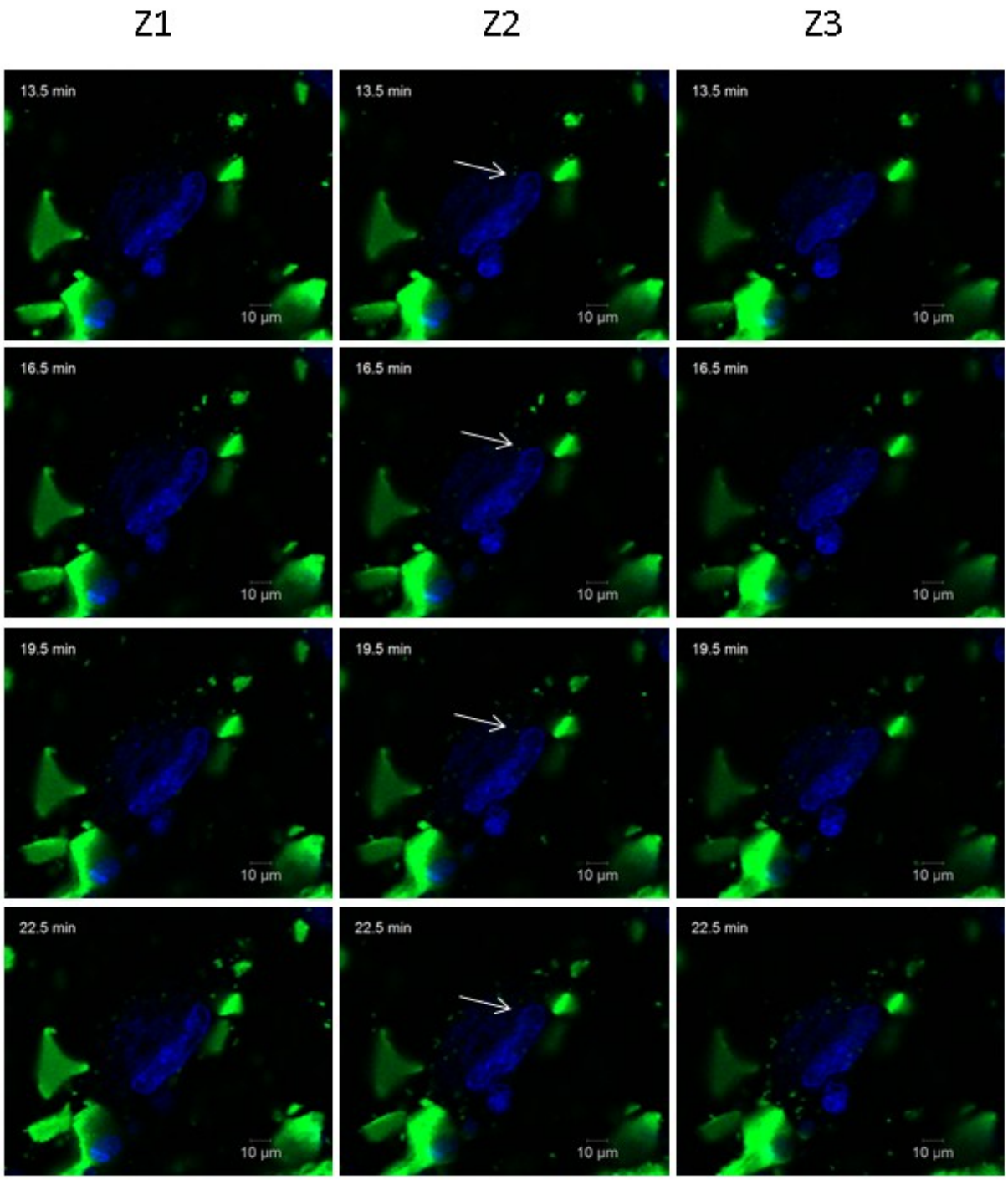

Figure 66: Confocal images of MDA-MB-231 cell exposure to ZnO-HCV-RGD-GFP NPs (green) showing the NPs inside the cell at Z2-height within the cells (white arrows) after different exposure time points. The NPs were observed at the same focal plane of the nucleus, and were not observed at Z heights just below and above Z2. MDA-MB-231 cells were incubated with 150 µg/ml ZnO-HCV-RGD-GFP NPs. Hoechst 33342 was used as viable nuclei stain (blue).

2. Plasma membrane staining of live MDA-MB-231 cells using CellMask Deep-Red

To further confirm the uptake of the ZnO-HCV-RGD–GFP NPs by the MDA-MB-231 cells, the plasma membrane of the MDA-MB-231 cells was stained with the CellMask™ Deep Red (Figure 67), and the uptake of the ZnO-HCV-RGD–GFP NPs by the cells was tracked over time. Figure 68 shows that binding of the particles to the plasma membrane of the cells was started shortly after incubation of the cells with the targeted ZnO NPs. Figure 68 also shows that the ZnO-HCV-RGD-GFP NPs had become internalised inside the cells (white arrow heads) and possibly dissolved inside the cells. At the end of imaging time (≈ 10 h), the cell membrane was surrounded by almost a complete layer of the ZnO-HCV-RGD-GFP NPs (Figure 68). A video that shows the uptake of the ZnO-HCV-RGD-GF NPs by live MDA-MB-231 cells is attached (Video 3, MDA-MB-231 cells, ZnO-HCV-RGD-GFP NPs, CellMask deep red).

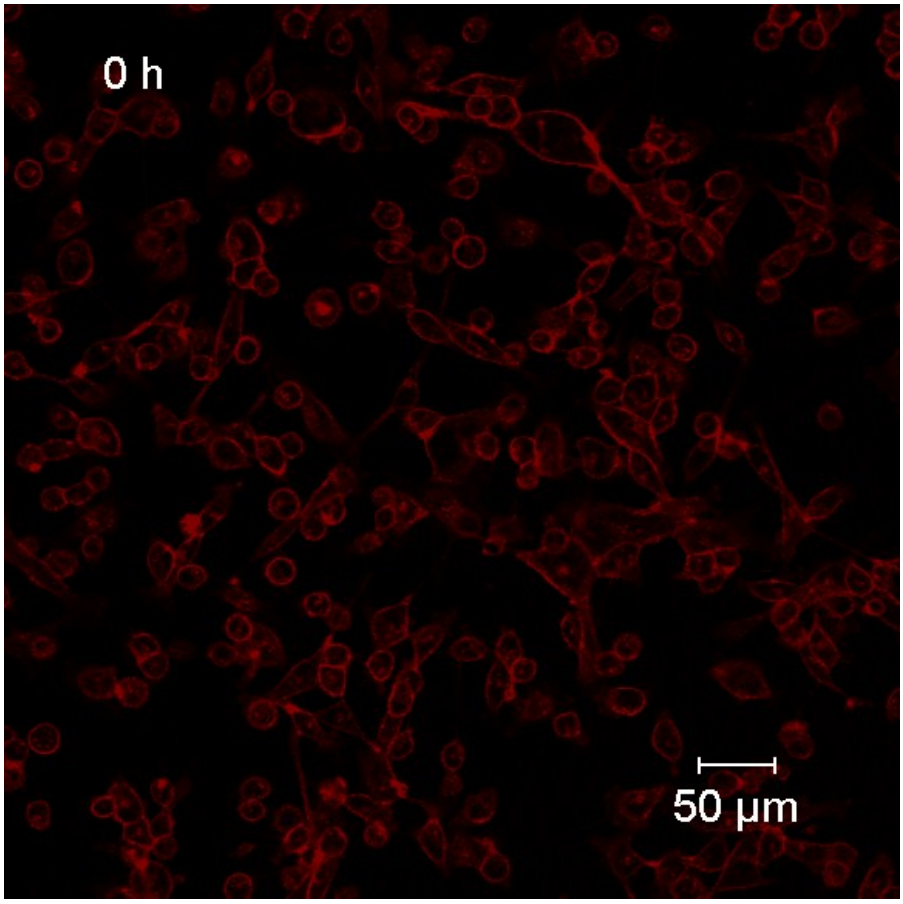

Figure 67: Confocal image of CellMask Deep Red staining of the plasma membrane of MDA-MB-231 cells before exposure to ZnO-HCV-RGD-GFP NPs. MDA-MB-231 cells were loaded with 5 µg/ml CellMask™ Deep Red plasma membrane stain in confocal imaging buffer for 5 min at 37°C.

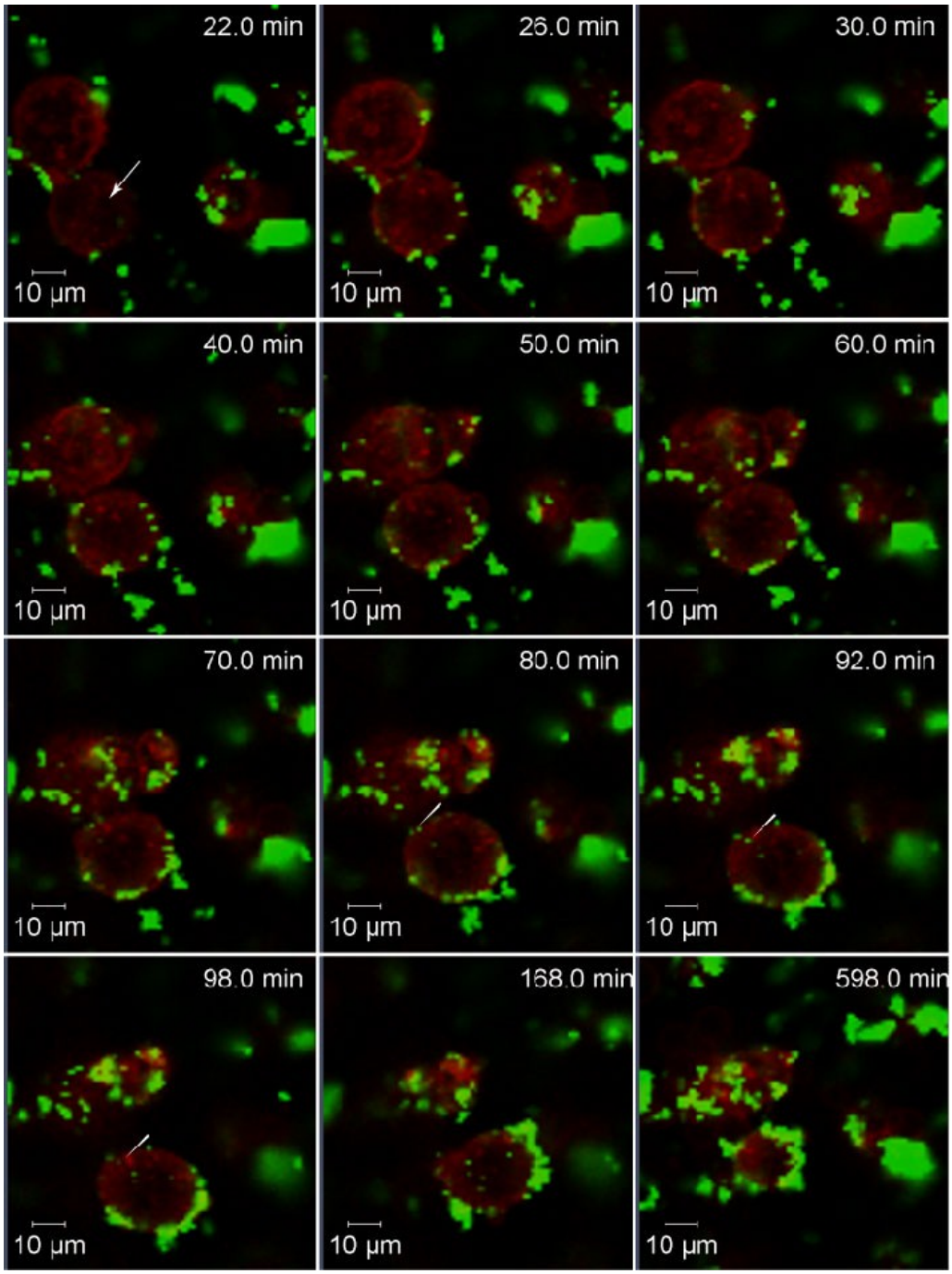

Figure 68: Confocal images showing uptake of ZnO-HCV-RGD-GFP by live MDA-MB-231 cells. The plasma membrane of the cells was stained with CellMask deep red stain (white arrow) and ZnO-HCV-RGD-GFP NPs were added to the cells at a final concentration of 150 µg/ml. The ZnO-HCV-RGD-GFP NPs (white arrow heads) started to bind to the plasma membrane, internalised, and dissolved inside the cell. The CellMask plasma membrane stain started to penetrate the cytoplasm after 30 min of incubation with the cells.

5.2.1.1.2 Dissolution of ZnO-HCV-RGD-GFP nanoparticles in MDA-MB-231 cells and rise of intracellular Zn^{2+}

The results illustrated in section 5.2.1.1.1 showed that the ZnO-HCV-RGD-GFP NPs bind to and are taken up by the MDA-MB-231 cells. After internalisation of the GFP labelled NPs, a diffuse green area could be observed inside the cells indicating that the particles could have dissolved. Figure 19 showed that the solubility of the ZnO-HCV-RGD-GFP NPs in the HEPES confocal imaging buffer at pH 7.4 was < 0.6 µg/ml Zn^{2+}. Therefore, any rise in intracellular Zn^{2+} upon exposure to ZnO-HCV-RGD-GFP NPs must be due to the acidic dissolution of these NPs inside the lysosomes and the local release of toxic Zn^{2+} ions after their internalisation. To confirm that dissolution of the RGD-targeted NPs inside the MDA-MB-231 cells had occurred, confocal imaging of cells incubated with 150 µg/ml of the ZnO-HCV-RGD-GFP NPs was carried out for 24 h using Zinquin- a dye sensitive to zinc ions. PI was used as a viability indicator. Bright field imaging was used to view the changes in cell morphology and to track uptake of the NPs by the cells.

Figure 69 shows that after 2 h exposure of the MDA-MB-231 cells to the ZnO-HCV-RGD-GFP NPs, the NPs were bound to the surface of the MDA-MB-231 and formed almost a complete layer around the cell. After uptake, the ZnO-HCV-RGD-GFP NPs dissolved in the highly acidic compartments of the lysosomes releasing zinc ions (Zn^{2+}) (Figure 70). This release of ionic zinc (Zn^{2+}) was accompanied by the increase in the intensity of Zinquin inside the cells (Figure 70), which was clear after 4 h of exposure (Figure 70, b). This rise in the intracellular zinc was toxic to the cells and resulted in cell death as indicated by the penetration of PI into the cells and the rise of its intracellular concentration (Figure 70, c and d). The rise of intracellular zinc ions over time was followed for 20 cells and a representative example is illustrated in Figure 71 (b and c). Analysis of the cells after exposure to the targeted ZnO-HCV-RGD-GFP showed that 20% of the cells in the imaging field died as early as 6 h exposure and almost 80% of the cells died after 12 h exposure.

The control elongated MDA-MB-231 cells, imaged under the same conditions, survived the laser, and did not show any morphological changes throughout the 24 h imaging time (Figure 72). Some cells, however, especially the round cells grown on the top of the elongated cells, died after 24 h of imaging. The change in the intensity of Zinquin

inside individual cells was not easy to track as the cells were alive and moving during imaging, therefore, the mean fluorescent intensity of Zinquin and PI was measured from different regions in the imaging field. The cells did not show any increase in intracellular zinc throughout the experiment (Figure 70, a). This confirms that the Zn^{2+} indicator did not fluoresce over time, in the absence of zinc. A video of intracellular dissolution of the targeted ZnO-HCV-RGD-GFP NPs by live MDA-MB-231 cells is attached (Video 4, MDA-MB-231 cells, ZnO-HCV-RGD-GFP NPs, Zinquin).

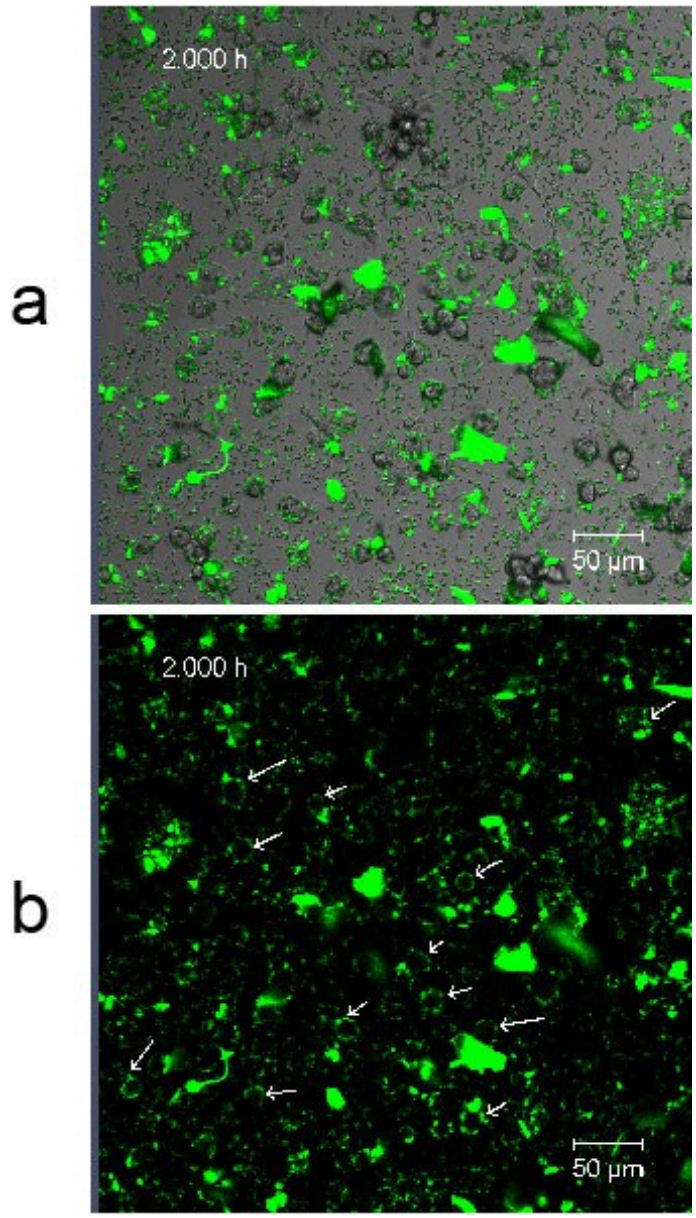

Figure 69: Confocal images of MDA-MB-231 cells showing binding of the ZnO-HCV-RGD-GFP NPs. (a) Bright field image of the MDA-MB-231 cells showing the bound ZnO-HCV-RGD-GFP NPs. (b) Green fluorescent channel image of ZnO-HCV-RGD-GFP NPs after 2 h of incubation with MDA-MB-231 cells. The targeted ZnO NPs were bound to the surface of the cells (white arrows in b).

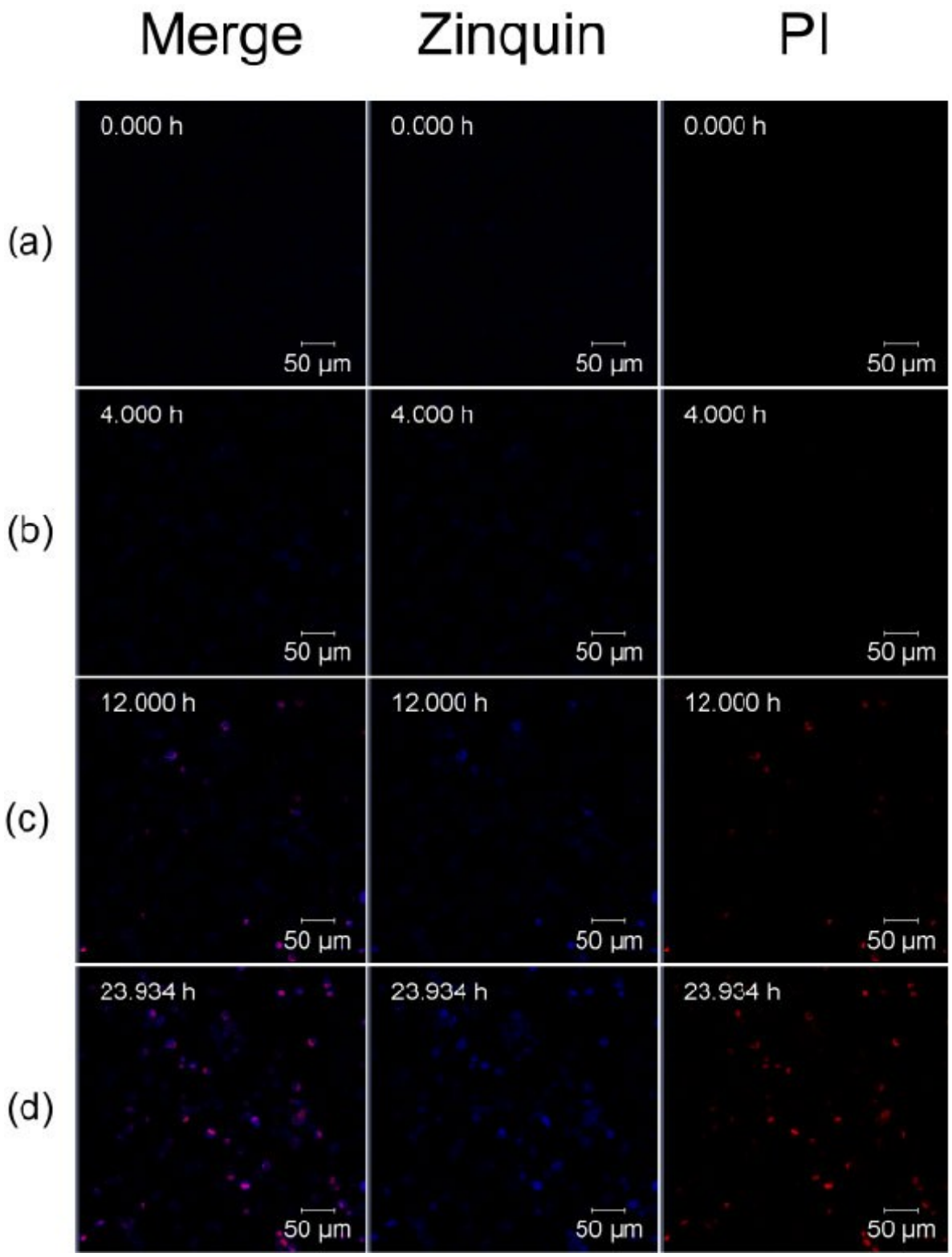

Figure 70: Confocal images showing dissolution of ZnO-HCV-RGD-GFP NPs after uptake by MDA-MB-231. The MDA-MB-231 cells were incubated with 150 µg/ml ZnO-HCV-RGD-GFP NPs, Zinquin (blue) was used as a cellular permeant Zn^{2+}-selective indicator, and confocal imaging was carried out for 24 h. PI (red) was used as a viability indicator. The ZnO-HCV-RGD-GFP NPs dissolved inside the cells over time and released Zn^{2+}, which was accompanied by the increase in the intensity of Zinquin (blue). Toxic levels of Zn^{2+} ions inside the cell resulted in loss of cell membrane integrity and cellular penetration of PI.

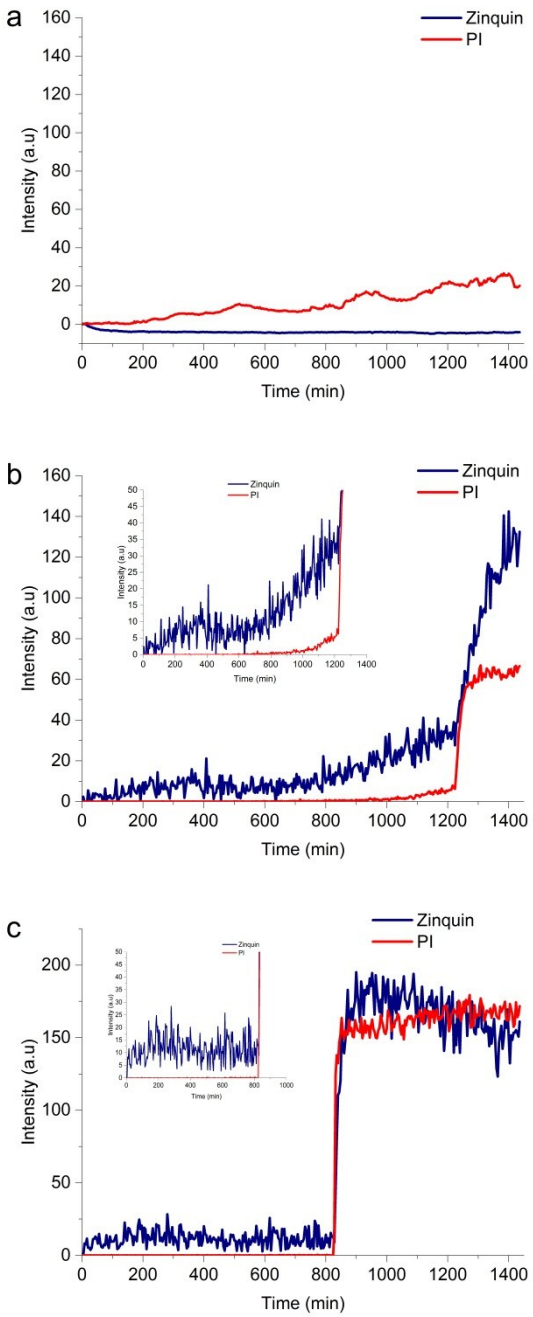

Figure 71: Intensity curves of Zinquin and PI in MDA-MB-231 cells after exposure to ZnO-HCV-RGD-GFP NPs. MDA-MB-231 cells were loaded with the cell-permeant Zn^{2+} indicator Zinquin-AM prior to incubation with (a) imaging buffer (nontreated control), (b, c) 150 µg/ml ZnO-HCV-RGD-GFP NPs. Zinquin fluoresces blue upon binding ionic zinc (Zn^{2+}). PI was included to stain the nuclei of dead cells (red). The insets in b and c are showing the gradual increase in FluoZin intensity over time. Images were acquired over a time course of 24 h. Fluorescent intensities were measured within a representative region of interest (ROI).

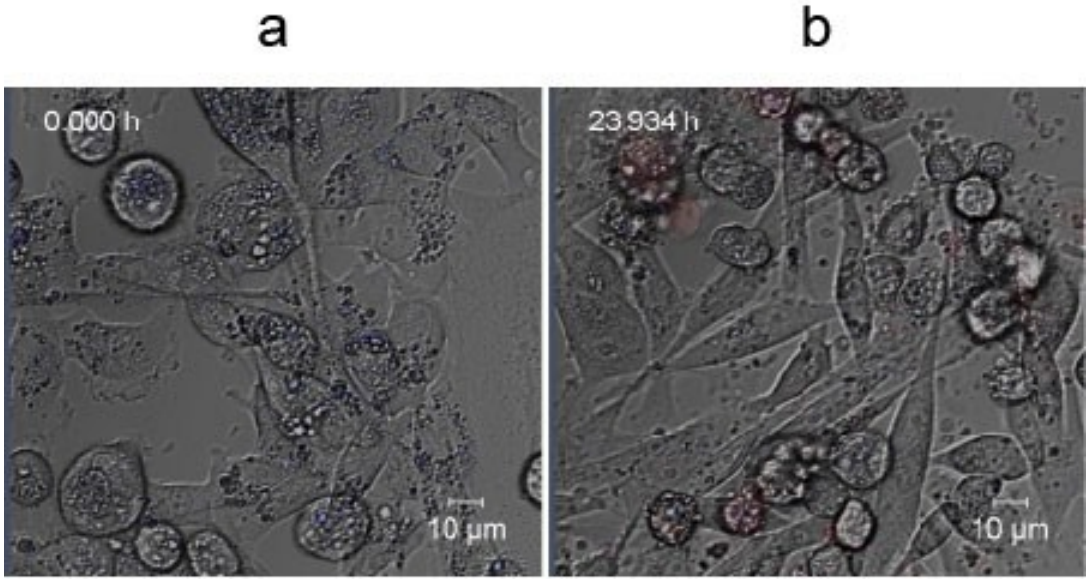

Figure 72: Confocal images of MDA-MB-231 cells incubated with HEPES confocal imaging buffer (pH 7.4) for 24 h showing the healthy morphology of the cells.

5.2.1.2 Uptake of ZnO-HCV-RGD-GFP nanoparticles into live MCF-7 cells

Binding and uptake of the ZnO-HCV-RGD-GFP NPs were also tracked over time in the ER+ and non-metastatic MCF-7 cells by 3D confocal microscopy. For this purpose, the cells were loaded with the live nuclei stain Hoechst 33342, and they were then incubated with the RGD-targeted ZnO NPs and images were acquired over a time period of 13 h. The red fluorescent viability dye PI was used to stain the nuclei of dead cells. Bright field imaging was used to view the changes in cell morphology and to track the uptake of the ZnO-HCV-RGD-GFP NPs.

The MCF-7 cells showed a lower expression of the integrin αvβ3 compared to the MDA-MB-231 cells (Figure 29). Therefore, the uptake of the targeted ZnO-HCV-RGD-GFP in the MDA-MB-231 cells was compared to that of the MCF-7 cells. As the MCF-7 cells showed almost 90% reduction in the viability after 3 h exposure to 100 µg/ml ZnO-HCV-RGD-GFP NPs using Alamar Blue assay (Figure 33), a lower dose of 75 µg/ml of the ZnO-HCV-RGD-GFP NPs was used for confocal microscopy. This dose was chosen in order to track the uptake of the targeted NPs before initiation of cellular death. The MCF-7 cells were exposed to 75 µg/ml ZnO NPs at 37°C for 13 h with images acquired at different Z-heights through the cell.

Before exposure to ZnO-HCV-RGD-GFP NPs, the MCF-7 cells had a healthy morphology and tended to grow in clusters (Figure 73, a). They were relatively consistent in size and shape in monolayer proliferation, and had big nuclei (Figure 73, a). All cells were viable as indicated by Hoechst stain of their nuclei and the absence of PI staining (Figure 73, a). Upon exposure to the ZnO-HCV-RGD-GFP NPs, and unlike the MDA-MB-231 cells, there was no obvious change in shape or shrinkage of the cell. On the contrary, the MCF-7 cells showed some swelling after 1 h exposure to the NPs (Figure 73, e). Extensions of large projections from the plasma membrane of the cells that extend into the matrix have developed (Figure 73, b (black arrows)). These projections surrounded the ZnO-HCV-RGD-GFP NPs and fused together so that the ZnO-HCV-RGD-GFP NPs has become completely engulfed (Figure 73, c-f). In contrast to the MDA-MB-231 cells, a lower binding of the ZnO-HCV-RGD-GFP NPs could be seen quantitatively for the MCF-7 cells. This is most probably due to the lower expression of the integrin αvβ3 on the surface of the cell membrane of the MCF-7 cells as shown in Figure 29.

After binding and uptake of the ZnO-HCV-RGD-GFP NPs by the MCF-7 cells, and like MDA-MB-231 cells, diffuse green fluorescence from the GFP could be observed inside the cells (Figure 73, f and Figure 74). This diffuse green fluorescence could be present due to dissolution of the ZnO-HCV-RGD-GFP NPs inside the highly acidic compartments of the lysosomes. Confocal microscope and orthogonal view of a stack of images of the MCF-7 cells showed that ZnO-HCV-RGD-GFP (white arrows) penetrated the cytoplasm of the MCF-7 cells after 81 min exposure (Figure 74).

After 4 h of incubation with the ZnO-HCV-RGD-GFP NPs, some MCF-7 cells started to die as indicated by the double staining of their nuclei, without obvious blebbing (Figure 75, a). After 5 h, however, more cells started to die and blebbing could be clearly observed with some cells after 10 h exposure (Figure 75, b-e (white arrows)). After blebbing, the MCF-7 cells lost their cell membrane integrity as indicated by the intracellular penetration of PI and the double staining of their nuclei (Figure 73, b-e). After 13 h of exposure to the ZnO-HCV-RGD-GFP NPs, 60% of the cells were dead (139/233 cells). A video that shows binding and uptake of the ZnO-HCV-RGD-GFP NPs by live MCF-7 cells and subsequent cell death is attached (Video 6, MCF-7, ZnO-HCV-RGD-GFP NPs, uptake).

Most of the control MCF-7 cells incubated with the HEPES confocal imaging buffer alone survived the laser power for the time of imaging (Figure 76). However, 11% (27/252 cells) of the cells did not withstand the laser and were dead at the end of imaging (Figure 76, b). A video of control MCF-7 cells is attached (Video 7, MCF-7, ZnO-HCV-RGD-GFP NPs, uptake).

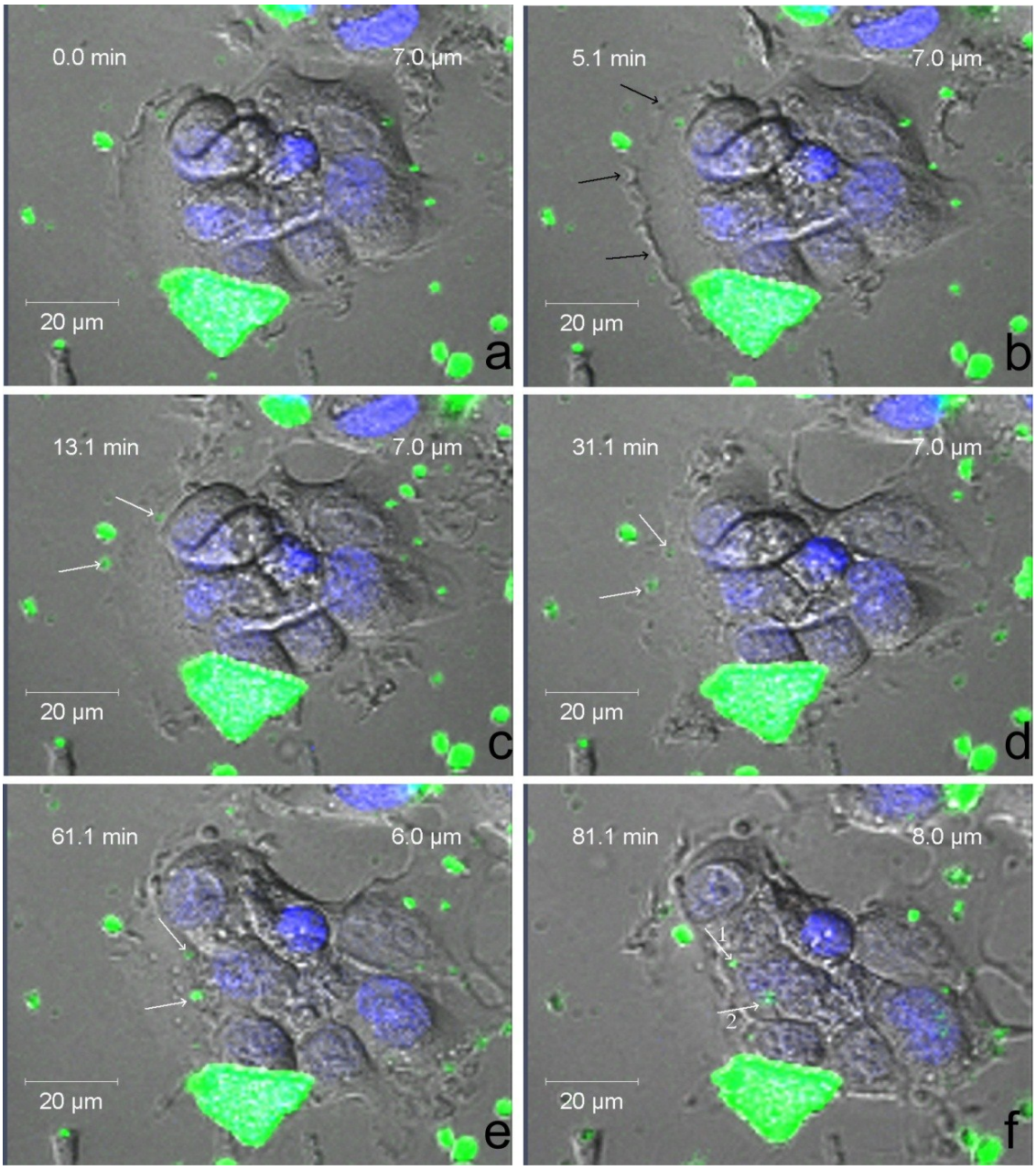

Figure 73: Confocal images showing uptake of 75 µg/ml ZnO-HCV-RGD-GFP NPs (white arrows) by MCF-7 cells at: (a-f) zero, 5, 13, 31, 61, and 81 min exposure, respectively. Cells developed extensions of large projections from the plasma membrane (black arrows) that extended into the cytoplasm to internalise the NPs. The orthogonal slice view through the ZnO-HCV-RGD-GFP NPs (white arrows 1 and 2) in image f is shown in Figure 74.

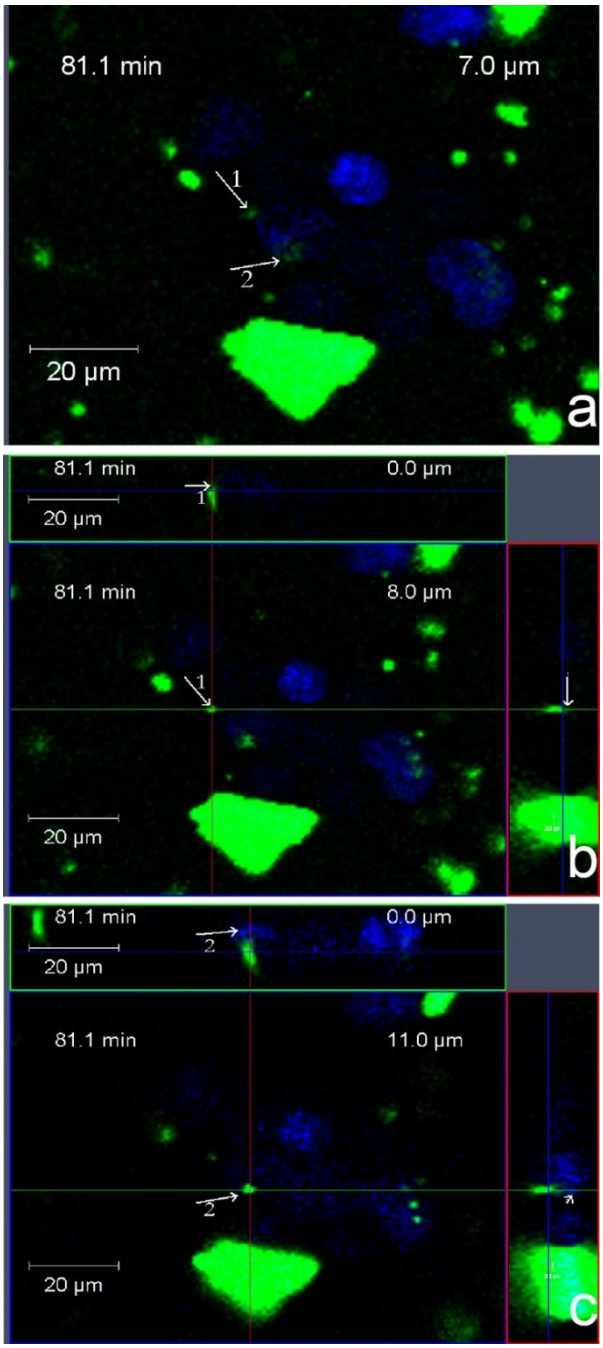

Figure 74: Confocal microscope image (a) and average projection through a stack of images (b, c) of ZnO-HCV-RGD-GFP NPs (1 and 2; respectively) penetrating the cytoplasm of MCF-7 cells after 81 min at 37°C (green=ZnO-HCV-RGD-GFP NPs, blue=nuclei, green line=XZ plane red line=YZ plane, blue line=XY). White arrows confirmed ZnO-HCV-RGD-GFP NPs presence inside the cells.

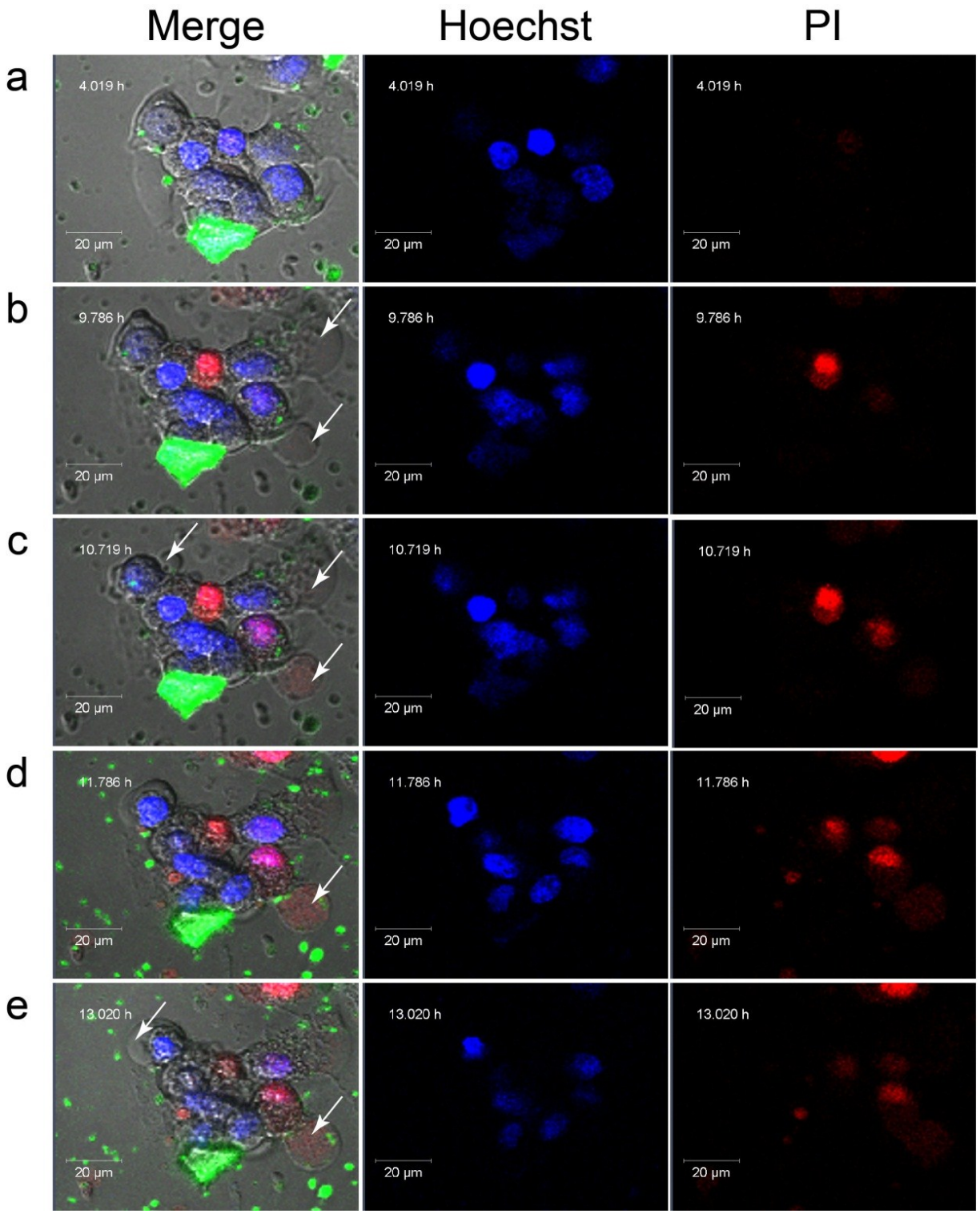

Figure 75: Confocal microscope images of MCF-7 after exposure to ZnO-HCV-RGD-GFP NPs (75 µg/ml) showing cell death. The cells lost their viability with time (image (a) to image (e)). Cells' death started with blebbing (white arrows) and PI (red) started to penetrate the cells due to a loss of cell membrane integrity. Hoechst 33342 (blue) was used to stain live cells' nuclei blue.

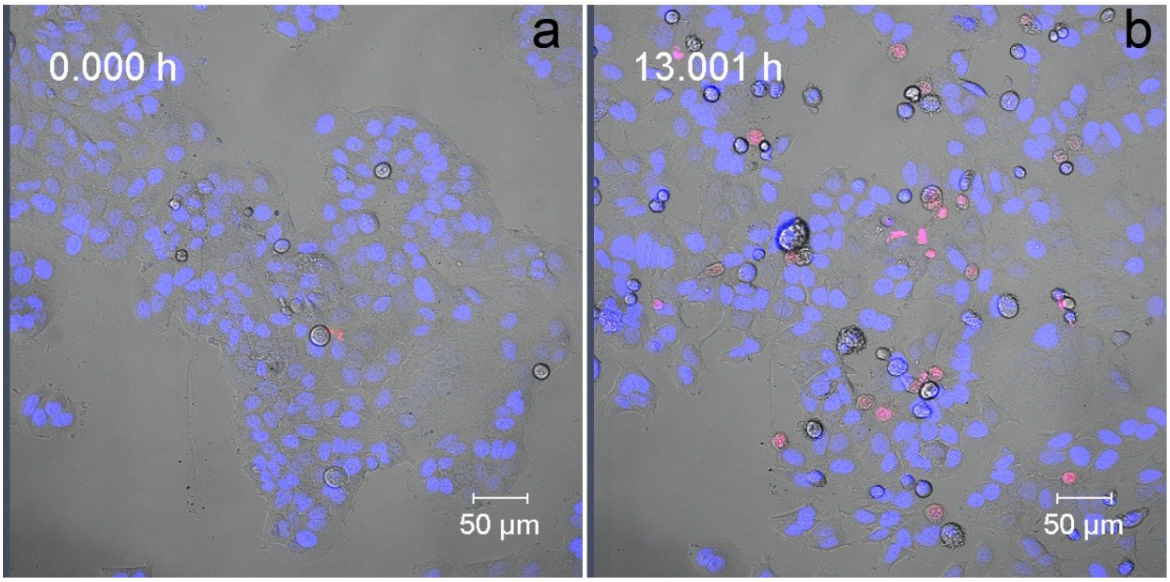

Figure 76: Confocal microscope images of control untreated MCF-7 incubated with HEPES confocal imaging buffer. (a) MCF-7 cells at 0 h exposure, (b) MCF-7 cells after 13 h of imaging showing that 11% of the cells (27/252) lost their viability due to laser damage of the cells. Hoechst 33342 (blue) was used to stain live cells nuclei blue. PI (red) was used as a viability indicator.

5.2.1.3 Uptake of ZnO-HCV-RGD-GFP nanoparticles into live MCF-10-2A cells

The MCF10-2A cells are healthy human breast cells. These cells are chosen to test the selectivity and differences in cellular responses of the ZnO-HCV-RGD-GFP NPs compared to breast cancer cells. Before exposure to ZnO-HCV-RGD-GFP NPs, the MCF-10-2A cells had a healthy morphology and tended to grow in clusters (Figure 77, a). The cells were relatively consistent in size and shape in monolayer proliferation, and had big nuclei. All cells were viable as indicated by Hoechst stain of their nuclei and the absence of PI staining (Figure 77, a). Upon exposure, the ZnO-HCV-RGD-GFP NPs showed low or no binding to the surface of the MCF-10-2A cells (Figure 77, b). This is probably due to the fact that they lack the integrin αvβ3 receptors on their surface, as has been already shown (Figure 29). However, extensions from the cell membrane of some cells were developed (Figure 77, c-d, arrows) and uptake of some of the ZnO-HCV-RGD-GFP NPs could be observed. The cells were alive after 2 h exposure to 150 µg/ml ZnO NPs (Figure 77, d), and this coincides with the viability assays (3h exposure to the ZnO-HCV-RGD-GFP NPs, Figure 34).

The control MCF-10-2A survived 2 h of imaging before they started to die in the confocal microscope (Figure 78). After 2 h imaging, 10% of the MCF-10-2A cells (29/277) lost

their viability due to laser damage of the cells (Figure 78, b) Therefore, comparisons to the MCF-7 and MDA-MB-231 cells using confocal microscopy were not feasible.

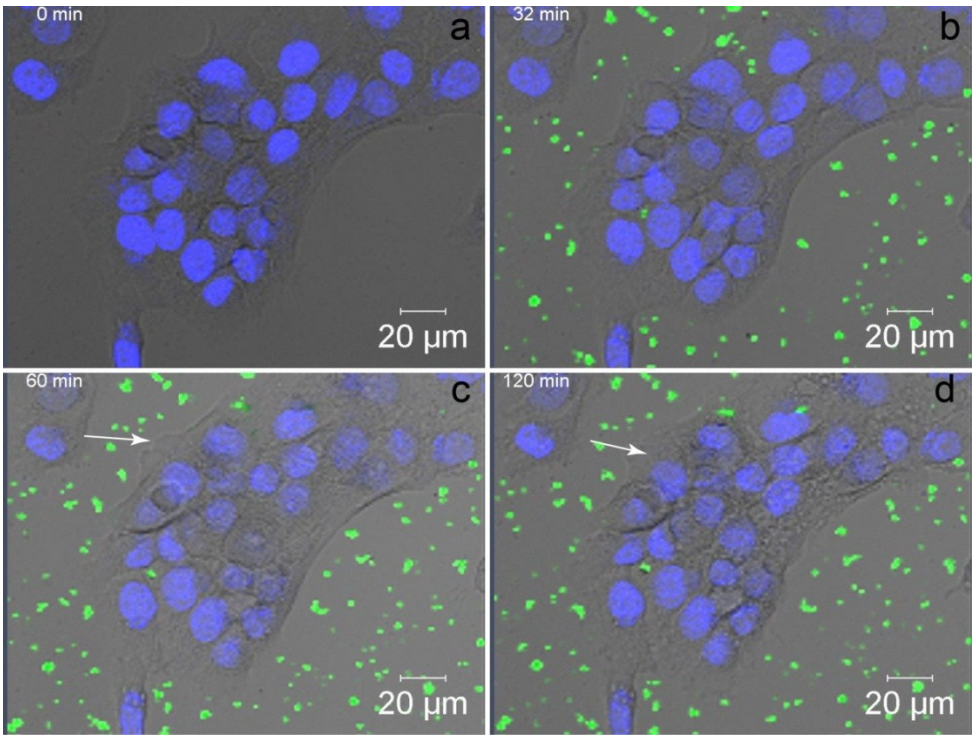

Figure 77: Confocal microscope images of MCF-10-2A after exposure to 150 µg/ml ZnO-HCV-RGD-GFP NPs for 2 h. (a) Zero time exposure to ZnO-HCV-RGD-GFP NPs. (b) After 32 min exposure cells started shrinking. (c, d) After 60 and 120 min exposure, cells started to develop extensions (white arrows) from the plasma membrane. Hoechst (blue) was used to stain live cells' nuclei blue.

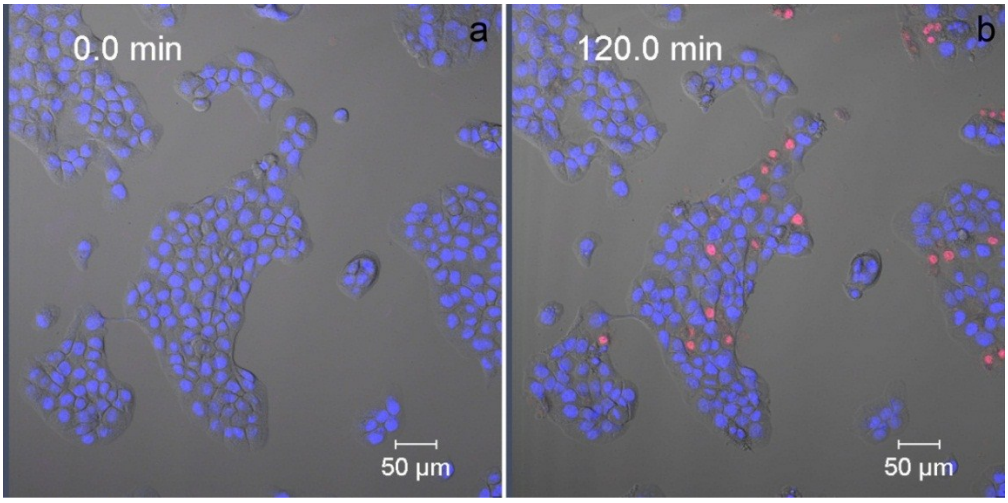

Figure 78: Confocal microscope images of control untreated MCF-10-2A cells incubated with HEPES confocal imaging buffer for 120 min. (a) The MCF-10-2A cells at zero time of imaging. (b) The MCF-10-2A cells after 2 h of imaging showing that 10% of the cells (29/277) lost their viability due to laser damage of the cells. Hoechst (blue) was used to stain live cells' nuclei blue. PI was used as a viability indicator.

5.2.1.4 Correlation of uptake and dissolution of bare ZnO nanoparticles by live MDA-MB-231 cells

The aim of this section was to compare binding, uptake and dissolution of the bare ZnO NPs, as well as its effect on the MDA-MB-231 cells viability to that of the targeted ZnO-HCV-RGD-GFP NPs. The MDA-MB-231 cells were used here because they expressed a higher percentage of the integrin αvβ3 receptors and therefore the effect of targeting can be investigated. The MDA-MB-231 cells were loaded with the cellular permeant Zn^{2+}-selective indicator, FluoZin3-AM, and were incubated with the bare ZnO NPs and images were acquired over a time period of 16 h. The red fluorescent viability dye PI was used to stain the nuclei of dead cells. Bright field imaging was used to view the changes in cell morphology and to track the uptake of the NPs. The results are summarised in the following sections.

1. Changes in cell morphology upon exposure to the bare ZnO NPs

As observed in the previous sections, the MDA-MB-231 cells displayed an elongated shape and adhered to the culture plates before exposure to the bare ZnO NPs (Figure 79, a). After exposure to 150 µg/ml of the bare ZnO NPs, the MDA-MB-231 cells immediately changed their morphology and they became round (Figure 79, b). After 2 h exposure, the cells shrank in size, and stopped moving (Figure 79, c). This alteration in morphology could probably again arise due to the release of soluble Zn^{2+} in the HEPES confocal imaging buffer. As illustrated in the ICP dissolution experiment (Figure 17, a), the bare ZnO NPs dispersions released about 4 µg/ml of ionic zinc (Zn^{2+}) in the HEPES confocal imaging buffer at pH 7.4.

The morphology of the untreated control cells, however, remained unaltered up to 16 h of imaging under the same conditions (Figure 80). All these cellular responses in the MDA-MB-231 cells to the bare ZnO NPs were comparable to those observed with the targeted ZnO NPs.

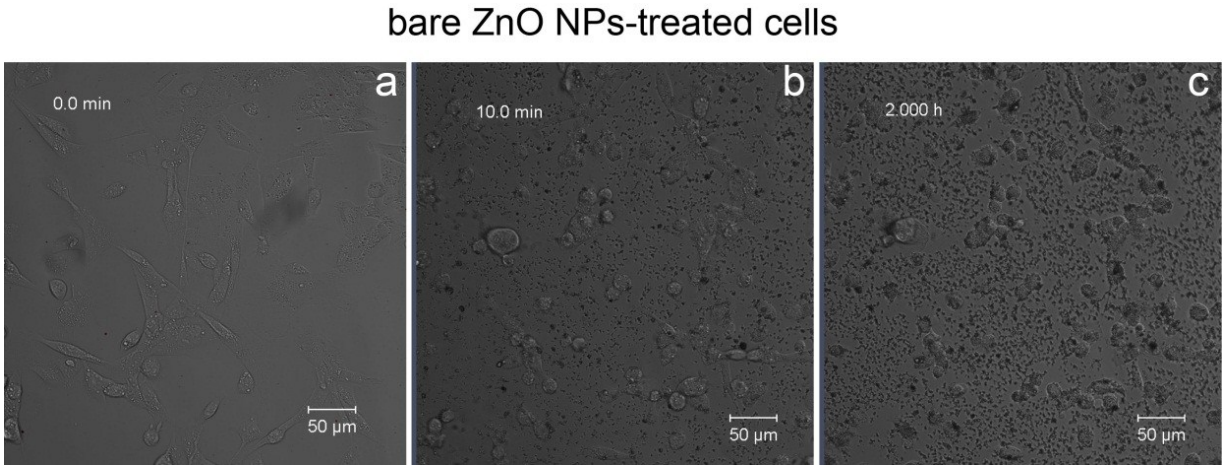

Figure 79: Bright-field confocal images of MDA-MB-231 cells exposed to the bare ZnO NPs. MDA-MB-231 cells were exposed to 150 µg/ml bare ZnO NPs for 2 h. The cells had altered morphology to control cells after exposure to 150 µg/ml bare ZnO NPs.

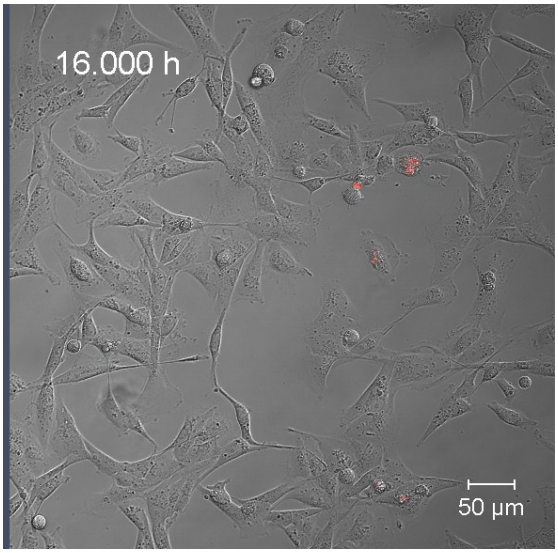

Figure 80: Bright-field confocal image of control MDA-MB-231 cells in HEPES confocal imaging buffer after 16 h of imaging. Cells were elongated and adhered to the plate.

2. Uptake and dissolution of the bare ZnO NPs by MDA-MB-231 cells

Uptake and dissolution of the bare ZnO NPs over time was tracked in the MDA-MB-231 cells (Figure 81). After the immediate loss of shape (Figure 81, a, arrow head) upon exposure to ZnO NPs, extracellular extensions of large projections from the plasma membrane of the cells that extend into the matrix had formed (Figure 81, b and c, white arrows). These projections surrounded the bare ZnO NPs and fused together so that the NPs aggregates were completely surrounded by the cells (Figure 81, c). The process of particle internalisation was accompanied by an increase in the intracellular zinc ions indicated by an

increase in the intensity of FluoZin green fluoresce (Figure 81, d). Blebbing (Figure 81, d, black arrow) and rupture of cell membrane, as indicated by penetration of the cell impermeant PI into the cell (Figure 81, f), were observed. A video that shows uptake and dissolution of the bare ZnO NPs by live MDA-MB-231 cells, is attached (Video 8, MDA-MB-231 cells, bare ZnO NPs, uptake, FluoZin).

Incubation with 150 µg/ml ZnO NPs lead to a steep increase in the FluoZin fluorescence inside the cells with time, which indicated rapid dissolution of the bare ZnO NPs inside the cells and a resulting increase in the intracellular levels of Zn^{2+} (Figure 81). In order to measure the amount of intracellular ionic zinc Zn^{2+} released and cell membrane integrity of the MDA-MB-231 exposed to the bare ZnO NPs, the fluorescent intensities of FluoZin and PI was measured for 17 cells in the imaging frame over 16 h exposure. The intensities of the ROI selected from the cells could not be averaged as the cells showed a heterogeneous response to the particles. However, representative ROIs are shown in Figure 82 (plot b and c). After exposure to the bare ZnO NPs, the MDA-MB-231 cells in the field of view reacted quite differently regarding the release of ionic zinc and subsequent cell death. This could indicate differences in the resistance of the cells' population to Zn^{2+} that requires further investigation (will be discussed in section 5.2.3). 41% of the MDA-MB-231 cells (7/ 17) required about 1-1.5 h to reach the maximum concentration of ionic zinc (Zn^{2+}) in the cytoplasm. In contrast, 59% cells (10/17) needed almost 3-4 h to achieve the highest levels of intracellular Zn^{2+}. Once the concentration of Zn^{2+} had reached a maximum inside the cell (the peak value of FluoZin), some cells died immediately (penetration of PI staining inside the cells). This correlation was monitored by increasing intracellular levels of PI and a drop in FluoZin dye (Figure 82, b), indicating a loss of plasma membrane integrity. Figure 82 C, shows other cell that survived longer time with the highest levels of Zn^{2+} (plateau of FluoZin), and could resist a high intracellular concentration of Zn^{2+} before they started to die. Figure 17 showed that the solubility of the bare ZnO NPs in the HEPES confocal imaging buffer at pH 7.4 was < 9 µg/ml Zn^{2+}. Therefore, any rise in intracellular Zn^{2+} upon exposure to the bare ZnO NPs must be due to the acidic dissolution of the ZnO NPs inside the lysosomes and the local release of toxic Zn^{2+} ions. A video that shows uptake and dissolution of the bare ZnO NPs by the MDA-MB-231 cells is attached (Video 9, MDA-MB-231 cells, bare ZnO NPs, dissolution, FluoZin).

In the untreated control cell sample (Figure 82, a), the MDA-MB-231 cells incubated with the HEPES confocal imaging buffer did not show any increase in FluoZin-3 fluorescence over the time of imaging. This confirms that the Zn^{2+} indicator did not fluoresce over time in the absence of zinc. Most cells did not suffer the fatal laser irradiation damage. However, 5% (7/140) of the cells were dead at the end of the experiment (Figure 80). A video of control MDA-MB-231 cells is attached (Video 10, control MDA-MB-231 cells, bare ZnO NPs, dissolution, FluoZin).

The rise of intracellular levels of Zn^{2+} and its effect on the cell viability in the MDA-MB-231 cells after exposure to $ZnCl_2$ was compared to those of the bare ZnO NPs. $ZnCl_2$ was used in a concentration of 250 µg/ml. This concentration of $ZnCl_2$ was chosen as it has the same Zn^{2+} concentration of 150 µg/ml ZnO. The same heterogeneity in the response of the MDA-MB-231 cells was observed after exposure to $ZnCl_2$. Incubation of the cells with $ZnCl_2$ resulted in an increase of FluoZin fluorescence (Figure 82, d). Moreover, the distribution of Zn^{2+} was more diffuse inside the cytoplasm, indicating a less local rise in intracellular Zn^{2+} concentrations. Muller *et al.* showed the same effect of $ZnCl_2$ in human monocyte derived macrophages [10].

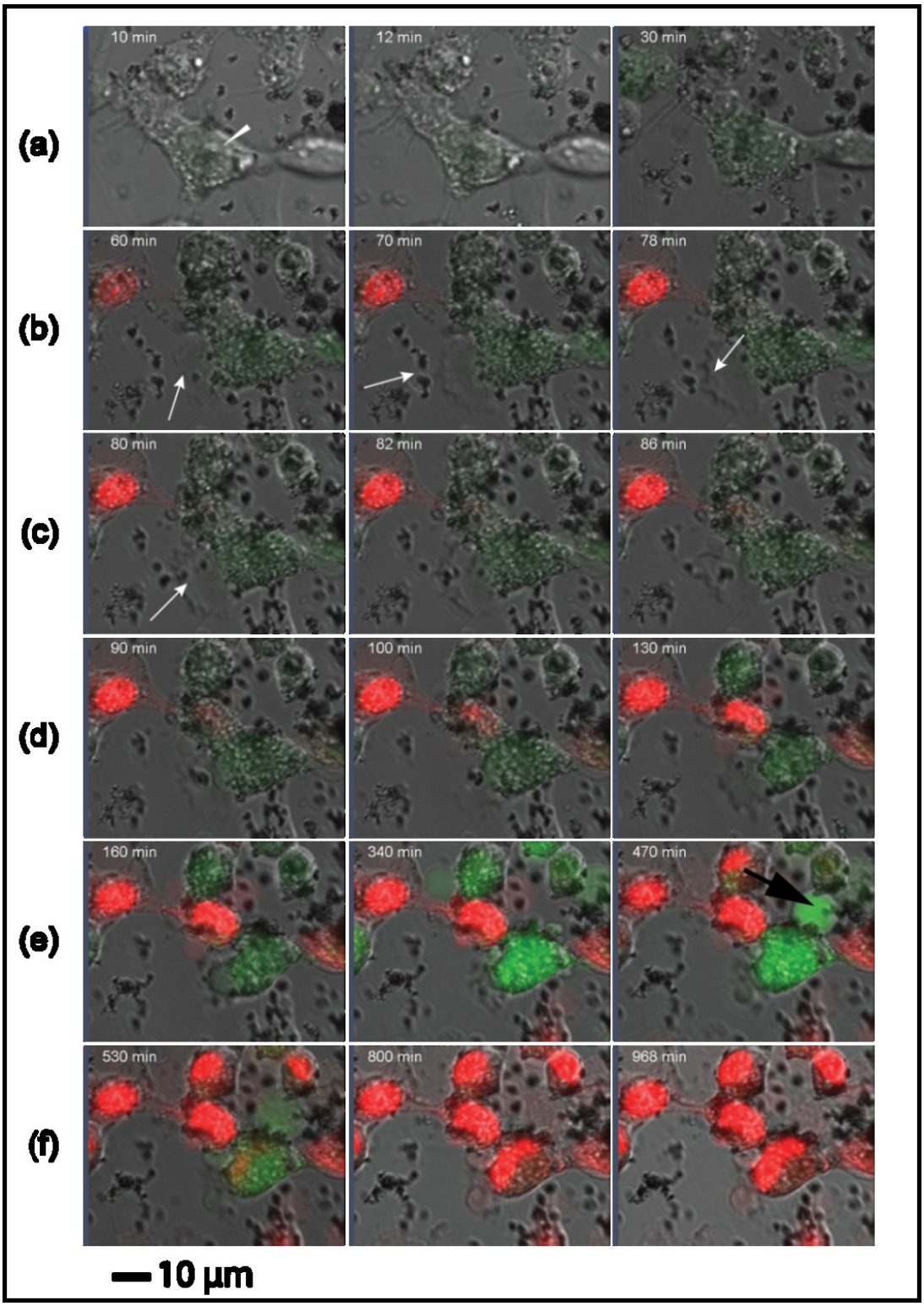

Figure 81: Confocal fluorescence and bright-field images of MDA-MB-231 cells showing internalization and dissolution of bare ZnO NPs. The MDA-MB-231 cells were loaded with the cell-permeant Zn^{2+} indicator FluoZin3-AM (green fluorescent) prior to incubation with 150 µg/ml ZnO for 16 h. (a) The MDA-MB-231 cells (white arrow head) lost its spindle shape and became round upon exposure to the bare ZnO NPs. (b-c) Uptake of the bare ZnO NPs (white arrows) by extracellular extensions of the plasma membrane. (e) Blebbing of the cells (black arrow), (f) Death of the cell and loss of cell membrane integrity. (a-f) Dissolution of the bare ZnO NPs inside the cells.

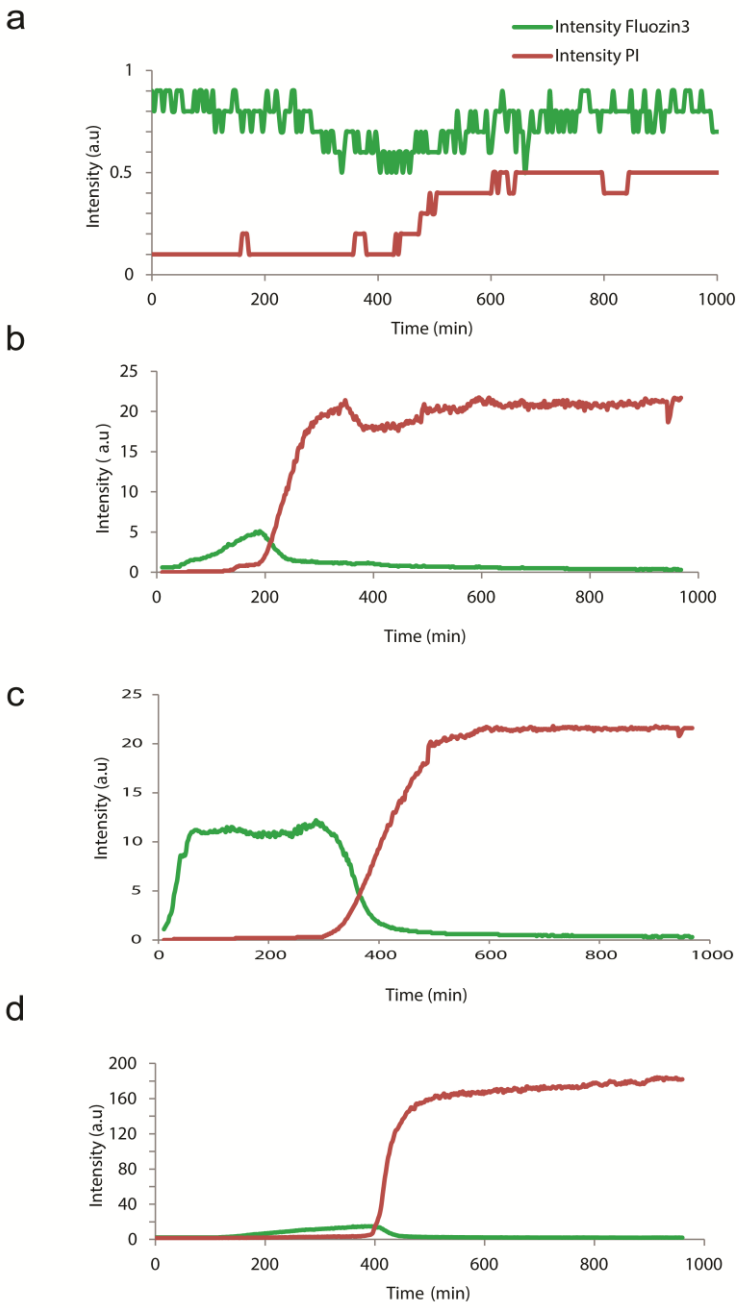

Figure 82: Intensity curves of FluoZin and PI in MDA-MB-231 cells after exposure to the bare ZnO NPs showing increase in intracellular Zn^{2+} and subsequent cell death. The MDA-MB-231 cells were loaded with the cell-permeant Zn^{2+} indicator FluoZin3-AM prior to incubation with (a) imaging buffer (NA control), (b, c) 150 µg/ml bare ZnO NPs, or (d) 250 µg/ml $ZnCl_2$ (with equivalent Zn^{2+} concentration from 150 µg/ml ZnO). FluoZin fluoresces green upon binding ionic zinc (Zn^{2+}). PI was included to stain the nuclei of dead cells (red). Images were acquired over a time course of 16 h.

3. Loss of cellular viability of the MDA-MB-231 cells after exposure to the bare ZnO NPs and $ZnCl_2$

The MDA-MB-231 cells lost their viability upon exposure to the bare ZnO NPs (150 μg/ml). There was a lot of heterogeneity in the resistance to the bare ZnO NPs within the cell population. Figure 83 shows the rise of intracellular Zn^{2+} and subsequent cell death of the MDA-MB-231 cells after 4 and 16 h exposure to the bare ZnO NPs and $ZnCl_2$. The MDA-MB-231 cells showed 54% (62/115 cells) and 100% (115/115) death after 4 and 16 h incubation with the bare ZnO NPs, respectively (Figure 83, A and B). The difference in the response of the MDA-MB-231 cells to the bare ZnO NPs could be due to the different local concentrations of the particles around the cells and their different agglomeration states or to the different sensitivity of the cells to ionic zinc.

After exposure of the MDA-MB-231 cells to $ZnCl_2$, 21 % of the cells (48/230) in the imaging view were dead after 4 h, while 90 % of the cells (207/230) were dead after 16 h of exposure (Figure 83, C and D). The differences in the cellular responses of the MDA-MB-231 cells to the ZnO and $ZnCl_2$ could be due to different mechanism of cytotoxicity. Eukaryotic cells have a remarkable ability to regulate their levels of intracellular zinc using several pathways [192]. Although cells are exposed to micromolar ranges of free zinc, the intracellular levels of free zinc that regulate the transcription of zinc influx, efflux or sequestration machinery are in the femtomolar range. The intracellular zinc homeostasis is maintained by several proteins, including the ZRTIRT-like protein (ZIP) family zinc transporters, zinc transporter (ZnT) family zinc transporters and zinc-sequestering metallothioneins [193-196]. While the released Zn^{2+} from $ZnCl_2$, which is taken up by Zn-receptors expressed on the surface of the cell membrane [197], is the cause of cytotoxicity, both the ZnO NPs and the intracellularly released Zn2+ could be the cause of toxicity after exposure to the bare ZnO NPs.

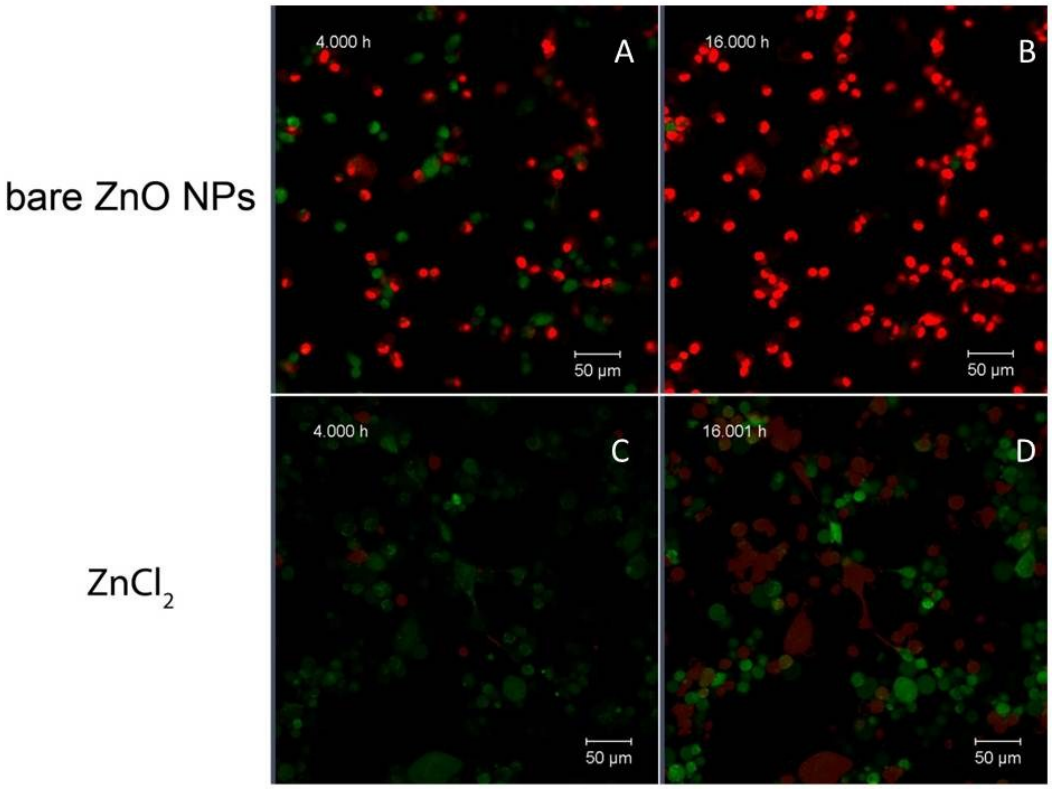

Figure 83: Confocal images of MDA-MB-231 cells showing rise of intracellular Zn^{2+} and subsequent cell death after exposure to (A and B) the bare ZnO NPs and (C and D) $ZnCl_2$. The MDA-MB-231 cells were loaded with the cell-permeant Zn^{2+} indicator FluoZin3-AM prior to incubation with 150 µg/ml of bare ZnO NPs or equivalent zinc ions concentration from $ZnCl_2$. Flouzin3 fluoresce green upon binding Zn^{2+}. PI was included to stain the nuclei of dead cells.

5.2.2 Binding and uptake of ZnO nanoparticles to breast cancer cells by electron microscopy

5.2.2.1 SEM analysis of binding of bare ZnO nanoparticles to MDA-MB-231 cells

To study the interaction of the particles with the plasma membrane of the MDA-MB-231 cells SEM and energy-dispersive X-ray spectroscopy (EDX) analysis were performed. Cells were incubated with 30 µg/ml of the bare ZnO NPs for 4 h, or cultured in the absence of the bare ZnO NPs for 4 h. After exposure to the bare ZnO NPs, the cells were fixed immediately to minimize any artefactal dissolution of the ZnO NPs during processing [10]. High resolution images of the MDA-MB-231 cells were taken at 2 keV using secondary electron (SE) detector (Figure 84). Large aggregate of ZnO NPs (1.1 µm) were observed on the surface of the MDA-MB-231 cells which appeared to be in the process of uptake (Figure 84, a). A more striking indication of the ZnO NPs uptake by the cells can be observed on the surface of the cells (indicated by arrows in Figure 84, b). The samples were then screened at 20 keV using the

back scattered electron (BSE) detector to locate areas with high atomic number (Z), and an EDX spectrum was acquired from those areas at 20 keV. Many regions with high atomic number (*Z*) were found in the BSE SEM images of the bare ZnO NPs-treated cells. The EDX spectra from treated cells clearly showed high intensity zinc peaks at 1.035, 8.639 and 9.572 keV from L, K-shells respectively (Figure 85).

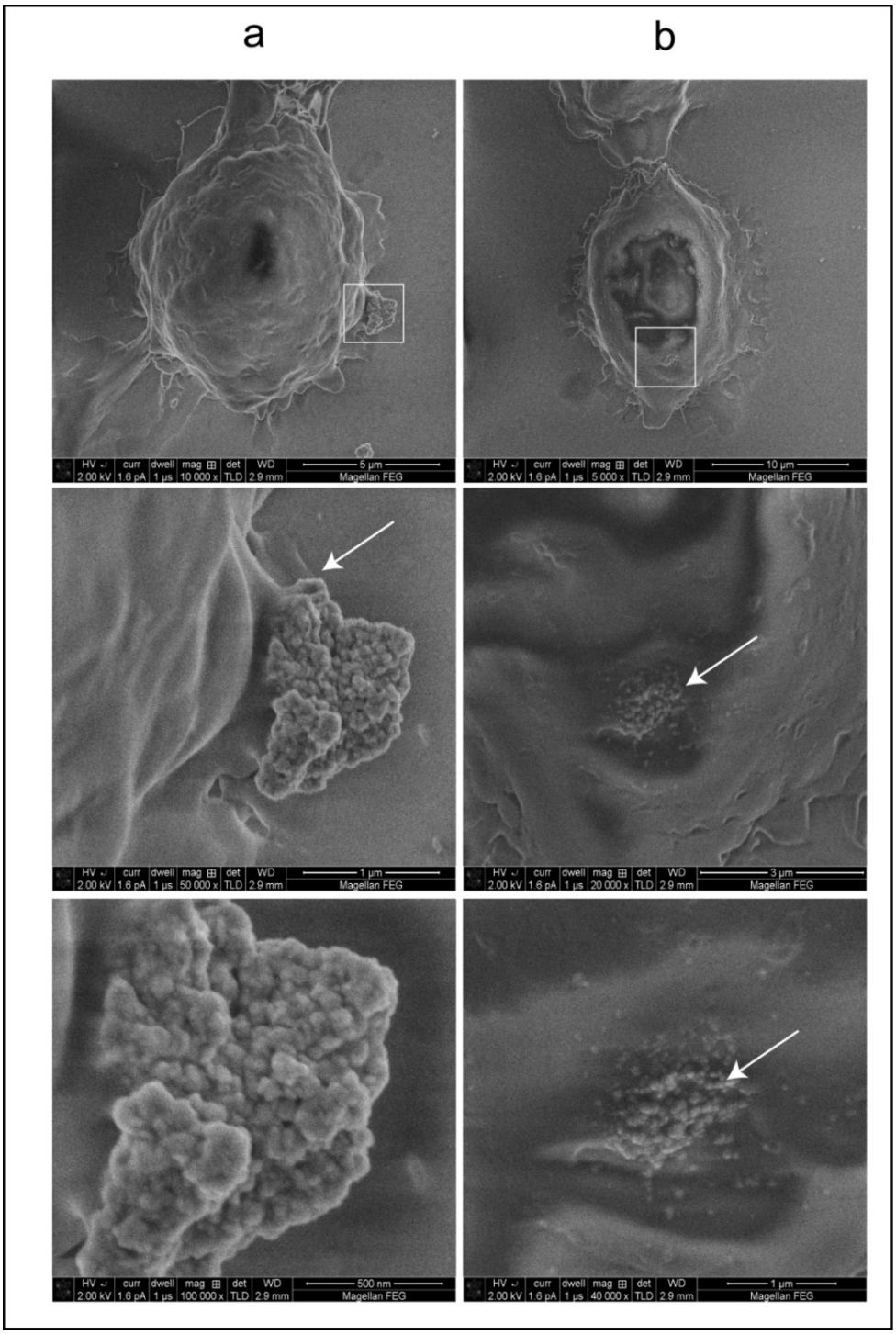

Figure 84: SEM images of MDA-MB-231 exposed to 150 µg/ml of the bare ZnO NPs for 4 h. Images show cells at increasing magnifications from the upper to the lower panels with ZnO NPs (arrows) bound to their surface (a) aggregates of ZnO NPs on the periphery of the cell and (b) ZnO NPs on the top of the cell.

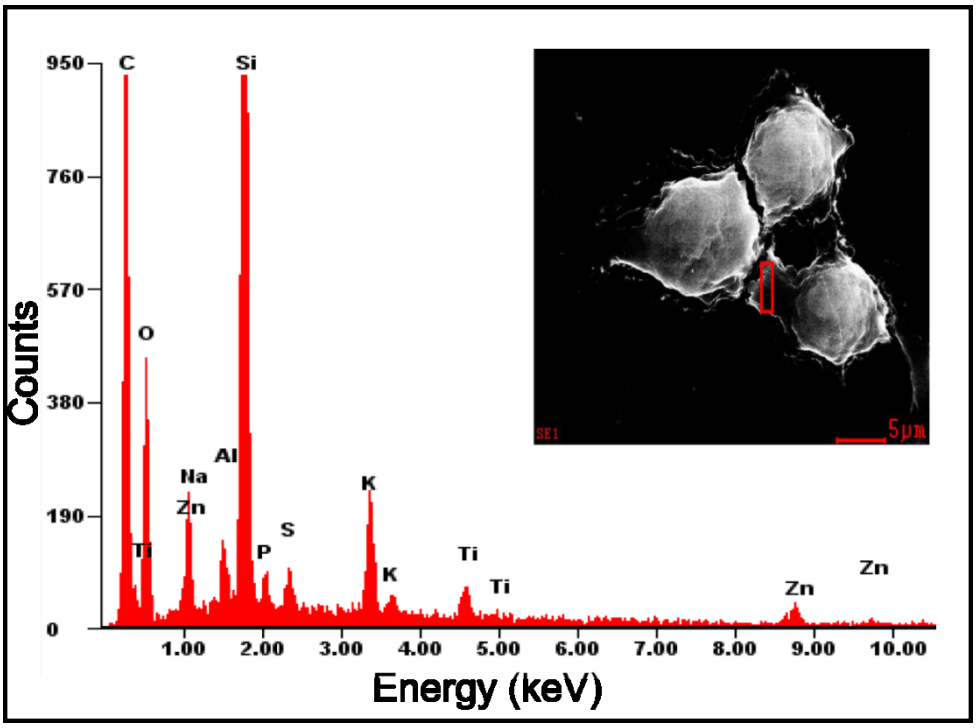

Figure 85: EDX spectra taken from the red box in the inset in the SE image of bare ZnO treated MDA-MB-231 cells.

5.2.2.2 TEM analysis of uptake of ZnO nanoparticles by breast cancer cell lines

5.2.2.2.1 TEM analysis of uptake of the bare ZnO nanoparticles by MCF-7 and MDA-MB-231 cells

To confirm the confocal microscopy findings of binding and uptake of the bare ZnO NPs, electron microscopy imaging and analysis of exactly the same cells imaged in the confocal microscopy was used. Electron microscopy was also used to study how the ultrastructure of the cells was altered by the ZnO NPs to produce clues about the mode of cell death.

5.2.2.2.1.1 TEM of MDA-MB-231 cells exposed to the bare ZnO nanoparticles

The MDA-MB-231 cells were exposed to a 20 µg/ml bare ZnO NPs for 6 and 24 h. Black NPs suggestive of ZnO NPs were observed on the surface of the cells after 6 h of exposure (Figure 86, A, black arrow). EDX spectra taken from the particles confirmed the presence of Zn L and K peaks at 1.011 and 8.615 keV, respectively (Figure 86, B; black arrow).

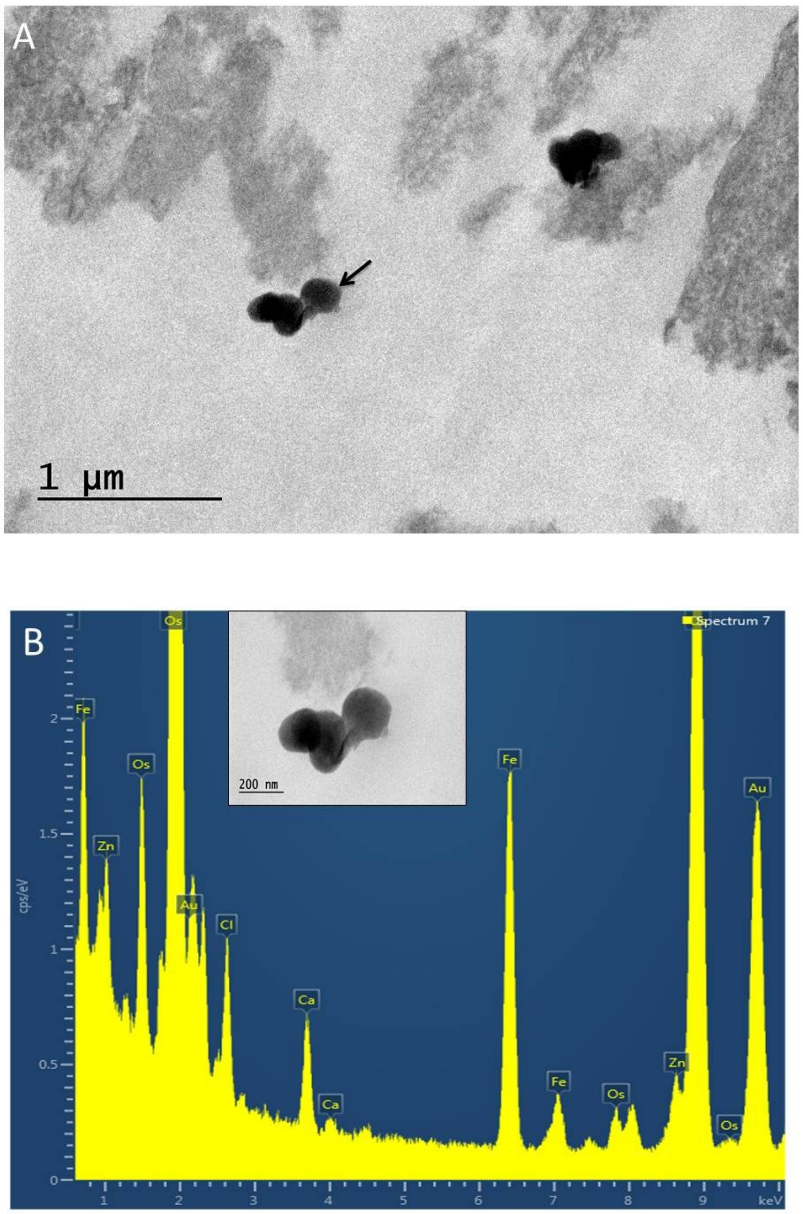

Figure 86: (A) BF TEM image of MDA-MB-231 cells exposed to 20 µg/ml bare ZnO NPs for 6 h showing ZnO NPs on the surface of the cells, (B) EDX spectra taken from the particles in the inset image and labelled with an arrow in (A) showing Zn L and K peaks at 1.011 and 8.615 keV, respectively. JEM 2100F operated at 300 kV was used to image the cells on a gold grid.

After 24 h exposure of the MDA-MB-231 cells to the bare ZnO NPs, the organisation of the cell was almost completely lost and the damage involves essentially all the subcellular structures (Figure 87). Irregular clumping of chromatin (Figure 87, black arrow), formation of small vacuoles inside the cells (Figure 87, white arrows), most likely, they are dilated vesicular endoplasmic reticulum or swollen and empty mitochondria [198]. Similar effects of Zn^{2+} were reported in literature; Zn^{2+} was reported to cause loss in integrity

of mitochondrial membranes, rupturing of plasma and nuclear membranes, separation of nuclear components, fragmentation of endoplasmic reticulum, and extensive autophagic vacuolization in hepatocytes [199].

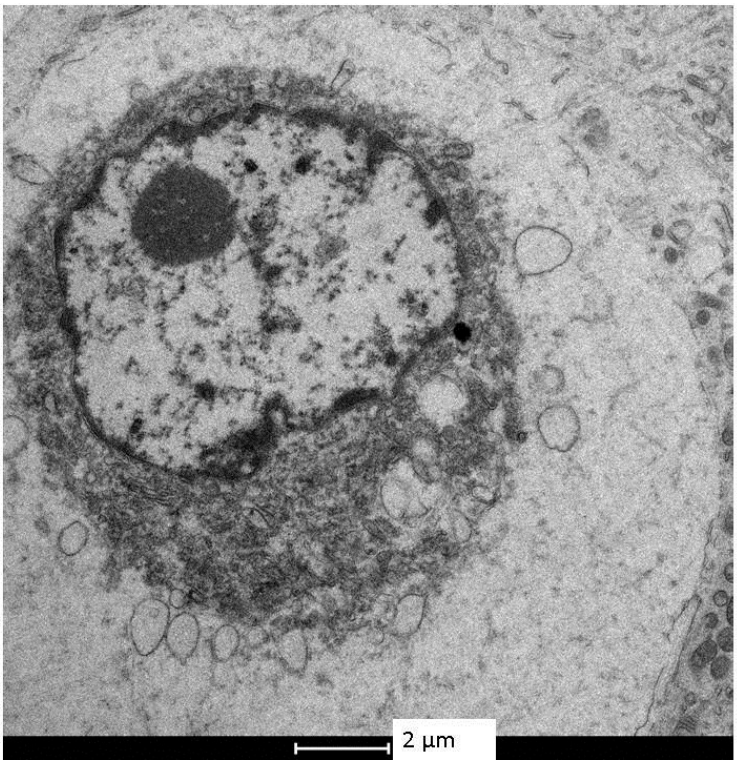

Figure 87: BF TEM image of MDA-MB-231 cells showing morphology indicative of late apoptosis after 24 h exposure to 20 µg/ml bare ZnO NPs. The organisation of the tumour cell is almost completely lost and the damage involves essentially all the subcellular structures. Irregular clumping of chromatin (black arrow). Small vacuoles formed inside the cells (white arrows), most likely, they are dilated endoplasmic reticulum. The cellular organelles were also disintegrated.

5.2.2.2.1.2 TEM of MCF-7 cells exposed to bare ZnO nanoparticles

Figure 88 shows black NPs, suggestive of ZnO NPs, inside and on the surface of the MCF-7 cells exposed to a 20 µg/ml bare ZnO NPs after 6 h of exposure. The presence of the ZnO NPs extracellularly is an indication that the particles are not dissolved outside the cells and any toxic effects are due to their intracellular dissolution and the release of Zn^{2+}.

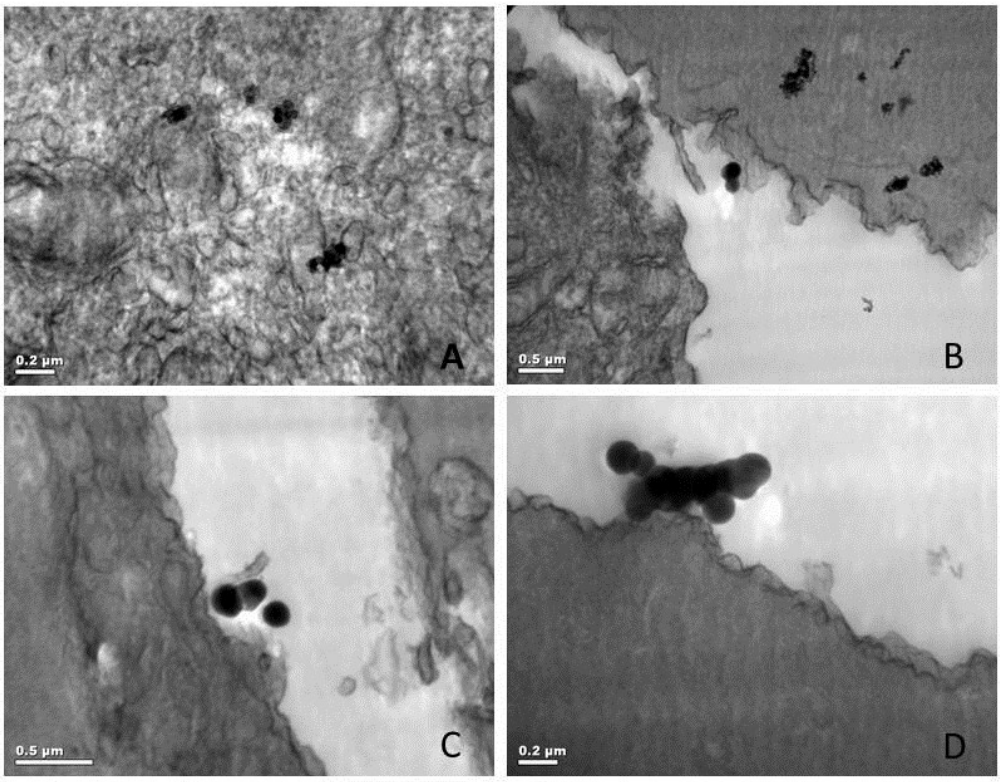

Figure 88: BF TEM images of MCF-7 cells exposed to 20 µg/ml bare ZnO NPs for 6 h showing (A) ZnO NPs inside the cells, (B) ZnO NPs inside and on the surface of the cell. (C, D) ZnO NPs on the cell membrane of the cells.

After 24 h exposure of the MDA-MB-231 cells to the bare ZnO NPs, mitochondria was swollen with less cristae (Figure 89, white arrows) compared to the untreated control (Figure 90, white arrows). Black NPs suggestive of ZnO were observed on the cell membrane and inside the MCF-7 cells after 24 h exposure to the ZnO NPs (Figure 91). The presence of the ZnO NPs extracellularly after 24 h of exposure is an indication that the NPs are not dissolved outside the cells and any toxic effects are due to their intracellular dissolution and the release of Zn^{2+}.

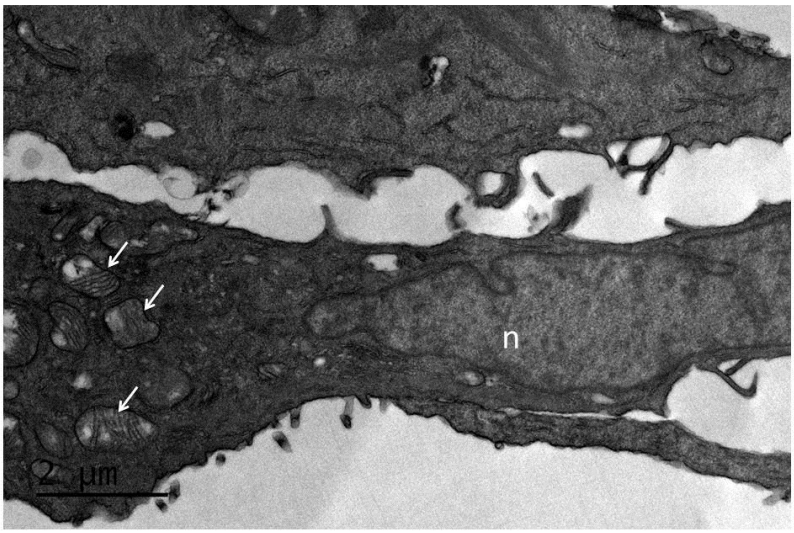

Figure 89: TEM image of MCF-7 cells exposed to 20 µg/ml ZnO NPs for 24 h showing swelling of the mitochondria (white arrow) with reduced cristae. n= nucleus.

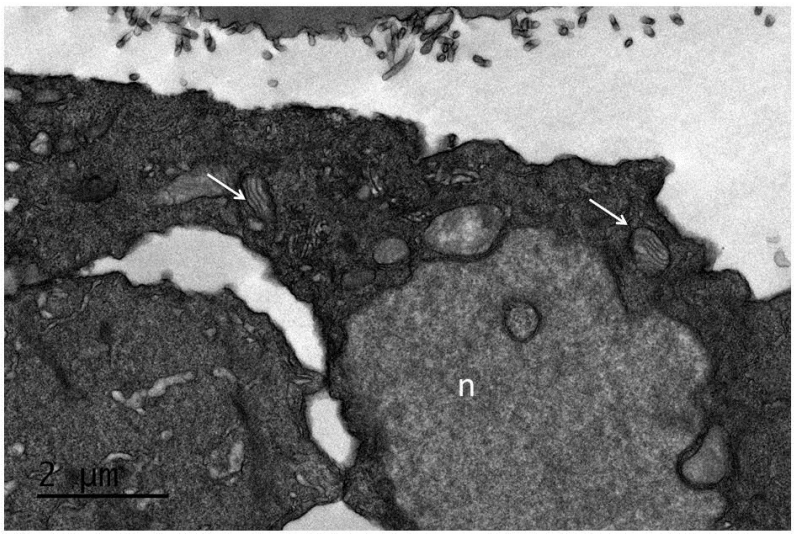

Figure 90: TEM image of control MCF-7 cells showing normal mitochondria (white arrow). n= nucleus.

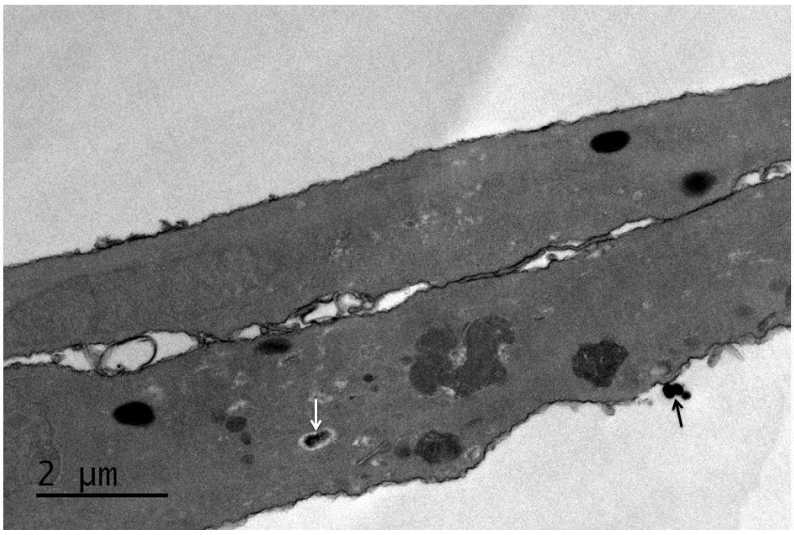

Figure 91: TEM image of MCF-7 cells showing bare ZnO NPs on the surface (black arrow) and inside the cells (white arrow) after 24 h exposure to 20 µg/ml bare ZnO NPs for 24 h.

5.2.2.2.2 TEM analysis of uptake of ZnO-HCV-RGD-GFP nanoparticles by MDA-MB-231 cells

To investigate binding and uptake of the targeted ZnO-HCV-RGD-GFP NPs to the MDA-MB-231 cells and to assess their effect on the cell, the MDA-MB-231 cells were incubated with the ZnO-HCV-RGD-GFP NPs and confocal live imaging was performed to track their binding to the cells. Upon exposure of the MDA-MB-231 cells to the ZnO-HCV-RGD-GFP NPs, agglomerates of the NPs had bound to the plasma membrane of the cells (Figure 92). This binding of the ZnO-HCV-RGD-GFP NPs to the cells was rapid, and the GFP labelled ZnO-HCV-RGD NPs bound to the surface of the cells after 22 min exposure (Figure 92, A). 3D images of the exposed cells showed green fluorescent diffused layer, which could indicate internalisation of the ZnO-HCV-RGD-GFP NPs, inside the cells (Figure 92, B and C).

Bright field TEM (BF-TEM) images of the MDA-MB-231 cells exposed to the ZnO-HCV-RGD-GFP NPs show 227.4x177.6 nm aggregate of NPs on the plasma membrane which were being internalised by the cells Figure 93 (A-D). Compared to the as-prepared ZnO NPs, the NPs within the aggregate were less spherical and the NPs had an altered appearance (Figure 93, E). High resolution phase contrast (HRTEM) image of the NPs, that shows the lattice

fringes of the NPs, is shown in Figure 93 (F). EDX spectra collected from the aggregates, in image (F) of Figure 93, confirmed the presence of Zn L peak at 1.015 keV (Figure 94).

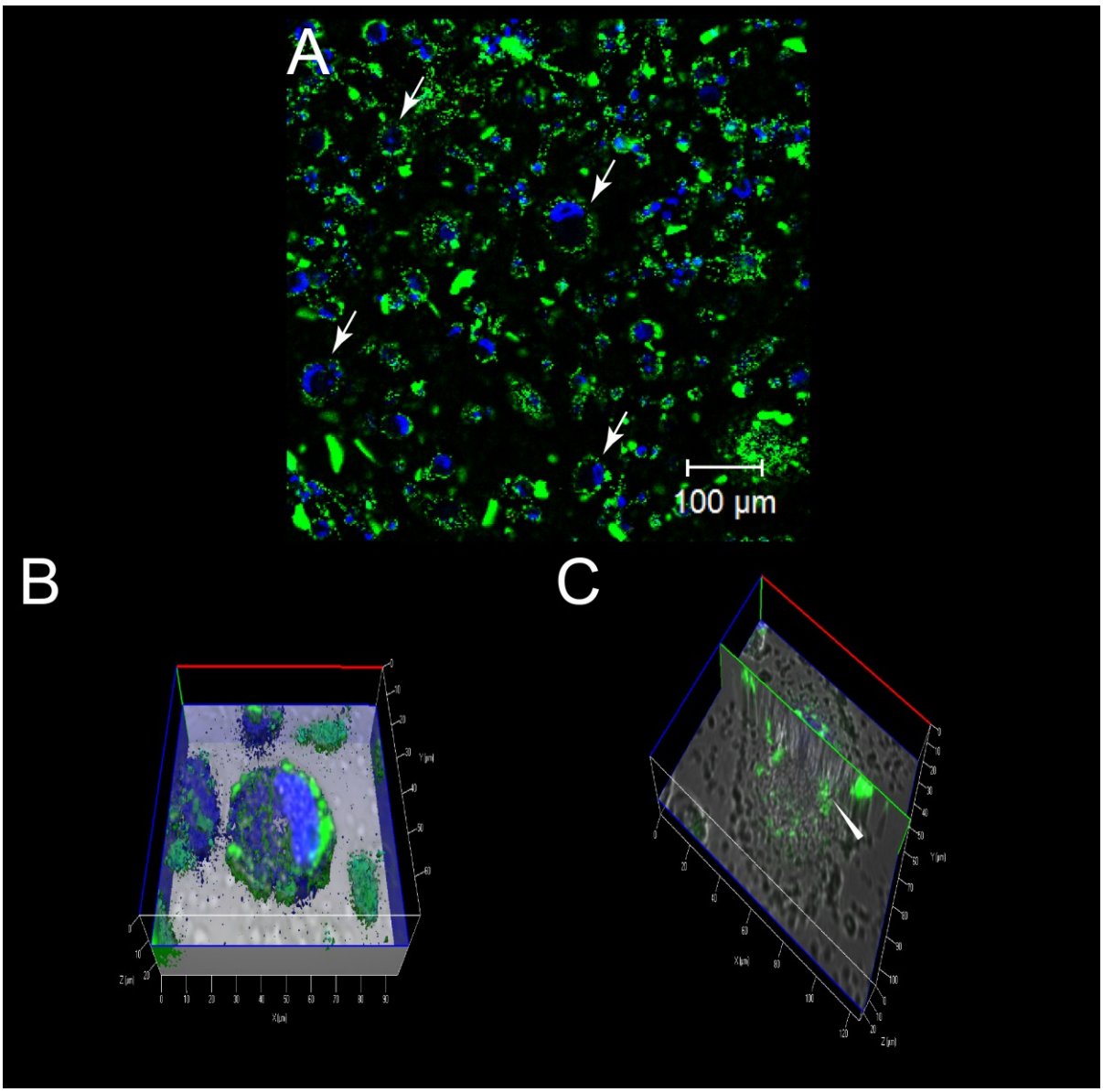

Figure 92: 2D (A) and 3D (B and C) confocal images of MDA-MB-231 incubated with GFP labelled ZnO-HCV-RGD NPs (arrows in (a) and arrow head in (C)) before TEM processing. Hoechst 33342 was used to stain the nuclei of live cells blue.

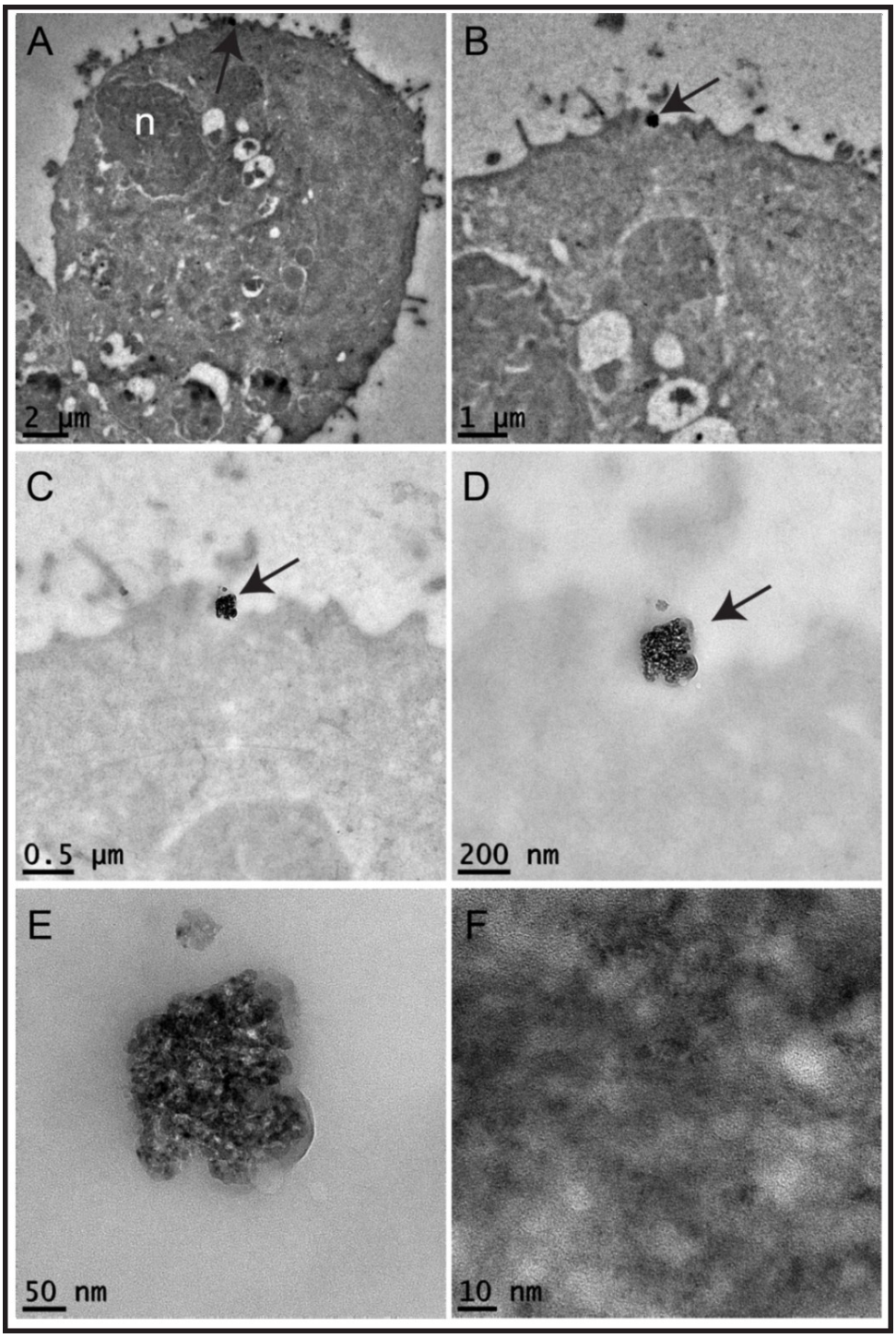

Figure 93: (A-D) BF-TEM images of MDA-MB-231 cells showing ZnO-HCV-RGD-GFP NPs (black arrows) bound to the plasma membrane and being endocytosed by the cells, (E) a higher magnification image showing non-spherical NPs with altered appearance, and (F) An HRTEM image showing lattice fringes. MDA-MB-231 cells were incubated with 150 µg/ml ZnO-HCV-RGD-GFP for 22 min before TEM processing. n= nucleus.

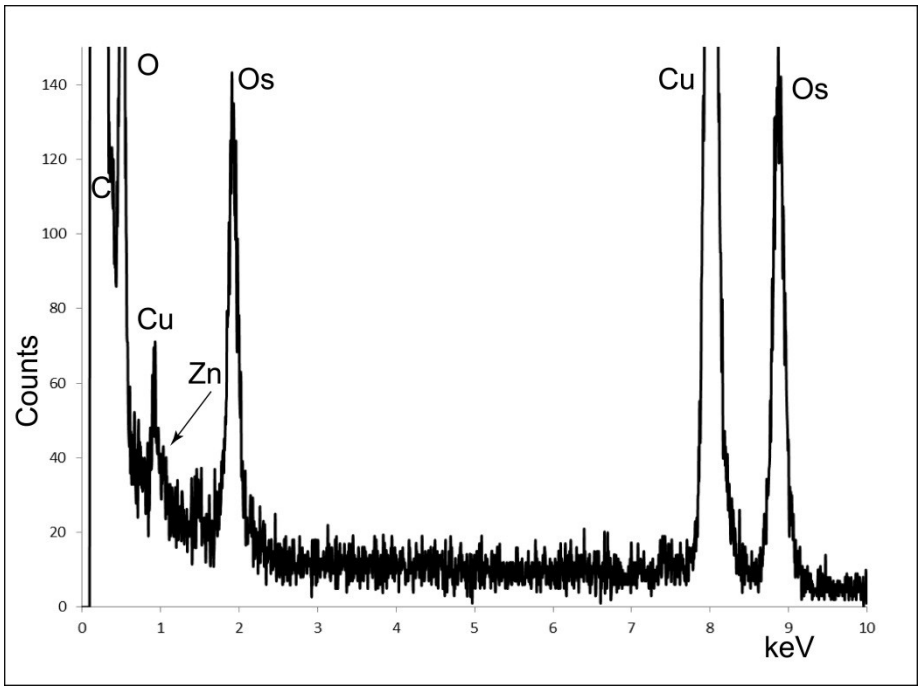

Figure 94: EDX spectra taken from the ZnO-HCV-RGD-GFP NPs labelled with an arrow in Figure 93.

BF-TEM image (Figure 95, A) of the MDA-MB-231 cells exposed to the targeted ZnO-HCV-RGD-GFP NPs also showed aggregates inside the cells. Energy-filtered TEM (EF-TEM) jump ratio mapping at Zn L2,3 edges confirmed that the crystalline precipitate was Zn-rich (Figure 95, B). Compared to the as-prepared ZnO NPs, morphology of the ZnO-HCV-RGD-GFP NPs inside the cells was again less spherical and the particles had an altered appearance (Figure 95, A). This could be again attributed to some dissolution of the particles while incubation with the imaging buffer and upon internalisation inside the cells. An HR-TEM image of the NPs that shows the lattice fringes is presented in Figure 95 (C). The corresponding FFT obtained from the image in Figure 95 (C) shows that the ZnO NPs were polycrystalline (Figure 95, D).

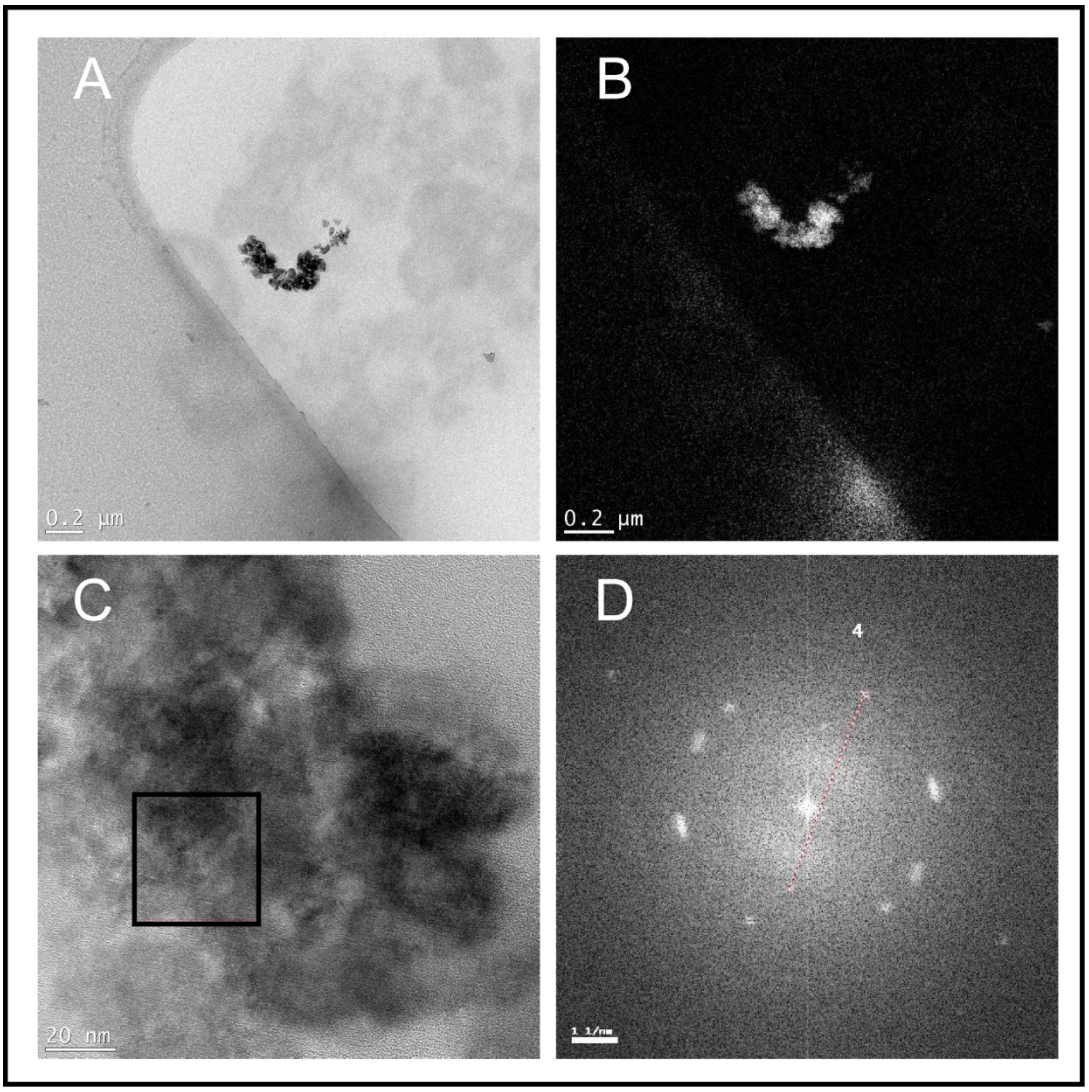

Figure 95: (A) A TEM image of MDA-MB-231 exposed to ZnO-HCV-RGD-GFP NPs showing particles inside vesicles inside the cells. (B) An EF-TEM jump ratio map showing Zn-rich deposits (light colored areas) taken at Zn L2,3 edge using 40 eV energy slit and using pre- and postedge energy windows centred at 995 ± 20 and 1040 ± 20 eV, respectively. (C) An HR-TEM image of particles showing crystalline lattice fringes taken at the Zn L2,3 edge using 40 eV energy slit and using pre- and post-edge energy windows centred at 995 ± 20 and 1040 ± 20 eV, respectively, and (D) the corresponding FFT obtained from the black box in image (C).

Since the Cu grid used with the cryosectioned TEM samples of the MDA-MB-231 cells exposed to the ZnO-HCV-RGD-GFP NPs was interfering with the EDX spectra of zinc, other sections of the ZnO-HCV-RGD-GFP NPs-exposed MDA-MB-231 cells were prepared onto a gold grid (Figure 96). BF-TEM images of the MDA-MB-231 cells showed aggregates of the ZnO-HCV-RGD-GFP NPs inside the cells (Figure 96, A and B), and on the plasma membrane of the cells which were being internalised by the MDA-MB-231 cells (Figure 96, C and D). The aggregate of the ZnO-HCV-RGD-GFP NPs found on the cell membrane of the cell in Figure 96 (C and D) was composed of smaller particles of 34.47 ± 9.78 nm. These particles

are smaller than the size of the original ZnO NPs measured by TEM, which was 56.7 ± 21.7 nm (section 3.2.1, Figure 6, a). The mottled appearance of these particles and their altered morphology compared to the original NPs could have arisen due to the dissolution of the ZnO-HCV-RGD-GFP NPs in the HEPES confocal imaging buffer while incubation with the cells. EDX spectra collected from the particles on the plasma membrane of the cells confirmed the presence of Zn L peak at 1.025 keV (Figure 97).

Remnants of the ZnO NPs could be seen inside vesicles in the MDA-MB-231 cells after exposure to ZnO-HCV-RGD-GFP NPs (Figure 98, A, area 1 and 2). These could be a result of dissolution of the ZnO NPs in the lysosomes after internalisation of the targeted ZnO-HCV-RGD-GFP NPs. EDX spectra from area 2 in Figure 98-A confirmed the presence of Zn L peak at 1.025 keV.

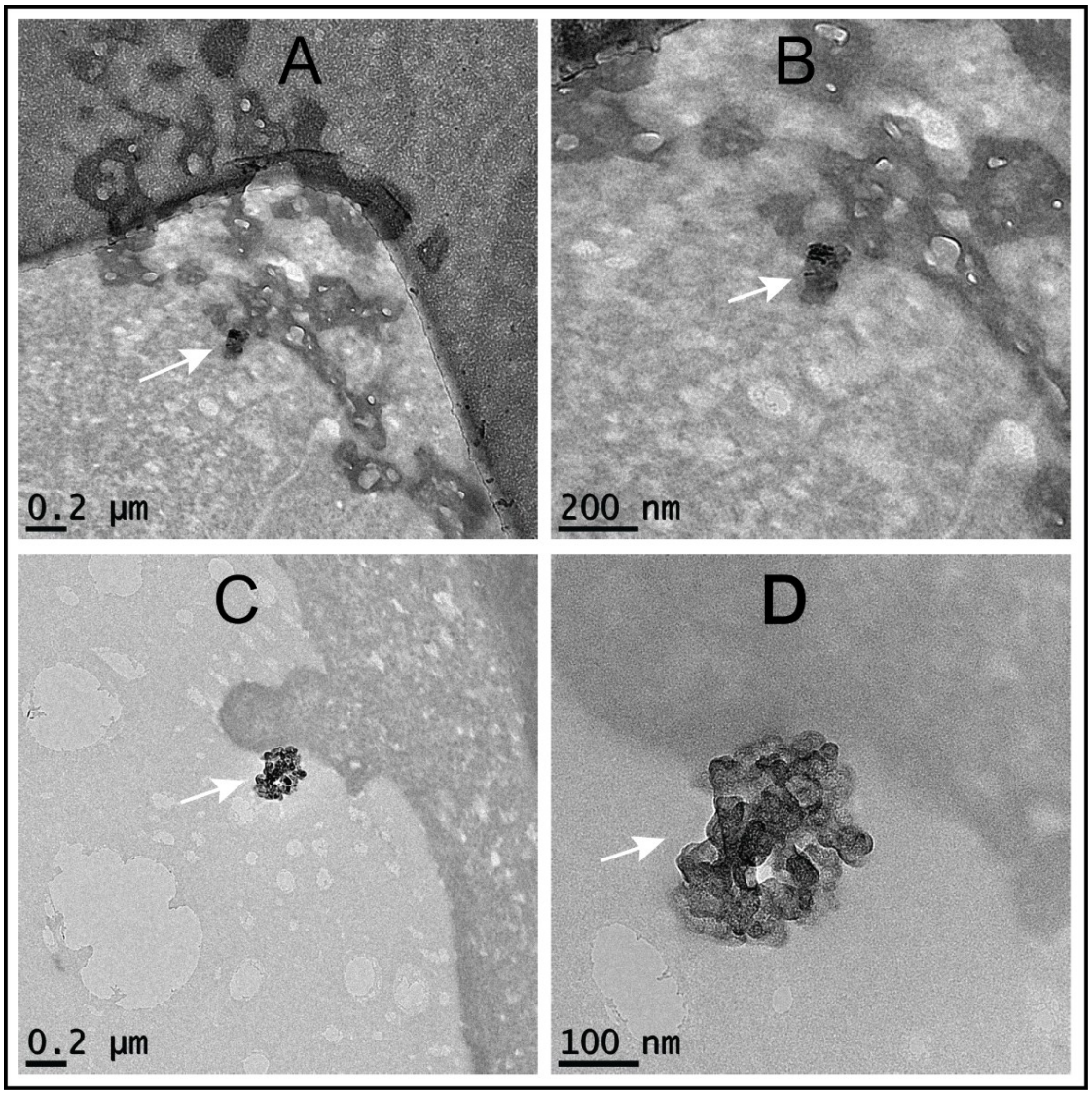

Figure 96: BF-TEM images of MDA-MB-231 exposed to ZnO-HCV-RGD-GFP NPs for 22 min and prepared cryogenically. NPs (arrows) were found inside the cells (A, B), and at the plasma membrane of the cells (C, D). The particles were composed of smaller particles of 34.47 ± 9.78 nm in diameter (D).

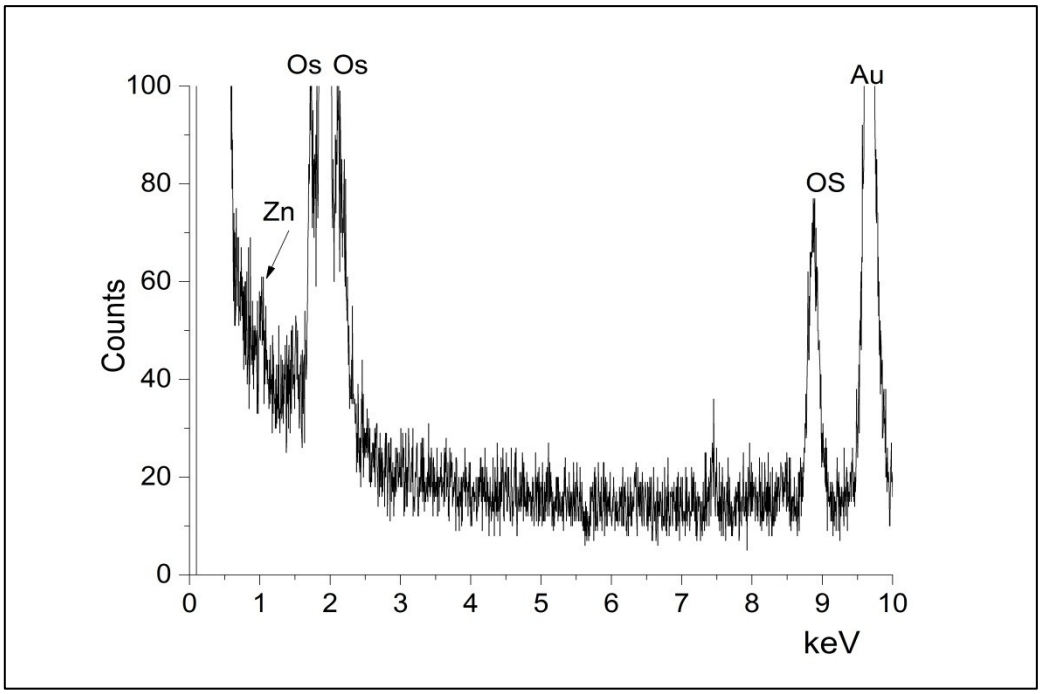

Figure 97: EDX spectra taken from the ZnO-HCV-RGD-GFP particles labelled with an arrow in Figure 96 (c and d).

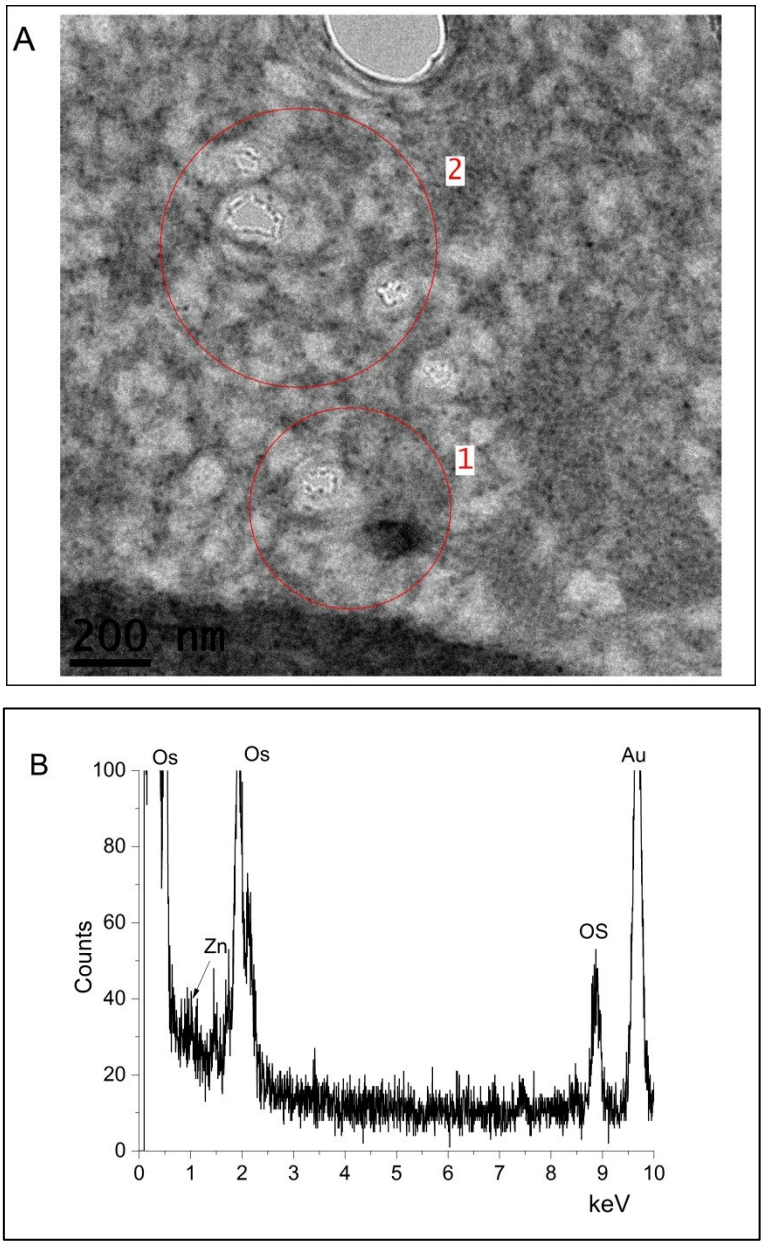

Figure 98: (A) BF-TEM images of MDA-MB-231 exposed to ZnO-HCV-RGD-GFP NPs. Cells were incubated with ZnO-HCV-RGD-GFP NPs for 22 min, fixed cryogenically prior to processing for TEM. The red circles outline vesicles inside the cells which contain ZnO-HCV-RGD-GFP NPs. (B) EDX spectra collected from area 2 in image A.

5.2.3 Cancer stem cell markers (CSCs)

The results of the uptake and the dissolution of the ZnO NPs obtained in this chapter showed heterogonous responses in the breast cancer cell lines. This heterogeneity in the response to the ZnO NPs was also observed within the same breast cancer cell line. Most cancers comprise a heterogeneous population of cells with different proliferative and tumorigenic potentials [200, 201]. According to the recent cancer stem cell hypothesis, a tumor consists of differentiated highly proliferative cells, and undifferentiated low-cycling

cells with self-renewal capacity, the so called cancer stem cells (CSCs) [202]. CSCs should have a higher resistance than the differentiated cancer cells, and may be highly resistant to radiation and chemotherapy [203]. Therefore, the heterogeneity in the types of breast cancer cells could be a factor that account for the observed heterogeneity in the response of the breast cancer cells to the ZnO NPs. Herein, the presence and the percentage of these CSCs expressed by the MCF-7 and the MDA-MB-23 1 cells was measured.

CSCs could be morphologically indistinct from the bulk of the cancer, therefore, the most effective method of identifying these cells is through differential cell surface protein expression [204]. Because these two cell types could account for the heterogeneity of the response and sensitivity of the tested breast cancer cells to ZnO NPs, a number of CSC markers were tested for both the MCF-7 and MDA-MB-231. However, the relevance of the current stem cell markers is still controversial [205].

Among the markers that are currently used to identify breast CSCs [206], the expression of CD44, CD24, CD90, and EpCAM (epithelial cell adhesion molecule) were tested. CSCs are reported as $CD44^{+}$, $CD24^{-}$, $EpCAM^{-/low}$ and $CD90^{-}$ [207]. In this study, the MDA-MB-231 cells and the MCF-7 showed different expression of these markers (Figure 99). While the MCF-7 were $CD44^{low}$ /$CD24^{+}$/ $EpCAM^{+}$ and $CD90^{+}$ (Figure 99, a), the MDA-MB-231 cells were $CD44^{+}$/$CD24^{-}$/$EpCAM^{low}$ and $CD90^{-}$ (Figure 99, b). This coincides with the published work for these cells [207, 208].

$CD44^{+}$/$CD24^{-}$ breast cancer cells were reported to disseminate in the bone marrow and they were also resistant to chemotherapy [209]. Therefore, the ability of ZnO NPs to eradicate these CSCs will further enrich the therapeutic value of this material for the treatment of cancer.

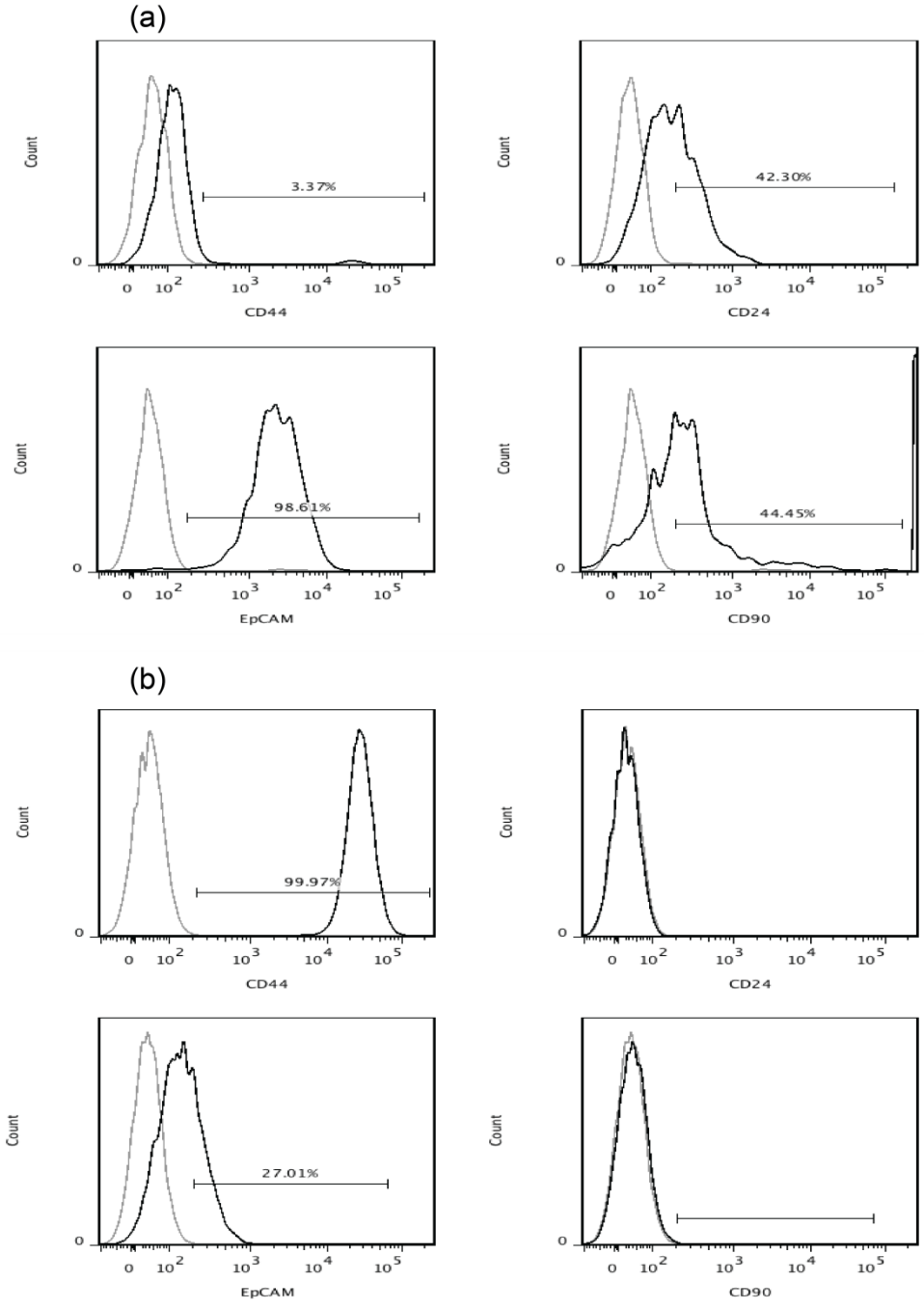

Figure 99: Flow cytometric analysis of expression of cancer stem cells (CSCs) markers; CD44/ CD24/ EpCAM and CD90 in (a) MCF-7 and (b) MDA-MB-231 cells.

5.3 Summary and conclusions

In this study, the targeted ZnO-HCV-RGD-GFP NPs were found to bind to the breast cancer MDA-MB-231 cells and to a lesser extent to the MCF-7 cells. This difference in binding of the breast cancer cells to the ZnO-HCV-RGD-GFP is probably due to higher expression of the integrin αvβ3 receptors in the former cells. After binding, the RGD-targeted ZnO NPs were internalised by both breast cancer cell lines. In the MDA-MB-231 cells, the RGD-targeted ZnO NPs were found inside pits at the plasma membrane and inside the cells, possibly in endosomes and in the cytoplasm of the cells. The mechanism of uptake of the ZnO-HCV-RGD-GFP NPs is most probably clathrin-mediated endocytosis. The bare ZnO NPs were also internalised by the MCF-7 and the MDA-MB-231 cells. The bare ZnO NPs were found to bind to the cell surface and have been internalised by pinocytosis. The presence of the bare and targeted ZnO NPs outside and inside the cells is an indication that the NPs have not dissolved outside the cells and any toxic effects are due to their intracellular dissolution and the release of Zn^{2+}.

ZnO NPs (both bare and targeted) dissolution was found to be dependent on the pH within various cell compartments (extracellular, intracellular and lysosomes). At extracellular pH 7.4, the dissolution was significantly less than that observed in the lysosomes at pH 5.2. Following their uptake, the NPs were most probably transported to early endosomes. The endosomes then fuse with low pH lysosomes, where the NPs dissolved to release Zn^{2+} which might enter the cellular cytosol. However, other cell components (e.g. Golgi apparatus pH=6.4, endosomes pH=6 [210, 211]) have a pH <7, and therefore the toxicity of ZnO NPs could be significant inside the cells. Once Zn^{2+} ions released inside the cells, it initiate toxic responses in the cells. The effect of Zn^{2+} on the apoptosis of cancer cells has been previously reported [5, 181]. It has been reported that Zn^{2+} mediated Tamoxifen-induced cell death in the MCF-7 breast cancer cells via increase in oxidative stress and induction of lysosomal membrane permeabilization [180]. This could explain why Zn^{2+} could directly correlate to cell death in breast cancer cells after exposure to the ZnO NPs.

The breast cancer cells showed heterogeneity in response to the ZnO NPs. This heterogeneity in breast cancers is already reported [212]. The MDA-MB-231 cells were

found to have the characteristics of CSCs while the MCF-7 cells did not show CSCs like properties. The heterogeneity in response of the MDA-MB-231 cells to the ZnO NPs and Zn^{2+} ions needs to be investigated. This heterogeneity of cancer cells introduces significant challenges in designing effective treatment strategies. Therefore, understanding and characterizing heterogeneity is crucial in the development of refined treatment strategies. The ability of ZnO NPs to kill the CSCs that could be resistant to classic treatments while possessing potent tumor-forming capacity is another advantage of using this material in cancer therapeutics.

The morphology of the bare and targeted ZnO NPs was changed upon exposure to the cells. This change in the morphology of the NP suggests that dissolution of the NPs had occurred in the intracellular environment. Muller *et al.*, (2010) also observed similar dissolution of ZnO NWs inside human monocyte derived macrophage cells triggered by the acidic pH of the lysosomes [10]. Interaction of the NPs with the amino acids and proteins present in the media during incubation and subsequent formation of the protein corona could also have account for the change in the morphology. However, in this work, the targeted ZnO-HCV-RGD-GFP NPs were added to the cells in HEPES confocal buffer at pH 7.4. Therefore, dissolution of these ZnO NPs inside the cells is the only reason that could account for the change in their morphology.

It was discussed earlier in section 4.3 of chapter 4 that the RGD-targeted ZnO NPs were more toxic to the MCF-7 and MDA-MB-231 cells than the bare NPs. In confocal microscopy, however, quantitative comparisons between the cytotoxicity of the targeted and the bare ZnO NPs could not be drawn due to the heterogeneity in the response to the bare and targeted ZnO NPs in each breast cancer cell line. For this reasons quantitative comparisons between the results of the viability assays and confocal microscopy was not feasible. However, the following factors should be taken into consideration even in the qualitative comparisons; DMEM media supplemented with FBS was used in the viability assays while HEPES confocal imaging buffer was used in confocal imaging. Therefore, the hydrodynamic size of the ZnO NP aggregates was different in these vehicles. Also, a protein corona on the surface of the ZnO NPs will develop when the NPs are suspended in media, but not in the HEPES confocal imaging buffer. Both factors could affect the bioreactivity of

the ZnO NPs. It is also worth to comment on the effect of the number of the ZnO NPs used per cell in the viability assays and confocal microscopy. Although the same density of the cells were plated per area in the 96 well plates, used for the viability assays, and the confocal microscopy culture plates, the number of particles exposed per cell was different in both cases. In the viability assays, 100 µL of the NPs dispersions were added to the cells plated on an area of 0.3165 cm^2, while 2 ml of the NPs dispersion in the confocal microscopy were added to the cells plated on an area of 3.143 cm^2. Whether the toxicity of the ZnO NPs is based on the number of particles per cell or a concentration dependent was not possible to measure, due to the limitations of the viability assays.

The intracellular dissolution, of the targeted and bare ZnO NPs showed differences between the kinetics of these processes. The bare ZnO NPs, showed a clear time dependent increase in intracellular dissolution while the targeted ZnO NPs showed a very low intracellular dissolution with time and then a sudden burst of ionic zinc release. Also, once the concentration of the released Zn^{2+} ions inside the cells reach toxic levels after exposure to the bare ZnO NPs, the cell lost the integrity of their cell membrane and a gradual drop on intracellular Zn^{2+} could be measured. With the targeted NPs, on the other hand, a sudden increase in cellular death was accompanied the sudden increase in the intracellular Zn^{2+}. This finding is most likely due to the different mechanisms of internalisation of the bare and the RGD-targeted NPs, and therefore altered intracellular distribution [91]. It has been reported that the RGD-grafted NPs enter cells through integrin-mediated endocytosis or clathrin-mediated endocytosis and are localised in perinuclear regions while the nontargeted NPs are transferred by different mechanisms [48, 213].

6 Plasma protein binding to bare zinc oxide nanoparticles and formation of protein corona

Adsorption of proteins from serum, and formation of NP-protein corona at the NPs surface may lead to a substantial change in the physicochemical properties of the NPs (size, shape, reactivity, surface area, *etc*.) [96, 107]. These changes of the NPs could, in turn, critically affect the interaction of these NPs with the cell membrane and eventually their biodistribution, uptake mechanisms, intracellular localisation of the NPs *in vivo* [60] and clearance mechanisms [214]. Consequently, understanding how, and why plasma proteins, are adsorbed to these NPs may be important for understanding their biological responses and will be the key point to the development of NPs with a long circulation time.

In *in vitro* viability assays, different media are used to culture cells. The composition of the media could largely affect the composition of protein corona around the NPs investigated, which in turn could affect the outcomes of the viability assays. Gabriele *et al.*, have shown that 15 nm gold (Au) NPs- protein corona was different in DMEM and RPMI medium supplemented with 10% FBS [215]. A Large time-dependent protein corona was formed in DMEM, while that in RPMI shows different dynamics with reduced protein coating. They also found that the average composition of protein corona does not reflect the relative abundance of serum proteins and that proteins/NP complexes formed affected the uptake and toxicity of these NPs. Rahman *et al.* also reported that the cellular/tissue responses depend on the composition of corona [97]. In this study, as discussed earlier in chapter 3, the protein corona formed on the surface of the bare ZnO NP changed their surface charge and this could highly affect the NP bioreactivity [136].

Tumour tissues are characterised by increased capillary permeability or what is called the ‘enhanced permeability and retention’ (EPR) effect. The EPR effect allows an increased rate of tumoural uptake of NPs [35]. However, the protein corona formed on the surface of NPs could act as ‘opsonins’. Opsonins can be recognised by scavenger receptors on the macrophage cell surface and internalised. This internalisation by macrophages leads to significant loss of NPs from the circulation. The macrophages responsible for the loss of injected dose of NPs are also known as the reticuloendothelial system (RES). IgG and IgM, to

a lesser extent, can act as an opsonin and promote phagocytosis of NPs by macrophages or other phagocytic cells [216, 217]. Therefore, characterisation of the composition of the protein corona is essential for prediction of the interaction of the protein-NPs complex with the immune system *in vivo*.

Only few studies on ZnO NP-protein interactions have been reported. In most studies, bovine serum albumin (BSA) was used as a model protein [218-220]. It was found that BSA interacts with ZnO NPs to form a stable hard corona [218, 220]. This interaction is spontaneous and electrostatic interactions dominate [221]. ZnO NP-protein corona equilibrium is achieved within the first few minutes of incubation [8]. The interaction of BSA with ZnO NPs occurs through Tryptophan residues of BSA [218, 219] and results in conformational changes to the BSA [218, 220].

The uptake and the toxicity of several classes of NPs have been shown to be reduced by the formation of protein corona in serum [59]. However, the toxicity of ZnO NPs to MCF-7 human breast cancer cell line was not reported to be reduced by serum [59]. The effect of the ZnO NP-protein corona on ZnO NPs uptake and lipid packing and the hydration state of the plasma membrane has also been investigated [60]. It has been reported that serum albumin enhances the membrane activity of ZnO NPs by stabilising the nanoscale size distribution of aqueous dispersions of ZnO NPs [60].

The composition of ZnO NP-protein corona was characterised only by Deng *et al.* [8]. Proteins with important biological functions were identified in the protein corona of ZnO NPs [8]. These include; immunoglobulins, lipoproteins, acute-phase proteins and proteins involved in complement pathways and coagulation. However, Deng *et al*. study used a high centrifugation force of 50,000 xg for long time (40 min) to pellet the NP-protein complex, which could result in the loss of the soft protein corona, and even part of the hard corona. They also used 2D gel electrophoresis to analyse the composition of the protein corona, which is not as sensitive as other protein analysis methods such as liquid chromatography/mass spectroscopy (LC/MS), and therefore, they reported one unknown protein in the corona.

In this study, the composition of protein corona formed from human plasma proteins onto the surface of the bare ZnO NPs at different temperatures, centrifugation forces and compositions, as well as concentrations of human plasma, was analysed by LC/MS.

6.1 Materials and Methods

6.1.1 Materials

DL-Dithiothreitol, iodoacetamide, ammonium bicarbonate, Acetonitrile, trifluoro acetic acid were purchased from Sigma Aldrich Ltd, UK and were of biological grade (>99% pure).

6.1.2 Preparation of human plasma

The whole blood was collected in sodium citrate tubes (BD Vacutainer), to prevent coagulation of the blood, and the plasma was separated from the blood cells by centrifugation for 5 min at 800 xg. The supernatant (plasma) was stored in aliquots at -80 °C. On thawing, the plasma was centrifuged for 2 min at 12,000 xg before use.

6.1.3 Incubation of human plasma proteins with the bare ZnO NPs

The ethanolic stock dispersion of the bare ZnO NPs was sonicated for 20 min and the bare ZnO NPs were then prepared in HEPES buffer at pH=7.4 (10 mM HEPES and 50 mM $NaCl_2$) at 10 mg/ml. The particles were then sonicated for 10 min, using table top sonicator. The bare ZnO NP-human plasma protein solutions were prepared by mixing human plasma (to a final concentration of 10% v/v) with the bare ZnO NPs (to a final concentration of 1 mg/ml). The NPs were then incubated with the plasma for 1 h at 4°C while rotating end over end. Several experiments indicated that incubation times longer than 1 h did not result in a significant change in the composition of adsorbed proteins [222]. Plasma without NPs was used as a control to ensure there was no protein precipitation. At the end of incubation time, samples were centrifuged at 16,000 xg for 15 min at 4°C. The supernatants were then removed and ZnO NPs, with the adsorbed proteins, were washed three times in HEPES buffer (10 mM HEPES+50 mM $NaCl_2$). The tube was changed after the first wash. The pellet was then processed for mass spectroscopy analysis. The experiment was repeated twice and the average result is presented.

To check for the presence of proteins in the last wash, a 200 µL aliquot taken from the supernatant was analysed for protein content by an acetone precipitation method [223]. The 200 µL sample of the supernatant was diluted six times with chilled acetone (-20°C). The sample was then mixed and stored for 60 min at -20°C. The sample was then centrifuged at 16,000 xg for 30 min at 4°C. The supernatant was carefully decanted so as not to dislodge the protein pellet. The protein pellet was then air dried for 10-20 min. Finally, the pellet was processed in the same way as the ZnO NP-protein corona pellet.

To study the effect of incubation temperature on the resulted protein corona, the experiment was repeated and the bare ZnO NPs were incubated with human plasma proteins at 37°C, and the same procedure was followed. The effect of centrifugation power on the NP-protein corona was investigated by centrifuging the NP-protein complex sample at 6,000 xg for 20 min, at end of incubation time. Finally, the effect of human plasma concentration was studied by increasing the final concentration of the plasma incubated with the bare ZnO NPs to 90%. The volume of plasma used per cm^2 of the particles was calculated. Assuming that the particles were spherical, their surface area was calculated from the equation: surface area of the particles= $4n\pi r^2$, where n: no of particles and r: radius of one particle. The number of the particles was calculated from their volume using the equation: Volume of the particles=$4/3\pi nr^3$, and using the density of ZnO which is 5.61 g/cm^3. The average particle size of the ZnO NPs in the vehicle (10 mM HEPES+ 50 mM NaCl) measured by DLS (Table 4) was used to calculate the radius of the NPs (r=560.5 nm).

6.1.4 Depletion of human plasma from serum albumin and immunoglobulins

Human serum albumin (HAS) and immunoglobulins G (IgG) were depleted from human plasma using the Spin Trap columns (GE Healthcare Life Sciences, UK), according to the manufacturer's protocol. The columns were prepacked with high performance Sepharose based media with an affinity for HSA and IgG. For protein corona analysis, the HSA and IgG depleted plasma was incubated with ZnO NPs, as described in section 6.1.3.

6.1.5 Preparation of bare ZnO NP-protein corona for mass spectroscopy

6.1.5.1 Reduction of the disulphide bonds

The resulting ZnO NP-protein complexes were reduced with 20 µL of the 5 mM DTT prepared in ammonium bicarbonate, incubated at 37°C for 30 min while shaking at 1,000 rpm. DTT is a reducing agent that prevents intramolecular and intermolecular disulphide bonds from forming between cysteine residues of proteins. The proteins were further reduced with 50 mM iodoacetamide prepared in 100 mM ammonium bicarbonate to a final concentration of 14 mM at 37°C for 30 min, while shaking at 1,000 rpm. Iodoacetamide is an alkylating agent that binds covalently with the thiol group of cysteine, so the protein cannot form disulphide bonds.

6.1.5.2 Proteolyzation of the adsorbed proteins

Trypsin is used to digest proteins (polypeptide) by cleaving the peptide chain at specific sites. Trypsin cleaves the peptide chain after Lysine (K) or Arginine (R) residues (amino acids), except when followed by a Proline (P) residue.

Trypsin was freshly prepared by dissolution in trypsin solubilisation buffer (acetic acid solution) (0.2 µg/µL). The solution was then neutralised using a trypsin reaction buffer (50 mM ammonium bicarbonate) to a final concentration of 20 ng/µL trypsin. The ZnO NP-protein corona complexes were proteolyzed with 40 ng trypsin overnight at 37°C. The resulting peptides were centrifuged at 16,000 xg for 10 min at 4°C. The supernatant was then collected without disturbing the particles.

6.1.5.3 Concentrating and purifying the peptides

The resulting peptides/and proteins were desalted using disposable Silica-C18 tip (Zip Tip, Millipore) with 0.1% trifluoro acetic acid (TFA). The peptides and proteins were eluted by pipetting the tip into the elution solution (0.1% TFA in 50% acetonitrile) at least three times. The sample was then dried by vacuum centrifugation using Speedvac (Thermo Scientific), dissolved in 0.1% formic acid. Finally, the sample was centrifuged for 5 min at 16,000 xg at 4°C and the supernatant was analysed by LC/MS (LTQ-Orbitrap Velos, Thermo scientific) coupled with Easy-nLC (Thermo Scientific). The LC/MS analysis was performed by the core

labs at King Abdullah University for Science and Technology (KAUST). Proteins were identified by their isoelectric points and mass using the ExPASy database (http://au.expasy.org/swiss-2dpage/viewer).

6.2 Results

The protein coronas from human serum proteins formed onto the surface of the bare ZnO NPs were composed of several proteins. No proteins were identified in the last wash of the corona-NP complex sample nor precipitated from the control protein sample. All the proteins identified in the ZnO NP-corona are listed in Table 9 at the end of this chapter.

6.2.1 Effect of incubation temperature

The bare ZnO NPs were incubated with the whole plasma at 4 and 37°C, and the ZnO NP-protein complex was centrifuged at 16,000 xg. The experiment was repeated twice and the average of the number of proteins identified in the corona is presented in Figure 100. The incubation temperature affected the composition and the percentage of adsorbed proteins in the ZnO NP-corona. The number of identified proteins in the human corona was 42 and 39 proteins after incubation with the bare ZnO NPs at 4 and 37°C, respectively (Figure 100, Table 9). It was found that, the lower molecular weight proteins (<20 kDa) were more bound to the NPs at lower temperature (4°C), and a higher percentage of the high molecular weight proteins (60-150 kDa) were bound to the bare ZnO NPs at 37°C. Therefore, a protein like clusterin (Apolipoprotein J), protein shroom3, and most of the IgG were missing from the corona when the particles were incubated with the serum at 37° C (Table 9). On the other hand other proteins (e.g. complement C5, gelsolin, hornerin, plasminogen, and suprabasin proteins) were identified in the protein corona at 37°C, but not at 4°C (Table 9).

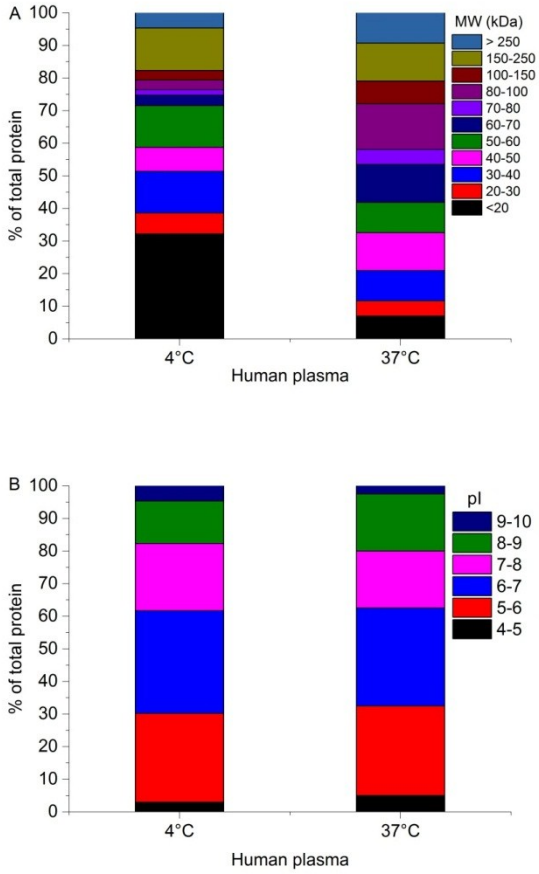

Figure 100: The protein corona identified on the surface of bare ZnO NPs classified according to their (A) molecular weight (MW) and (B) isoelectric point (pI). Bare ZnO NPs were incubated with human plasma (total concentration of 10%) for 1 h at either 4 or 37°C. The NP-protein complex was then centrifuged at 16,000 xg, washed three times and processed for LC/MS.

6.2.2 Effect of albumin and IgG depletion

Human plasma consists of more than 289 proteins [224]. The most abundant plasma proteins are HSA and IgG, and they tend to obscure the signals of less abundant proteins [225]. The high abundance of albumin and IgG also interferes with the detection of other proteins by preventing a sufficient amount of less abundant proteins from being included in the analysis [225]. By depleting samples of albumin and IgG, the quality of the analysis can be greatly enhanced. Depletion of the two proteins removes more than 60% of the total protein content in human plasma, allowing proteins normally obscured by albumin and IgG to be visualized.

Bare ZnO NPs were incubated with the whole and depleted plasma at 37°C, and the ZnO NP-protein complex was centrifuged at 16,000 xg. The number of proteins identified in

the protein corona from albumin and IgG depleted human plasma was 31, while those obtained from the whole plasma were 39 (Figure 101, Table 9). More types of apolipoproteins and complement factor proteins were found in the depleted corona but not in the non-depleted one. For example complement component C6, could be part of the soft corona, was detected in the depleted plasma but not in the whole plasma when centrifuged at 16,000 xg.

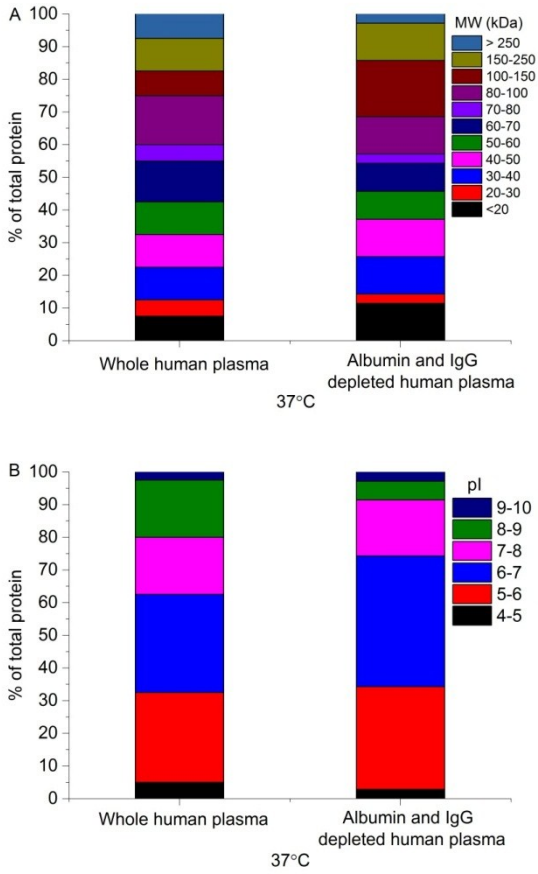

Figure 101: The protein corona identified on the surface of bare ZnO NPs classified according to their (A) molecular weight (MW) and (B) isoelectric point (pI). Bare ZnO NPs were incubated for 1 h with either whole or albumin and IgG depleted human plasma (total concentration of 10%) at 37°C. The NP-protein complex was then centrifuged at 16,000 xg, washed three times and processed for LC/MS.

6.2.3 Effect of centrifugation force

Higher numbers of proteins in the ZnO-NP corona were identified at lower centrifugation force; 39 proteins were identified in the ZnO NP-protein corona at 16,000 xg while 57 proteins were identified at 6,000 xg (Figure 102, Table 9). This is expected, since the adsorption of proteins on the surface of nanoparticle is governed by protein–nanoparticle

binding affinities, as well as protein–protein interactions [226]. Therefore, the NP-protein corona is composed of a dynamic layer of proteins, low affinity proteins being gradually replaced by lower abundance, higher affinity proteins [33]. These low affinity proteins form the “soft corona”, while the higher affinity proteins form the “hard corona” [97]. The hard corona proteins interact directly with the nanomaterial surface, while the soft corona proteins interact with the hard corona via weak protein–protein interactions [98]. Therefore upon centrifugation at high speed, most of the soft corona is depleted and probably part of the hard corona. Deng *et al.* [8] for example, used 50,000 xg centrifugation force which could result in the loss of most proteins in the corona.

The centrifugation force affected the apolipoproteins composition of the ZnO NP-corona; Anastellin, Antithrombin, most of the complement components, some immunoglobulins, and clusterin, for example, were identified at 6,000 xg force but not at 16,000 xg (Table 9). However, some other proteins like apolipoproteins, albumin, most complement components, coagulation factors, plasminogen, and prothrombin were identified at both centrifugation forces, which could imply their strong interaction with the ZnO NPs surface (Table 9).

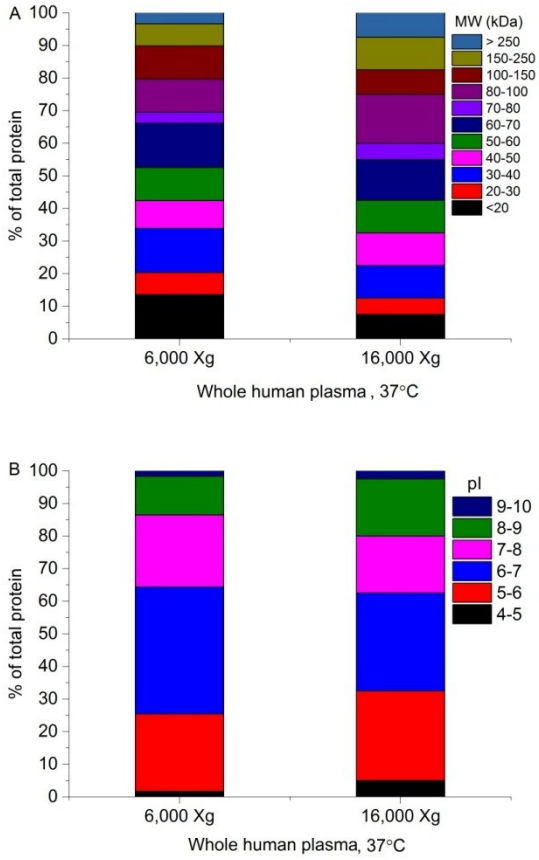

Figure 102: The protein corona identified on the surface of bare ZnO NPs classified according to their (A) molecular weight (MW) and (B) isoelectric point (pI). Bare ZnO NPs were incubated with human plasma (total concentration of 10%) for 1 h at 37°C. The NP-protein complex was then centrifuged either at 16,000 or 6,000 xg, washed three times and processed for LC\MS.

6.2.4 Effect of human plasma concentration

It has been shown that the total number of proteins in the corona adsorbed on the surface of NPs increase with increasing concentration of the serum [97]. The same study, however, showed that the amount of the highly abundant proteins like albumin is not affected, while the amount of some other proteins could reduce by increasing the concentration of the plasma. Therefore, it was important here to study the effect of increasing plasma concentration on the protein corona formed on the surface of the ZnO NPs. In their study of the ZnO NP-protein corona, Deng *et al.* [8] used only one concentration of the plasma (10% v/v of the plasma to NPs).

A total of 57 proteins were identified in the corona when bare ZnO NPs were incubated with whole human plasma at a concentration of 10% v/v (119 ml/cm^2), while a

higher number of 108 proteins where identified in the corona when bare ZnO NPs were incubated with 90% v/v (596 ml/m^2) human plasma (Table 9). Many proteins were identified in the ZnO NP-corona only when high plasma concentration was used. Examples of proteins identified when a higher plasma concentration was used: proteins include: many complement factor proteins, many immunoglobulins, most of the coagulation factors, which is required for integrin-mediated platelet adhesion [227], like coagulation V, X, XI, XIII B, fermitin family homolog 3, which is required for integrin-mediated platelet adhesion [227], and radixin, which plays a crucial role in the binding of actin filaments to the plasma membrane [228] (Table 9).

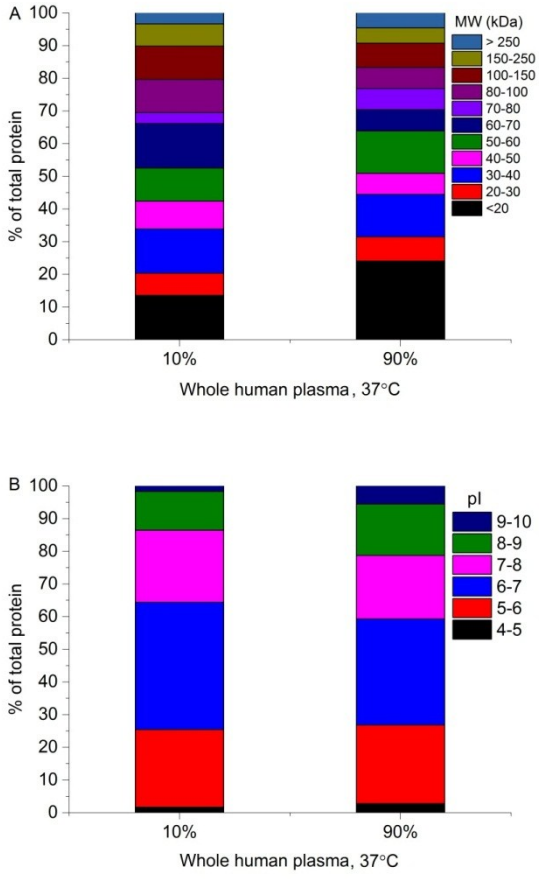

Figure 103: Protein corona identified on the surface of bare ZnO NPs classified according to their (A) molecular weight (MW) and (B) isoelectric point (pI). Bare ZnO NPs were incubated with human plasma (total concentration of 10% (10 or 90%, in which the ratio of plasma to NPs is 119 ml/cm^2 or 596 ml/cm^2, respectively) for 1 h at 37°C. The NP-protein complex was then centrifuged either at 6,000 xg, washed three times and processed for LC/MS.

6.3 Summary and conclusions

It is important to understand the role of protein binding to ZnO NPs as this may affect the extent of interaction of the NPs with cells by modifying what the cell "sees". In addition, protein corona can result in modifying the solubility of the NPs by formation of soluble complexes [49]. Therefore, understanding the composition of plasma proteins bound to ZnO NPs is important in predicting their biodistribution, biocompatibility and therapeutic efficacy. Although several experiments have been conducted to study the interaction of proteins with a range of NPs, a comprehensive picture is still missing. This could be due to the different conditions under which experiments have been performed. Therefore, this field is in need of more studies to further our understanding of protein corona formation and its biological consequences [229].

In this study, many factors were found to affect the protein corona composition of the ZnO NPs. These include the incubation temperature, the percentage of the plasma used, centrifugation force, and depletion of the plasma from HSA and IgG. All these factors had to be taken into consideration when studying the protein corona of the ZnO NPs since the type of protein bound to the ZnO NPs could dictate the bioreactivity of these NPs. In this study, the identified proteins in the ZnO NPs corona at different conditions are summarized in Table 9.

We found that, the lower molecular weight proteins (<20 kDa) were more likely to be bound to the NPs at lower temperature, and a higher percentage of the high molecular weight proteins (60-150 kDa) were bound to the bare ZnO NPs at 37°C. Therefore, a protein like clusterin (Apolipoprotein J) was missing from the corona when the particles were incubated with the serum at 37°C. On the other hand, complement C5, gelsolin, hornerin, plasminogen, and suprabasin proteins were identified in the protein corona at 37°C, but not at 4°C. More types of apolipoproteins and complement factor proteins were found in the depleted corona but not in the non-depleted one. For example complement component C6, could be part of the soft corona, it was only detected when the plasma was depleted. The centrifugation force affected the apolipoproteins composition of the ZnO NP-corona; anastellin, Antithrombin, most of the complement components, some immunoglobulins, and clusterin were identified at low centrifugation force but not at 16,000 xg. However,

albumin and IgG and plasminogen were identified at both centrifugation forces, which could imply their strong interaction with the ZnO NPs surface. Many proteins were identified in the ZnO NP-corona only when high plasma concentration was used. Examples of these proteins include: many complement factor proteins (which is involved in inflammatory responses in the body [230]), most of the coagulation factors, like coagulation V, X, XI, XIII B, fermitin family homolog 3 (which is required for integrin-mediated platelet adhesion [227]), and radixin, which plays a crucial role in the binding of actin filaments to the plasma membrane [228]. Apolipoproteins E, which was reported to be involved in the mediation of the transport of drugs bound to NPs across the BBB [231], on the other hand, was identified in the ZnO NP-corona at all conditions. This was also the case with some other proteins like fibrinogen (alpha and beta), coagulation factor XIII A, prothrombin, most of the apolipoproteins, and most of the complement components. This could imply the strong interaction of these proteins with the surface of the ZnO NPs.

It has been reported that the nanoparticle's composition and surface chemistry dictate the extent and specificity of protein binding [217]. However, although the same chemical composition of the ZnO NPs was used in our study and Deng, *et al.* [8] study, there were differences in the corona obtained. The pregnancy zone protein and hepatogolbin proteins were not identified in our study. Many other proteins were identified in our study but not in their study but not in Deng's *et al.* study [8]. This could indicate the effect of experimental conditions on the corona formed. This again emphasizes the fact that rigorous conditions should be applied when conducting these studies in order to draw the right comparisons and conclusions.

The development of targeted ZnO NPs for clinical applications in breast cancer will depend on a deeper understanding of the targeted ZnO NP/protein interaction. The interaction between a NP and the cell membrane is mainly controlled by the adsorbed protein at the NP surface. Although we assessed the protein corona adsorbed onto the surface of the bare ZnO NPs, the protein corona adsorbed onto the RGD-targeted ZnO NPs has to be assessed. This is because the functional groups could strongly affect the type of protein, the amount, and also the conformation [24]. Future work should be aimed at studying the protein corona formed from human plasma onto the targeted ZnO-HCV-RGD-

GFP NPs, and to test whether this corona will affect targeting of the NPs to the integrin αvβ3 receptors on the breast cancer cells. In a preliminary experiment, the ZnO-HCV-RGD-GFP NPs were suspended in DMEM in the presence and absence of FBS and were introduced to the MDA-MB-231 cells under flow using a flow chamber. Binding of the ZnO-HCV-RGD-GFP ZnO NPs to the cells was tracked using confocal microscope. The targeted NPs were more homogenously distributed in the DMEM media supplemented with 10% FBS. Under flow, the ZnO-HCV-RGD-GFP NPs were rolling over and binding the MDA-MB-231 cells, binding was most likely mediated by integrin (data not shown). Proteins did not affect binding of the targeted ZnO NPs to the surface of the cells. However, quantification of binding in the presence and absence of FBS is required. No nonspecific binding of the targeted ZnO-HCV-RGD-GFP NPs to the glass of the chamber was observed in a control experiment without the cells (date not shown).

Table 9: Proteins detected on the surface of bare ZnO NPs after 1 h exposure to human plasma.

No.	Identified proteins	4°C, 10% plasma, 16,000 xg	37°C, 10% plasma, 16,000 xg	37°C, 10% depleted plasma, 16,000	37°C, 10% plasma, 6,000 xg	37°C, 90% plasma, 6,000 xg
1	Actin, cytoplasmic 1 OS=Homo sapiens GN=ACTB PE=1 SV=1				X	
2	Actin, cytoplasmic 2, N-terminally processed OS=Homo sapiens GN=ACTG1 PE=4 SV=1					X
3	Alpha-1-antitrypsin OS=Homo sapiens GN=SERPINA1 PE=1 SV=3				X	X
4	Alpha-2-antiplasmin OS=Homo sapiens GN=SERPINF2 PE=1 SV=3					X
5	Alpha-2-HS-glycoprotein OS=Homo sapiens GN=AHSG PE=4 SV=1			X		X
6	Alpha-2-macroglobulin OS=Homo sapiens GN=A2M PE=4 SV=1	X	X	X	X	X
7	Anastellin OS=Homo sapiens GN=FN1 PE=4 SV=1	X			X	X
8	Antithrombin-III OS=Homo sapiens GN=SERPINC1 PE=1 SV=1				X	
9	Apolipoprotein A-I OS=Homo sapiens GN=APOA1 PE=4 SV=1	X		X	X	X
10	Apolipoprotein A-II OS=Homo sapiens GN=APOA2 PE=1 SV=1	X		X	X	X
11	Apolipoprotein A-IV OS=Homo sapiens GN=APOA4 PE=1 SV=3	X	X	X	X	X
12	Apolipoprotein B-100 OS=Homo sapiens GN=APOB PE=1 SV=2	X	X	X	X	X
13	Apolipoprotein C-II OS=Homo sapiens GN=APOC2 PE=1 SV=1					X
14	Apolipoprotein C-III OS=Homo sapiens GN=APOC3 PE=1 SV=1		X	X	X	X
15	Apolipoprotein E OS=Homo sapiens GN=APOE PE=1 SV=1	X	X	X	X	X
16	Apolipoprotein L1 OS=Homo sapiens GN=APOL1 PE=4 SV=1	X	X	X		X
17	Apolipoprotein (a) OS=Homo sapiens GN=LPA PE=1 SV=1					X
18	Beta-2-glycoprotein 1 OS=Homo sapiens GN=APOH PE=1 SV=3				X	X
19	C4B1 OS=Homo sapiens GN=C4B PE=4 SV=1					X

No.	Identified proteins	4°C, 10% plasma, 16,000 xg	37°C, 10% plasma, 16,000 xg	37°C, 10% depleted plasma, 16,000	37°C, 10% plasma, 6,000 xg	37°C, 90% plasma, 6,000 xg
20	C4b-binding protein alpha chain OS=Homo sapiens GN=C4BPA PE=1 SV=2	X			X	X
21	C4b-binding protein beta chain OS=Homo sapiens GN=C4BPB PE=1 SV=1					X
22	Carboxypeptidase N catalytic chain OS=Homo sapiens GN=CPN1 PE=1 SV=1					X
23	CD5 antigen-like OS=Homo sapiens GN=CD5L PE=1 SV=1					X
24	Ceruloplasmin OS=Homo sapiens GN=CP PE=1 SV=1				X	X
25	Clusterin OS=Homo sapiens GN=CLU PE=1 SV=1	X			X	X
26	Coagulation factor V OS=Homo sapiens GN=F5 PE=1 SV=4					X
27	Coagulation factor X OS=Homo sapiens GN=F10 PE=1 SV=2					X
28	Coagulation factor XI OS=Homo sapiens GN=F11 PE=3 SV=1					X
29	Coagulation factor XII OS=Homo sapiens GN=F12 PE=1 SV=3		X	X	X	X
30	Coagulation factor XIII A chain OS=Homo sapiens GN=F13A1 PE=1 SV=4	X	X	X	X	X
31	Coagulation factor XIII B chain OS=Homo sapiens GN=F13B PE=1 SV=3					X
32	Complement C1q subcomponent subunit A OS=Homo sapiens GN=C1QA PE=1 SV=2				X	
33	Complement C1q subcomponent subunit B (Fragment) OS=Homo sapiens GN=C1QB PE=4 SV=1		X		X	X
34	Complement C1q subcomponent subunit C OS=Homo sapiens GN=C1QC PE=1 SV=3				X	X
35	Complement C1r subcomponent OS=Homo sapiens GN=C1R PE=1 SV=2	X	X		X	X
36	Complement C1s subcomponent OS=Homo sapiens GN=C1S PE=1 SV=1	X	X		X	X
37	Complement C3 OS=Homo sapiens GN=C3 PE=1 SV=2	X	X	X	X	X

No.	Identified proteins	4°C, 10% plasma, 16,000 xg	37°C, 10% plasma, 16,000 xg	37°C, 10% depleted plasma, 16,000	37°C, 10% plasma, 6,000 xg	37°C, 90% plasma, 6,000 xg
38	Complement component C4B OS=Homo sapiens GN=C4B-1 PE=4 SV=1	X	X	X	X	
39	Complement C5 OS=Homo sapiens GN=C5 PE=1 SV=4		X	X	X	X
40	Complement component C6 OS=Homo sapiens GN=C6 PE=1 SV=3			X	X	
41	Complement component C8 beta chain OS=Homo sapiens GN=C8B PE=1 SV=3				X	
42	Complement component C9 OS=Homo sapiens GN=C9 PE=1 SV=2				X	X
43	Complement factor B (Fragment) OS=Homo sapiens GN=CFB PE=3 SV=1			X	X	X
44	Complement factor D OS=Homo sapiens GN=CFD PE=1 SV=5					X
45	Complement factor H OS=Homo sapiens GN=CFH PE=1 SV=4	X		X	X	X
46	Dynactin subunit 1 OS=Homo sapiens GN=DCTN1 PE=4 SV=1					X
47	Desmoglein-1 OS=Homo sapiens GN=DSG1 PE=1 SV=2		X			
48	Desmoplakin OS=Homo sapiens GN=DSP PE=1 SV=3		X			
49	Desmocollin-1 Isoform 1BOS=Homo sapiens GN=DSC1		X	X		
50	Fermitin family homolog 3 OS=Homo sapiens GN=FERMT3 PE=1 SV=1					X
51	Fibrinogen alpha chain OS=Homo sapiens GN=FGA PE=1 SV=2	X	X	X	X	X
52	Fibrinogen beta chain OS=Homo sapiens GN=FGB PE=1 SV=2	X	X	X	X	X
53	Ficolin-3 OS=Homo sapiens GN=FCN3 PE=1 SV=2				X	X
54	Filamin-A OS=Homo sapiens GN=FLNA PE=2 SV=1					X
55	Gelsolin OS=Homo sapiens GN=GSN PE=1 SV=1		X	X	X	X
56	Glyceraldehyde-3-phosphate dehydrogenase OS=Homo sapiens GN=GAPDH PE=3 SV=1		X			
57	Hornerin OS=Homo sapiens GN=HRNR PE=1 SV=2		X			

No.	Identified proteins	4°C, 10% plasma, 16,000 xg	37°C, 10% plasma, 16,000 xg	37°C, 10% depleted plasma, 16,000	37°C, 10% plasma, 6,000 xg	37°C, 90% plasma, 6,000 xg
58	Haptoglobin-related protein OS=Homo sapiens GN=HPR PE=1 SV=2					X
59	HCG1745306, isoform CRA_a OS=Homo sapiens GN=HBA2 PE=3 SV=1					X
60	Heparin cofactor 2 OS=Homo sapiens GN=SERPIND1 PE=1 SV=3				X	X
61	Histidine-rich glycoprotein OS=Homo sapiens GN=HRG PE=1 SV=1				X	X
62	HPX protein OS=Homo sapiens GN=HPX PE=2 SV=1					X
63	Hemopexin OS=Homo sapiens GN=HPX PE=1 SV=2				X	
64	Ig alpha-1 chain C region OS=Homo sapiens GN=IGHA1 PE=1 SV=2				X	X
65	Ig gamma-1 chain C region OS=Homo sapiens GN=IGHG1 PE=1 SV=1	X	X		X	X
66	Ig gamma-2 chain C region OS=Homo sapiens GN=IGHG2 PE=1 SV=2	X			X	X
67	Ig gamma-3 chain C region OS=Homo sapiens GN=IGHG3 PE=1 SV=2	X	X		X	X
68	Ig heavy chain V-I region V35 OS=Homo sapiens PE=1 SV=1					X
69	Ig heavy chain V-III region BRO OS=Homo sapiens PE=1 SV=1	X				X
70	Ig heavy chain V-III region TIL OS=Homo sapiens PE=1 SV=1	X				
71	Ig heavy chain V-III region CAM OS=Homo sapiens PE=1 SV=1					X
72	Ig heavy chain V-III region KOL OS=Homo sapiens PE=1 SV=1					X
73	Ig kappa chain V-I region HK101 (Fragment) OS=Homo sapiens PE=4 SV=1					X
74	Ig kappa chain V-II region RPMI 6410 OS=Homo sapiens PE=4 SV=1					X
75	Ig kappa chain V-II region TEW OS=Homo sapiens PE=1 SV=1					X
76	Ig kappa chain V-III region HIC OS=Homo sapiens PE=2 SV=2					X
77	Ig kappa chain V-II region Cum OS=Homo sapiens PE=1 SV=1	X				

No.	Identified proteins	4°C, 10% plasma, 16,000 xg	37°C, 10% plasma, 16,000 xg	37°C, 10% depleted plasma, 16,000	37°C, 10% plasma, 6,000 xg	37°C, 90% plasma, 6,000 xg
78	Ig kappa chain V-III region SIE OS=Homo sapiens PE=1 SV=1	X			X	
79	Ig kappa chain V-III region B6 OS=Homo sapiens PE=1 SV=1	X				
80	Ig lambda chain V-I region BL2 OS=Homo sapiens PE=2 SV=1					X
81	Ig lambda chain V-I region NEWM OS=Homo sapiens PE=1 SV=1					X
82	Ig lambda chain V-I region WAH OS=Homo sapiens PE=1 SV=1					X
83	Ig lambda chain V-III region LOI OS=Homo sapiens PE=1 SV=1					X
84	Ig lambda chain V-I region HA OS=Homo sapiens PE=1 SV=1	X				
85	Ig lambda chain V-III region SH OS=Homo sapiens PE=1 SV=1	X				
86	Ig lambda chain V-IV region Bau OS=Homo sapiens PE=1 SV=1	X				
87	Ig lambda chain V-IV region Hil OS=Homo sapiens PE=1 SV=1	X				X
88	Ig lambda-2 chain C regions OS=Homo sapiens GN=IGLC2 PE=1 SV=1	X			X	X
89	Ig kappa chain C region OS=Homo sapiens GN=IGKC PE=1 SV=1	X	X		X	X
90	Isoform 2 of Ig mu chain C region OS=Homo sapiens GN=IGHM	X				
91	Ig lambda-like polypeptide 5 OS=Homo sapiens GN=IGLL5 PE=2 SV=2	X			X	X
92	Ig mu chain C region OS=Homo sapiens GN=IGHM PE=1 SV=3	X	X		X	X
93	Ig J chain OS=Homo sapiens GN=IGJ PE=1 SV=4	X	X			X
94	Insulin-like growth factor-binding protein 3 OS=Homo sapiens GN=IGFBP3 PE=4 SV=1					X
95	Insulin-like growth factor-binding protein 5 OS=Homo sapiens GN=IGFBP5 PE=1 SV=1					X
96	Insulin-like growth factor-binding protein complex acid labile subunit OS=Homo sapiens GN=IGFALS PE=4 SV=1				X	X

No.	Identified proteins	4°C, 10% plasma, 16,000 xg	37°C, 10% plasma, 16,000 xg	37°C, 10% depleted plasma, 16,000	37°C, 10% plasma, 6,000 xg	37°C, 90% plasma, 6,000 xg
97	Integrin alpha-IIb OS=Homo sapiens GN=ITGA2B PE=1 SV=3					X
98	Integrin beta-3 OS=Homo sapiens GN=ITGB3 PE=4 SV=1					X
99	Inter-alpha (Globulin) inhibitor H2 OS=Homo sapiens GN=ITIH2 PE=2 SV=1					X
100	Inter-alpha-trypsin inhibitor heavy chain H1 OS=Homo sapiens GN=ITIH1 PE=2 SV=1	X	X	X	X	X
101	Inter-alpha-trypsin inhibitor heavy chain H2 OS=Homo sapiens GN=ITIH2 PE=1 SV=2		X	X	X	
102	inter-alpha-trypsin inhibitor heavy chain H4 OS=Homo sapiens GN=ITIH4 PE=4 SV=1			X	X	X
103	Junction plakoglobin OS=Homo sapiens GN=JUP PE=1 SV=3		X			
104	Kininogen-1 OS=Homo sapiens GN=KNG1 PE=1 SV=2			X	X	X
105	Keratinocyte proline-rich protein OS=Homo sapiens GN=KPRP PE=1 SV=1		X			
106	Mannan-binding lectin serine protease 1(Isoform 4 of) OS=Homo sapiens GN=MASP1					X
107	Methylcytosine dioxygenase TET3 OS=Homo sapiens GN=TET3 PE=2 SV=3					X
108	Peptidyl-prolyl cis-trans isomerase A OS=Homo sapiens GN=PPIA PE=1 SV=2					X
109	Plasma kallikrein light chain (Fragment) OS=Homo sapiens GN=KLKB1 PE=3 SV=1					X
110	Plasma protease C1 inhibitor OS=Homo sapiens GN=SERPING1 PE=3 SV=1					X
111	Plasma serine protease inhibitor OS=Homo sapiens GN=SERPINA5 PE=1 SV=3					X
112	Plasminogen OS=Homo sapiens GN=PLG PE=1 SV=2		X	X	X	X
113	Platelet basic protein OS=Homo sapiens GN=PPBP PE=1 SV=3					X
114	Platelet factor 4 variant OS=Homo sapiens GN=PF4V1 PE=1 SV=1					X

No.	Identified proteins	4°C, 10% plasma, 16,000 xg	37°C, 10% plasma, 16,000 xg	37°C, 10% depleted plasma, 16,000	37°C, 10% plasma, 6,000 xg	37°C, 90% plasma, 6,000 xg
115	Platelet glycoprotein Ib beta chain OS=Homo sapiens GN=GP1BB PE=4 SV=1					X
116	Profilin-1 OS=Homo sapiens GN=PFN1 PE=1 SV=2					X
117	Prothrombin OS=Homo sapiens GN=F2 PE=1 SV=2	X	X	X	X	X
118	Putative annexin A2-like protein OS=Homo sapiens GN=ANXA2P2 PE=5 SV=2		X	X		
119	Radixin OS=Homo sapiens GN=RDX PE=2 SV=1					X
120	REVERSED Fibrinogen beta chain OS=Homo sapiens GN=FGB PE=1 SV=2					X
121	Secreted phosphoprotein 24 OS=Homo sapiens GN=SPP2 PE=1 SV=1					X
122	Selenoprotein P (Fragment) OS=Homo sapiens GN=SEPP1 PE=4 SV=1					X
123	Serum albumin OS=Homo sapiens GN=ALB PE=4 SV=2	X	X		X	X
124	Serum amyloid P-component OS=Homo sapiens GN=APCS PE=1 SV=2					X
125	Shroom3 OS=home sapiens GN=SHROOM3 PE=1 SV=2	X				
126	Sulfhydryl oxidase 1 OS=Homo sapiens GN=QSOX1 PE=1 SV=3					X
127	Suprabasin OS=Homo sapiens GN=SBSN PE=4 SV=1		X	X		
128	Transcription initiation factor TFIID subunit 9B OS=Homo sapiens GN=TAF9B PE=1 SV=1	X				X
129	Talin 1 OS=Homo sapiens GN=TLN1 PE=2 SV=1					X
130	Tetranectin OS=Homo sapiens GN=CLEC3B PE=4 SV=1		X	X		
131	Transthyretin OS=Homo sapiens GN=TTR PE=3 SV=1				X	X
132	Tubulin beta chain OS=Homo sapiens GN=TUBB PE=3 SV=1					X
133	Vitamin K-dependent protein C heavy chain OS=Homo sapiens GN=PROC PE=3 SV=1					X

No.	Identified proteins	4°C, 10% plasma, 16,000 xg	37°C, 10% plasma, 16,000 xg	37°C, 10% depleted plasma, 16,000	37°C, 10% plasma, 6,000 xg	37°C, 90% plasma, 6,000 xg
134	Vitamin K-dependent protein S OS=Homo sapiens GN=PROS1 PE=1 SV=1	X	X		X	X
135	Vitronectin OS=Homo sapiens GN=VTN PE=1 SV=1		X	X	X	X

7 Synthesis of ZnO nanowires (NWs) and their toxicity to MDA-MB-231 breast cancer cells

Among the various morphologies of ZnO NMS, nanowires (NWs) have recently attracted particular attention due to their unique one dimensional structure with highly controlled length and diameters. Compared to ZnO NPs, the ZnO NWs have the advantage of efficient tumor targeting due to the polyvalency effect, which are characterised by the simultaneous binding of multiple ligands on one biological entity [232], and the potential for multifunctional agents. ZnO is a wide band gap semiconductor (3.37 eV) with high exciton binding energy (60 meV), which leads to efficient excitonic blue and near-UV emission [233] with potential use as optical probes for bioimaging applications [234]. The use of ZnO NWs for bioimaging has the advantage of enhancing the intensity of the luminescence of ZnO [12].

High aspect ratio ZnO NWs have been shown to exhibit toxic effects on a number of prokaryotic and eukaryotic cells [235]. They also demonstrated successful results in breast cancer photodynamic therapy [85]. It has been reported that ZnO NWs significantly improved the antitumor activity of the conventional drug Daunorubicin against hepatocarcinoma cells [86].

In this study, the ZnO NWs were synthesized by both template assisted and template free electrodeposition and they were characterised by SEM and TEM. Because the amount of the NWS obtained by template electrodeposition was low, free electrodeposition of ZnO NWs on glass was used to prepare the ZnO NWs for cell exposure experiments. The effect of the in-house prepared ZnO NWs on the metabolic activity of the MDA-MB-231 was assessed using the ATP assay.

7.1 Synthesis of 1D ZnO nanostructures

Some of the several methods developed to synthesize ZnO NWs will be discussed in this chapter with the focus on electrochemical method.

ZnO is a versatile functional material and it has a rich family of 1D nanostructures such as nanotubes, nanorods, nanowires, nanobelts, nanorings, and nanosprings [116].

Various chemical, electrochemical and physical deposition techniques have been used to synthesize 1D ZnO nanostructures with different diameter and length [188]. The growth mechanisms of 1D ZnO nanostructures in all these techniques are based on two main methods; vapour-phase method and solution-phase method. These methods are discussed in details by Singh in his comprehensive review paper about the growth and synthesis of ZnO NWs [236]. Some of these methods will be discussed here with the focus on the solution phase methods.

7.1.1 Vapour phase method

The vapour phase method is a well-developed method which gives good crystallinity and controlled morphology of the prepared nanostructures [237-239]. However, it requires sophisticated equipment and conditions (e.g. high vacuum and temperature). In this method, condensed or powder source material is vaporised at high temperature, then the resultant vapour phase condenses at certain conditions of temperature, pressure, substrate, *etc.* to produce the desired nanostructure. To control the diameter, aspect ratio and crystallinity different techniques are employed, these include thermal chemical vapour deposition (CVD) [240-243], metal-organic chemical vapour deposition (MOCVD) [244], pulsed laser deposition (PLD) [245] and direct thermal evaporation [246, 247]. These growth methods are based on two mechanisms: vapour-liquid-solid (VLS) or vapour-solid (VS) [236].

7.1.2 Solution phase method

The solution phase method is a less complicated and a more recent growth method. Herein, the deposition operates at a lower temperature and under atmospheric pressure, thus reducing the cost and the complexity of fabrication. ZnO NWs and nanorods growth has been successfully achieved in high yields in solution. In order to guide and confine the growth direction, a number of approaches have been used. These can be grouped into template-free method and template-assisted methods.

7.1.2.1 Template-assisted method

This method makes use of periodically structured templates to define the morphology and size of nanostructures. A variety of templates have been used to produce 1D nanostructures, for example, anodic aluminium oxide membranes (AAM) have hexagonally

ordered nanochannels which can be filled to form 1D nanostructures. ZnO NWs have been successfully obtained by template assisted electrodeposition [248, 249].

7.1.2.2 Template-Free Method

Recent progress using solution phase techniques has resulted in the creation of 1D ZnO nanostructures by template-free methods. There are three common approaches to fabricate 1D nanostructures by this method, these include hydrothermal [250-252], chemical bath deposition (CBD) [253], and electrochemical deposition (ECD) [254, 255]. These methods benefits from the inherent anisotropic growth of ZnO because of variation in surface energy due to its surface polarity along the c-axis in the layered wurtzite structure [116]. A seeding layer on the substrate which could be ZnO powder, Zn powder or ZnO NPs and molecular capping agents, such as surfactants [256] can also be used to control the growth of more complex 1D ZnO nanostructures. The molecular capping agents control the kinetics of nanocrystal growth by preferentially adsorbing to specific crystal facets or by chelating the Zn^{2+} ion in solution, thus modifying the growth process.

7.1.3 Electrochemical deposition (ECD)

This method has several key advantages over the other deposition techniques, including simplicity, low temperature, low cost, and scalability [188, 257-259]. It employs a potential applied between two electrodes immersed in a solution which contains a salt of the metal species to be deposited. A third electrode (reference electrode) is used to monitor the reaction. Using this method, the morphology of the obtained nanostructures is largely influenced by a number of parameters, namely, electrolyte pH, the temperature of the solution [258, 260, 261], stirring rates, type and concentration of precursor and the applied potential [258, 262]. Ryan and co-workers have reported the effect of ECD time and substrate surface preparation on the growth of ZnO nanorods and nanoplates [263].

The first deposition of ZnO films by electrochemical method from aqueous solutions have been reported by both Izaki's group and Lincot's group in 1996 [264]. Izaki and Omi (1996) [265] cathodically deposited transparent ZnO films from aqueous zinc nitrate ($Zn(NO_3)_2$) solution on a glass substrate coated with tin oxide. On the other hand, Peulon *et al.* [188] used zinc chloride ($ZnCl_2$) to deposit ZnO films on tin oxide deposited on

glass substrate. Two years later, Lincot's group reported a detailed mechanism of the process [188]. They concluded that the deposition temperature and the bath composition are the key parameters that determine the quality of the deposited films. At temperatures below 50°C, amorphous insulating zinc hydroxide films are formed, whereas, well-crystallized and semi-conducting zinc oxide films are obtained at higher temperatures.

7.1.3.1 Template-free electrodeposition of ZnO nanowires

As mentioned earlier, several studies have been reported on the synthesis of ZnO NWs and nanorods by template-free electrodeposition [253, 255, 266, 267] . In this method ZnO NWs are achieved by utilising the intrinsic anisotropic crystallographic structure of a targeted material. Wong *et al.*,[267] for example, have grown ZnO nanorods on polycrystalline Zn foil by cathodic electrodeposition in an aqueous solution of $CaCl_2$ at 80°C.

7.1.3.2 Template – assisted electrodeposition of ZnO nanowires

Among various NWs fabrication methods, template synthesis combined with electrodeposition is an effective and an elegant method for preparing 1D nanostructure. As mentioned earlier, this method uses a template to direct the 1D growth. ZnO NWs have been electrodeposited into two kinds of templates, AAM and track-etched polycarbonate templates with cylindrical channels. The obtained NWs shape, direction and size are all determined by the architecture of the porous template. In template assisted ECD, the ions in the electrolyte solution can access deep inside the pores of the template for the deposition process.

In general, the template assisted electrodeposition of 1D nanostructure follows the following scheme (Figure 104). Firstly, one side of the template is coated with a thin layer of metal (Au, Ag, etc.) to act as the working electrode in the three electrode electro-chemical cell. Secondly, the deposition of the 1D structure occurs inside the nanopores of the template, starting from the deposited metal side. Secondly, the 1D nanostructure, which could be NWs or nanotubes, will be formed in the nanopores of the template after electrodeposition under proper conditions for certain duration. The duration of electrochemical deposition will determine the length of the prepared wires. Finally the deposited NWs can be obtained by the removal of the conductive layer and the template.

The templates can be removed by dissolving them in a solvent in which the desired wires are insoluble [268, 269].

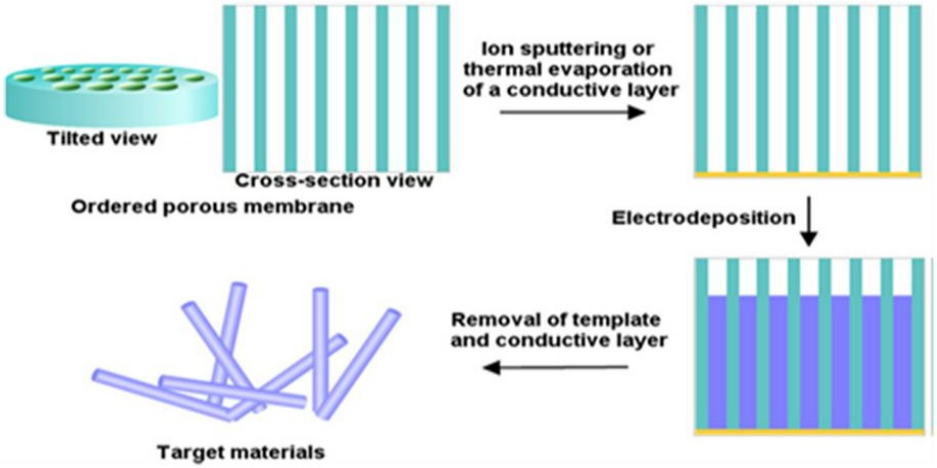

Figure 104: Schematic of electrosynthesis of nanomaterials within a template containing cylindrical pores (adapted from [268]).

Template assisted ECD of ZnO NWs has been obtained by direct one step and indirect ECD. The one step ECD of ZnO NWs using templates is suggested as follows; hydroxide ions are first generated in the mild acidic solution of Zn^{2+} by the reduction of an oxygen precursor which could be either dissolved oxygen, nitrate ions or hydrogen peroxide as shown in equations 1, 2 and 3, respectively. The formation of the hydroxide ions increases the pH in the vicinity of the working electrode causing precipitation of Zn^{2+} ions as zinc hydroxide at the cathode (equation 4). Finally, zinc hydroxide spontaneously dehydrates into ZnO (equation 4). ZnO particles precipitate on the working electrode at the base of the membrane channels and then ZnO nanorods grow due to the transport of Zn^{2+} and the hydroxide precursor from the bulk solution to the working electrode. The indirect ECD of ZnO NWs is based on electrodeposition of Zn metal and then oxidation of metallic zinc NWs by annealing the templates to obtain ZnO NWs arrays.

$$O_2 + 2H_2O + 4e^- \rightarrow 4OH^-$$ **Equation 1**

$$No_3^- + H_2O + 2e^- \rightarrow No_2^- + 2OH^-$$ **Equation 2**

$$H_2O_2 + 2e^- \rightarrow 2OH^-$$ **Equation 3**

$$Zn^{2+} + 2OH^- \leftrightarrow Zn(OH)_2 \rightarrow ZnO_{(s)} + H_2O$$ **Equation 4**

Two types of membranes have been used for template assisted electrodeposition of ZnO NWs; AAM [248, 249] and nuclear track-etched polymer (polycarbonate) membranes [270]. Compared to inorganic membranes, polycarbonate membranes are flexible and can be used in some special circumstances. Track-etched polycarbonate membranes can be easily removed to release the as-deposited nanostructures by dissolving in dichloromethane or chloroform solvents. They are commercially available with a wide range of pore diameters (10 - 2000 nm), however their pore density is relatively low (10^9 pores/cm^2), an order of magnitude smaller than AAM. Additionally, some channels may intersect within the membranes due to the pore-production process [268].

ZnO NWs were electrochemically produced within track etched polycarbonate membranes (PCM) in an aqueous solution of potassium chloride and zinc chloride using H_2O_2 as an oxygen precursor [271]. Lai and Riley [272], 2006, synthesised ZnO nanorods by electrodeposition into polycarbonate membranes. In the presence of Zn^{2+} ions, monocrystaline ZnO NWs were grown using nitrate ions (0.01 M $Zn(NO_3)_2$) at a constant potential of -0.7 V at 90 °C, while polycrystals were deposited from peroxide ions at a fixed potential of -0.2 V at 22 °C. [270, 273] also managed to fabricate ZnO NWs using PCM. The ECD was conducted under -0.8 V at 90°C [273] and under -0.7 V at 70°C [270] in 0.1 M $Zn(NO_3)_2$ solution. They suggested that increasing the temperature of deposition increases the structural quality of the obtained wires. Recently, Sharma *et al.* [269] synthesized ZnO NWs using 0.1 M $Zn(NO_3)_2$ at 75 °C. The electrodeposition was performed at different potentials of -0.8, -1.0 and -1.2 V. They concluded that the ZnO NWs grown at higher negative potential have a higher fraction of large size crystallites and are polycrystalline in nature. Another recent fabrication of ZnO NWs using polycarbonate templates has been carried out by Müller *et al.* [10]. High aspect ratio ZnO NWs were prepared by ECD into PCM in an aqueous solution of 0.1 M $Zn(NO_3)_2$ solution under -0.8 potential and at 65^{o}C [261].

7.2 Materials and Methods

7.2.1 Materials

All materials were of analytical grade and used without further purification. Zinc nitrate ($Zn(NO_3)_2$.6H2O) (assay ≥ 99.0%) was obtained from Sigma-Aldrich. Zinc standard in nitric acid at 1000 ppm was supplied by MBA Analytical Ltd, UK. PCMs were obtained from Agar

Scientific (Dorset, UK). Dichloromethane was supplied from VWR. KCl (99%) was purchased from BDH. $ZnCl_2$ (98%) was obtained from Sigma-Aldrich. Ethanol (absolute, 99.9%) and hexane (95%) were from VWR.

7.2.2 ZnO nanowires template- assisted electrodeposition

Nanoporous track-etched polycarbonate membranes were used as templates for ZnO NWs growth by electrochemical deposition.

1. <u>Electrodeposition</u>

ZnO NWs were fabricated by electrodeposition into nuclepore PCMs according to Müller *et al.* with modifications. The membrane was 6 µm thick, 25 mm in diameter, and the pore density was 6 x 10^8 pores/cm^2. The nominal pore size of the membrane was 50 nm. One side of the membrane was coated with layer of gold, 100 nm thick, by sputter deposition, using Emitech k575X sputter coater, to serve as a working electrode. The counter electrode used was a platinum mesh and Ag/AgCl/KCl (3.5 M) electrode was used as the reference electrode. Based on previous work, electrodeposition was conducted using 0.1 M $Zn(NO_3)_2$ aqueous solution under a constant potential of -0.8 V vs. Ag/AgCl and at 70 °C with an accuracy of ±1 °C, using a hot plate (Heidolph Instruments) equipped with a temperature sensor. The ECD was carried out for 30 min. Before starting electrodeposition, the membrane was left in the cell with $Zn(NO_3)_2$ solution for 15 min to equilibrate the temperature and dislodge air bubbles from the membrane and allow its wetting. As mentioned earlier, ZnO precipitation in this system is induced by the formation of hydroxide ions generated by reduction of the nitrate ions in the aqueous solution as shown in equations 2 and 4 previously described in section 7.1.3.2.

2. <u>Liberation of ZnO nanowires from their template and purification</u>

After electrodeposition, the electrolyte solution was discarded and the polycarbonate template was removed from the electrodeposition cell, the area of the membrane exposed to electrodeposition (≈1cm^2) was incubated in 2 ml dichloromethane for 1 h to dissolve the PCM. The solution was then gently agitated to dislodge the NWs, and the gold foil was then removed with a pair of forceps. After that, the ZnO NWs were collected by centrifugation at 3000 xg for 10 min and the resulting pellets were washed six times with 2 ml

dichloromethane to remove the undissolved polycarbonate residue. Finally, the dichloromethane was evaporated from the pellet using a stream of nitrogen and the resulted wires were suspended in pure ethanol to serve as the stock solution.

In order to study how the ZnO NWs dislodged from the gold layer, a piece of the whole membrane with gold was removed from the dichloromethane after few minutes of incubation of the membrane with dichloromethane, then it was examined under SEM after coating with gold to prevent charging. To check the reproducibility of the aspect ratio of the obtained wires by template assisted electrodeposition, another two batches of the ZnO nanowires were prepared and the length of the wires obtained from each batch was characterised.

7.2.3 Zinc oxide nanowires deposition on gold coated glass plates (template free method)

1. <u>Preparation of the working electrode</u>

The working electrode for the cathodic deposition of ZnO NWs was a 12 nm gold film sputtered on glass prepared by Emitech k575X sputter coater. The microscope glass slides (VWR) were successively washed prior to sputtering in Acetone (VWR, 99.9%), methanol (VWR, 99.8%), 1.0 M Sodium Hydroxide (NaOH) (VWR, 99%), and deionized water (Purite deionizer). The electrical connection between the sample and an electrical wire was achieved by a drop of silver paint (Agar). The contact was then covered with copper tape and insulating paint (Miccro Super XP200 Lacquer, Hi-Tek Products Ltd). Before deposition, the electrode was cleaned with compressed air.

2. <u>Electrodeposition</u>

Potassium Chloride (KCl, 0.1 M) was used as the supporting electrolyte and Zinc Chloride ($ZnCl_2$, 0.1 mM) was used as the zinc precursor. All the chemicals were of analytical grade and used without further purification. Oxygen gas (O_2) (BOC Gases Ltd) was bubbled for 30 min prior to electrodeposition so that the solution becomes saturated with O_2. Bubbling was maintained during the deposition. The temperature was kept constant at 85 °C, with an accuracy of ±1 °C, using a hot plate (Heidolph Instruments) equipped with a temperature sensor. The electrochemical cell employed a three-electrode setup. The gold coated glass

slide served as the working electrode while a platinum mesh and a Ag/AgCl/KCl (3.5 M) electrode were used as the counter and reference electrode, respectively. Electrodeposition was performed under the potentiostatic transient mode, with a potential of -0.9 V vs. Ag/AgCl. A potentiostat (Princenton VersaSTAT 3) connected to a PC was used to control the potential and measure the current. The deposition was terminated when the desired amount of charge had passed through the system. The deposited films were gently soaked in deionized water, dried in ambient atmosphere and stored in a desiccator.

3. Liberation of Nanowires from the substrate

In order to liberate the NWs from the substrate, the gold film was oxidized by the application of an anodic potential. Potassium Chloride (KCl, 0.05 M) (VWR, 100%) was used as the electrolyte in a similar setup as for electrodeposition. A potential of 1.4 V Ag/AgCl was maintained until all of the gold was oxidized. The substrate was left to dry in ambient atmosphere. The electrical connections were carefully removed and the substrates were sonicated in ethanol for 5 min. The ethanol dispersion of the wires was transferred to 50 mL centrifuge tubes and hexane was added so that the hexane: ethanol ratio was 2:1. The NWs were then collected by centrifugation at 4500 rpm for 15 min and allowed to dry. The resulting precipitates were redispersed in ethanol and transferred to eppendorf tubes.

7.2.4 Characterisation of ZnO nanowires

After the preparation of the ZnO NWs, different techniques were used to characterise their shape, size and structure. Information on the morphology and size of ZnO NWs was obtained by SEM and TEM. Energy dispersive X-ray (EDX) was used for chemical analysis.

7.2.4.1 Scanning electron microscopy (SEM)

Information on the morphology of the NWs prepared by both template assisted and template free methods was obtained by SEM (LEO 1525) operating in secondary electron mode at 5 kV using the In lens detector.

After electrochemical deposition of ZnO NWs into the polycarbonate template, the template was incubated with dichloromethane for few minutes and a piece of the whole membrane coated with a layer of gold, was removed from the dichloromethane solution and imaged in the SEM on an aluminium stub. To prevent sample charging, the sample was

coated with 5 nm gold layer. Also, after liberation of the ZnO NWs from their template, a drop of the NWs dispersed in ethanol was transferred to an aluminium stub and then dried at ambient temperature. The wires were then examined in the SEM after coating with gold to prevent charging.

After electrochemical deposition of ZnO NWs on glass substrate, the dried substrate with the ZnO NWs was transferred to an aluminium stub and the wires were examined in the SEM after coating with gold to prevent charging. Also, after liberation of the ZnO NWs from their substrate, a drop of the NWs dispersed in ethanol was transferred to an aluminium stub and then dried at ambient temperature. The wires were then examined in the SEM after coating with gold to prevent charging. The size distribution of the ZnO NWs was calculated using SEM images and ImageJ software (http://rsbweb.nih.gov/ij/).

7.2.4.2 Transmission electron microscopy (TEM)

The shape and the structure of the ZnO NWs prepared by template electrodeposition was also assessed in the JEOL 2000 (Peabody, MA, USA) operated at 200 kV. Microfilms were prepared by immersing lacy carbon coated copper TEM grids (Agar Scientific Ltd, UK) into the ethanolic ZnO NWs dispersions and drying at RT. The diameter and length of the ZnO NWs was calculated using bright-field TEM images and ImageJ software (http://rsbweb.nih.gov/ij/). Chemical characterisation of the ZnO NWs prepared into the polycarbonate template was studied using EDX.

7.2.5 ATP viability assay

The MDA-MB-231 cells were plated in flat-bottomed 96- well plates (Fisher Scientific Ltd, UK) as described in section 4.1.2 of this study. The template assisted electrodeposition produced a low yield of the ZnO NWs, while a reasonable yield could be obtained by electrodeposition of the NWs on glass substrates; therefore, electrodeposition on glass was used to prepare ZnO NWs for the ATP viability assay. Suspensions of the ZnO NWs were prepared in ethanol, to ensure the NWs sterility for the assays; ethanol was then evaporated in sterile conditions at RT. The NWs were suspended aseptically in the same DMEM media used to test the viability of the bare and the targeted ZnO NPs and stored at 4°C. The ZnO NWs stock dispersions were first sonication for 20 s on a bench sonicator and

working concentrations of 20, 30 and 50 µg/ml were freshly prepared in DMEM supplemented with 1% FBS and directly applied to the MDA-MB-231 cells for 24 and 48 h. The assay was repeated twice and the result was represented as average viability ± SD. Statistical analysis was carried out using a paired Student's *t*-test. The level of significance was accepted at p≤0.05. The levels of significance was indicated by the Asterisks: *p < = 0.05, **p < = 0.01 [160].

7.3 Results and Discussion

7.3.1 Characterisation of zinc oxide nanowires

High aspect ratio ZnO NWs were successfully fabricated by electrodeposition into high quality polycarbonate membrane filters and gold coated glass substrates and the obtained ZnO NWs have a very smooth flat surface.

7.3.1.1 ZnO nanowires template- assisted electrodeposition

Size and morphology of the ZnO NWs

Examination of the PCM by SEM after few minutes of incubation with dichloromethane revealed that the ZnO NWs do not detach themselves directly at the point of attachment with gold, but they rather break close to the gold layer, and this occurs as soon as the polycarbonate membrane starts to dissolve. After breakage, residues of the wires could be observed clearly attached to the gold layer (Figure 105, A). The as-prepared ZnO NWs had a tapered shape with a broad base and a narrow tip (Figure 105, A). After 1 h incubation of the ZnO NWs in dichloromethane and subsequent cleaning, the wires were successfully liberated from their template and appeared clean (Figure 105, B, C). The TEM images also showed a high degree of agglomeration of the wires (Figure 105, D). There was a variation in the length of the ZnO NWs due to their damage during liberation from the polycarbonate templates and subsequent purification, the frequency distribution of the ZnO NWs after centrifugation is shown in Figure 106. The average length of the wires was 1462 ± 673 nm (n=343). Chemical analysis of the prepared ZnO NWs confirmed the presence of zinc (Zn Lα and Kα peaks) (Figure 107).

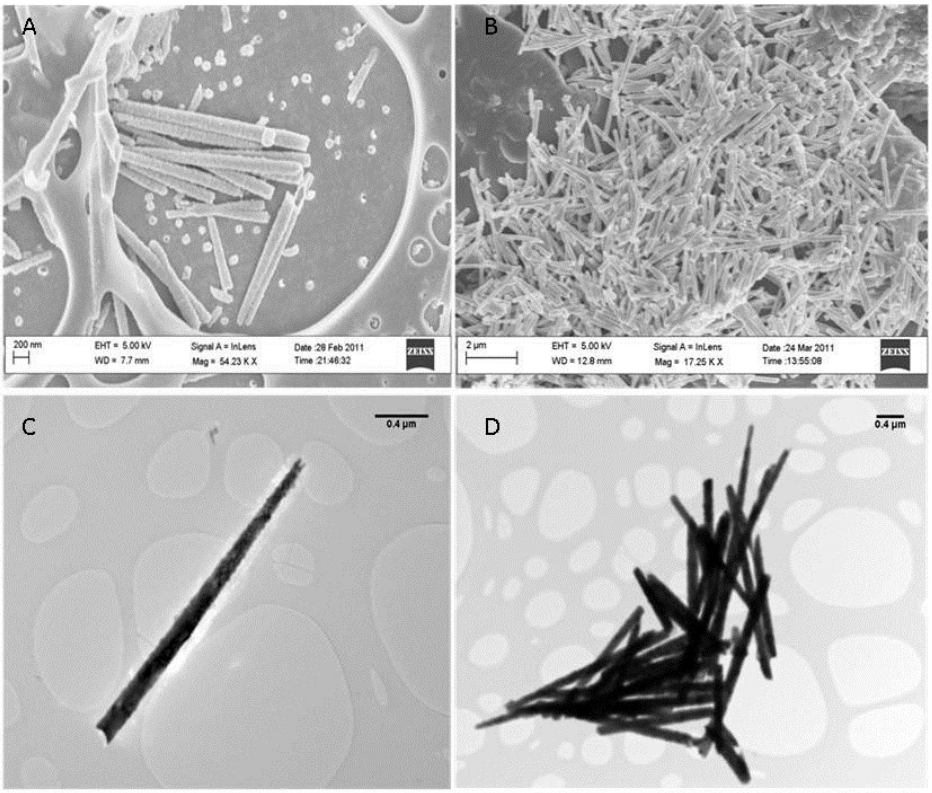

Figure 105: Characterisation of ZnO NWs prepared by template assisted electrodeposition. (A) SEM image of ZnO NWs after few minutes of incubation of the polycarbonate templates with dichloromethane. (B) SEM image of the purified ZnO NWs. (C) TEM image of an individual purified ZnO nanowire. (D) TEM image of aggregated ZnO NWs.

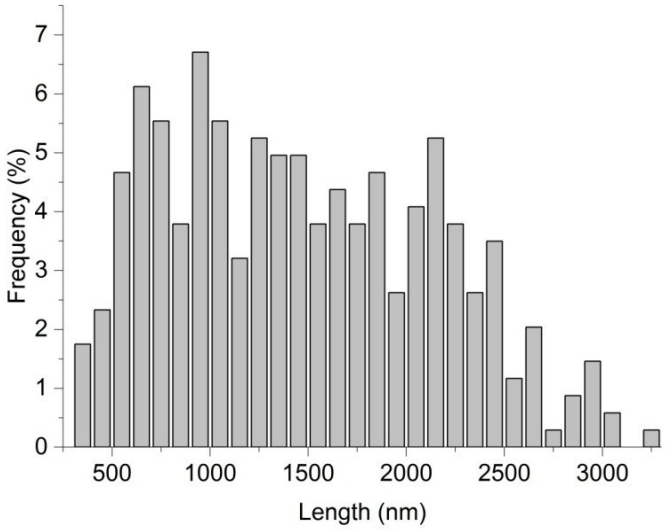

Figure 106: Length frequency distribution curve of ZnO NWs prepared by polycarbonate template electrodeposition. Average size =1462 ± 673 nm (n=343).

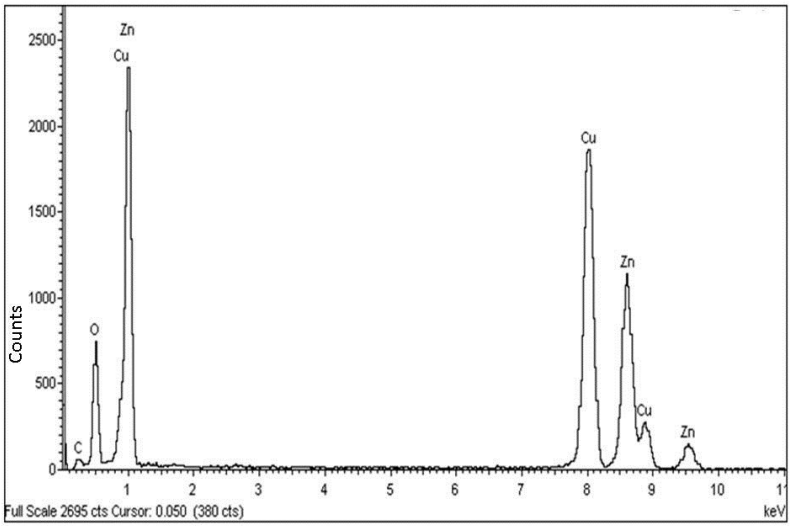

Figure 107: EDX spectra of the electrodeposited ZnO NWs.

7.3.1.2 Zinc oxide nanowires electrodeposited on glass substrates

The ZnO NWs prepared by electrochemical deposition on glass substrates were successfully liberated from their substrates (Figure 108). The wires had a uniform diameter 37 ± 12 nm (n=259) throughout their length, but showed a variation in the length with an average of 330 ± 344 nm (n=1750). The diameter and length frequency distribution of the ZnO NWs are presented in Figure 109 and Figure 110, respectively.

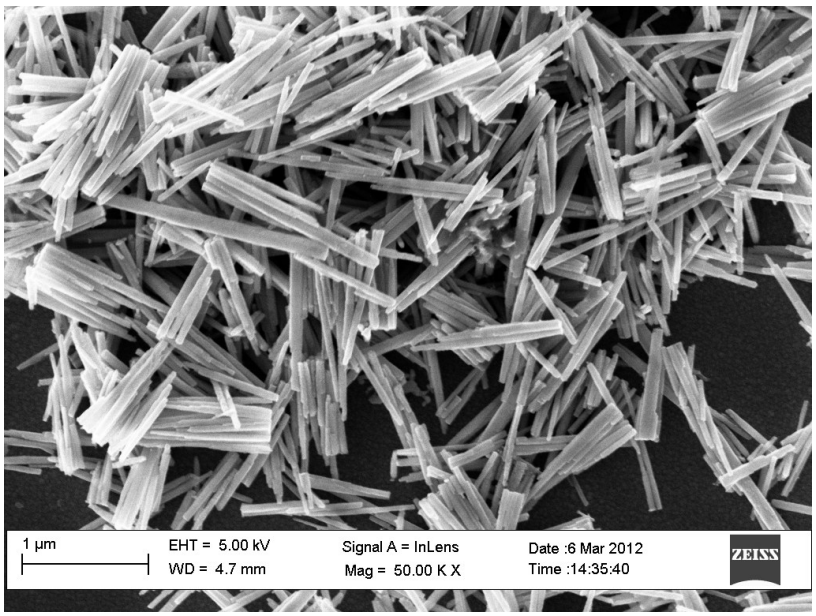

Figure 108: SEM image of ZnO NWs prepared by electrodeposition on glass plates after liberation from the substrate.

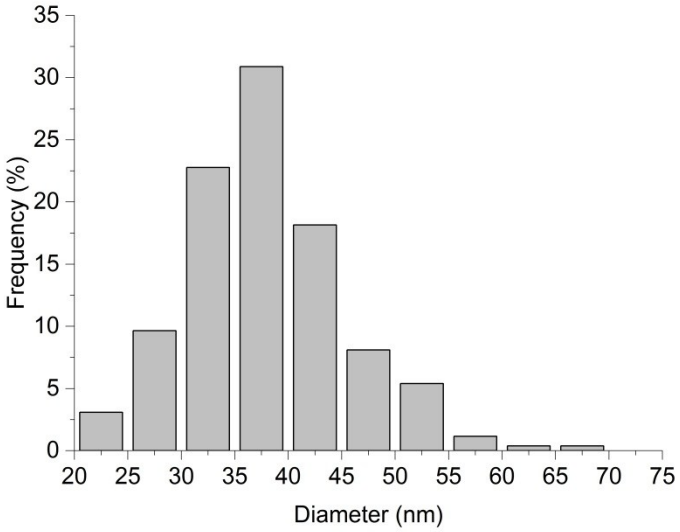

Figure 109: Diameter frequency distribution curve of ZnO NWs prepared on glass substrates. Average diameter =37 ± 12 nm (n=259).

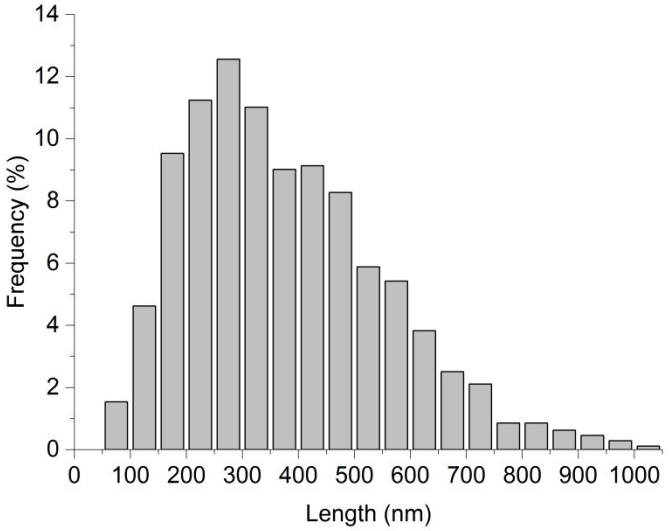

Figure 110: Length frequency distribution curve of ZnO NWs prepared on glass substrates. Average length =330 ± 344 nm (n=1750).

7.3.2 Toxicity of ZnO NWs to the MDA-MB-231 cells

The ATP assay showed that the ZnO NWs resulted in a dose and time dependent toxicity in the MDA-MB-231 cells (Figure 111). The toxicity of the NWs to the cells was statistically significant after exposure to 30 and 50 µg/ml ZnO NWs for 24 h and 48 h. Figure 112 shows

the dose response curve of the MDA-MB-231 cells to the ZnO NWs after 24 h with an IC_{50} of 24 µg/ml.

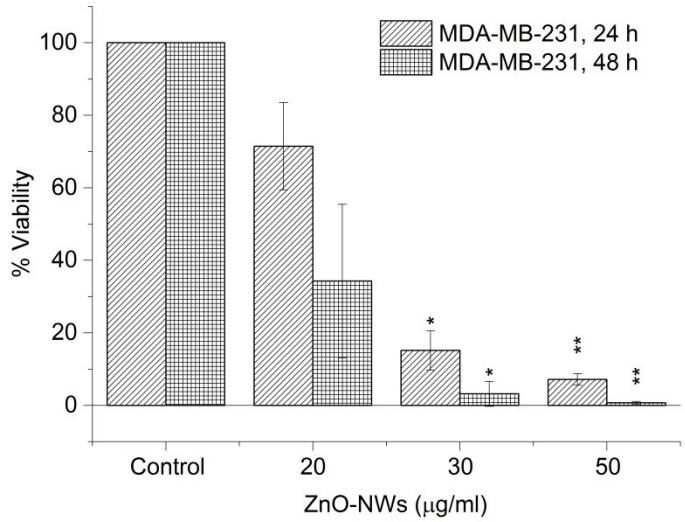

Figure 111: ATP viability assay of MDA-MB-231 cells exposed to ZnO NWs. Experiments were repeated in duplicates (n=2) and represented as the mean ± SD. *P ≤ 0.05, **P ≤ 0.01.

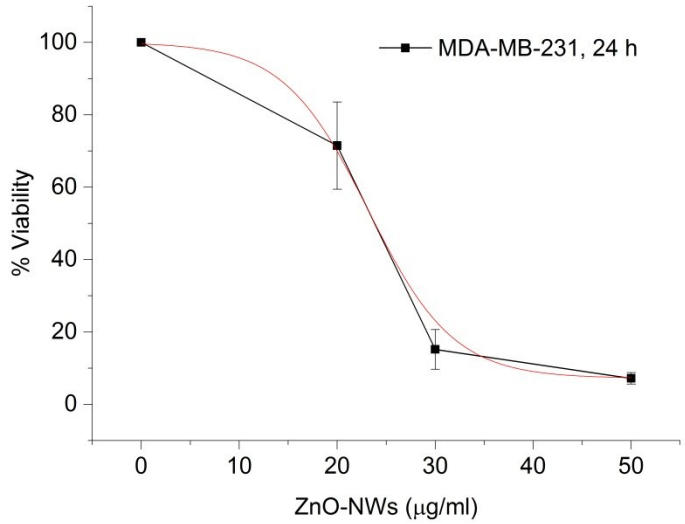

Figure 112: Dose response sigmoidal fit of viability of MDA-MB-231 cells exposed to ZnO NWs for 24 h. IC_{50}= 24 µg/ml. The values represent the mean ± STD of two experiments each performed in triplicate.

7.4 Summary and conclusions

High aspect ratio ZnO NWs were successfully fabricated by electrodeposition into high quality polycarbonate membranes filters and gold coated glass substrates and the obtained ZnO NWs have a very smooth flat surface. The template assisted electrodeposition produced a low yield of the ZnO NWs while a reasonable yield could be obtained by free electrodeposition of the NWs on glass substrates. A methodology to release the wires from the template by anodic oxidation for gold was established and, therefore, electrodeposition on glass was used to prepare ZnO NWs for the ATP viability assay. The ZnO NWs prepared on glass substrates had a uniform diameter of 37 ± 12 nm (n=259) throughout their length and they had a length of 330 ± 344 nm (n=1750).

Toxicity assays showed that the ZnO NWs resulted in a dose and time dependent reduction in the viability of the MDA-MB-231 cells (Figure 111) with an IC_{50} of 24 µg/ml after 24 h exposure (Figure 112). This IC_{50} of the ZnO NWs in the MDA-MB-231 cells after 24 h exposure is lower than that obtained for the bare ZnO NPs, which was 36 µg/ml (Figure 44). This indicates that the ZnO NWs were more toxic to the MDA-MB-231 cells than the ZnO NPs. The cytotoxic responses to the ZnO NWs in the MCF-7 cells, as well as the healthy MCF-10-2A cells, have to be further investigated.

8 Conclusions and Future work

8.1 Conclusions

This thesis developed a platform technology where the local release of high dose of Zn^{2+} from ZnO NMs, coupled to simultaneous targeted-delivery, can be used for effective treatment of a range of cancer cells including the triple negative resistant tumours.

Taken together, the results of this work have enabled us to propose a new mechanism for ZnO NMS uptake and cytotoxicity in the breast cancer MCF-7 and MDA-MB-231 cells. In brief, upon being added to the culture medium, ZnO NPs are rapidly coated by serum proteins. The protein corona induces the formation of small aggregates of ZnO NPs that are taken up by the cells, possibly by non-specific endocytosis for the bare ZnO NPs, and a combination of endocytosis and receptor mediated processes for the targeted ZnO-HCV-RGD-GFP NPs. The ZnO-protein corona complex is then transported, most probably, into lysosomes by vesicles. Inside the lysosomes, the ZnO NPs rapidly dissolved to release zinc ions (Zn^{2+}). The released zinc ions induce a cascade of cellular events that lead to cellular death.

The ZnO NPs (both bare and targeted) induced necrosis in the MCF-7, but apoptosis in the MDA-MB-231 cells at concentrations 10-60 μg/ml. The cytotoxicity of the bare and the targeted ZnO NPs to the MCF-7 was dose - but not time- dependent. The MCF-7 cells showed all signs of necrosis, which includes a sudden drop in the metabolic activity at concentrations around the 24 h IC_{50}, and cell lysis with high release of LDH after 24 h exposure to the bare ZnO NPs. In the MDA-MB-231 cells, on the other hand, the bare and targeted ZnO NPs showed a time and dose dependent cytotoxicity with signs of apoptosis which includes a linear reduction in the metabolic activity and the low release of LDH after 24 h exposure to the ZnO NPs. In the Annexin V/7AAD assay, the MDA-MB-231 cells showed significant time and dose dependent increase in the apoptotic population, while MCF-7 cells, in contrast, did not show any increase in the apoptotic population, compared to the untreated controls at any tested concentration. The confocal imaging of these cells exposed to the ZnO NPs supported these findings. The MDA-MB-231 cells undergoing cell death

displayed distinct morphological features typical of apoptotic cells such as shrinkage and blebbing, while the MCF-7 cells did not display these features.

The toxic susceptibility of the cells to the ZnO NPs to the cells used in this study was as follows; MCF-7> MDA-MB-231> MCF-10-2A cells. The bare ZnO NP showed a selective toxicity to the breast cancer cell lines compared to the healthy breast epithelial cells at concentrations 25-40 μg/ml of the bare ZnO NPs after 3 h exposure. A dose of 35 μg/ml of the bare ZnO NPs could be used as a toxic dose to the breast MCF-7 and MDA-MB-231 cancer cells with minimal toxic effects on the healthy breast MCF-10-2A cells, which showed >65% viability at this concentration. The higher sensitivity of the breast cancer cells compared to the healthy breast epithelial cells to ZnO is not fully understood, however, this could be related to the effect of ionic zinc. It has been reported that zinc may protect normal human lymphocytes against DNA-damaging action and increase this action in human myelogenous lukemia K562 cancer cells, which indicates the dual action of this element in dependency of target cells and can be useful in cancer therapy [274].

The RGD-targeting of the ZnO NPs to the integrin αvβ3 receptors led to an increase in the toxicity of the ZnO NPs to the breast cancer cells that over express the integrin αvβ3. The combination of RGD-targeting and the inherent selective toxicity of the ZnO NMs to breast cancer cells but not the healthy epithelial cells will open new options for this material in cancer therapy.

High aspect ratio ZnO NWs were successfully fabricated by electrodeposition and the obtained NWs have a very smooth flat surface with a uniform diameter. The ZnO NWs resulted in a dose and time dependent toxicity in the MDA-MB-231 cells with an IC_{50} lower than that of the bare ZnO NPs.

8.2 Future work

- In this thesis three cell lines (two cancer cell lines and a control cell line), three ZnO NPs (bare, targeted and NWs), and three viability assays (Alamar Blue, LDH and ATP) were used in this study. However, not all of the combinations were tested. This is because the toxicity assays are very lengthy and months of work were needed to optimize the conditions of each of the assays used. For example which cell culture medium to use to preserve cell metabolism and minimise dissolution of the ZnO NPs. Such conditions also include, the incubation time of the NPs with the cells as well as with cell culture medium. Different cells could have been tested using the same culture medium to save time, however our results showed that this is not correct (which may explain a lot of the discrepancy between data reported in the literature), so months have been spent to optimise the culturing protocols to perform highly controlled experiments. Ideally a complete data set should be generated to draw conclusions. Nevertheless, the results of this thesis show significant differences between the MCF-7 and MDA-MB-231 cells and in one assay a comparison to the healthy cells was conducted. A large advancement over what has been done in the literature in development of assays to test the toxicity ZnO nanomaterials has been achieved. The future work will cover all the other possible combinations.

- Although we have proposed new mechanism by which targeted and bare ZnO NPs destroy cancer cells, the underlying mechanism by which they exert their toxicity requires further investigations. Qualitative and quantitative changes in cancer cell death are essential determinants of malignant disease responsiveness to therapy [275]. Therefore, by better understanding the mechanisms of action, and cellular consequences, resulting from ZnO NMs interactions with cancer cells and their mechanisms of action, the inherent toxicity and selectivity of ZnO NMS against cancer may be further improved to make them attractive new anti-cancer agents. This could be achieved by further investigations into ZnO-induced mechanisms of cell death, and to accurately and dynamically differentiate between necrosis and apoptosis by using specific intracellular enzymes (apoptotic markers) that are activated in apoptosis (e.g. caspase-3, 7, and 9 [276]). This could also be achieved by suing well-known anti-apoptotic genes (e.g. Bcl-2), which inhibit most types of apoptotic cell death [277], and therefore it could be possible to indirectly discriminate between the two cell deaths. Cell

cycle analysis of breast cells after exposure to the ZnO NPs will help understanding the genetic responses of the cells after exposure. This could be achieved by flow cytometry analysis of cells exposed to the ZnO NPs. It has also been reported that ZIP10, a receptor that control zinc influx into the cytosol, plays an essential role in the migratory activity of highly metastatic MDA-MB-231 breast cancer cells [197]. Therefore, the involvement of the ZIP10 and other zinc receptors in the uptake of ZnO NMs or zinc ions after ZnO NMs treatments is worthy of further investigation.

- The reported alteration in the intracellular distribution of NMS after uptake, because of the RGD targeting [91], necessitates further investigations into the subcellular localization of both the bare and the RGD-grafted ZnO NPs. Mapping the subcellular localization of the ZnO NPs (both bare and targeted) could provide insights into the observed higher breast cancer toxicity of RGD-targeted ZnO NPs, compared to the bare NPs, as well as their different intracellular dissolution profiles.

- An avenue of future work would be to further widen the window in which the ZnO NPs only show toxicity to the breast cancer cells. This could be achieved by the use of a combination of attaching targeting ligands to the surface of the particles and the incorporation of dopants (e.g. Al, Cr) into the ZnO, to tune the solubility and bioreactivity of the ZnO NPs, to generate a system that is biocompatible with healthy cells and therefore can be applied in biomedical applications. In addition, other variables could be explored, such as varying the size or charge of the ZnO NPs. Use of PEG-ylation to increase the colloidal stability of the ZnO NPs and non-specific adsorption of proteins should also be studied.

- Quantification of the effect of serum proteins on the binding and internalization of bare and targeted ZnO NMS by breast cancer and healthy cells need further investigations. This could be achieved by FACS and also by conducting confocal experiments on live breast cancer cells in a chamber of controlled temperature and under 5% CO_2 with the use of ZnO NMS prepared in cell culture media with and without FBS. Preliminary flow chamber experiments, conducted in this study, looked extremely promising and will also help to assess the effect of protein corona on the RGD-targeting efficiency of the ZnO NMS to integrin αvβ3 receptors.

- Although the RGD-targeted ZnO NPs showed a higher toxicity to the breast cancer cells than the bare NPs, and they were shown to bind to the integrin αvβ3 receptors expressed on the surface of the breast cancer cells, quantification of the amount of this binding is crucial. This could be achieved by conducting flow cytometry assays of breast cells exposed to the RGD-targeted ZnO NPs and to the negative control ZnO-GGG NPs. Comparisons of binding of the RGD-targeted ZnO NPs before and after either blocking or knock-out of the integrin αvβ3 receptors could also help to quantify binding of the targeted ZnO NPs to the breast cancer cells. Blocking of the integrin αvβ3 receptors can be achieved by exposure of the breast cancer cells to RGD protein before ZnO NPs treatment. The knock down of the integrin αvβ3 receptors can be achieved by siRNA transfection.

- Although the RGD peptide is an effective ligand for tumor targeting of the integrin αvβ3 receptors, which are selectively expressed on breast cancer cells, optimization of delivery of ZnO NMs could be achieved by considering other candidates. Such alternative candidates, which have also been shown to target breast cancer cells, include GSPQCPGGFNCPRCDCGAGY [278] and ASANPFPTKALL [279]. Future work should explore these options.

- The future work will also aim to correlate our promising in vitro results with in vivo models of breast cancer in mice. This can be achieved by IV injection of the RGD-targeted ZnO NPs in a mammary breast cancer model and monitor the distribution of these NPs. The in vivo distribution of the RGD-targeted ZnO NPs could be monitored via radionuclide-based imaging techniques, such as positron emission tomography (PET) with 64Cu-Labeled RGD-targeted ZnO NPs [25]. PET is very sensitive, quantitative, and clinically relevant with superb tissue penetration [21]. Particle agglomeration is commonly observed in studies involving ZnO NPs [19], particularly when diluted in media with high ionic strength (> 10 mM). This agglomeration can affect their bioavailability and could impose significant challenges for designing in vivo toxicological studies; however there are successful methods available to improve the colloidal stability of these particles.

- The addition of chemotherapeutic molecules (e.g. epiruibicin, formulated as a Cl- salt and compatible with the processing of the ZnO NMs) into the ZnO mixture during growth so that the drug is incorporated into the ZnO matrix, could also help to treat the disease. This method has been previously used to incorporate phthalocyanine molecules into ZnO nanostructures in our laboratory (unpublished data). Using this synthesis method, the ZnO NMs can be used as vector that can target of the chemotherapeutic drug to breast cancer cells, by using targeting ligands, as well as the synergistic effect of ZnO NMs their after dissolution inside the cancer cells.

List of Figures

List of Tables

References

1. Brigger, I., C. Dubernet, and P. Couvreur, *Nanoparticles in cancer therapy and diagnosis.* Advanced Drug Delivery Reviews, 2012. **64**: p. 24-36.

2. Prasad, A.S., *Zinc in human health: Effect of zinc on immune cells.* Molecular Medicine, 2008. **14**(5-6): p. 353-357.

3. Vallee, B.L. and D.S. Auld, *Zinc coordination, function, and structure of zinc enzymes and other proteins*. Biochemistry, 1990. **29**(24): p. 5647-5659.

4. Dineley, K.E., T.V. Votyakova, and I.J. Reynolds, *Zinc inhibition of cellular energy production: implications for mitochondria and neurodegeneration.* Journal of Neurochemistry, 2003. **85**(3): p. 563-570.

5. Franklin, R.B. and L.C. Costello, *The Important Role of the Apoptotic Effects of Zinc in the Development of Cancers.* Journal of Cellular Biochemistry, 2009. **106**(5): p. 750-757.

6. Hanley, C., J. Layne, A. Punnoose, K.M. Reddy, I. Coombs, A. Coombs, K. Feris, and D. Wingett, *Preferential killing of cancer cells and activated human T cells using ZnO nanoparticles.* Nanotechnology, 2008. **19**(29).

7. Rasmussen, J.W., E. Martinez, P. Louka, and D.G. Wingett, *Zinc Oxide Nanoparticles for Selective Destruction of Tumor Cells and Potential for Drug Delivery Applications.* Expert Opinion on Drug Delivery, 2010. **7**(9): p. 1063-77.

8. Deng, Z.J., G. Mortimer, T. Schiller, A. Musumeci, D. Martin, and R.F. Minchin, *Differential plasma protein binding to metal oxide nanoparticles.* Nanotechnology, 2009. **20**(45).

9. Yu, M.K., J. Park, and S. Jon, *Targeting Strategies for Multifunctional Nanoparticles in Cancer Imaging and Therapy.* Theranostics, 2012. **2**(1): p. 3-44.

10. Muller, K.H., J. Kulkarni, M. Motskin, A. Goode, P. Winship, J.N. Skepper, M.P. Ryan, and A.E. Porter, *pH-dependent toxicity of high aspect ratio ZnO nanowires in macrophages due to intracellular dissolution.* ACS Nano, 2010. **4**(11): p. 6767-79.

11. Sasidharan, A., P. Chandran, D. Menon, S. Raman, S. Nair, and M. Koyakutty, *Rapid dissolution of ZnO nanocrystals in acidic cancer microenvironment leading to preferential apoptosis.* Nanoscale, 2011. **3**(9): p. 3657-3669.

12. Hong, H., J. Shi, Y. Yang, Y. Zhang, J.W. Engle, R.J. Nickles, X. Wang, and W. Cai, *Cancer-targeted optical imaging with fluorescent zinc oxide nanowires.* Nano Letters, 2011. **11**(9): p. 3744-50.

13. Buzea, C., I.I. Pacheco, and K. Robbie, *Nanomaterials and nanoparticles: Sources and toxicity.* Biointerphases, 2007. **2**(4): p. Mr17-Mr71.

14. Nel, A.X., T. Madler, L. Li, N., *Toxic potential of materials at the nanolevel.* Science, 2006. **311**(5761): p. 622-627.

15. Gwinn, M.R. and V. Vallyathan, *Nanoparticles: Health effects - Pros and cons.* Environmental Health Perspectives, 2006. **114**(12): p. 1818-1825.

16. Kroll, A., M.H. Pillukat, D. Hahn, and J. Schnekenburger, *Interference of engineered nanoparticles with in vitro toxicity assays.* Archives of Toxicology, 2012. **86**(7): p. 1123-1136.

17. Maynard, A.D., *Nanotechnology: The next big thing, or much ado about nothing?* Annals of Occupational Hygiene, 2007. **51**(1): p. 1-12.

18. Rushton, E.K., J. Jiang, S.S. Leonard, S. Eberly, V. Castranova, P. Biswas, A. Elder, X.L. Han, R. Gelein, J. Finkelstein, and G. Oberdorster, *Concept of Assessing Nanoparticle Hazards Considering Nanoparticle Dosemetric and Chemical/Biological Response Metrics.* Journal of Toxicology and Environmental Health-Part a-Current Issues, 2010. **73**(5-6): p. 445-461.

19. Dhawan, A. and V. Sharma, *Toxicity assessment of nanomaterials: methods and challenges.* Analytical and Bioanalytical Chemistry, 2010. **398**(2): p. 589-605.

20. Kroll, A., C. Dierker, C. Rommel, D. Hahn, W. Wohlleben, C. Schulze-Isfort, C. Gobbert, M. Voetz, F. Hardinghaus, and J. Schnekenburger, *Cytotoxicity screening of 23 engineered nanomaterials using a test matrix of ten cell lines and three different assays.* Particle and Fibre Toxicology, 2011. **8**(9).

21. Jeng, H.A. and J. Swanson, *Toxicity of metal oxide nanoparticles in mammalian cells.* Journal of Environmental Science and Health Part a-Toxic/Hazardous Substances & Environmental Engineering, 2006. **41**(12): p. 2699-2711.

22. Landsiedel, R., L. Ma-Hock, A. Kroll, D. Hahn, J. Schnekenburger, K. Wiench, and W. Wohlleben, *Testing Metal-Oxide Nanomaterials for Human Safety.* Advanced Materials, 2010. **22**(24): p. 2601-2627.

23. Sarkar, A., M. Ghosh, and P.C. Sil, *Nanotoxicity: Oxidative Stress Mediated Toxicity of Metal and Metal Oxide Nanoparticles.* Journal of Nanoscience and Nanotechnology, 2014. **14**(1): p. 730-743.

24. Palombo, M., M. Deshmukh, D. Myers, J.M. Gao, Z. Szekely, and P.J. Sinko, *Pharmaceutical and Toxicological Properties of Engineered Nanomaterials for Drug Delivery.* Annual Review of Pharmacology and Toxicology, Vol 54, 2014. **54**: p. 581-598.

25. Punnoose, A., K. Dodge, J.W. Rasmussen, J. Chess, D. Wingett, and C. Anders, *Cytotoxicity of ZnO Nanoparticles Can Be Tailored by Modifying Their Surface Structure: A Green Chemistry Approach for Safer Nanomaterials.* ACS sustainable chemistry & engineering, 2014. **2**(7): p. 1666-1673.

26. Nair, S., A. Sasidharan, V. Divya Rani, D. Menon, S. Nair, K. Manzoor, and S. Raina, *Role of size scale of ZnO nanoparticles and microparticles on toxicity toward bacteria and osteoblast cancer cells.* Journal of Materials Science: Materials in Medicine, 2009. **20**(0): p. 235-241.

27. Han, X., J.N. Finkelstein, A. Elder, J. Jiang, P. Biswas, and G. Oberdorster, *Evaluating Pulmonary Toxicity of Nanoparticles.* American Journal of Respiratory and Critical Care Medicine, 2009. **179**.

28. Jiang, J., G. Oberdorster, A. Elder, R. Gelein, P. Mercer, and P. Biswas, *Does nanoparticle activity depend upon size and crystal phase?* Nanotoxicology, 2008. **2**(1): p. 33-42.

29. Sayes, C.M., K.L. Reed, and D.B. Warheit, *Assessing toxicity of fine and nanoparticles: Comparing in vitro measurements to in vivo pulmonary toxicity profiles.* Toxicological Sciences, 2007. **97**(1): p. 163-180.

30. Valsami-Jones, E., D. Berhanu, A. Dybowska, S. Misra, A.R. Boccaccini, T.D. Tetley, S.N. Luoma, and J.A. Plant, *Nanomaterial synthesis and characterization for toxicological studies: TiO_2 case study.* Mineralogical Magazine, 2008. **72**(1): p. 515-519.

31. Hussain, S.M., L.K. Braydich-Stolle, A.M. Schrand, R.C. Murdock, K.O. Yu, D.M. Mattie, J.J. Schlager, and M. Terrones, *Toxicity Evaluation for Safe Use of Nanomaterials: Recent Achievements and Technical Challenges.* Advanced Materials, 2009. **21**(16): p. 1549-1559.

32. Li, S.D. and L. Huang, *Pharmacokinetics and biodistribution of nanoparticles.* Molecular Pharmaceutics, 2008. **5**(4): p. 496-504.

33. Limbach, L.K., Y. Li, R.N. Grass, T.J. Brunner, M.A. Hintermann, M. Muller, D. Gunther, and W.J. Stark, *Oxide nanoparticle uptake in human lung fibroblasts: effects of particle size, agglomeration, and diffusion at low concentrations.* Environmental science & technology, 2005. **39**(23): p. 9370-9376.

34. Sakamoto, J.H., A.L. van de Ven, B. Godin, E. Blanco, R.E. Serda, A. Grattoni, A. Ziemys, A. Bouamrani, T. Hu, S.I. Ranganathan, E. De Rosa, J.O. Martinez, C.A. Smid, R.M. Buchanan, S.-Y. Lee, S. Srinivasan, M. Landry, A. Meyn, E. Tasciotti, X. Liu, P. Decuzzi, and M. Ferrari, *Enabling individualized therapy through nanotechnology.* Pharmacological Research, 2010. **62**(2): p. 57-89.

35. Wang, J.Q., M.H. Sui, and W.M. Fan, *Nanoparticles for Tumor Targeted Therapies and Their Pharmacokinetics.* Current Drug Metabolism, 2010. **11**(2): p. 129-141.

36. Torchilin, V.P., *Recent advances with liposomes as pharmaceutical carriers.* Nature Reviews Drug Discovery, 2005. **4**(2): p. 145-160.

37. Gabizon, A., *Tailoring liposomes for cancer drug delivery: from the bench to the clinic.* Annales de biologie clinique (Paris), 1993. **51**(9): p. 811-3.

38. Peer, D., J.M. Karp, S. Hong, O.C. FaroKHzad, R. Margalit, and R. Langer, *Nanocarriers as an emerging platform for cancer therapy.* Nature Nanotechnology, 2007. **2**(12): p. 751-760.

39. Ciruelos, E. and C. Jackisch, *Evaluating the role of nab-paclitaxel (Abraxane) in women with aggressive metastatic breast cancer.* Expert Review of Anticancer Therapy, 2014. **14**(5): p. 511-521.

40. Eifler, A.C. and C.S. Thaxton, *Nanoparticle therapeutics: FDA approval, clinical trials, regulatory pathways, and case study.* Methods in Molecular Biology, 2011. **726**: p. 325-38.

41. Allen, T.M. and P.R. Cullis, *Drug delivery systems: Entering the mainstream.* Science, 2004. **303**(5665): p. 1818-1822.

42. Li, Q., X. Wang, X. Lu, H. Tian, H. Jiang, G. Lv, D. Guo, C. Wu, and B. Chen, *The incorporation of daunorubicin in cancer cells through the use of titanium dioxide whiskers.* Biomaterials, 2009. **30**(27): p. 4708-4715.

43. Zhang, H.J., B.A. Chen, H. Jiang, C.L. Wang, H.P. Wang, and X.M. Wang, *A strategy for ZnO nanorod mediated multi-mode cancer treatment.* Biomaterials, 2011. **32**(7): p. 1906-1914.

44. Muhammad, F., M. Guo, W. Qi, F. Sun, A. Wang, Y. Guo, and G. Zhu, *pH-Triggered controlled drug release from mesoporous silica nanoparticles via intracelluar dissolution of ZnO nanolids.* Journal of American Chemical Society (JACS), 2011. **133**(23): p. 8778-81.

45. Hall, J.B., M.A. Dobrovolskaia, A.K. Patri, and S.E. McNeil, *Characterization of nanoparticles for therapeutics.* Nanomedicine (Lond), 2007. **2**(6): p. 789-803.

46. Zhao, F., Y. Zhao, Y. Liu, X.L. Chang, C.Y. Chen, and Y.L. Zhao, *Cellular Uptake, Intracellular Trafficking, and Cytotoxicity of Nanomaterials.* Small, 2011. **7**(10): p. 1322-1337.

47. Holgate, S.T., *Exposure, Uptake, Distribution and Toxicity of Nanomaterials in Humans.* Journal of Biomedical Nanotechnology, 2010. **6**(1): p. 1-19.

48. Sahay, G., D.Y. Alakhova, and A.V. Kabanov, *Endocytosis of nanomedicines.* Journal of Controlled Release, 2010. **145**(3): p. 182-195.

49. Xia, T., M. Kovochich, M. Liong, L. Madler, B. Gilbert, H.B. Shi, J.I. Yeh, J.I. Zink, and A.E. Nel, *Comparison of the Mechanism of Toxicity of Zinc Oxide and Cerium Oxide Nanoparticles Based on Dissolution and Oxidative Stress Properties.* ACS Nano, 2008. **2**(10): p. 2121-2134.

50. Germain, R.N., *An innately interesting decade of research in immunology.* Nature Medicine, 2004. **10**(12): p. 1307-1320.

51. Conner, S.D. and S.L. Schmid, *Regulated portals of entry into the cell.* Nature, 2003. **422**(6927): p. 37-44.

52. Mayor, S., R.G. Parton, and J.G. Donaldson, *Clathrin-Independent Pathways of Endocytosis.* Cold Spring Harbor Perspectives in Biology, 2014. **6**(6).

53. Premanathan, M., K. Karthikeyan, K. Jeyasubramanian, and G. Manivannan, *Selective toxicity of ZnO nanoparticles toward Gram-positive bacteria and cancer cells by apoptosis through lipid peroxidation.* Nanomedicine-Nanotechnology Biology and Medicine, 2011. **7**(2): p. 184-192.

54. Colon, G., B.C. Ward, and T.J. Webster, *Increased osteoblast and decreased Staphylococcus epidermidis functions on nanophase ZnO and TiO_2.* Journal of Biomedical Materials Research Part A, 2006. **78A**(3): p. 595-604.

55. Ivask, A., K. Juganson, O. Bondarenko, M. Mortimer, V. Aruoja, K. Kasemets, I. Blinova, M. Heinlaan, V. Slaveykova, and A. Kahru, *Mechanisms of toxic action of Ag, ZnO and CuO nanoparticles to selected ecotoxicological test organisms and mammalian cells in vitro: A comparative review.* Nanotoxicology, 2014. **8**: p. 57-71.

56. Bondarenko, O., K. Juganson, A. Ivask, K. Kasemets, M. Mortimer, and A. Kahru, *Toxicity of Ag, CuO and ZnO nanoparticles to selected environmentally relevant test organisms and mammalian cells in vitro: a critical review.* Archives of Toxicology, 2013. **87**(7): p. 1181-1200.

57. Vandebriel, R.J. and W.H. De Jong, *A review of mammalian toxicity of ZnO nanoparticles.* Journal of Nanotechnology, Science and Applications, 2012. **5**: p. 61-71.

58. Bacchetta, R., E. Moschini, N. Santo, U. Fascio, L. Del Giacco, S. Freddi, M. Camatini, and P. Mantecca, *Evidence and uptake routes for Zinc oxide nanoparticles through the gastrointestinal barrier in Xenopus laevis.* Nanotoxicology, 2014. **8**(7): p. 728-44.

59. Jingwen, S., L.K. Hanna, J. Katarina, G. Vladimir, X. Lisong, L. Jiangtian, B. Terrance, G.-B. Alfonso, U. Abdusalam, M. Mamoun, M. Sanjay, M. Ralf, E.K. Valerian, and F. Bengt, *Microsomal Glutathione Transferase 1 Protects Against Toxicity Induced by Silica Nanoparticles but Not by Zinc Oxide Nanoparticles.* ACS Nano, 2012.

60. Churchman, A.H., R. Wallace, S.J. Milne, A.P. Brown, R. Brydson, and P.A. Beales, *Serum albumin enhances the membrane activity of ZnO nanoparticles.* Chemical communications (Cambridge, England), 2013. **49**(39): p. 4172-4174.

61. Gojova, A., B. Guo, R.S. Kota, J.C. Rutledge, I.M. Kennedy, and A.I. Barakat, *Induction of inflammation in vascular endothelial cells by metal oxide nanoparticles: Effect of particle composition.* Environmental Health Perspectives, 2007. **115**(3): p. 403-409.

62. Reddy, K.M., K. Feris, J. Bell, D.G. Wingett, C. Hanley, and A. Punnoose, *Selective toxicity of zinc oxide nanoparticles to prokaryotic and eukaryotic systems.* Applied Physics Letters, 2007. **90**(21).

63. Yang, H., C. Liu, D.F. Yang, H.S. Zhang, and Z.G. Xi, *Comparative study of cytotoxicity, oxidative stress and genotoxicity induced by four typical nanomaterials: the role of particle size, shape and composition.* Journal of Applied Toxicology, 2009. **29**(1): p. 69-78.

64. Li, Z., R.S. Yang, M. Yu, F. Bai, C. Li, and Z.L. Wang, *Cellular Level Biocompatibility and Biosafety of ZnO Nanowires.* Journal of Physical Chemistry C, 2008. **112**(51): p. 20114-20117.

65. Deng, X., Q. Luan, W. Chen, Y. Wang, M. Wu, H. Zhang, and Z. Jiao, *Nanosized zinc oxide particles induce neural stem cell apoptosis.* Nanotechnology, 2009. **20**(11).

66. Huang, C.C., R.S. Aronstam, D.R. Chen, and Y.W. Huang, *Oxidative stress, calcium homeostasis, and altered gene expression in human lung epithelial cells exposed to ZnO nanoparticles.* Toxicology in Vitro, 2010. **24**(1): p. 45-55.

67. Yuan, J.H., Y. Chen, H.X. Zha, L.J. Song, C.Y. Li, J.Q. Li, and X.H. Xia, *Determination, characterization and cytotoxicity on HELF cells of ZnO nanoparticles.* Colloids and Surfaces B-Biointerfaces, 2010. **76**(1): p. 145-150.

68. Song, W.H., J.Y. Zhang, J. Guo, J.H. Zhang, F. Ding, L.Y. Li, and Z.T. Sun, *Role of the dissolved zinc ion and reactive oxygen species in cytotoxicity of ZnO nanoparticles.* Toxicology Letters, 2010. **199**(3): p. 389-397.

69. Heng, B.C., X.X. Zhao, S.J. Xiong, K.W. Ng, F.Y.C. Boey, and J.S.C. Loo, *Toxicity of zinc oxide (ZnO) nanoparticles on human bronchial epithelial cells (BEAS-2B) is accentuated by oxidative stress.* Food and Chemical Toxicology, 2010. **48**(6): p. 1762-1766.

70. Pujalte, I., I. Passagne, B. Brouillaud, R. Daculsi, M. Treguer, C. Ohayon-Courtes, and B. L'Azou, *Study of different metallic nanoparticles on human kidney cells: Toxicity and oxidative stress.* Toxicology Letters, 2011. **205**: p. S172-S172.

71. Franklin, N.M., N.J. Rogers, S.C. Apte, G.E. Batley, G.E. Gadd, and P.S. Casey, *Comparative toxicity of nanoparticulate ZnO, bulk ZnO, and $ZnCl_2$ to a freshwater microalga (Pseudokirchneriella subcapitata): The importance of particle solubility.* Environmental Science & Technology, 2007. **41**(24): p. 8484-8490.

72. Berg, J.M. and Y.G. Shi, *The galvanization of biology: A growing appreciation for the roles of zinc.* Science, 1996. **271**(5252): p. 1081-1085.

73. Snitsarev, V., T. Budde, T.P. Stricker, J.M. Cox, D.J. Krupa, L. Geng, and A.R. Kay, *Fluorescent detection of Zn^{2+}-rich vesicles with zinquin: Mechanism of action in lipid environments.* Biophysical Journal, 2001. **80**(3): p. 1538-1546.

74. Stefanidou, M., C. Maravelias, A. Dona, and C. Spiliopoulou, *Zinc: a multipurpose trace element.* Archives of toxicology, 2006. **80**(1): p. 1-9.

75. Pierrel, F., P.A. Cobine, and D.R. Winge, *Metal Ion availability in mitochondria.* Biometals, 2007. **20**(3-4): p. 675-682.

76. Martin-Gonzalez, A., S. Borniquel, S. Diaz, R. Ortega, and J.C. Gutierrez, *Ultrastructural alterations in ciliated protozoa under heavy metal exposure.* Cell Biology International, 2005. **29**(2): p. 119-126.

77. Canzoniero, L.M.T., D.M. Turetsky, and D.W. Choi, *Measurement of intracellular free zinc concentrations accompanying zinc-induced neuronal death.* Journal of Neuroscience, 1999. **19**(19): p. art. no.-RC31.

78. Sharma, V., D. Anderson, and A. Dhawan, *Zinc Oxide Nanoparticles Induce Oxidative Stress and Genotoxicity in Human Liver Cells (HepG2).* Journal of Biomedical Nanotechnology, 2011. **7**(1): p. 98-99.

79. Sharma, V., D. Anderson, and A. Dhawan, *Zinc oxide nanoparticles induce oxidative DNA damage and ROS-triggered mitochondria mediated apoptosis in human liver cells (HepG2).* Apoptosis, 2012. **17**(8): p. 852-870.

80. Wang, L.J., L. Wang, W.J. Ding, and F. Zhang, *Acute Toxicity of Ferric Oxide and Zinc Oxide Nanoparticles in Rats.* Journal of Nanoscience and Nanotechnology, 2010. **10**(12): p. 8617-8624.

81. Matsumura, Y. and H. Maeda, *A new concept for macromolecular therapeutics in cancer chemotherapy: mechanism of tumoritropic accumulation of proteins and the antitumor agent smancs.* Cancer Research, 1986. **46**(12 Pt 1): p. 6387-92.

82. Nie, S., Y. Xing, G.J. Kim, and J.W. Simons, *Nanotechnology applications in cancer.* Annual Review of Biomedical Engineering, 2007. **9**: p. 257-88.

83. McNeil, S.E., *Nanotechnology for the biologist.* Journal of Leukocyte Biology, 2005. **78**(3): p. 585-94.

84. Banerjee, H.N. and M. Verma, *Application of nanotechnology in cancer.* Technology in cancer research & treatment, 2008. **7**(2): p. 149-54.

85. Kishwar, S., M.H. Asif, O. Nur, M. Willander, and P.O. Larsson, *Intracellular ZnO Nanorods Conjugated with Protoporphyrin for Local Mediated Photochemistry and Efficient Treatment of Single Cancer Cell.* Nanoscale Research Letters, 2010. **5**(10): p. 1669-1674.

86. Zhang, H., B. Chen, H. Jiang, C. Wang, H. Wang, and X. Wang, *A strategy for ZnO nanorod mediated multi-mode cancer treatment.* Biomaterials, 2011. **32**(7): p. 1906-1914.

87. Muharnmad, F., M.Y. Guo, W.X. Qi, F.X. Sun, A.F. Wang, Y.J. Guo, and G.S. Zhu, *pH-Triggered Controlled Drug Release from Mesoporous Silica Nanoparticles via Intracelluar Dissolution of ZnO Nanolids.* Journal of the American Chemical Society, 2011. **133**(23): p. 8778-8781.

88. Punnoose, A., M.R. Kongara, and D. Winget, *Preferential Killing of Cancer Cells and Activated Human T-Cells*, B.S. University, Editor. 2009: USA.

89. Sudhagar, S., S. Sathya, K. Pandian, and B.S. Lakshmi, *Targeting and sensing cancer cells with ZnO nanoprobes in vitro.* Biotechnology Letters, 2011. **33**(9): p. 1891-1896.

90. Mitra, S., B. Subia, P. Patra, S. Chandra, N. Debnath, S. Das, R. Banerjee, S.C. Kundu, P. Pramanik, and A. Goswami, *Porous ZnO nanorod for targeted delivery of doxorubicin: in vitro and in vivo response for therapeutic applications.* Journal of Materials Chemistry, 2012. **22**(45): p. 24145-24154.

91. Danhier, F., A. Le Breton, and V. Preat, *RGD-Based Strategies To Target Alpha(v) Beta(3) Integrin in Cancer Therapy and Diagnosis.* Molecular Pharmaceutics, 2012. **9**(11): p. 2961-2973.

92. Daniels, T.R., T. Delgado, G. Helguera, and M.L. Penichet, *The transferrin receptor part II: Targeted delivery of therapeutic agents into cancer cells.* Clinical Immunology, 2006. **121**(2): p. 159-176.

93. Misra, R., S. Acharya, and S.K. Sahoo, *Cancer nanotechnology: application of nanotechnology in cancer therapy.* Drug Discovery Today, 2010. **15**(19-20): p. 842-50.

94. Shen, Y.F., J.M. Jacobs, D.G. Camp, R.H. Fang, R.J. Moore, R.D. Smith, W.Z. Xiao, R.W. Davis, and R.G. Tompkins, *Ultra-high-efficiency strong cation exchange LC/RPLC/MS/MS for high dynamic range characterization of the human plasma proteome.* Analytical Chemistry, 2004. **76**(4): p. 1134-1144.

95. Mahmoudi, M., I. Lynch, M.R. Ejtehadi, M.P. Monopoli, F.B. Bombelli, and S. Laurent, *Protein-Nanoparticle Interactions: Opportunities and Challenges.* Chemical Reviews, 2011. **111**(9): p. 5610-5637.

96. Lynch, I., T. Cedervall, M. Lundqvist, C. Cabaleiro-Lago, S. Linse, and K.A. Dawson, *The nanoparticle - protein complex as a biological entity; a complex fluids and surface science challenge for the 21st century.* Advances in Colloid and Interface Science, 2007. **134-35**: p. 167-174.

97. Masoud Rahman, S.L., Nancy Tawil, L'Hocine Yahia, Morteza Mahmoudi, *Protein-Nanoparticle Interactions: The Bio-Nano Interface*, ed. B. Martinac. Vol. 15. 2013: Springer-Verlag Berlin Heidelberg. 33.

98. Walkey, C.D. and W.C.W. Chan, *Understanding and controlling the interaction of nanomaterials with proteins in a physiological environment.* Chemical Society Reviews, 2012. **41**(7): p. 2780-2799.

99. Sahneh, F.D., C. Scoglio, and J. Riviere, *Dynamics of Nanoparticle-Protein Corona Complex Formation: Analytical Results from Population Balance Equations.* PlOS ONE, 2013. **8**(5).

100. Arnaud, C.H., *Probing Nanotoxicity: Analytical methods provide insight into hazards of nanomaterials.* Chemical and Engineering News, 2010. **88**(13): p. 32-34.

101. Deng, Z.J., M. Liang, I. Toth, M. Monteiro, and R.F. Minchin, *Plasma protein binding of positively and negatively charged polymer-coated gold nanoparticles elicits different biological responses.* Nanotoxicology, 2013. **7**(3): p. 314-22.

102. Fertsch-Gapp, S., M. Semmler-Behnke, A. Wenk, and W.G. Kreyling, *Binding of polystyrene and carbon black nanoparticles to blood serum proteins.* Inhalation Toxicology, 2011. **23**(8): p. 468-75.

103. Huang, R., R.P. Carney, F. Stellacci, and B.L. Lau, *Protein-nanoparticle interactions: the effects of surface compositional and structural heterogeneity are scale dependent.* Nanoscale, 2013. **5**(15): p. 6928-35.

104. Feliu, N., M.V. Walter, M.I. Montanez, A. Kunzmann, A. Hult, A. Nystrom, M. Malkoch, and B. Fadeel, *Stability and biocompatibility of a library of polyester dendrimers in comparison to polyamidoamine dendrimers.* Biomaterials, 2012. **33**(7): p. 1970-1981.

105. Huhn, D., K. Kantner, C. Geidel, S. Brandholt, I. De Cock, S.J.H. Soenen, P.R. Gil, J.M. Montenegro, K. Braeckmans, K. Mullen, G.U. Nienhaus, M. Klapper, and W.J. Parak, *Polymer-Coated Nanoparticles Interacting with Proteins and Cells: Focusing on the Sign of the Net Charge.* ACS Nano, 2013. **7**(4): p. 3253-3263.

106. Chakraborti, S., S. Bhattacharya, R. Chowdhury, and P. Chakrabarti, *The Molecular Basis of Inactivation of Metronidazole-Resistant Helicobacter pylori Using Polyethyleneimine Functionalized Zinc Oxide Nanoparticles.* PlOS ONE, 2013. **8**(8).

107. Lundqvist, M., J. Stigler, G. Elia, I. Lynch, T. Cedervall, and K.A. Dawson, *Nanoparticle size and surface properties determine the protein corona with possible implications for biological impacts.* Proceedings of the National Academy of Sciences of the United States of America (PNAS), 2008. **105**(38): p. 14265-70.

108. Goy-Lopez, S., J. Juarez, M. Alatorre-Meda, E. Casals, V.F. Puntes, P. Taboada, and V. Mosquera, *Physicochemical Characteristics of Protein-NP Bioconjugates: The Role of Particle Curvature and Solution Conditions on Human Serum Albumin Conformation and Fibrillogenesis Inhibition.* Langmuir, 2012. **28**(24): p. 9113-9126.

109. Gebauer, J.S., M. Malissek, S. Simon, S.K. Knauer, M. Maskos, R.H. Stauber, W. Peukert, and L. Treuel, *Impact of the nanoparticle-protein corona on colloidal stability and protein structure.* Langmuir, 2012. **28**(25): p. 9673-9.

110. Tenzer, S., D. Docter, S. Rosfa, A. Wlodarski, J. Kuharev, A. Rekik, S.K. Knauer, C. Bantz, T. Nawroth, C. Bier, J. Sirirattanapan, W. Mann, L. Treuel, R. Zellner, M. Maskos, H. Schild, and R.H. Stauber, *Nanoparticle Size Is a Critical Physicochemical Determinant of the Human Blood Plasma Corona: A Comprehensive Quantitative Proteomic Analysis.* ACS Nano, 2011. **5**(9): p. 7155-7167.

111. Lesniak, A., A. Campbell, M.P. Monopoli, I. Lynch, A. Salvati, and K.A. Dawson, *Serum heat inactivation affects protein corona composition and nanoparticle uptake.* Biomaterials, 2010. **31**(36): p. 9511-9518.

112. Gref, R., M. Luck, P. Quellec, M. Marchand, E. Dellacherie, S. Harnisch, T. Blunk, and R.H. Muller, *'Stealth' corona-core nanoparticles surface modified by polyethylene glycol (PEG): influences of the corona (PEG chain length and surface density) and of the core composition on phagocytic uptake and plasma protein adsorption.* Colloids and Surfaces B-Biointerfaces, 2000. **18**(3-4): p. 301-313.

113. Mirshafiee, V., M. Mahmoudi, K. Lou, J. Chengd, and M.L. Kraft, *Protein corona significantly reduces active targeting yield.* Chemical communications (Cambridge, England), 2013. **49**(25): p. 2557-2559.

114. Okochi, M., T. Sugita, S. Furusawa, M. Umetsu, T. Adschiri, and H. Honda, *Peptide array-based characterization and design of ZnO-high affinity peptides.* Biotechnology and Bioengineering, 2010. **106**(6): p. 845-51.

115. Lin, W., Y. Xu, C.-C. Huang, Y. Ma, K.B. Shannon, D.-R. Chen, and Y.-W. Huang, *Toxicity of nano- and micro-sized ZnO particles in human lung epithelial cells.* Journal of Nanoparticle Research, 2008. **11**(1): p. 25-39.

116. Wang, Z.L., *Zinc oxide nanostructures: growth, properties and applications.* Journal of Physics-Condensed Matter, 2004. **16**(25): p. R829-R858.

117. Cheng, C., *Toxicology of Nanoparticles after Cellular Uptake*, in *Department of Engineering*. 2010, University of Cambridge.

118. Moos, P.J., K. Chung, D. Woessner, M. Honeggar, N.S. Cutler, and J.M. Veranth, *ZnO Particulate Matter Requires Cell Contact for Toxicity in Human Colon Cancer Cells.* Chemical Research in Toxicology, 2010. **23**(4): p. 733-739.

119. Zhang, Y., Y. Chen, P. Westerhoff, K. Hristovski, and J.C. Crittenden, *Stability of commercial metal oxide nanoparticles in water.* Water Research, 2008. **42**(8-9): p. 2204-12.

120. French, R.A., A.R. Jacobson, B. Kim, S.L. Isley, R.L. Penn, and P.C. Baveye, *Influence of ionic strength, pH, and cation valence on aggregation kinetics of titanium dioxide nanoparticles.* Environmental Science & Technology, 2009. **43**(5): p. 1354-9.

121. Zhou, D. and A.A. Keller, *Role of morphology in the aggregation kinetics of ZnO nanoparticles.* Water Research, 2010. **44**(9): p. 2948-56.

122. Bian, S.-W., I.A. Mudunkotuwa, T. Rupasinghe, and V.H. Grassian, *Aggregation and Dissolution of 4 nm ZnO Nanoparticles in Aqueous Environments: Influence of pH, Ionic Strength, Size, and Adsorption of Humic Acid.* Langmuir, 2011. **27**(10): p. 6059-6068.

123. Zhang, J., G. Dong, A. Thurber, Y. Hou, M. Gu, D.A. Tenne, C.B. Hanna, and A. Punnoose, *Tuning the properties of ZnO, hematite, and Ag nanoparticles by adjusting the surface charge.* Advanced Materials, 2012. **24**(9): p. 1232-7.

124. Gilbert, B., S.C. Fakra, T. Xia, S. Pokhrel, L. Madler, and A.E. Nel, *The Fate of ZnO Nanoparticles Administered to Human Bronchial Epithelial Cells.* ACS Nano, 2012. **6**(6): p. 4921–4930.

125. Reed, R.B., D.A. Ladner, C.P. Higgins, P. Westerhoff, and J.F. Ranville, *Solubility of nano-zinc oxide in environmentally and biologically important matrices.* Environmental Toxicology and Chemistry, 2012. **31**(1): p. 93-99.

126. Turney, T.W., M.B. Duriska, V. Jayaratne, A. Elbaz, S.J. O'Keefe, A.S. Hastings, T.J. Piva, P.F. Wright, and B.N. Feltis, *Formation of zinc-containing nanoparticles from Zn^{2+} ions in cell culture media: implications for the nanotoxicology of ZnO.* Chemical Research in Toxicology, 2012. **25**(10): p. 2057-66.

127. Lombi, E., E. Donner, E. Tavakkoli, T.W. Turney, R. Naidu, B.W. Miller, and K.G. Scheckel, *Fate of Zinc Oxide Nanoparticles during Anaerobic Digestion of Wastewater and Post-Treatment Processing of Sewage Sludge.* Environmental Science & Technology, 2012. **46**(16): p. 9089-9096.

128. Lv, J., S. Zhang, L. Luo, W. Han, J. Zhang, K. Yang, and P. Christie, *Dissolution and Microstructural Transformation of ZnO Nanoparticles under the Influence of Phosphate.* Environmental Science & Technology, 2012. **46**(13): p. 7215-7221.

129. Ma, R., C. Levard, F.M. Michel, G.E. Brown, and G.V. Lowry, *Sulfidation Mechanism for Zinc Oxide Nanoparticles and the Effect of Sulfidation on Their Solubility.* Environmental Science & Technology, 2013. **47**(6): p. 2527-2534.

130. Nyffenegger, R.M., B. Craft, M. Shaaban, S. Gorer, G. Erley, and R.M. Penner, *A hybrid electrochemical/chemical synthesis of zinc oxide nanoparticles and optically intrinsic thin films.* Chemistry of Materials, 1998. **10**(4): p. 1120-1129.

131. Piao, L.H., K.H. Lee, W.J. Kwon, S.H. Kim, and S. Yoon, *The simple and facile methods to improve dispersion stability of nanoparticles: Different chain length alkylcarboxylate mixtures.* Journal of Colloid and Interface Science, 2009. **334**(2): p. 208-211.

132. Estrella, V., T.A. Chen, M. Lloyd, J. Wojtkowiak, H.H. Cornnell, A. Ibrahim-Hashim, K. Bailey, Y. Balagurunathan, J.M. Rothberg, B.F. Sloane, J. Johnson, R.A. Gatenby, and R.J. Gillies, *Acidity Generated by the Tumor Microenvironment Drives Local Invasion.* Cancer Research, 2013. **73**(5): p. 1524-1535.

133. Kato, Y., S. Ozawa, C. Miyamoto, Y. Maehata, A. Suzuki, T. Maeda, and Y. Baba, *Acidic extracellular microenvironment and cancer.* Cancer Cell International, 2013. **13**.

134. Tannock, I.F. and D. Rotin, *Acid Ph in Tumors and Its Potential for Therapeutic Exploitation.* Cancer Research, 1989. **49**(16): p. 4373-4384.

135. Harush-Frenkel, O., E. Rozentur, S. Benita, and Y. Altschuler, *Surface charge of nanoparticles determines their endocytic and transcytotic pathway in polarized MDCK cells.* Biomacromolecules, 2008. **9**(2): p. 435-443.

136. Verma, A. and F. Stellacci, *Effect of Surface Properties on Nanoparticle-Cell Interactions.* Small, 2010. **6**(1): p. 12-21.

137. Holliday, D.L. and V. Speirs, *Choosing the right cell line for breast cancer research.* Breast Cancer Research, 2011. **13**(4).

138. Brenton, J.D., L.A. Carey, A.A. Ahmed, and C. Caldas, *Molecular classification and molecular forecasting of breast cancer: Ready for clinical application?* Journal of Clinical Oncology, 2005. **23**(29): p. 7350-7360.

139. Sirohi, B., M. Arnedos, S. Popat, S. Ashley, A. Nerurkar, G. Walsh, S. Johnston, and I.E. Smith, *Platinum-based chemotherapy in triple-negative breast cancer.* Annals of Oncology, 2008. **19**(11): p. 1847-1852.

140. Lacroix, M. and G. Leclercq, *Relevance of breast cancer cell lines as models for breast tumours: an update.* Breast Cancer Research and Treatment, 2004. **83**(3): p. 249-289.

141. Andrade, F.O., M.K. Nagamine, A. De Conti, L.M. Chaible, C.C. Fontelles, A.A. Jordao, H. Vannucchi, M.L.Z. Dagli, B.K. Bassoli, F.S. Moreno, and T.P. Ong, *Efficacy of the dietary histone deacetylase inhibitor butyrate alone or in combination with vitamin A against proliferation of MCF-7 human breast cancer cells.* Brazilian Journal of Medical and Biological Research, 2012. **45**(9): p. 841-850.

142. Snider, N.T., P.J. Altshuler, and M.B. Omary, *Modulation of cytoskeletal dynamics by mammalian nucleoside diphosphate kinase (NDPK) proteins.* Naunyn Schmiedebergs Arch Pharmacol, 2014.

143. Baxi, S.M., W. Tan, S.T. Murphy, T. Smeal, and M.J. Yin, *Targeting 3-phosphoinoside-dependent kinase-1 to inhibit insulin-like growth factor-I induced AKT and p70 S6 kinase activation in breast cancer cells.* PlOS ONE, 2012.

144. Gamble, L.J., A.V. Borovjagin, and Q.L. Matthews, *Role of RGD-containing ligands in targeting cellular integrins: Applications for ovarian cancer virotherapy (Review).* Experimental and Therapeutic Medicine, 2010. **1**(2): p. 233-240.

145. Albelda, S.M., S.A. Mette, D.E. Elder, R.M. Stewart, L. Damjanovich, M. Herlyn, and C.A. Buck, *Integrin Distribution in Malignant-Melanoma - Association of the Beta-3-Subunit with Tumor Progression.* Cancer Research, 1990. **50**(20): p. 6757-6764.

146. Gasparini, G., P.C. Brooks, E. Biganzoli, P.B. Vermeulen, E. Bonoldi, L.Y. Dirix, G. Ranieri, R. Miceli, and D.A. Cheresh, *Vascular integrin alpha(v)beta3: a new prognostic indicator in breast cancer.* Clinical Cancer Research, 1998. **4**(11): p. 2625-34.

147. Brooks, P.C., R.A.F. Clark, and D.A. Cheresh, *Requirement of Vascular Integrin Alpha(V)Beta(3) for Angiogenesis.* Science, 1994. **264**(5158): p. 569-571.

148. Lin, R.Y., K. Dayananda, and T.J. Chen, *Targeted RGD nanoparticles for highly sensitive in vivo integrin receptor imaging.* Contrast Media & Molecular Imaging, 2012. **7**(1): p. 7–18.

149. Liu, Z., F. Wang, and X. Chen, *Integrin alpha(v)beta(3)-Targeted Cancer Therapy.* Drug Development Research, 2008. **69**(6): p. 329-339.

150. Guo, Z., B. He, H. Jin, H. Zhang, W. Dai, L. Zhang, H. Zhang, X. Wang, J. Wang, X. Zhang, and Q. Zhang, *Targeting efficiency of RGD-modified nanocarriers with different ligand intervals in response to integrin alphavbeta3 clustering.* Biomaterials, 2014. **35**(23): p. 6106-17.

151. Morlieras, J., S. Dufort, L. Sancey, C. Truillet, A. Mignot, F. Rossetti, M. Dentamaro, S. Laurent, L. Vander Elst, R.N. Muller, R. Antoine, P. Dugourd, S. Roux, P. Perriat, F. Lux, J.L. Coll, and O. Tillement, *Functionalization of small rigid platforms with cyclic RGD peptides for targeting tumors overexpressing alphavbeta3-integrins.* Bioconjugate Chemistry, 2013. **24**(9): p. 1584-97.

152. Lincz, L.F., *Deciphering the apoptotic pathway: All roads lead to death.* Immunology and Cell Biology, 1998. **76**(1): p. 1-19.

153. Fink, S.L. and B.T. Cookson, *Apoptosis, Pyroptosis, and Necrosis: Mechanistic Description of Dead and Dying Eukaryotic Cells.* Infection and Immunity, 2005. **73**(4): p. 1907-1916.

154. Guerriero, J.L., D. Ditsworth, Y.J. Fan, F.P. Zhao, H.C. Crawford, and W.X. Zong, *Chemotherapy Induces Tumor Clearance Independent of Apoptosis.* Cancer Research, 2008. **68**(23): p. 9595-9600.

155. Fulda, S., *Tumor resistance to apoptosis.* International Journal of Cancer, 2009.

156. Mommsen, T.P. and T.W. Moon, *Biochemistry and Molecular Biology of Fishes*. Biochemistry and Molecular Biology of Fishes, ed. T.P. Mommsen and T.W. Moon. Vol. 6. 2005: Elsevier Science Bv, Sara Burgerhartstraat 25, Po Box 211, 1000 Ae Amsterdam, Netherlands.

157. Rathinam, R. and S.K. Alahari, *Important role of integrins in the cancer biology.* Cancer Metastasis Reviews, 2010. **29**(1): p. 223-37.

158. Korzeniewski, C. and D.M. Callewaert, *An enzyme-release assay for natural cytotoxicity.* Journal of Immunological Methods, 1983. **64**(3): p. 313-20.

159. Kimura, Y., R. Dargusch, D. Schubert, and H. Kimura, *Hydrogen sulfide protects HT22 neuronal cells from oxidative stress.* Antioxidants & Redox Signaling, 2006. **8**(3-4): p. 661-670.

160. Leahey, E., *Alphas and asterisks: The development of statistical significance testing standards in sociology.* Social Forces, 2005. **84**(1): p. 1-24.

161. Lin, W.S., Y. Xu, C.C. Huang, Y.F. Ma, K.B. Shannon, D.R. Chen, and Y.W. Huang, *Toxicity of nano- and micro-sized ZnO particles in human lung epithelial cells.* Journal of Nanoparticle Research, 2009. **11**(1): p. 25-39.

162. Sharma, V., R.K. Shukla, N. Saxena, D. Parmar, M. Das, and A. Dhawan, *DNA damaging potential of zinc oxide nanoparticles in human epidermal cells.* Toxicology Letters, 2009. **185**(3): p. 211-218.

163. Dive, C., C.D. Gregory, D.J. Phipps, D.L. Evans, A.E. Milner, and A.H. Wyllie, *Analysis and Discrimination of Necrosis and Apoptosis (Programmed Cell-Death) by Multiparameter Flow-Cytometry.* Biochimica Et Biophysica Acta, 1992. **1133**(3): p. 275-285.

164. Fabio Pastorino, C.B., Monica Loi , Daniela Di Paolo, Annarita Di Fiore, Patrizia Perri , and G.P.a.M. Ponzoni, *Nanocarrier-Mediated Targeting of Tumor and Tumor Vascular Cells Improves Uptake and Penetration of Drugs into Neuroblastoma.* Frontiers in Oncology, 2013. **3**.

165. Guarnieri, D., S. Sabella, O. Muscetti, V. Belli, M.A. Malvindi, S. Fusco, E. De Luca, P.P. Pompa, and P.A. Netti, *Transport across the cell-membrane dictates nanoparticle fate and toxicity: a new paradigm in nanotoxicology.* Nanoscale, 2014. **6**(17): p. 10264-10273.

166. Alkilany, A.M., P.K. Nagaria, C.R. Hexel, T.J. Shaw, C.J. Murphy, and M.D. Wyatt, *Cellular Uptake and Cytotoxicity of Gold Nanorods: Molecular Origin of Cytotoxicity and Surface Effects.* Small, 2009. **5**(6): p. 701-708.

167. Yu, J., M. Baek, H.E. Chung, and S.J. Choi, *Effects of physicochemical properties of zinc oxide nanoparticles on cellular uptake*, in *International Conference on Safe Production and Use of Nanomaterials*. 2011, Journal of Physics: Conference Series

168. Decker, T. and M.L. Lohmann-Matthes, *A quick and simple method for the quantitation of lactate dehydrogenase release in measurements of cellular cytotoxicity and tumor necrosis factor (TNF) activity.* Journal of Immunological Methods, 1988. **115**(1): p. 61-9.

169. Essmann, F., I.H. Engels, G. Totzke, K. Schulze-Osthoff, and R.U. Janicke, *Apoptosis resistance of MCF-7 breast carcinoma cells to ionizing radiation is independent of p53 and cell cycle control but caused by the lack of caspase-3 and a caffeine-inhibitable event.* Cancer Research, 2004. **64**(19): p. 7065-7072.

170. Janicke, R.U., M.L. Sprengart, M.R. Wati, and A.G. Porter, *Caspase-3 is required for DNA fragmentation and morphological changes associated with apoptosis.* Journal of Biological Chemistry, 1998. **273**(16): p. 9357-9360.

171. Hsiao, I.L. and Y.J. Huang, *Effects of serum on cytotoxicity of nano-and micro-sized ZnO particles.* Journal of Nanoparticle Research, 2013.

172. Xiong, D., T. Fang, L. Yu, X. Sima, and W. Zhu, *Effects of nano-scale TiO_2, ZnO and their bulk counterparts on zebrafish: Acute toxicity, oxidative stress and oxidative damage.* Science of the Total Environment, 2011. **409**(8): p. 1444-1452.

173. Kerr, J.F.R., C.M. Winterford, and B.V. Harmon, *Apoptosis - Its Significance in Cancer and Cancer-Therapy.* Cancer, 1994. **73**(8): p. 2013-2026.

174. Fadok, V.A., D.R. Voelker, P.A. Campbell, J.J. Cohen, D.L. Bratton, and P.M. Henson, *Exposure of phosphatidylserine on the surface of apoptotic lymphocytes triggers specific recognition and removal by macrophages.* Journal of immunology, 1992. **148**(7): p. 2207-2216.

175. Silva, M.T., *Secondary necrosis: The natural outcome of the complete apoptotic program.* FEBS Letters, 2010. **584**(22): p. 4491-4499.

176. Wyllie, A.H., Kerr, J.F. and Currie, A.R. , *Cell death: the significance of apoptosis.* International Review of Cytology, 1980. **68,**: p. 251–306.

177. Rampersad, S.N., *Multiple Applications of Alamar Blue as an Indicator of Metabolic Function and Cellular Health in Cell Viability Bioassays.* Sensors, 2012. **12**(9): p. 12347-12360.

178. Cree, I.A. and P.E. Andreotti, *Measurement of cytotoxicity by ATP-based luminescence assay in primary cell cultures and cell lines.* Toxicology in Vitro, 1997. **11**(5): p. 553-556.

179. Adam, N., C. Schmitt, J. Galceran, E. Companys, A. Vakurov, R. Wallace, D. Knapen, and R. Blust, *The chronic toxicity of ZnO nanoparticles and $ZnCl_2$ to Daphnia magna and the use of different methods to assess nanoparticle aggregation and dissolution.* Nanotoxicology, 2014. **8**(7): p. 709-717.

180. Hwang, J.J., H.N. Kim, J. Kim, D.H. Cho, M.J. Kim, Y.S. Kim, Y. Kim, S.J. Park, and J.Y. Koh, *Zinc(II) ion mediates tamoxifen-induced autophagy and cell death in MCF-7 breast cancer cell line.* Biometals, 2010. **23**(6): p. 997-1013.

181. Rudolf, E., K. Rudolf, and M. Cervinka, *Zinc induced apoptosis in HEP-2 cancer cells: The role of oxidative stress and mitochondria.* Biofactors, 2005. **23**(2): p. 107-120.

182. van Engeland, M., L.J.W. Nieland, F.C.S. Ramaekers, B. Schutte, and C.P.M. Reutelingsperger, *Annexin V-affinity assay: A review on an apoptosis detection system based on phosphatidylserine exposure.* Cytometry, 1998. **31**(1): p. 1-9.

183. Ingrid Schmid, W.J.K., Christel H. Uittenbogaart, Jonathan Braun, and and J.V. Giorgi, *Dead cell discrimination with 7-amino-actinomcin D in combination with dual color immunofluorescence in single laser flow cytometry.* Cytometry Part A, 1992. **13**: p. 204-208

184. Provinciali, M., G. Distefano, and N. Fabris, *Dose-dependent opposite effect of zinc on apoptosis in mouse thymocytes.* International Journal of Immunopharmacology, 1995. **17**(9): p. 735-744.

185. Ng, K.W., S.P.K. Khoo, B.C. Heng, M.I. Setyawati, E.C. Tan, X.X. Zhao, S.J. Xiong, W.R. Fang, D.T. Leong, and J.S.C. Loo, *The role of the tumor suppressor p53 pathway in the*

cellular DNA damage response to zinc oxide nanoparticles. Biomaterials, 2011. **32**(32): p. 8218-8225.

186. Ahmed, F.N., *Examination of Mediator composition and p53 in distinct breast cancer lines: MCF7 and MDA-MB-231*, in *Department of Chemistry and Biochemistry*. 2011, University of Colorado at Boulder.

187. Pujalte, I., I. Passagne, B. Brouillaud, M. Treguer, E. Durand, C. Ohayon-Courtes, and B. L'Azou, *Cytotoxicity and oxidative stress induced by different metallic nanoparticles on human kidney cells.* Particle and Fibre Toxicology, 2011. **8**.

188. Peulon, S. and D. Lincot, *Mechanistic Study of Cathodic Electrodeposition of Zinc Oxide and Zinc Hydroxychloride Films from Oxygenated Aqueous Zinc Chloride Solutions.* Journal of The Electrochemical Society, 1998. **145**(3): p. 864-874.

189. Karnovsky, M.J., *A formaldehyde-gluteraldehyde fixative of high osmolality for use in electron-microscopy*. Current Contents/Life Sciences, 1985(15): p. 20-20.

190. Taherian, A., X.L. Li, Y.Q. Liu, and T.A. Haas, *Differences in integrin expression and signaling within human breast cancer cells.* Bmc Cancer, 2011. **11**.

191. Lymburner, S., S. McLeod, M. Purtzki, C. Roskelley, and Z.M. Xu, *Zinc inhibits magnesium-dependent migration of human breast cancer MDA-MB-231 cells on fibronectin.* Journal of Nutritional Biochemistry, 2013. **24**(6): p. 1034-1040.

192. Colvin, R.A., N. Davis, R.W. Nipper, and P.A. Carter, *Zinc transport in the brain: Routes of zinc influx and efflux in neurons.* Journal of Nutrition, 2000. **130**(5): p. 1484s-1487s.

193. Palmiter, R.D. and L.P. Huang, *Efflux and compartmentalization of zinc by members of the SLC30 family of solute carriers.* Pflugers Archiv-European Journal of Physiology, 2004. **447**(5): p. 744-751.

194. Kambe, T., Y. Yamaguchi-Iwai, R. Sasaki, and M. Nagao, *Overview of mammalian zinc transporters.* Cellular and Molecular Life Sciences, 2004. **61**(1): p. 49-68.

195. Liuzzi, J.P. and R.J. Cousins, *Mammalian zinc transporters.* Annual Review of Nutrition, 2004. **24**: p. 151-172.

196. McMahon, R.J. and R.J. Cousins, *Mammalian zinc transporters.* Journal of Nutrition, 1998. **128**(4): p. 667-670.

197. Kagara, N., N. Tanaka, S. Noguchi, and T. Hirano, *Zinc and its transporter ZIP10 are involved in invasive behavior of breast cancer cells.* Cancer Science, 2007. **98**(5): p. 692-697.

198. Ometto, C., C. Fabris, C. Milanesi, G. Jori, M.J. Cook, and D.A. Russell, *Tumour-localising and -photosensitising properties of a novel zinc(II) octadecylphthalocyanine.* British Journal of Cancer, 1996. **74**(12): p. 1891-1899.

199. Leland, H.V., *Ultrastructural changes in the hepatocytes of juvenile rainbow trout and mature brown trout exposed to copper or zinc.* Environmental Toxicology and Chemistry, 1983. **2**(3): p. 353-368.

200. Al-Hajj, M., M.W. Becker, M. Wichal, I. Weissman, and M.F. Clarke, *Therapeutic implications of cancer stem cells.* Current Opinion in Genetics & Development, 2004. **14**(1): p. 43-47.

201. Selby, P., J.P. Bizzari, and R.N. Buick, *Therapeutic implications of a stem cell model for human breast cancer: a hypothesis.* Cancer treatment reports, 1983. **67**(7-8): p. 659-63.

202. Greve, B., R. Kelsch, K. Spaniol, H.T. Eich, and M. Gotte, *Flow cytometry in cancer stem cell analysis and separation.* Cytometry A, 2012. **81**(4): p. 284-93.

203. Kakarala, M. and M.S. Wicha, *Implications of the cancer stem-cell hypothesis for breast cancer prevention and therapy.* Journal of Clinical Oncology, 2008. **26**(17): p. 2813-2820.

204. Fillmore, C. and C. Kuperwasser, *Human breast cancer stem cell markers CD44 and CD24: enriching for cells with functional properties in mice or in man?* Breast Cancer Research, 2007. **9**(3): p. 303.

205. Jaggupilli, A. and E. Elkord, *Significance of CD44 and CD24 as Cancer Stem Cell Markers: An Enduring Ambiguity.* Clinical & Developmental Immunology, 2012.

206. Al-Hajj, M., M.S. Wicha, A. Benito-Hernandez, S.J. Morrison, and M.F. Clarke, *Prospective identification of tumorigenic breast cancer cells.* Proceedings of the National Academy of Sciences of the United States of America (PNAS), 2003. **100**(7): p. 3983-8.

207. Prat, A., J.S. Parker, O. Karginova, C. Fan, C. Livasy, J.I. Herschkowitz, X.P. He, and C.M. Perou, *Phenotypic and molecular characterization of the claudin-low intrinsic subtype of breast cancer.* Breast Cancer Research, 2010. **12**(5).

208. Sheridan, C., H. Kishimoto, R.K. Fuchs, S. Mehrotra, P. Bhat-Nakshatri, C.H. Turner, R. Goulet, S. Badve, and H. Nakshatri, *CD44(+)/CD24(-) breast cancer cells exhibit enhanced invasive properties: an early step necessary for metastasis.* Breast Cancer Research, 2006. **8**(5): p. 13.

209. Burdick, M.M., K.A. Henson, L.F. Delgadillo, Y.E. Choi, D.J. Goetz, D.F. Tees, and F. Benencia, *Expression of E-selectin ligands on circulating tumor cells: cross-regulation with cancer stem cell regulatory pathways?* Frontiers in Oncology, 2012. **2**: p. 103.

210. Wu, M.M., J. Llopis, S. Adams, J.M. McCaffery, M.S. Kulomaa, T.E. Machen, H.P.H. Moore, and R.Y. Tsien, *Organelle pH studies using targeted avidin and fluorescein-biotin.* Chemistry & Biology, 2000. **7**(3): p. 197-209.

211. Llopis, J., M.M. Wu, S. Adams, J.M. McCaffery, T.E. Machen, H.P.H. Moore, and R.Y. Tsien, *Organelle pH studies using targeted avidin and fluorescein-biotin, and green fluorescent proteins.* Journal of Physiology-London, 2000. **527**: p. 14s-14s.

212. Shipitsin, M., L.L. Campbell, P. Argani, S. Werernowicz, N. Bloushtain-Qimron, J. Yao, T. Nikolskaya, T. Serebryiskaya, R. Beroukhim, M. Hu, M.K. Halushka, S. Sukumar, L.M. Parker, K.S. Anderson, L.N. Harris, J.E. Garber, A.L. Richardson, S.J. Schnitt, Y. Nikolsky, R.S. Gelman, and K. Polyak, *Molecular definition of breast tumor heterogeneity.* Cancer Cell, 2007. **11**(3): p. 259-273.

213. Danhier, F., B. Vroman, N. Lecouturier, N. Crokart, V. Pourcelle, H. Freichels, C. Jerome, J. Marchand-Brynaert, O. Feron, and V. Preat, *Targeting of tumor endothelium by RGD-grafted PLGA-nanoparticles loaded with Paclitaxel.* Journal of Controlled Release, 2009. **140**(2): p. 166-173.

214. Dobrovolskaia, M.A. and S.E. Mcneil, *Immunological properties of engineered nanomaterials.* Nature Nanotechnology, 2007. **2**(8): p. 469-478.

215. Maiorano, G., S. Sabella, B. Sorce, V. Brunetti, M.A. Malvindi, R. Cingolani, and P.P. Pompa, *Effects of Cell Culture Media on the Dynamic Formation of Protein-Nanoparticle Complexes and Influence on the Cellular Response.* ACS Nano, 2010. **4**(12): p. 7481-7491.

216. Nagayama, S., K. Ogawara, Y. Fukuoka, K. Higaki, and T. Kimura, *Time-dependent changes in opsonin amount associated on nanoparticles alter their hepatic uptake characteristics.* International Journal of Pharmaceutics, 2007. **342**(1-2): p. 215-221.

217. Aggarwal, P., J.B. Hall, C.B. McLeland, M.A. Dobrovolskaia, and S.E. McNeil, *Nanoparticle interaction with plasma proteins as it relates to particle biodistribution, biocompatibility and therapeutic efficacy.* Advanced Drug Delivery Reviews, 2009. **61**(6): p. 428-437.

218. Bhunia, A.K., P.K. Samanta, S. Saha, and T. Kamilya, *ZnO nanoparticle-protein interaction: Corona formation with associated unfolding.* Applied Physics Letters, 2013. **103**(14).

219. Chakraborti, S., P. Joshi, D. Chakravarty, V. Shanker, Z.A. Ansari, S.P. Singh, and P. Chakrabarti, *Interaction of polyethyleneimine-functionalized ZnO nanoparticles with bovine serum albumin.* Langmuir, 2012. **28**(30): p. 11142-52.

220. Kathiravan, A., G. Paramaguru, and R. Renganathan, *Study on the binding of colloidal zinc oxide nanoparticles with bovine serum albumin.* Journal of Molecular Structure, 2009. **934**(1-3): p. 129-137.

221. Bardhan, M., G. Mandal, and T. Ganguly, *ZnO nanoparticle-protein interaction: Corona formation with associated unfolding.* Journal of Applied Physics, 2009. **106**(3).

222. Tenzer, S., D. Docter, J. Kuharev, and A. Musyanovych, *Rapid formation of plasma protein corona critically affects nanoparticle pathophysiology.* Nature Nanotechnology, 2013. **8**: p. 772–781.

223. Jiang, L., L. He, and M. Fountoulakis, *Comparison of protein precipitation methods for sample preparation prior to proteomic analysis.* Journal of Chromatography A, 2004. **1023**(2): p. 317-320.

224. Anderson, N.L. and N.G. Anderson, *The human plasma proteome: History, character, and diagnostic prospects (vol 1, pg 845, 2002).* Molecular & Cellular Proteomics, 2003. **2**(1): p. 50-50.

225. Steel, L.F., M.G. Trotter, P.B. Nakajima, T.S. Mattu, G. Gonye, and T. Block, *Efficient and specific removal of albumin from human serum samples.* Molecular & Cellular Proteomics, 2003. **2**(4): p. 262-270.

226. Cedervall, T., I. Lynch, S. Lindman, T. Berggard, E. Thulin, H. Nilsson, K.A. Dawson, and S. Linse, *Understanding the nanoparticle-protein corona using methods to quantify exchange rates and affinities of proteins for nanoparticles.* Proceedings of the National Academy of Sciences of the United States of America (PNAS), 2007. **104**(7): p. 2050-2055.

227. UniPort. *Fermitin family homolog 3*. [cited Sep. 2014; Available from: http://www.uniprot.org/uniprot/Q86UX7.

228. *Radixin*. Sep. 2014]; Available from: http://www.uniprot.org/uniprot/P35241.

229. Pino, P.d., B. Pelaz, Q. Zhang, P. Maffre, G.U. Nienhaus, and W.J. Parak, *Protein corona formation around nanoparticles – from the past to the future.* Materials Horizons, 2014. **1**(3): p. 301.

230. Vogt, W., *Activation of the Complement-System.* Agents and Actions, 1983. **13**(5-6): p. 391-397.

231. Kreuter, J., D. Shamenkov, V. Petrov, P. Ramge, K. Cychutek, C. Koch-Brandt, and R. Alyautdin, *Apolipoprotein-mediated transport of nanoparticle-bound drugs across the blood-brain barrier.* Journal of drug targeting, 2002. **10**(4): p. 317-325.

232. Mammen, M., S.K. Choi, and G.M. Whitesides, *Polyvalent interactions in biological systems: Implications for design and use of multivalent ligands and inhibitors.* Angewandte Chemie-International Edition, 1998. **37**(20): p. 2755-2794.

233. Ozgur, U., Y.I. Alivov, C. Liu, A. Teke, M.A. Reshchikov, S. Dogan, V. Avrutin, S.J. Cho, and H. Morkoc, *A comprehensive review of ZnO materials and devices.* Journal of Applied Physics, 2005. **98**(4).

234. Kachynski, A.V., A.N. Kuzmin, M. Nyk, I. Roy, and P.N. Prasad, *Zinc oxide nanocrystals for nonresonant nonlinear optical microscopy in biology and medicine.* Journal of Physical Chemistry C, 2008. **112**(29): p. 10721-10724.

235. Wang, X.L., F. Yang, W. Yang, and X.R. Yang, *A study on the antibacterial activity of one-dimensional ZnO nanowire arrays: effects of the orientation and plane surface.* Chemical Communications, 2007(42): p. 4419-4421.

236. Singh, D.P., *Synthesis and Growth of ZnO Nanowires.* Science of Advanced Materials, 2010. **2**(3): p. 245-272.

237. Huang, M.H., Y.Y. Wu, H. Feick, N. Tran, E. Weber, and P.D. Yang, *Catalytic growth of zinc oxide nanowires by vapor transport.* Advanced Materials, 2001. **13**(2): p. 113-116.

238. Lee, J.S., K. Park, M.I. Kang, I.W. Park, S.W. Kim, W.K. Cho, H.S. Han, and S. Kim, *ZnO nanomaterials synthesized from thermal evaporation of ball-milled ZnO powders.* Journal of Crystal Growth, 2003. **254**(3-4): p. 423-431.

239. Zhao, Q.X., P. Klason, and M. Willander, *Growth of ZnO nanostructures by vapor-liquid-solid method.* Applied Physics a-Materials Science & Processing, 2007. **88**(1): p. 27-30.

240. Jie, J.S., G.Z. Wang, Y.M. Chen, X.H. Han, Q.T. Wang, B. Xu, and J.G. Hou, *Synthesis and optical properties of well-aligned ZnO nanorod array on an undoped ZnO film.* Applied Physics Letters, 2005. **86**(3).

241. Chang, P.C., Z.Y. Fan, D.W. Wang, W.Y. Tseng, W.A. Chiou, J. Hong, and J.G. Lu, *ZnO nanowires synthesized by vapor trapping CVD method.* Chemistry of Materials, 2004. **16**(24): p. 5133-5137.

242. Geng, C.Y., Y. Jiang, Y. Yao, X.M. Meng, J.A. Zapien, C.S. Lee, Y. Lifshitz, and S.T. Lee, *Well-aligned ZnO nanowire arrays fabricated on silicon substrates.* Advanced Functional Materials, 2004. **14**(6): p. 589-594.

243. Zhang, H.Z., X.C. Sun, R.M. Wang, and D.P. Yu, *Growth and formation mechanism of c-oriented ZnO nanorod arrays deposited on glass.* Journal of Crystal Growth, 2004. **269**(2-4): p. 464-471.

244. Park, W.I., D.H. Kim, S.W. Jung, and G.C. Yi, *Metalorganic vapor-phase epitaxial growth of vertically well-aligned ZnO nanorods.* Applied Physics Letters, 2002. **80**(22): p. 4232-4234.

245. Zeng, J.N., J.K. Low, Z.M. Ren, T. Liew, and Y.F. Lu, *Effect of deposition conditions on optical and electrical properties of ZnO films prepared by pulsed laser deposition.* Applied Surface Science, 2002. **197**: p. 362-367.

246. Dai, Z.R., Z.W. Pan, and Z.L. Wang, *Novel nanostructures of functional oxides synthesized by thermal evaporation.* Advanced Functional Materials, 2003. **13**(1): p. 9-24.

247. Kong, Y.C., D.P. Yu, B. Zhang, W. Fang, and S.Q. Feng, *Ultraviolet-emitting ZnO nanowires synthesized by a physical vapor deposition approach.* Applied Physics Letters, 2001. **78**(4): p. 407-409.

248. Li, Y., G.S. Cheng, and L.D. Zhang, *Fabrication of highly ordered ZnO nanowire arrays in anodic alumina membranes.* Journal of Materials Research, 2000. **15**(11): p. 2305-2308.

249. Zheng, M.J., L.D. Zhang, G.H. Li, and W.Z. Shen, *Fabrication and optical properties of large-scale uniform zinc oxide nanowire arrays by one-step electrochemical deposition technique.* Chemical Physics Letters, 2002. **363**(1-2): p. 123-128.

250. Guo, M., P. Diao, and S.M. Cai, *Hydrothermal growth of well-aligned ZnO nanorod arrays: Dependence of morphology and alignment ordering upon preparing conditions.* Journal of Solid State Chemistry, 2005. **178**(6): p. 1864-1873.

251. Yamabi, S. and H. Imai, *Growth conditions for wurtzite zinc oxide films in aqueous solutions.* Journal of Materials Chemistry, 2002. **12**(12): p. 3773-3778.

252. Sun, Y., N.A. Fox, D.J. Riley, and M.N.R. Ashfold, *Hydrothermal growth of ZnO nanorods aligned parallel to the substrate surface.* Journal of Physical Chemistry C, 2008. **112**(25): p. 9234-9239.

253. Vayssieres, L., *Growth of arrayed nanorods and nanowires of ZnO from aqueous solutions.* Advanced Materials, 2003. **15**(5): p. 464-466.

254. Hames, Y., Z. Alpaslan, A. Kosemen, S.E. San, and Y. Yerli, *Electrochemically grown ZnO nanorods for hybrid solar cell applications.* Solar Energy, 2010. **84**(3): p. 426-431.

255. Cao, B.Q., Y. Li, G.T. Duan, and W.P. Cai, *Growth of ZnO nanoneedle arrays with strong ultraviolet emissions by an electrochemical deposition method.* Crystal Growth & Design, 2006. **6**(5): p. 1091-1095.

256. Xu, C.K., G.D. Xu, Y.K. Liu, and G.H. Wang, *A simple and novel route for the preparation of ZnO nanorods.* Solid State Communications, 2002. **122**(3-4): p. 175-179.

257. Lincot, D., *Electrodeposition of semiconductors.* Thin Solid Films, 2005. **487**(1-2): p. 40-48.

258. Zeng, H.B., J.B. Cui, B.Q. Cao, U. Gibson, Y. Bando, and D. Golberg, *Electrochemical Deposition of ZnO Nanowire Arrays: Organization, Doping, and Properties.* Science of Advanced Materials, 2010. **2**(3): p. 336-358.

259. Ayati, N.S., E. Akbari, S.P. Marashi, and S. Saramad, *Template assisted Growth of Zinc Oxide-based nanowires and piezoelectric properties.* Ultrafine Grained and Nano-Structured Materials Iv, 2014. **829**: p. 757-761.

260. Guo, M., C. Yang, M. Zhang, Y. Zhang, T. Ma, X. Wang, and X. Wang, *Effects of preparing conditions on the electrodeposition of well-aligned ZnO nanorod arrays.* Electrochimica Acta, 2008. **53**(14): p. 4633-4641.

261. Maas, M.G., E.J.B. Rodijk, A.W. Maijenburg, D.H.A. Blank, and J.E. ten Elshof, *Microstructure development in zinc oxide nanowires and iron oxohydroxide nanotubes*

by cathodic electrodeposition in nanopores. Journal of Materials Research, 2011. **26**(17): p. 2261-2267.

262. Pruna, A., D. Pullini, and D.B. Mataix, *Influence of Deposition Potential on Structure of ZnO Nanowires Synthesized in Track-Etched Membranes.* Journal of the Electrochemical Society, 2012. **159**(4): p. E92-E98.

263. Illy, B., B.A. Shollock, J.L. MacManus-Driscoll, and M.P. Ryan, *Electrochemical growth of ZnO nanoplates.* Nanotechnology, 2005. **16**(2): p. 320-324.

264. Peulon, S. and D. Lincot, *Cathodic electrodeposition from aqueous solution of dense or open-structured zinc oxide films.* Advanced Materials, 1996. **8**(2): p. 166-&.

265. Izaki, M. and T. Omi, *Transparent zinc oxide films prepared by electrochemical reaction.* Applied Physics Letters, 1996. **68**(17): p. 2439-2440.

266. Yoshida, T., D. Komatsu, N. Shimokawa, and H. Minoura, *Mechanism of cathodic electrodeposition of zinc oxide thin films from aqueous zinc nitrate baths.* Thin Solid Films, 2004. **451**: p. 166-169.

267. Wong, M.H., A. Berenov, X. Qi, M.J. Kappers, Z.H. Barber, B. Illy, Z. Lockman, M.P. Ryan, and J.L. MacManus-Driscoll, *Electrochemical growth of ZnO nano-rods on polycrystalline Zn foil.* Nanotechnology, 2003. **14**(9): p. 968-973.

268. Lai, M. and D.J. Riley, *Templated electrosynthesis of nanomaterials and porous structures.* Journal of Colloid and Interface Science, 2008. **323**(2): p. 203-212.

269. Sharma, S.K., A. Rammohan, and A. Sharma, *Templated one step electrodeposition of high aspect ratio n-type ZnO nanowire arrays.* Journal of Colloid and Interface Science, 2010. **344**(1): p. 1-9.

270. Sima, M., I. Enculescu, M. Sima, and E. Vasile, *Semiconductor nanowires obtained by template method.* Journal of Optoelectronics and Advanced Materials, 2007. **9**(5): p. 1551-1554.

271. Leprince-Wang, Y., A. Yacoubi-Ouslim, and G.Y. Wang, *Structure study of electrodeposited ZnO nanowires.* Microelectronics Journal, 2005. **36**(7): p. 625-628.

272. Lai, M. and D.J. Riley, *Templated electrosynthesis of zinc oxide nanorods.* Chemistry of Materials, 2006. **18**(9): p. 2233-2237.

273. Sima, M., I. Enculescu, and E. Vasile, *Growth of ZnO micro and nanowires using the template method.* Journal of Optoelectronics and Advanced Materials, 2006. **8**(2): p. 825-828.

274. Sliwinski, T., A. Czechowska, M. Kolodziejczak, J. Jajte, M. Wisniewska-Jarosinska, and J. Blasiak, *Zinc salts differentially modulate DNA damage in normal and cancer cells.* Cell Biology International, 2009. **33**(4): p. 542-547.

275. Holdenrieder, S. and P. Stieber, *Apoptotic markers in cancer.* Clinical Biochemistry, 2004. **37**(7): p. 605-617.

276. Budihardjo, I., H. Oliver, M. Lutter, X. Luo, and X.D. Wang, *Biochemical pathways of caspase activation during apoptosis.* Annual Review of Cell and Developmental Biology, 1999. **15**: p. 269-290.

277. Hockenbery, D.M., Z.N. Oltvai, X.M. Yin, C.L. Milliman, and S.J. Korsmeyer, *Bcl-2 Functions in an Antioxidant Pathway to Prevent Apoptosis.* Cell, 1993. **75**(2): p. 241-251.

278. Krag, D.N., G.S. Shukla, G.P. Shen, S. Pero, T. Ashikaga, S. Fuller, D.L. Weaver, S. Burdette-Radoux, and C. Thomas, *Selection of tumor-binding ligands in cancer patients with phage display libraries.* Cancer Research, 2006. **66**(15): p. 7724-7733.

279. Wang, R., L. Zhang, H. Zhang, X. Wei, Y. Yang, S. Zhang, J. Wu, M. Wu, Y. Cao, and R. Niu, *In Vivo Selection of Phage Sequences and Characterization of Peptide-specific Binding to Breast Cancer Cells.* Chinese Journal of Clinical Oncology, 2008. **5**: p. 128-131.

Appendix

Formulation for Minimum Essential Medium (MEM).

Minimum Essential Medium (MEM), Life technologies, catalogue number: 31095029			
Components	**Molecular Weight**	**Concentration (mg/L)**	**Concentration (mM)**
Amino acids			
L-Arginine hydrochloride	211.0	126.0	0.5971564
L-Cystine	240.0	24.0	0.1
L-Glutamine	146.0	292.0	2.0
L-Histidine hydrochloride-H2O	210.0	42.0	0.2
L-Isoleucine	131.0	52.0	0.39694658
L-Leucine	131.0	52.0	0.39694658
L-Lysine hydrochloride	183.0	73.0	0.3989071
L-Methionine	149.0	15.0	0.10067114
L-Phenylalanine	165.0	32.0	0.19393939
L-Threonine	119.0	48.0	0.40336135
L-Tryptophan	204.0	10.0	0.04901961
L-Tyrosine	181.0	36.0	0.19889502
L-Valine	117.0	46.0	0.3931624
Vitamins			
Choline chloride	140.0	1.0	0.007142857
D-Calcium pantothenate	477.0	1.0	0.002096436
Folic Acid	441.0	1.0	0.0022675737

Minimum Essential Medium (MEM), Life technologies, catalogue number: 31095029			
Niacinamide	122.0	1.0	0.008196721
Pyridoxal hydrochloride	204.0	1.0	0.004901961
Riboflavin	376.0	0.1	2.6595744E-4
Thiamine hydrochloride	337.0	1.0	0.002967359
i-Inositol	180.0	2.0	0.011111111
Inorganic salts			
Calcium Chloride ($CaCl_2$-$2H_2O$)	147.0	264.0	1.7959183
Magnesium Sulfate ($MgSO_4$-7H2O)	246.0	200.0	0.8130081
Potassium Chloride (KCl)	75.0	400.0	5.3333335
Sodium Bicarbonate ($NaHCO_3$)	84.0	2200.0	26.190475
Sodium Chloride (NaCl)	58.0	6800.0	117.24138
Sodium Phosphate monobasic (NaH_2PO_4-	156.0	158.0	1.0128205
Other components			
D-Glucose (Dextrose)	180.0	1000.0	5.5555553
Phenol Red	376.4	10.0	0.026567481

Formulation for Dulbecco's Modified Eagle Medium (DMEM).

Dulbecco's Modified Eagle Medium (DMEM) (1X) liquid (high glucose), Life technologies, catalogue number: 11880028			
Components	**Molecular Weight**	**Concentration (mg/L)**	**Concentration (mM)**
Amino acids			
Glycine	75.0	30.0	0.4
L-Arginine hydrochloride	211.0	84.0	0.39810428
L-Cystine 2HCl	313.0	63.0	0.20127796
L-Histidine hydrochloride-H2O	210.0	42.0	0.2
L-Isoleucine	131.0	105.0	0.8015267
L-Leucine	131.0	105.0	0.8015267
L-Lysine hydrochloride	183.0	146.0	0.7978142
L-Methionine	149.0	30.0	0.20134228
L-Phenylalanine	165.0	66.0	0.4
L-Serine	105.0	42.0	0.4
L-Threonine	119.0	95.0	0.79831934
L-Tryptophan	204.0	16.0	0.078431375
L-Tyrosine	181.0	72.0	0.39779004
L-Valine	117.0	94.0	0.8034188
Vitamins			
Choline chloride	140.0	4.0	0.028571429
D-Calcium pantothenate	477.0	4.0	0.008385744
Folic Acid	441.0	4.0	0.009070295

Dulbecco's Modified Eagle Medium (DMEM) (1X) liquid (high glucose), Life technologies, catalogue number: 11880028			
Niacinamide	122.0	4.0	0.032786883
Pyridoxine hydrochloride	206.0	4.0	0.019417476
Riboflavin	376.0	0.4	0.0010638298
Thiamine hydrochloride	337.0	4.0	0.011869436
i-Inositol	180.0	7.2	0.04
Inorganic salts			
Calcium Chloride (CaCl2-2H2O)	147.0	264.0	1.7959183
Ferric Nitrate (Fe(NO3)3"9H2O)	404.0	0.1	2.4752476E-4
Magnesium Sulfate (MgSO4-7H2O)	246.0	200.0	0.8130081
Potassium Chloride (KCl)	75.0	400.0	5.3333335
Sodium Bicarbonate (NaHCO3)	84.0	3700.0	44.04762
Sodium Chloride (NaCl)	58.0	6400.0	110.344826
Sodium Phosphate monobasic (NaH2PO4-	154.0	141.0	0.91558444
Other components			
D-Glucose (Dextrose)	180.0	1000.0	5.5555553
Sodium Pyruvate	110.0	110.0	1.0

Formulation for of DMEM/F-12 Medium.

DMEM/F-12 (1:1), catalogue no. 11320-033, Life technologies, catalog Number(s) 11320033 , 11320074 , 11320082			
Components	**Molecular Weight**	**Concentration (mg/L)**	**Concentration (mM)**
Amino acids			
Glycine	75.0	18.75	0.25
L-Alanine	89.0	4.45	0.049999997
L-Arginine hydrochloride	211.0	147.5	0.69905216
L-Asparagine-H2O	150.0	7.5	0.05
L-Aspartic acid	133.0	6.65	0.05
L-Cysteine hydrochloride-H2O	176.0	17.56	0.09977272
L-Cystine 2HCl	313.0	31.29	0.09996805
L-Glutamic Acid	147.0	7.35	0.05
L-Glutamine	146.0	365.0	2.5
L-Histidine hydrochloride-H2O	210.0	31.48	0.14990476
L-Isoleucine	131.0	54.47	0.41580153
L-Leucine	131.0	59.05	0.45076334
L-Lysine hydrochloride	183.0	91.25	0.4986339
L-Methionine	149.0	17.24	0.11570469
L-Phenylalanine	165.0	35.48	0.2150303
L-Proline	115.0	17.25	0.15
L-Serine	105.0	26.25	0.25
L-Threonine	119.0	53.45	0.44915968
L-Tryptophan	204.0	9.02	0.04421569
L-Tyrosine disodium salt dihydrate	261.0	55.79	0.21375479

DMEM/F-12 (1:1), catalogue no. 11320-033, Life technologies, catalog Number(s) 11320033 , 11320074 , 11320082			
L-Valine	117.0	52.85	0.4517094
Vitamins			
Biotin	244.0	0.0035	1.4344263E-5
Choline chloride	140.0	8.98	0.06414285
D-Calcium pantothenate	477.0	2.24	0.0046960167
Folic Acid	441.0	2.65	0.0060090707
Niacinamide	122.0	2.02	0.016557377
Pyridoxine hydrochloride	206.0	2.013	0.009771844
Riboflavin	376.0	0.219	5.824468E-4
Thiamine hydrochloride	337.0	2.17	0.0064391694
Vitamin B12	1355.0	0.68	5.0184503E-4
i-Inositol	180.0	12.6	0.07
Inorganic salts			
Calcium Chloride ($CaCl_2$) (anhyd.)	111.0	116.6	1.0504504
Cupric sulfate ($CuSO_4$.5H2O)	250.0	0.0013	5.2E-6
Ferric Nitrate ($Fe(NO_3)_3$.9H2O)	404.0	0.05	1.2376238E-4
Ferric sulfate (FeSO4-7H2O)	278.0	0.417	0.0015
Magnesium Chloride (anhydrous)	95.0	28.64	0.30147368
Magnesium Sulfate ($MgSO_4$) (anhyd.)	120.0	48.84	0.407
Potassium Chloride (KCl)	75.0	311.8	4.1573334
Sodium Bicarbonate ($NaHCO_3$)	84.0	2438.0	29.02381
Sodium Chloride (NaCl)	58.0	6995.5	120.61207

DMEM/F-12 (1:1), catalogue no. 11320-033, Life technologies, catalog Number(s) 11320033 , 11320074 , 11320082			
Sodium Phosphate dibasic (Na_2HPO_4)	142.0	71.02	0.50014085
Sodium Phosphate monobasic (NaH_2PO_4.H2O)	138.0	62.5	0.45289856
Zinc sulfate ($ZnSO_4$ .7H2O)	288.0	0.432	0.0015
Other components			
D-Glucose (Dextrose)	180.0	3151.0	17.505556
Hypoxanthine Na	159.0	2.39	0.015031448
Linoleic Acid	280.0	0.042	1.4999999E-4
Lipoic Acid	206.0	0.105	5.097087E-4
Phenol Red	376.4	8.1	0.021519661
Putrescine 2HCl	161.0	0.081	5.031056E-4
Sodium Pyruvate	110.0	55.0	0.5
Thymidine	242.0	0.365	0.0015082645

Formulation for Leibovitz's L-15 Medium.

Leibovitz's L-15 Medium, ATCC 30-2008	
Components	**Concentration (mg/L)**
Amino Acids	
L-Alanine	225.00
L-Arginine (free base)	225.00
L-Asparagine·H_2O	250.00
L-Cysteine (free base)	120.00
L-Glutamine	300.00
Glycine	200.00
L-Histidine (free base)	250.00
L-Isoleucine	125.00
L-Leucine	125.00
L-Lysine·HCl	93.70
L-Methionine	75.00
L-Phenylalanine	125.00
L-Serine	200.00
L-Threonine	300.00
L-Tryptophan	020.00
L-Tyrosine·2Na·2H2O	430.00
L-Valine	100.00
Vitamins	
Choline Chloride	1.00
Riboflavin-5-PO4·Na·2H2O	0.10
Folic Acid	1.00
myo-Inositol	2.00
Nicotinamide	1.00
D-Pantothenic Acid (hemicalcium)	1.00
Pyridoxine·HCl	1.00

Leibovitz's L-15 Medium, ATCC 30-2008	
Thiamine·PO4·Cl·2H2O	1.00
Inorganic salts	
$CaCl_2$ (anhydrous)	140.00
$MgCl_2$·6H2O	200.00
MgSO4 (anhydrous)	97.67
KCl	400.00
KH_2PO_4 (anhydrous)	60.00
NaCl	8000.00
Na_2HPO_4 (anhydrous)	190.00
Other components	
D-Galactose	900.00
Phenol Red, Sodium Salt	10.00
Sodium Pyruvate	550.00